THE IMPACT OF VISCOUS SELF-ASSEMBLED PHASE FORMATION ON THE AGEING AND ATMOSPHERIC LIFETIMES OF ORGANIC AEROSOL PROXIES

By

ADAM MILSOM

A thesis submitted to the University of Birmingham for the degree of

DOCTOR OF PHILOSOPHY

School of Geography, Earth and Environmental Sciences

College of Life and Environmental Sciences

University of Birmingham

July 2021

"All we have to decide is what to do with the time that is given us."

— Gandalf, The Fellowship of the Ring by J. R. R. Tolkien.

[43,000 words]

Abstract

Atmospheric aerosols are key components of the atmosphere. They nucleate cloud droplets and facilitate the transport of particle-bound components around the atmosphere. This has an impact on the climate and air quality. The phase state of atmospheric aerosols can affect their ability to form cloud droplets and their atmospheric lifetime. Organic compounds are found in aerosol emissions. Some of these compounds, such as fatty acids, are surface active and can affect the cloud formation potential of an aerosol particle. Specifically, oleic acid is an unsaturated fatty acid found as a major component of cooking emissions. Recently, a study on an oleic acid aerosol proxy has shown that the formation of viscous 3-D self-assembled nanostructures is possible, affecting oleic acid reactivity.

This thesis takes this novel concept of nanostructure formation in atmospheric aerosol proxies and aims to explore what the potential atmospheric impact could be. This was done by applying X-ray scattering techniques to levitated droplets and surface coatings of the fatty acid aerosol proxy. Development of a method for determining reaction kinetics from these measurements is presented along with a first quantification of the effect of self-assembly on reaction kinetics, later being extended to different nanostructures. Experiments on reactivity and water uptake described here probe the proxy from nanometre-scale films to micrometre-scale droplets and bulk mixtures, demonstrating the versatility of the range of experimental techniques used to probe the proxy. The atmospheric implications of nanostructure formation are discussed via numerical modelling and observations from experiments on these proxies, highlighting the potential impact on aerosol atmospheric lifetime and implications for the atmosphere.

Acknowledgements

I did not think that after starting in Reading autumn 2017, I would be finishing in Birmingham summer 2021!

Without funding from the NERC SCENARIO DTP (award number NE/L002566/1) and support from the CENTA DTP, this work would not have been possible. Many thanks to Wendy Neal at SCENARIO and Mica Jones at CENTA for providing admin support.

I have met and worked with a brilliant group of people over the course of my PhD. Without them, this thesis would not have been possible:

I would like to thank my main supervisor, Dr Christian Pfrang, for providing me this opportunity and for being a great support. I have enjoyed working with you, even when carrying out experiments at 2 am at Diamond fuelled by coffee or moving heavy equipment around the lab. Your general positive and calm demeanour is a real strength, especially when things do not go to plan and some improvisation was required! My co-supervisor, Dr Adam M. Squires (University of Bath), has also been brilliant. You were the first person I met in Reading at the SCENARIO interview day poster session. I must have left a good impression and I am still confused by the "Wotsit" question. Again, I have enjoyed presenting and discussing my work with you and Christian. I have really benefited from your ability to explain complex things concisely and with good examples. Thank you also for letting me use the SAXS instrument at Bath and being part of your group's Teams meetings during the pandemic. A big thanks goes to them too! Prof. Rob MacKenzie is thanked for becoming my Birmingham second supervisor. Thanks for your encouraging words at the GRS3 meetings.

Other group members past and present have been great friends and helpers. Kaan Alkan was particularly helpful at the beginning of my PhD, showing me the basics of the lab. Ben Woden provided an encyclopaedic knowledge of random things and was particularly fun to have beamtimes with. Random “5-minute” conversations with Curtis Gubb and others in the lab normally lasted a whole afternoon.

There have been numerous helpers at beamtimes. I particularly would like to thank Prof. Nick J. Terrill for continued support for all things SAXS at Diamond, along with the rest of the I22 beamline staff including Dr Andy Smith, Dr Tim Snow and Dr Olga Shebanova. Dr Andy D. Ward (Central Laser Facility) is also thanked for setting up and supporting Raman experiments at I22. A big thanks to Dr Maximilian W. A. Skoda, who introduced me (along with Ben Woden) to the world of neutrons and the perils of fitting models to the data. Thanks also goes to Dr Eleonore Mason for inviting me to her GI-SAXS beamtime to test out her humidity setup. It turned out to be very useful! Jacob Boswell has been a keen helper at beamtimes and remains the best at focussing the Raman laser.

Finally and most importantly, the people outside of work. I would like to thank my parents, Alan and Zahia, for deciding to get married and have two amazing and humble children. Thanks to Miriam for being my sister and a good support throughout. A special mention goes to Vera Çağlayan. I met you on day one of my PhD in Reading and since then you have changed many things for the better. You have been my anchor. Her papatya bana seni hatırlatıyor.

List of figures and tables

Figures:

Tables:

List of abbreviations

ACMW – Air-contrast-matched water

BDF – Backward differentiation formula

BMP – Bulk mixing parameter

BSR – Bulk saturation ratio

CCN – Cloud condensation nuclei

CPP – Critical packing parameter

DE – Differential evolution

DLS – Diamond light source

EDB – Electro-dynamic balance

FLIM – Fluorescence lifetime imaging microscopy

FWHM – Full width half-maximum

GI-SAXS – Grazing-incidence small-angle X-ray scattering

HOMEChem – House observations of microbial and environmental chemistry

IPCC – Intergovernmental panel on climate change

IR – Infra-red

KM-GAP – Kinetic multi-layer model of gas-particle interactions in aerosols and clouds

KM-SUB – Kinetic multi-layer model of aerosol surface and bulk chemistry

LLC – Lyotropic liquid crystal

MCMC – Markov chain Monte Carlo

MOCCIE – Modelling consortium for chemistry of indoor environments

NR – Neutron reflectometry

OA – Oleic acid

ODE – Ordinary differential equation

PAH – Polycyclic aromatic hydrocarbon

PAN – Peroxyacetyl nitrate

POA – Primary organic aerosol

POM – Polarising optical microscopy

PRA – Pöschl-Rudich-Ammann framework

RH – Relative humidity

RPi – Raspberry Pi

SAXS – Small-angle X-ray scattering

SLD – Scattering length density

SO – Sodium oleate

SOA – Secondary organic aerosol

STLR – Surface-to-total loss ratio

SVOC – Semi-volatile organic compound

UV – Ultra-violet

VOC – Volatile organic compound

WAXS – Wide-angle X-ray scattering

TABLE OF CONTENTS

1 CHAPTER 1: INTRODUCTION

1.1 The atmosphere

1.1.1 Atmospheric structure

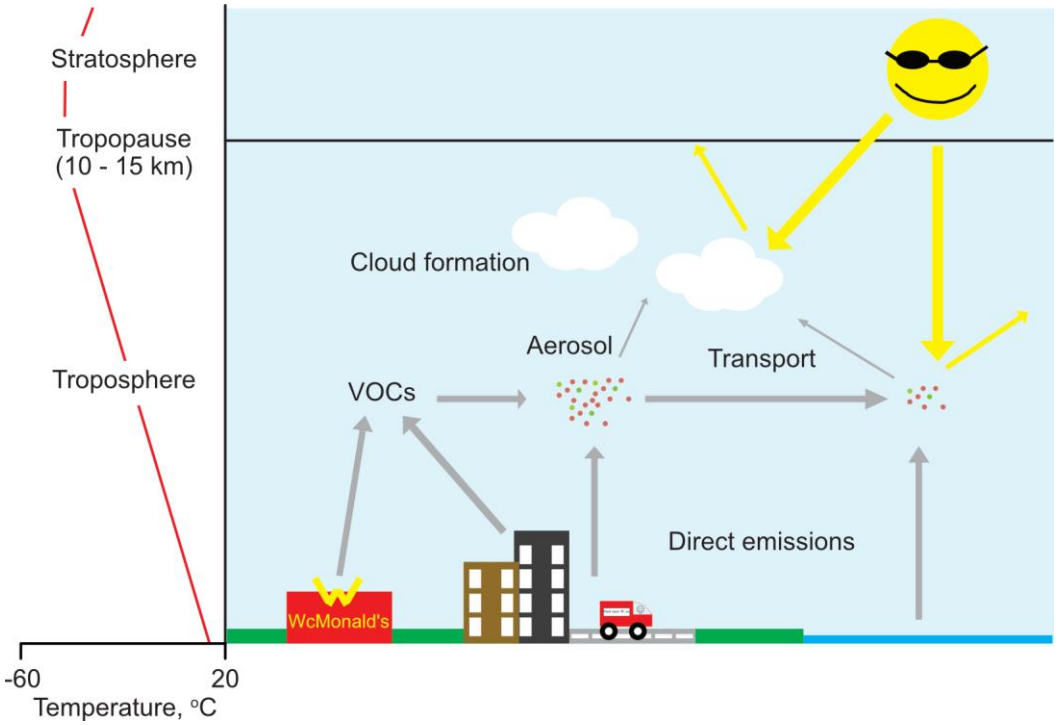

Figure 1-1. A schematic representation of aerosols in the atmosphere, focussing on the troposphere. Not to scale.

The word atmosphere comes from the Greek word *atmos* meaning 'vapour'. The atmosphere is therefore accurately described as a sphere of vapour (or gas). Going from the lowest altitude to the highest, the layers are named as: the troposphere (0 to 10-15km), stratosphere (from the tropopause to 45-55 km), mesosphere (from the stratopause to 80-90 km), thermosphere and the exosphere (Seinfeld and Pandis, 2006). Fig. 1-1 is a vertical cross-section of the atmosphere, focussing on aerosols in the troposphere.

The two layers focussed on in atmospheric chemistry are the troposphere and stratosphere. The troposphere extends from 0 to 10-15 km altitude depending on the time of year. There is a decrease in temperature with height and mixing within this

region is rapid. In the stratosphere temperature increases with altitude, meaning vertical mixing in this layer is slow.

The troposphere contains ~ 80% of the mass of the atmosphere (Seinfeld and Pandis, 2006). It is the most changeable and directly affected layer with respect to human impacts. Anthropogenic pollutants are emitted directly into the troposphere. Clouds formed in the troposphere can reflect the sun's radiation and their formation is affected by human activity (Boucher et al., 2013). It is therefore clear that a better understanding of the chemistry of this layer is necessary to be able to explain current and future climate behaviour and observations on a range of timescales. The focus of this thesis is on proxies for aerosols emitted into the troposphere.

1.1.2 Temperature, humidity and pressure

Temperature decreases in the troposphere with a dry lapse rate of 9.7 K km^{-1} (Seinfeld and Pandis, 2006). Relative humidity (RH) is defined as the ratio of the partial pressure of water vapour (p_{water}) with the saturation vapour pressure of water at that temperature (p^{o}_{water}).

$$RH = 100 \times \frac{p_{water}}{p^{o}_{water}} \quad (1\text{-}1)$$

The saturation vapour pressure of water is dependent on temperature. A rising parcel of air will increase in RH quite rapidly – resulting in saturation and eventual cloud droplet formation. Atmospheric chemistry experiments therefore need to take RH into account.

Pressure decreases with altitude and is defined as the force per unit area (N m^{-2} or Pa) that a vertical column of air exerts on a particular point at a defined altitude. It therefore has a mass and acceleration (due to gravity) dependence. This column of air has an imaginary top where the pressure (and mass) at that altitude is zero. At ground level,

atmospheric pressure is at a maximum for a column of air directly above that point. If one were to move higher in altitude in that column of air, the atmospheric pressure would be smaller because the mass of the air above that point is smaller than it was at ground level.

1.1.3 **Oxidants**

The three major oxidants in the atmosphere are ozone (O_3), OH and NO_3 (Chapleski et al., 2016; Seinfeld and Pandis, 2006). O_3 and OH are the most important oxidants during the daytime because their production mechanisms are photochemical in nature (Finlayson-Pitts and Pitts, 2000).

O_3 is a natural reactive oxidant produced in the atmosphere. Stratospheric O_3 is a vital part of the Earth's structure as it provides a natural barrier to high-energy solar UV radiation. This stratospheric 'ozone layer' is a term familiar to many.

O_3 concentrations in the troposphere can vary from 10 ppb in pristine sea-level conditions (Seinfeld and Pandis, 2006) to > 100 ppb in particularly polluted areas, with indoor concentrations generally mirroring the trends observed outdoors (Weschler, 2000).

Anthropogenic O_3 is produced mainly by reaction of O_2 with ground state $O(^3P)$ radicals that result from photolytic dissociation of NO_2 (Finlayson-Pitts and Pitts, 2000).

$$NO_2 \xrightarrow{h\nu} NO + O(^3P)$$

Reaction 1. Formation of $O(^3P)$ from NO_2.

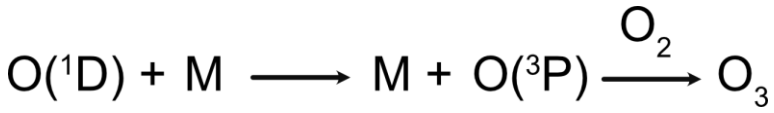

Reaction 2. Formation of O_3 radical from $O(^1D)$, $O(^3P)$ and a non-reactive species "M".

The interaction of aerosols with ozone, particularly in the troposphere, is a well-established area of aerosol research. This thesis features studies carrying out ozonolysis on an organic aerosol proxy, following reaction kinetics and nano-structural changes.

OH radical production in the atmosphere depends on the photolysis of tropospheric O_3 to form an excited singlet oxygen atom ($O(^1D)$). This excited species goes on to react with water to produce two molecules of OH (Seinfeld and Pandis, 2006).

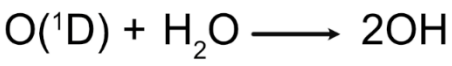

Reaction 3. Formation of OH radical from an excited singled oxygen and water.

If water is not present in this system, then the O atom can recombine with a molecule of O_2 to reform O_3. This is termed a null cycle and happens alongside the production of OH. Reaction 3 implies that at higher tropospheric relative humidity, the production of OH radical would also be higher. This reaction will happen in the day time due to the photochemical activation of an O_3 molecule which is crucial for the production of an excited singlet $O(^1D)$.

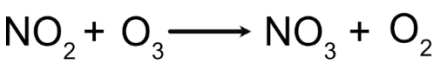

Reaction 4. Formation of NO_3 radical from NO_2 and O_3.

Nitrate radicals (NO_3) are formed by the reaction of NO_2 with O_3 (Reaction 3). They dominate oxidation at night time due to the lack of photo-induced production and the fact that NO_3 is photo-labile, allowing concentrations to build-up during the night. NO_3

absorbs light strongly in the red region (620-670 nm) (Finlayson-Pitts and Pitts, 2000). This makes it capable of being detected by conventional spectroscopy (Becerra and Pfrang, 2016). This oxidant has been reviewed in detail with respect to its physics, chemistry and the atmosphere by Wayne *et. al.* (Wayne et al., 1991) and, along with OH (Heard and Pilling; 2003), is not studied in this thesis. These two species have lifetimes in the sub-second to second range. These lifetimes are short compared with ozone, which has a tropospheric half-life in the order of days (Goldberg et al., 2015).

1.2 Atmospheric aerosols

1.2.1 Sources and composition

Aerosols are suspensions of condensed phase matter in a gas, with sizes ranging from the nanometre to the micrometre scale for those of atmospheric relevance (Seinfeld and Pandis, 2006). They are formed either by direct emission into the atmosphere (primary aerosol) or by condensation of gaseous precursors such as volatile and semi-volatile organic compounds (VOCs and SVOCs) (secondary aerosol).

Aerosols of atmospheric relevance can range from a few nm to ~ 10 μm in diameter. They can be broadly separated into "fine" (< 2.5 μm) and "coarse" (> 2.5 μm) modes (Seinfeld and Pandis, 2006). Particulate matter with a diameter < 2.5 μm is denoted as $PM_{2.5}$. Aerosols up to a size of ~ 100 nm are in the nucleation and Aitken modes, produced by the condensation of hot vapours and new particle nucleation. Loss due to coagulation with other particles dominates. Between 100 nm and 2.5 μm is the accumulation mode, where droplets are formed and grow by condensation around nuclei and coagulation with smaller particles.

Coarse particles are generally produced mechanically by processes such as volcano eruptions, dust transported by the wind and sea sprays (Seinfeld and Pandis, 2006). These are also examples of primary emissions, which dominate the coarse mode.

Atmospheric aerosols can be transported over long distances. This is exemplified by the recent observation of smoke from a Californian wildfire over Leipzig, Germany (Baars et al., 2021). This is a distance of over 9,000 km.

Aerosol composition can vary with environment, location, season and time (Fu et al., 2008; Jimenez et al., 2009; Li et al., 2021; Wang et al., 2020a, 2020b) and can be broadly split into an inorganic and organic fraction. The inorganic fraction can include metals, metal salts, sulfur- and nitrogen-containing salts (Kirpes et al., 2019; Li et al., 2018; Zhao et al., 2020). The organic fraction includes a host of molecules with a range of functionalities such as: polycyclic aromatic hydrocarbons (PAHs) – harmful to human health; alkyls, alkenes, alcohols, sugars and fatty acids (Chan and Yao, 2008; Vicente et al., 2021). Primary organic aerosols are referred to as POA, whereas secondary organic aerosols are referred to as SOA.

Aerosols are also present in the indoor environment (Abbatt and Wang, 2020; Patel et al., 2020). Common activities such as cooking and cleaning emit a range of compounds, some of which can go on to form indoor aerosols (Mattila et al., 2020). This is becoming a hot topic as relatively little is known about the evolution of indoor air pollution compared with the outdoor environment. This has motivated recent large-scale and long-term research projects such as the Modelling Consortium for Chemistry of Indoor Environments (MOCCIE) (Shiraiwa et al., 2019) and House Observations of Microbial and Environmental Chemistry (HOMEChem) projects (Farmer et al., 2019).

Cooking particulate emissions can comprise a range of molecules and the ageing of cooking emissions has been followed in real-time on the indoor (Zeng et al., 2020) and urban scale (Wang et al., 2020a). A common theme coming from these cooking emission studies is the presence of fatty acid molecules in large amounts, including oleic acid. In the studies presented in this thesis, this point is emphasised regularly. Processes that affect the properties of oleic acid, such as chemical reactivity and hygroscopicity, are likely to impact particulate matter containing oleic acid.

1.2.2 **Atmospheric impact**

Cloud droplet formation is described by Köhler theory (Köhler, 1936). Essentially, it describes the supersaturation (RH > 100 %) needed for a droplet to grow. This equilibrium supersaturation is a function of the radius of and chemical composition of the particle. Although the effect of organic material on cloud droplet formation is more complex (Kanakidou et al., 2005), traditional Köhler theory describes the fundamental factors determining cloud droplet nucleation.

At equilibrium, the chemical potential of the water vapour above a droplet at a given diameter (D_p) and that within the aqueous phase is equal. There is no net movement of water molecules across the phase boundary. The general Köhler equation is presented below and it defines the equilibrium ambient water saturation ratio (p_{water} / p^o_{water}) (Seinfeld and Pandis, 2006).

$$ln\left(\frac{p_{water}}{p^o_{water}}\right) = \frac{A}{D_p} - \frac{B}{D_p^3} \quad (1\text{-}2)$$

A/D_p describes the effect of curvature (the Kelvin effect):

$$A = \frac{4M_{water}\,\sigma_{water}}{RT\,\rho_{water}} \quad (1\text{-}3)$$

Where M_{water} is the molar mass of water; σ_{water} is the surface tension of water; R is the gas constant; T is temperature and ρ_{water} is the density of water.

B/D_p^3 describes the effect of a solute (the Raoult effect):

$$B = \frac{6n_s M_{water}}{\pi \rho_{water}} \quad (1\text{-}4)$$

Where n_s is the number of moles of solute. Larger particles increase the likelihood of droplet growth by decreasing the saturation ratio. The relationship between surface tension (free energy) and droplet diameter is governed by the Kelvin effect. Indeed, the Kelvin effect predicts that it cannot rain as the surface energies associated with the formation of the smallest of water droplets are too high and therefore the droplets would not exist for long enough to grow. This limitation of the Kelvin effect is addressed by the presence of nucleating species, such as atmospheric aerosol particles, to facilitate droplet growth and therefore enable the existence of clouds and precipitation.

The Raoult effect is the effect that adding a solute to a solvent has in reducing the vapour pressure above the liquid, inferring that this decreases the amount of water being lost from a droplet. If this is so, then increasing the molarity of the salt in the droplet therefore decreases S_{eq} and droplet growth may happen at lower supersaturations.

Note that the Kelvin effect scales with $1/D_p$ whereas the Raoult effect scales with $1/D_p^3$. This therefore means that the Raoult effect drops off quickly as the droplet grows.

The addition of organic molecules, specifically surfactants, to a droplet has effects on both the Kelvin and Raoult terms. This is discussed in 1.2.4.

There is a clear link between atmospheric aerosols and clouds. Indeed, a whole chapter of the Intergovernmental Panel on Climate Change (IPCC) 5th report is entitled “Clouds

and Aerosols" (Boucher et al., 2013). Clouds are formed by condensation of water vapour onto cloud condensation nuclei (CCN), which themselves are aerosols.

A key interaction between aerosols and clouds is their effect on cloud droplet concentration. A large aerosol concentration can cause a larger number of smaller droplets to form (Fan et al., 2018). Smaller droplets scatter light of shorter wavelengths more efficiently and therefore affect cloud radiative forcing via a change in cloud albedo (reflectivity) (Seinfeld and Pandis, 2006). Aerosol-cloud interactions represent a large uncertainty in estimating the indirect climate forcing effect of aerosols (Penner et al., 2011). This marriage between aerosols and clouds therefore has implications for the climate. It follows that processes affecting an aerosol's CCN ability, such as oxidation and water uptake, would have indirect climatic effects.

Oxidation of the organic matter in aerosol particles can induce cloud droplet activation via the increased hygroscopicity of the oxygenated products (Slade et al., 2017). This is due to the increased hydrophilicity of the polar functional groups formed during oxidation (Farmer et al., 2015). A linear increase of hygroscopicity with aerosol O:C ratio has been determined at urban sites, highlighting this relationship between oxidation state and hygroscopicity from field measurements (Hong et al., 2018; Wu et al., 2016). Though aerosol hygroscopicity is dominated by the inorganic fraction, the uncertainties associated with the organic fraction are still to be resolved.

Virtanen *et al*. reacted pine VOCs with different oxidants, resulting in SOAs with different particle diameters (Virtanen et al., 2010). O_3-oxidised particles were much smaller than OH-oxidised ones. This variation in size distribution could have

implications for the size-dependent scattering properties of atmospheric aerosols and therefore atmospheric albedo (Finlayson-Pitts and Pitts, 2000).

There is a link between the aerosol age, organic fraction and the hygroscopicity of tropospheric aerosols (Gunthe et al., 2011). Generally, a higher organic fraction decreases the hygroscopicity of aerosols due to the hydrophobic nature of organic molecules. For example recently, cooking organic aerosols have been linked with decreased aerosol hygroscopicity and CCN ability (Liu et al., 2021). A review on the hygroscopicity of tropospheric aerosols at various locations in China has highlighted the uncertainty regarding the effect of the organic fraction on aerosol hygroscopicity (Peng et al., 2020). Some studies have suggested that organics make a substantial contribution to aerosol water content, such as the findings of Jin *et al.* who estimated that organic material contributed to 30 ± 22 % to aerosol water content in urban Beijing, China (Jin et al., 2020). Others suggest that there is a limited contribution of organics to the hygroscopicity of aerosols (*e.g.* Ding *et al.* – measurements and predictions of hygroscopicity) (Ding et al., 2019).

This thesis investigates the effect on both oxidation kinetics and water uptake of nanostructure formation in an aerosol proxy, with climatic implications arising from the logic presented here.

1.2.3 **Aerosol phase state**

Aerosol phase state (solid, semi-solid or liquid) can influence aerosol heterogeneous processes such as oxidation and water uptake via differences in particle viscosity and small molecule diffusivity through them (Koop et al., 2011; Reid et al., 2018; Shiraiwa et al., 2011). Globally, aerosol phase state is variable and is determined by a number of

factors including local meteorology, season and particle composition (Schmedding et al., 2020; Shiraiwa et al., 2017; Slade et al., 2019; Virtanen et al., 2010). Indoor aerosol phase state is also variable (Cummings et al., 2020). In viscous states, gas-particle interactions are reduced and the rate of particle ageing is diminished (Berkemeier et al., 2016; Mikhailov et al., 2009; Zhou et al., 2019).

Viscous phases induce diffusion gradients during water uptake, contributing to an increased equilibration time for such particles (Renbaum-Wolff et al., 2013; Zobrist et al., 2011). Particle viscosity has also been observed to increase with oxidation (Hosny et al., 2016). Such phase gradients have been observed in this thesis (see chapter 7).

Harmful aerosol components such as peroxyacetyl nitrates (PANs) and PAHs can be transported far from their sources (Kang et al., 2017; Zhang et al., 2009). The transport of PAH-containing particulate matter has been linked with an increased risk of ill-health; it was suggested that the formation of a viscous organic layer, protecting the particle's contents, contributed to the protection of PAHs (Shrivastava et al., 2017). The overall phase state of a particle, dependent on temperature and humidity, can also effect the long-range transport of such molecules (Mu et al., 2018).

1.2.4 Surfactant aerosols

Surfactants are surface active molecules which are characterised by a hydrophilic head and hydrophobic tail (Shaw, 1992) (see Fig. 1-3 in section 1.3.1). In aqueous media, they tend to concentrate at the air-water interface, with their hydrophobic tails pointing into the air. This changes the surface free energy of a water droplet by shielding the strong interactions between surface water molecules. The result is a decrease in surface tension.

Surface coatings have been identified on atmospheric aerosol samples, some of which include surface active molecules such as fatty acids (Kirpes et al., 2019; Tervahattu, 2002; Tervahattu et al., 2005). They are also present in biogenic sources such as pollenkitt, found on the surface of pollen grains (Prisle et al., 2019). Surface active material has been linked with an increase in CCN ability of aerosol samples (Facchini et al., 1999, 2000; Nguyen et al., 2017). This is due to the decrease in droplet surface tension caused by the surfactants, which causes the Kelvin effect to dominate CCN formation (Bzdek et al., 2020; Ovadnevaite et al., 2017). The representation of surface activity in global modelling of cloud activation remains a challenge and is dependent on how surfactant surface-bulk partitioning is represented (Lowe et al., 2016; Prisle et al., 2012).

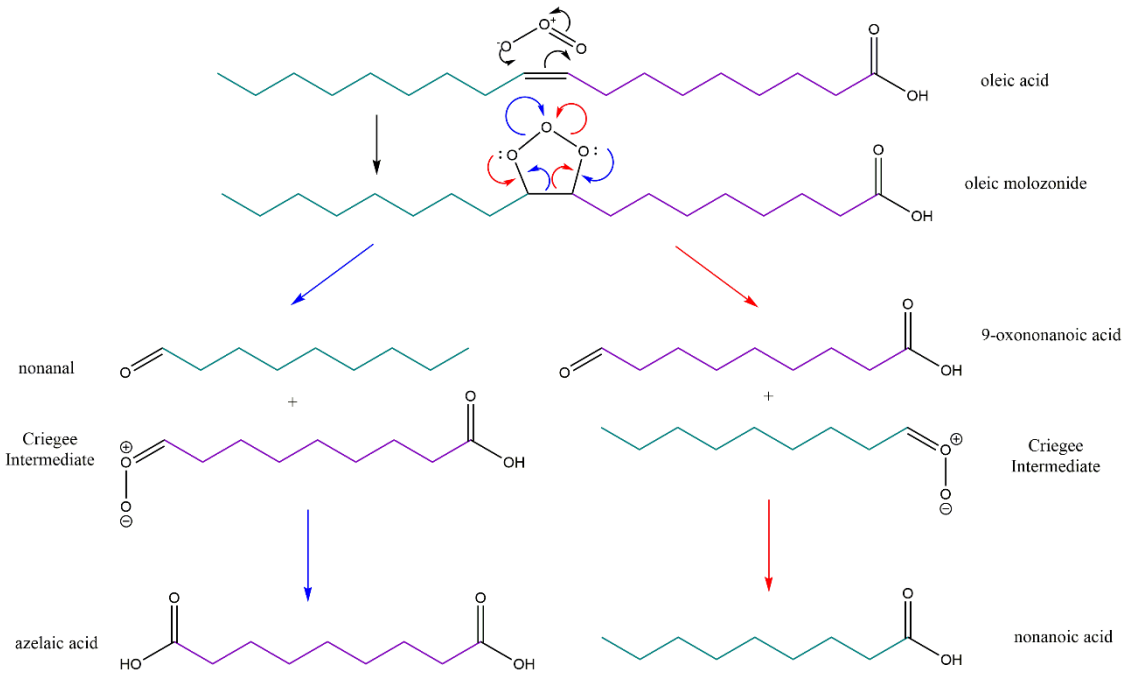

Figure 1-2. Oleic acid ozonolysis reaction scheme showing the breaking of the C=C bond and the formation of the major reaction products: Nonanal, 9-oxononanoic acid, azelaic acid, nonanoic acid and Criegee intermediates. Reproduced from Woden et al. (2021) under the Creative Commons Attribution 4.0 License.

Fatty acids are surfactants used as markers for cooking emissions (Wang et al., 2020a). They are found in common cooking oils such as olive oil (Zahardis et al., 2006b) and have been detected as an emission from different types of cuisine (Alves et al., 2020; Vicente et al., 2021; Zeng et al., 2020). Two of the most common fatty acids emitted by cooking are stearic acid and its unsaturated analogue, oleic acid (Fig. 1-2) (Wang et al., 2020a). In particular, oleic acid has been the proxy of choice for a reactive organic aerosol due to its abundance in aerosol marine and cooking emissions and being readily available (Hearn et al., 2005; Milsom et al., 2021; Pfrang et al., 2017; Woden et al., 2021; Zahardis and Petrucci, 2007). This thesis focusses on an oleic acid-based proxy for organic aerosols.

Oleic acid has been identified in organic coatings and on the surface of atmospheric aerosols (Kirpes et al., 2019; Tervahattu et al., 2005). Coatings of organic material on indoor surfaces have been observed as a result of cooking, with qualitative evidence that fatty acids are present (Or et al., 2020; Schwartz-Narbonne and Donaldson, 2019). These films are likely to include oleic acid because of its abundance in most cooking emission studies. A recent study followed the evolution of indoor cooking emissions and observed oleic acid decay and the appearance of decay products in real-time (Zeng et al., 2020). During another recent indoor air pollution campaign in a residential flat, oleic acid was measured to be ~ 2.5-fold more abundant indoors compared to outdoors and, again, reactant and product evolution was observed (Lyu et al., 2021).

Oleic acid ozonolysis is one of the bread-and-butter reactions used to simulate the oxidation of organic material in the atmosphere (Zahardis and Petrucci, 2007). This reaction is summarised in Fig. 1-2 and shows the formation of the primary ozonolysis products: nonanal, 9-oxononanoic acid, nonanoic acid, azelaic acid and Criegee intermediates. In particular, 9-oxononanoic acid and azelaic acid have been used as markers for oleic acid oxidation (Lyu et al., 2021; Zeng et al., 2020).

The Criegee intermediates produced by the initial reaction can go on to form higher molecular weight products. The formation of high-molecular-weight reaction products has been confirmed (Reynolds et al., 2006; Zahardis et al., 2006a) and has been linked with an increase in particle viscosity (Hosny et al., 2016). These molecules are also thought to make up a viscous crust of material which acts as a diffusive barrier to oxidation, a concept gaining some traction in recent literature (Pfrang et al., 2011; Zhou et al., 2013, 2019). In this thesis, an experimental observation of a surface layer is

presented along with some modelling evidence of the inhibition of oxidation by such a surface layer (see chapters 3 and 7).

Some of the reaction products, namely azelaic acid and nonanoic acid, are surface active (King et al., 2009; Tuckermann, 2007). With surface active material acting as both reactants and products, processes which affect the oxidation of oleic acid would have implications for the amount of surfactant present in an aerosol. This would also have an effect on aerosol hygroscopicity via changes to the Raoult effect (a colligative property) and the Kelvin effect, discussed previously. Ozonolysis of oleic acid monolayers on an aqueous surface showed that a surface active product film persisted after oxidation at low temperature (Woden et al., 2021). This study provided experimental evidence that oleic acid ozonolysis products can remain at the air-water interface. This concept is further explored in a study on coatings of a semi-solid form of oleic acid in capillary tubes arising from this thesis, showing that unreacted surfactant material remains after extensive oxidation (see chapter 2) (Milsom et al., 2021).

Wang and Yu recently used atmospheric measurements to estimate oleic acid atmospheric reactive lifetime of oleic acid against ozone to be ~1 – 6 h, dependent on ambient conditions and based on atmospheric measurements (Wang et al., 2021). This increases to ~14 h after subsequent ageing of the cooking aerosol. Their estimated lifetimes are longer than corresponding laboratory experiments: e.g. at 50 ppb ozone, oleic acid lifetimes are 89 min (ambient) and 78 min (laboratory measurements at the air-water interface, King et al. 2009). Their ambient measurements the decay rate of the *trans* isomer of oleic acid (elaidic acid) was 0.62 of measured oleic acid decays, they point towards “stearic configuration” as an explanation. This thesis explores molecular

self-organisation as a possible explanation of the increased atmospheric lifetime of oleic acid.

1.3 Self-assembly of surfactant lipids

1.3.1 Lyotropic liquid crystal (LLC) phase formation

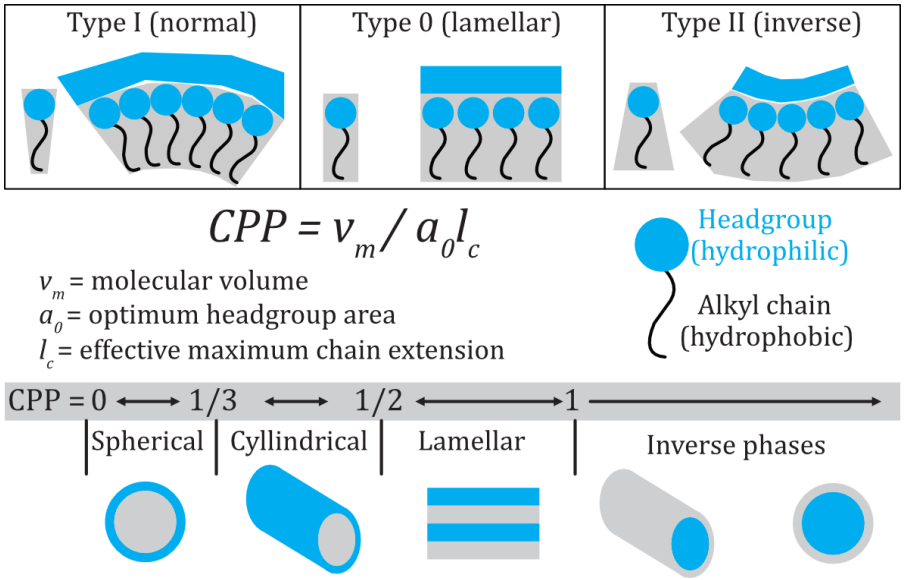

Figure 1-3. A schematic representation of lipid LLC phase formation, defining the critical packing parameter (CPP) which determines which LLC phase forms. Based on Kulkarni et al. (2011).

Lipid surfactants, such as oleic acid and sodium oleate, can form self-assembled nanostructures in contact with water. These are called lyotropic liquid crystal (LLC) phases (Tiddy, 1980). These phases are split into “oil-in-water” (type I - normal) and “water-in-oil” (type II - inverse) phases. All of the phases studied in this thesis are inverse (type II) topology phases, where there is an excess of organic material in the liquid crystal structure (see Fig. 1-3).

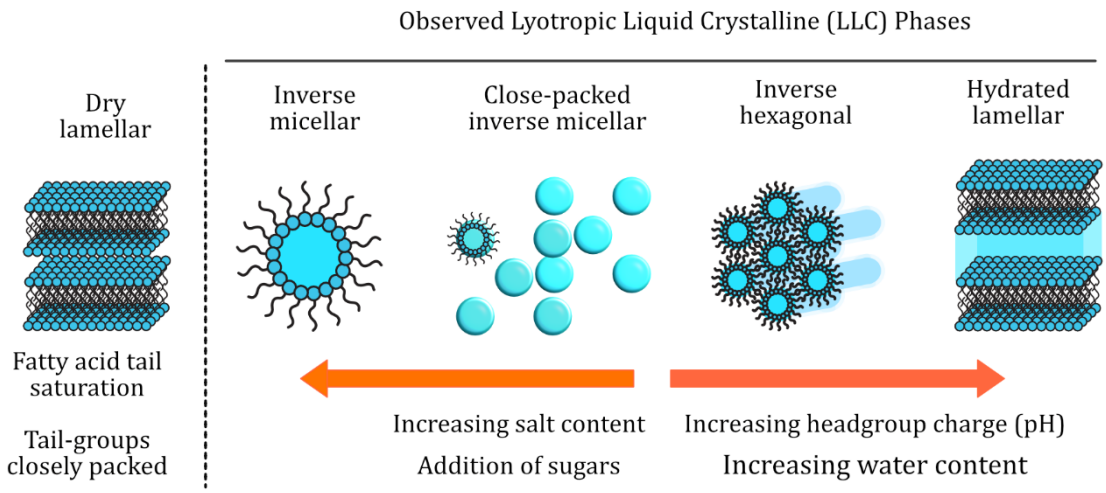

Figure 1-4. Cartoons of the LLC phases observed in this thesis along with indications of how phases change with mixture composition.

The lamellar phase consists of a 1-D stack of lipid bilayers which can exist as fluid, gel or crystalline types. The hydrocarbon chains are hidden from the water interface. The inverse hexagonal phase is a collection of cylindrical micelles arranged on a 2-D lattice. The close-packed inverse micellar phase is a collection of spherical micelles fixed on a 3-D lattice with a particular symmetry (*e.g.* Fd3m) (Seddon et al., 1990). The disordered inverse micellar phase consists of inverse micelles which are not close-packed and are less restricted in their movement. A schematic of these phases is presented in Fig. 1-4 and chapter 6 explores the phase space accessible to the fatty acid proxy studied in this thesis.

The formation of each phase depends on the size and shape of the surfactant molecule. In particular the relationship between surfactant headgroup area (a_0), length of the

surfactant chain (l_c) and surfactant volume (v_m) is key in determining the resulting LLC phase. These factors are related through the critical packing parameter (CPP), also known as the shape factor (Kulkarni et al., 2011).

$$CPP = \frac{v_m}{a_0 l_c} \tag{1-5}$$

When the CPP is < 1, normal topology phases are formed. CPP > 1 means that inverse topology phases form. CPP = 1 is the lamellar phase, which has no curvature. The phases studied in this thesis all have a CPP ≥ 1.

Thermodynamically, the structure formed at a given composition is the structure with the lowest free energy of inter- and intra-aggregate interactions (Tiddy, 1980).

$$F_{total} = F_{intra} + F_{inter} \tag{1-6}$$

$$F_{intra} = F^{el} + F^{s} + F^{chain} \tag{1-7}$$

$$F_{inter} = F^{el} + F^{vdw} + F^{hyd} \tag{1-8}$$

Using the notation of Tiddy, the total free energy of interaction (F_{total}) for each LLC phase under the same conditions is the sum of the free energies of inter- (F_{inter}) and intra-aggregate (F_{intra}) interactions.

F_{intra} has contributions from: (I) the electrostatic forces between ionic surfactants and counter-ions (F^{el}) - the ionic strength of the aqueous phase would therefore affect the energy of this interaction; (II) From steric repulsion between adjacent headgroups and between alkyl chains at the surface of the aggregate (F^{s}) – the effective headgroup area can change with headgroup charge and the addition of additives to the system (see chapter 5 and 6) (Kulkarni et al., 2011); and (III) The conformation of the alkyl chains, which pack differently for each nanostructure (F^{chain}).

F_{inter} has contributions from: (I) F^{el}; (II) van der Waals attraction forces between aggregates (F^{vdw}); and forces mediated by the solvent (F^{hyd}).

There are therefore a number of factors at play when considering LLC phase formation. At the same temperature and pressure, the key parameters determining the geometry of the LLC phase (a_0, l_c and v_m) are influenced by the headgroup charge (*e.g.* pH of the system), nature of the surfactant (*e.g.* unsaturated vs. saturated fatty acid) and additives added to the aqueous phase (*e.g.* addition of sugars and NaCl to the system). See chapter 6 for an exploration of the phase space accessible to the oleic acid-sodium oleate proxy.

The viscosity of LLC phases can vary by orders of magnitude and exhibit complex viscoelastic behaviour (Mezzenga et al., 2005). When a constant stress is applied, viscous materials strain (deform) linearly with time whereas elastic materials respond immediately to the stress and return back to their original state once the stress is removed. Viscoelastic materials have properties of both. Back-of-the-envelope calculations of the complex viscosity derived from measurements of the rheology of LLC phases give values of ~ 10^5 Pa s for the close-packed inverse micellar phase (Fd3m symmetry), ~ 10^4 Pa s for the inverse hexagonal phase, and ~ 10^2 Pa s for the hydrated lamellar phase (Mezzenga et al., 2005; Pfrang et al., 2017). These values are firmly in the semi-solid regime and have implications for the atmospheric processing of such material due to the reduced diffusivity of small molecules such as ozone and water through such media (Shiraiwa et al., 2011).

1.3.2 Small-angle X-ray scattering (SAXS)

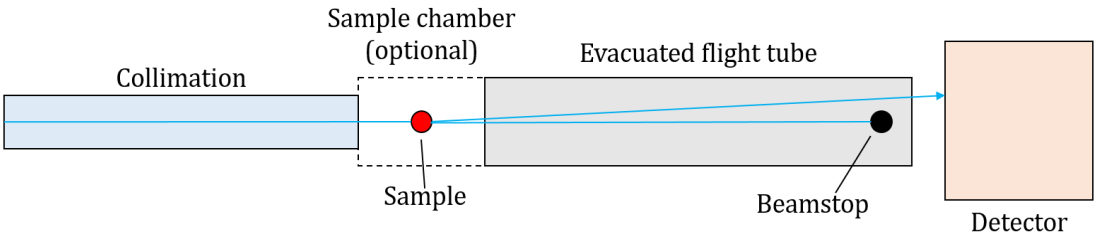

Figure 1-5. Schematic of the SAXS experiment. Based on Pauw (2013).

SAXS is an X-ray scattering technique which probes aggregate materials on the nanoscale (~ 1 – 70 nm resolution) (Pauw, 2013; Putnam et al., 2007). Scattering arises from the difference in electron density between two media. The larger this contrast, the more intense the scattering.

LLC phases return Bragg scattering peaks in the SAXS pattern, which is a plot of scattered intensity vs momentum transfer (q). q is related to the spacing between equivalent scattering planes (d) (Putnam et al., 2007).

$$q = \frac{2\pi}{d} \tag{1-9}$$

$$d = \frac{\lambda}{2\sin(\theta)} \tag{1-10}$$

d is related to the scattering angle (2θ) and X-ray wavelength (λ) via the Bragg equation (Eq. 1-10). From these measurements, nano-structural parameters can be calculated such as the spacing between lamellar bilayers and the size of spherical micelles (Kulkarni et al., 2011). The change in d-spacing measured as a function of humidity exposure is exploited in chapter 5 for different nanostructures in order to estimate nanostructure hygroscopicity.

A schematic of the basic SAXS experiment is presented in Fig. 1-5. Essentially, a collimated X-ray beam is directed at a sample and scattered X-rays are detected by a 2-D detector a certain distance away from the sample – the sample-to-detector distance. A beam-stop is required just before the detector because most X-rays are not scattered and over-exposure of the detector to this radiation can cause damage. This is especially true where there is a very high intensity synchrotron X-ray source.

Synchrotron SAXS experiments allow for flexibility in the sample environment. Laboratory-based SAXS instruments require a vacuum due to the scattering contribution of ambient air. Samples need to be in vacuum-proof containers. This is not required for synchrotron SAXS experiments because scattering from the sample is easily distinguishable from any background air scattering, thus allowing for an ambient condition sample environment such as the acoustic levitator used in this thesis and preceding work (Pfrang et al., 2017; Seddon et al., 2016). The I22 beamline at the Diamond Light Source (UK) specialises in SAXS experiments with versatile sample environments (Smith et al., 2021).

Experiments closely related to SAXS are Grazing-Incidence (GI)-SAXS (Narayanan and Konovalov, 2020) and Neutron Reflectometry (NR) (Penfold and Thomas, 1990). These techniques follow the same principles as SAXS with the addition that very small angles of incidence are used (~ 0.4 º for GI-SAXS; ~ 0.5 – 2.5 º for NR). This allows us to probe the structure of materials at the surface, measuring the orientation of LLC phases and providing a depth-resolved surface structure. These techniques are used and described in more detail in chapter 2 and 4 to study films deposited on silicon substrates subjected to simulated atmospheric processing. Schematics of these techniques are also presented in chapter 4.

1.3.3 Atmospheric context

The concept of surfactant aggregation in an atmospheric aerosol context is a relatively novel and understudied one. Tabazadeh presented a theoretical study on the possibility of micelle formation in organic aerosols containing anionic surfactants (Tabazadeh, 2005). In that study, the author relates micelle formation with the removal of an organic layer coating the surface of sea spray aerosols and with the apparent decrease in reactivity of organics in atmospheric aerosols (Maria et al., 2004). It was assumed that only normal topology micelles were formed and physical experiments were not carried out to support the theory.

More recently, the possibility of LLC phase formation was explored by taking advantage of the synchrotron SAXS experiment in combination with acoustic levitation (Pfrang et al., 2017; Seddon et al., 2016). Here, an oleic acid-sodium oleate proxy, which is the basis for the proxy used in this thesis, was shown to assume a range of LLC phases under different humidity conditions. This slowed down oleic acid ozonolysis kinetics. The atmospheric implications of which have previously been discussed and are highlighted in the studies forming this thesis.

1.4 Experimental methods for aerosol proxies

This thesis presents laboratory experiments on a fatty acid aerosol proxy. An overview of the laboratory-based techniques commonly used to probe such samples is presented here.

1.4.1 Coatings

As a surfactant, oleic acid and other atmospheric surfactant molecules have been studied as a monolayer at the air-water interface and probed by NR (King et al., 2020; Pfrang et al., 2014; Sebastiani et al., 2018; Woden et al., 2018, 2021). If deuterated, a special mixture of D_2O and H_2O can be used as the aqueous sub-phase which matches the neutron scattering ability of the air. This means that an NR experiment on such a system, consisting of a monolayer of deuterated oleic acid floating on air-contrast-matched water (ACMW), would return a signal that can only come from the floating monolayer. This makes NR a particularly sensitive technique. Recent work (in which this author was involved) has demonstrated the utility of this method, where a film of deuterated products persisted after ozonolysis of oleic acid monolayers at low (close to 0 ^{o}C) temperatures (Woden et al., 2021). The low-background characteristic of NR enabled this observation. A study presented in chapter 4 of this thesis presents NR data from a film of oleic acid-sodium oleate deposited on solid silicon substrates, linking the 2-D monolayer work with the 3-D investigations carried out in this thesis. NR is described in more detail in that study.

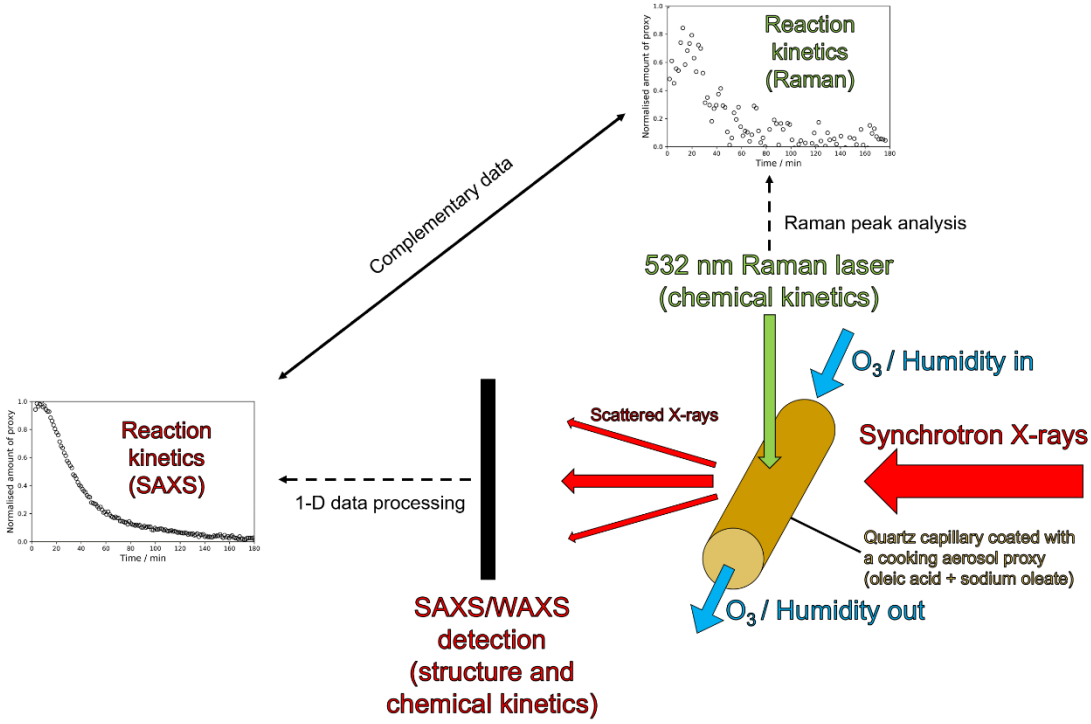

Figure 1-6. Schematic of the coated capillary simultaneous SAXS/WAXS-Raman experiments carried out at the Diamond Light Source.

Quartz capillary coatings of aerosol proxies have the advantage that their environment is highly controllable, with fast changes in RH and ozone concentration possible (Fig. 1-6). In combination with a synchrotron SAXS experiment and simultaneous Raman spectroscopy, time-resolved structural and kinetic data can be obtained (Milsom et al., 2021; Pfrang et al., 2017; Seddon et al., 2016). Moreover, the intense nature of synchrotron X-rays allows SAXS patterns to be collected in ~ 1 s, depending on the sample. The sample can be translated so that different sections along the capillary are probed. This is the basis for chapter 2 and 5, where changes in the SAXS pattern with ozone exposure and humidity change were observed and combined with simultaneous Raman spectroscopy in order to assess the reactivity and hygroscopicity of these nanostructured fatty acid aerosol proxies.

1.4.2 **Single-particle levitation**

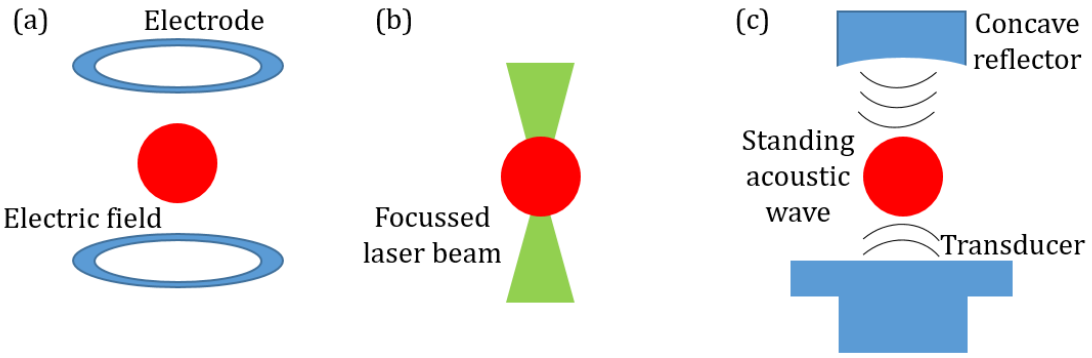

Figure 1-7. Schematic representations of three common methods of single-particle levitation. (a) Electro-dynamic levitation; (b) Optical levitation; (c) Acoustic levitation.

Single-particle techniques allow the experimentalist to probe what happens to a single aerosol particle when subjected to atmospheric processing (Krieger et al., 2012). This removes the averaging effect that analysing ensemble aerosol samples has on the experimental results.

The levitation of single particles has been a method of choice for study in the laboratory (Mason et al., 2007). This has the advantage of a contactless sample environment, removing any effect a deposition surface might have on the process being studied, such as crystallisation. The accessibility of a levitated droplet has enabled a range of techniques to be used in conjunction with levitation including: Mie scattering (Zobrist et al., 2011), Raman spectroscopy (Davies and Wilson, 2016; Gallimore et al., 2018), mass spectrometry (Westphall et al., 2008), X-ray scattering (Pfrang et al., 2017; Seddon et al., 2016) and other spectroscopic techniques (Cohen et al., 2020; Jones et al., 2021).

Example methods of levitation are summarised in Fig. 1-7 and a brief description of each is presented here.

Electrostatic levitation uses an electrodynamic balance (EDB) to levitate droplets (Krieger et al., 2012; Richards et al., 2020). A charged droplet is held in place by AC and DC electric fields which can be altered to hold the droplet in place. The DC field stabilises the droplet in the vertical direction as it oscillates due to gravity. A key advantage of the EDB is that the mass of the particle can be determined via the voltage needed to keep the particle levitated, this has been exploited in the atmospheric literature along with the application of Mie scattering to determine the size of spherical droplets (Lee et al., 2012; Zobrist et al., 2011).

Optical levitation was developed in the 1970s and has found an application in a range of sciences, including atmospheric science (Ashkin, 1997). It involves trapping a particle in a focussed laser beam. The key forces acting on an optically trapped droplet are gravity and an optical force consisting of a scattering and gradient force. The scattering force is dependent on the intensity of the laser light and counteracts gravity. The gradient force is a function of the light intensity profile of the laser beam, which therefore requires the laser light intensity profile to be such that this gradient produces a force in the direction of the focal point of the laser beam (Ashkin, 1997). Particles can be levitated on the micrometre scale and Raman spectroscopy experiments are possible with the backscattered laser light. This has enabled measurements of the diffusion coefficient of water through μm-scale droplets of viscous aerosol proxies (Davies and Wilson, 2016). A drawback of optical levitation is that the optical forces are dependent on the refractive index of the levitated material. If this changes as a result of some chemical or physical process, the particle may be lost from the trap.

Acoustic levitation uses the acoustic force generated by an ultrasonic soundwave (Brandt, 2001). A standing acoustic wave is generated by a vibrating cylinder

(transducer) which is positioned opposite a concave reflector. A series of pressure nodes, which sit in potential wells, result from this standing wave. The number of nodes is dependent on the frequency of the sound wave (100 kHz used in this thesis) and the transducer-reflector distance (Xie and Wei, 2001). Acoustic levitation has the advantage that the limitation is the mass of the sample. The phase, optical and electrostatic characteristics of the particle have little impact on the experimentalist's ability to levitate the particle. This makes acoustic levitation an ideal tool for the study of semi-solid, occasionally optically opaque LLC phases presented in this thesis and in the preceding literature (Pfrang et al., 2017; Seddon et al., 2016). Note that a significant drawback of acoustic levitation is that a particle needs to be large enough in order to be stable to focus a laser beam or direct an X-ray beam at the particle.

1.4.3 **Modelling aerosol reactivity**

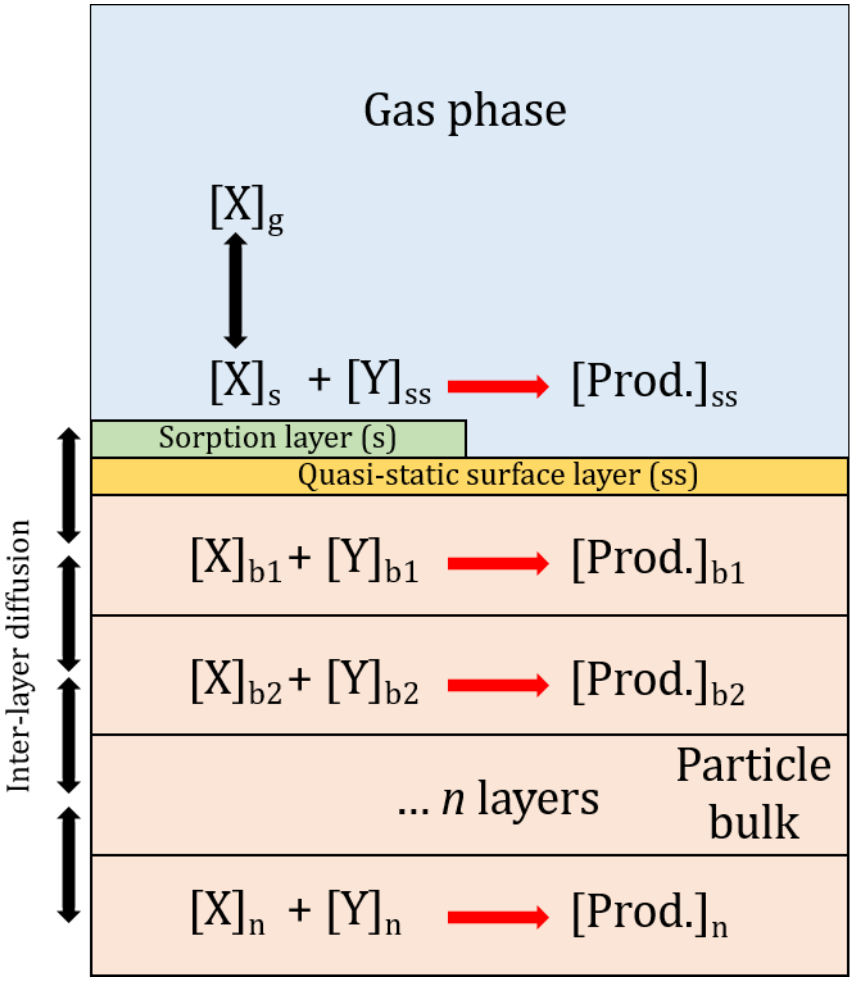

Figure 1-8. Schematic of the KM-SUB model implementation in this thesis, based on Shiraiwa et al (2010). A reactive gas (X), condensed phase (Y) and reaction products (Prod.) are represented.

In order to describe the potential atmospheric impact or the "big picture" of laboratory-based proxy systems, computational models based on theory can be created. Matching the model output with experimental observations by adjusting model input parameters is termed optimisation and allows the modeller to access parameters which are otherwise not measureable (or at least difficult to measure) experimentally.

Multi-layer models of aerosol heterogeneous processes have become useful tools in linking the laboratory with atmospheric impact. The kinetic multi-layer model of aerosol surface and bulk chemistry (KM-SUB) developed by Shiraiwa *et al.* is an example of such a model, which is based on the Pöschl-Rudich-Ammann framework of gas-particle interactions (Pöschl et al., 2007; Shiraiwa et al., 2010). The KM-SUB model is described in great detail by Shiraiwa *et al.*, therefore the salient points are outlined here (Fig. 1-8).

KM-SUB splits an aerosol particle into multiple layers (or shells). Diffusion of each species between each of these layers and the reaction of species within these layers are explicitly treated in the model. This requires input parameters such as reaction rate coefficients and diffusion coefficients for each chemical species. Surface processes are treated separately by defining a quasi-static 2-D surface layer of condensed phase species and a sorption layer of adsorbed gas-phase species. An extension of KM-SUB including gas-particle partitioning (KM-GAP) includes heat transfer, the evaporation of semi-volatile species from the particle and adaptable model layer thicknesses which depend on the number of molecules in each layer.

The model consists of a set of differential equations which describe the change in the number of each species in each model layer over time. These differential equations include reactive and diffusional gain and loss terms for each species.

A high spatial resolution is desirable for this kind of modelling because the assumption is that each model layer is well-mixed. This is more important for highly viscous systems.

Ideally, as many of the input parameters should be constrained to known values as possible. However, there exist algorithms designed for global optimisation of model parameters – *i.e.* which find a parameter set which returns a model output closest to the experimental output by minimising a loss function. One such algorithm used for this particular kind of model is the differential evolution algorithm (Berkemeier et al., 2017; Storn and Price, 1997). Essentially an initial population of parameter sets is sampled. These parameter sets are assessed against each other and the best ones are selected to continue to the next generation. Parameter sets are then mutated randomly and the assessment of fitness to the experiment takes place again. This is iterated until some convergence criterion is met.

The differential evolution algorithm is favoured for its relatively fast convergence to a global minimum, especially for computationally expensive models (such as KM-SUB) which have many varying parameters. In the KM-SUB modelling study in chapter 3, I present an adjustment to the initial sampling procedure as well as introduce a multi-objective optimisation, which simultaneously optimises a model to multiple datasets.

Limitations to this kind of multi-layer modelling arise from the computational cost of increasing model complexity. Adding extra species to the KM-SUB model requires the definition of differential equations for that species in each model layer. For a model with 100 layers, 101 extra differential equations (including the 2-D surface layer) must be written. This is already a significant computational cost. Therefore, products are sometimes lumped together. This is the case in the reaction scheme used in chapter 3 and by Hosny *et al*., who modelled the oleic acid-ozone reaction system in a similar way by representing all non-volatile 9-carbon products as one model component (Hosny et al., 2016).

Estimation of parameter uncertainty is a challenge, again because of the computational cost of these models. Bayesian methods such as Markov Chain Monte Carlo (MCMC) (Foreman-Mackey et al., 2013; Goodman and Weare, 2010) and nested sampling (Skilling, 2004, 2006) would be ideal for parameter uncertainty determination. Essentially, these methods sample a parameter set from a given parameter space provided by the user. Some likelihood parameter is calculated for that parameter set based on the fit of the model to the data. In MCMC sampling, the next set of parameters is chosen based on the likelihood of the previous step in the chain (a Markov chain). The chain of parameter values eventually converges around a mean value and a probability distribution for each parameter can be obtained from the converged chain. Nested sampling works in a similar way, the difference being that nested shells, each with increasing likelihoods, are sampled from and then combined to give both parameter distributions and an estimation of the evidence for that model being a good descriptor of the data. MCMC and nested sampling are used in chapter 4, where a computationally inexpensive model is fitted to NR data and parameter distributions and model selection is performed. The application of Bayesian methods to more expensive models is the subject of ongoing work by this author.

1.5 **Thesis overview**

This thesis presents a collection of studies concerning the effect of semi-solid nanostructure formation (or self-assembly) on the reactivity and water uptake behaviour of a proxy for organic aerosol containing a surfactant fatty acid (oleic acid). Each study, while being a standalone work, feeds into the general narrative that "surfactant nanostructure formation can impact on key atmospheric aerosol processes such as chemical oxidation and water uptake, affecting the atmospheric lifetime of such aerosols" – a notion presented to the reader in each study.

Firstly, a quantification of the effect of self-assembly on the reactivity of the proxy as a µm-scale coating is presented in chapter 2. This study is further enhanced by a kinetic multi-layer modelling study in chapter 3 based on the experimental data presented in chapter 2, revealing the formation of a product surface layer and drawing implications for the atmospheric lifetime of such coatings. Chapter 4 takes these films from the µm- to the nm-scale with spin-coating. A neutron-based technique, combined with interfacial model fitting reveals that the surface structure of such coatings can change with simulated atmospheric ageing (oxidation and humidity changes). Chapter 2 and 4 both conclude that unreacted self-assembled starting material is present after extensive oxidation – a theme throughout the thesis. Chapter 5 presents a first step towards quantifying the effect of different nanostructures have on reactivity and hygroscopicity, concluding that the specific nanostructure formed can have an effect on these properties. Chapter 6 explores the phase space accessible to this proxy with the addition of other commonly-emitted molecules, revealing a range of possible nanostructures, each with their own set of physical properties. Chapter 7 reports the observation and potential atmospheric significance of a crystalline organic phase in levitated particles of this

proxy. Simultaneous and spatially resolved X-ray scattering data reveal phase gradients and the formation of large aggregate products on the surface of an oxidising particle. Chapter 8 presents a new experimental method for following water uptake and phase transition in a levitated self-assembled particle along with the development and application of a model for water uptake, enabling the determination of water diffusivity in each observed nanostructure.

This thesis represents a multi-disciplinary approach to a relatively novel concept in aerosol multi-phase processes: the formation of surfactant nanostructures. X-ray scattering-based techniques are the workhorses for studying such systems; familiar to the soft matter chemist, not so familiar to the atmospheric chemist. With this in mind, the introduction to each chapter provides the atmospheric background necessary to motivate the work. The salient points of the mostly soft matter analysis techniques used are then presented, providing a baseline knowledge to the reader.

A comment at the end of each chapter is written in order to link each self-contained work to the rest of the thesis and any future or ongoing work and to highlight challenges with those particular studies. A statement on the contributions of others is also presented at the end of each chapter.

1.6 References

Abbatt, J. P. D. and Wang, C.: The atmospheric chemistry of indoor environments, Environ. Sci. Process. Impacts, 22(1), 25–48, doi:10.1039/c9em00386j, 2020.

Alves, C. A., Vicente, E. D., Evtyugina, M., Vicente, A. M., Nunes, T., Lucarelli, F., Calzolai, G., Nava, S., Calvo, A. I., Alegre, C. del B., Oduber, F., Castro, A. and Fraile, R.: Indoor and outdoor air quality: A university cafeteria as a case study, Atmos. Pollut.

Res., 11(3), 531–544, doi:10.1016/j.apr.2019.12.002, 2020.

Ashkin, A.: Optical trapping and manipulation of neutral particles using lasers, Proc. Natl. Acad. Sci., 94(10), 4853–4860, doi:10.1073/pnas.94.10.4853, 1997.

Baars, H., Radenz, M., Floutsi, A. A., Engelmann, R., Althausen, D., Heese, B., Ansmann, A., Flament, T., Dabas, A., Trapon, D., Reitebuch, O., Bley, S. and Wandinger, U.: Californian wildfire smoke over Europe: A first example of the aerosol observing capabilities of Aeolus compared to ground-based lidar, Geophys. Res. Lett., 1–10, doi:10.1029/2020gl092194, 2021.

Becerra, R. and Pfrang, C.: Kinetic Studies of Nitrate Radicals: Flash Photolysis at 193 nm, Int. J. Chem. Kinet., 48(12), 806–811, doi:10.1002/kin.21035, 2016.

Berkemeier, T., Steimer, S. S., Krieger, U. K., Peter, T., Pöschl, U., Ammann, M. and Shiraiwa, M.: Ozone uptake on glassy, semi-solid and liquid organic matter and the role of reactive oxygen intermediates in atmospheric aerosol chemistry, Phys. Chem. Chem. Phys., 18(18), 12662–12674, doi:10.1039/c6cp00634e, 2016.

Berkemeier, T., Ammann, M., Krieger, U. K., Peter, T., Spichtinger, P., Pöschl, U., Shiraiwa, M. and Huisman, A. J.: Technical note: Monte Carlo genetic algorithm (MCGA) for model analysis of multiphase chemical kinetics to determine transport and reaction rate coefficients using multiple experimental data sets, Atmos. Chem. Phys., 17(12), 8021–8029, doi:10.5194/acp-17-8021-2017, 2017.

Boucher, O., Randall, D., Artaxo, P., Bretherton, C., Feingold, G., Forster, P., Kerminen, V.-M., Kondo, Y., Liao, H., Lohmann, U., Rasch, P., Satheesh, S. K., Sherwood, S., Stevens, B. and Zhang, X. Y.: Clouds and Aerosols, in Climate Change 2013 - The Physical Science Basis, edited by Intergovernmental Panel on Climate

Change, pp. 571–658, Cambridge University Press, Cambridge., 2013.

Brandt, E. H.: Acoustic physics. Suspended by sound., Nature, 413(6855), 474–475, doi:10.1038/35097192, 2001.

Bzdek, B. R., Reid, J. P., Malila, J. and Prisle, N. L.: The surface tension of surfactant-containing, finite volume droplets, Proc. Natl. Acad. Sci. U. S. A., 117(15), 8335–8343, doi:10.1073/pnas.1915660117, 2020.

Chan, C. K. and Yao, X.: Air pollution in mega cities in China, Atmos. Environ., 42(1), 1–42, doi:10.1016/j.atmosenv.2007.09.003, 2008.

Chapleski, R. C., Zhang, Y., Troya, D. and Morris, J. R.: Heterogeneous chemistry and reaction dynamics of the atmospheric oxidants, O3, NO3, and OH, on organic surfaces, Chem. Soc. Rev., 45(13), 3731–3746, doi:10.1039/c5cs00375j, 2016.

Cohen, L., Quant, M. I., Quant, M. I., Donaldson, D. J. and Donaldson, D. J.: Real-Time Measurements of pH Changes in Single, Acoustically Levitated Droplets Due to Atmospheric Multiphase Chemistry, ACS Earth Sp. Chem., 4(6), 854–861, doi:10.1021/acsearthspacechem.0c00041, 2020.

Cummings, B. E., Li, Y., Decarlo, P. F., Shiraiwa, M. and Waring, M. S.: Indoor aerosol water content and phase state in U.S. residences: Impacts of relative humidity, aerosol mass and composition, and mechanical system operation, Environ. Sci. Process. Impacts, 22(10), 2031–2057, doi:10.1039/d0em00122h, 2020.

Davies, J. F. and Wilson, K. R.: Raman Spectroscopy of Isotopic Water Diffusion in Ultraviscous, Glassy, and Gel States in Aerosol by Use of Optical Tweezers, Anal. Chem., 88(4), 2361–2366, doi:10.1021/acs.analchem.5b04315, 2016.

Ding, J., Zhang, Y. F., Zhao, P. S., Tang, M., Xiao, Z. M., Zhang, W. H., Zhang, H. T., Yu, Z. J., Du, X., Li, L. W., Yuan, J. and Feng, Y. C.: Comparison of size-resolved hygroscopic growth factors of urban aerosol by different methods in Tianjin during a haze episode, Sci. Total Environ., 678, 618–626, doi:10.1016/j.scitotenv.2019.05.005, 2019.

Facchini, M. C., Mircea, M., Fuzzi, S. and Charlson, R. J.: Cloud albedo enhancement by surface-active organic solutes in growing droplets, Nature, 401(6750), 257–259, doi:10.1038/45758, 1999.

Facchini, M. C., Decesari, S., Mircea, M., Fuzzi, S. and Loglio, G.: Surface tension of atmospheric wet aerosol and cloud/fog droplets in relation to their organic carbon content and chemical composition, Atmos. Environ., 34(28), 4853–4857, doi:10.1016/S1352-2310(00)00237-5, 2000.

Fan, J., Rosenfeld, D., Zhang, Y., Giangrande, S. E., Li, Z., Machado, L. A. T., Martin, S. T., Yang, Y., Wang, J., Artaxo, P., Barbosa, H. M. J., Braga, R. C., Comstock, J. M., Feng, Z., Gao, W., Gomes, H. B., Mei, F., Pöhlker, C., Pöhlker, M. L., Pöschl, U. and de Souza, R. A. F.: Substantial convection and precipitation enhancements by ultrafine aerosol particles, Science, 359(6374), 411–418, doi:10.1126/science.aan8461, 2018.

Farmer, D. K., Cappa, C. D. and Kreidenweis, S. M.: Atmospheric Processes and Their Controlling Influence on Cloud Condensation Nuclei Activity, Chem. Rev., 115(10), 4199–4217, doi:10.1021/cr5006292, 2015.

Farmer, D. K., Vance, M. E., Abbatt, J. P. D., Abeleira, A., Alves, M. R., Arata, C., Boedicker, E., Bourne, S., Cardoso-Saldaña, F., Corsi, R., Decarlo, P. F., Goldstein, A. H., Grassian, V. H., Hildebrandt Ruiz, L., Jimenez, J. L., Kahan, T. F., Katz, E. F.,

Goldberg, D. L., Vinviguerra, T. P., Hosley, K. M., Loughner, C. P., Canty, T. P., Salawitch, R. J. and Dickerson, R. R., Evidence for an invrease in the ozone photochemical lifetime in the eastern United States using a regional air quality model, J. Geophys. Res. Atmos., 120(12), 12778–12793, doi: https://doi.org/10.1002/2015JD023930, 2015.

Heard, D. E. and Pilling, M. J.: Measurement of OH and HO_2 in the Troposphere, Chem. Rev., 103(12), 5163–5198, doi: 10.1021/cr020522s, 2003.

Mattila, J. M., Nazaroff, W. W., Novoselac, A., O'Brien, R. E., Or, V. W., Patel, S., Sankhyan, S., Stevens, P. S., Tian, Y., Wade, M., Wang, C., Zhou, S. and Zhou, Y.: Overview of HOMEChem: House Observations of Microbial and Environmental Chemistry, Environ. Sci. Process. Impacts, 21(8), 1280–1300, doi:10.1039/c9em00228f, 2019.

Finlayson-Pitts, B. J. and Pitts, J. N.: Chemistry of the Upper and Lower Atmosphere, 1st ed., Elsevier, Cambridge., 2000.

Foreman-Mackey, D., Hogg, D. W., Lang, D. and Goodman, J.: emcee : The MCMC Hammer , Publ. Astron. Soc. Pacific, 125(925), 306–312, doi:10.1086/670067, 2013.

Fu, P., Kawamura, K., Okuzawa, K., Aggarwal, S. G., Wang, G., Kanaya, Y. and Wang, Z.: Organic molecular compositions and temporal variations of summertime mountain aerosols over Mt. Tai, North China Plain, J. Geophys. Res. Atmos., 113(19), 1–20, doi:10.1029/2008JD009900, 2008.

Gallimore, P. J., Davidson, N. M., Kalberer, M., Pope, F. D. and Ward, A. D.: 1064 nm Dispersive Raman Microspectroscopy and Optical Trapping of Pharmaceutical Aerosols, Anal. Chem., 90(15), 8838–8844, doi:10.1021/acs.analchem.8b00817, 2018.

Goodman, J. and Weare, J.: Ensemble samplers with affine invariance, Commun. Appl. Math. Comput. Sci., 5(1), 65–80, doi:10.2140/camcos.2010.5.65, 2010.

Gunthe, S. S., Rose, D., Su, H., Garland, R. M., Achtert, P., Nowak, A., Wiedensohler, A., Kuwata, M., Takegawa, N., Kondo, Y., Hu, M., Shao, M., Zhu, T., Andreae, M. O. and Pöschl, U.: Cloud condensation nuclei (CCN) from fresh and aged air pollution in the megacity region of Beijing, Atmos. Chem. Phys., 11(21), 11023–11039, doi:10.5194/acp-11-11023-2011, 2011.

Hearn, J. D., Smith, G. D. and Lovett, A. J.: Ozonolysis of oleic acid particles: evidence for a surface reaction and secondary reactions involving Criegee intermediates, Phys. Chem. Chem. Phys., 7(3), 501–511, doi:10.1039/b414472d, 2005.

Hong, J., Xu, H., Tan, H., Yin, C., Hao, L., Li, F., Cai, M., Deng, X., Wang, N., Su, H., Cheng, Y., Wang, L., Petäjä, T. and Kerminen, V.-M.: Mixing state and particle hygroscopicity of organic-dominated aerosols over the Pearl River Delta region in China, Atmos. Chem. Phys., 18(19), 14079–14094, doi:10.5194/acp-18-14079-2018, 2018.

Hosny, N. A., Fitzgerald, C., Vyšniauskas, A., Athanasiadis, A., Berkemeier, T., Uygur, N., Pöschl, U., Shiraiwa, M., Kalberer, M., Pope, F. D. and Kuimova, M. K.: Direct imaging of changes in aerosol particle viscosity upon hydration and chemical aging, Chem. Sci., 7(2), 1357–1367, doi:10.1039/c5sc02959g, 2016.

Jimenez, J. L., Canagaratna, M. R., Donahue, N. M., Prevot, A. S. H., Zhang, Q., Kroll, J. H., DeCarlo, P. F., Allan, J. D., Coe, H., Ng, N. L., Aiken, A. C., Docherty, K. S., Ulbrich, I. M., Grieshop, A. P., Robinson, A. L., Duplissy, J., Smith, J. D., Wilson, K. R., Lanz, V. A., Hueglin, C., Sun, Y. L., Tian, J., Laaksonen, A., Raatikainen, T.,

Rautiainen, J., Vaattovaara, P., Ehn, M., Kulmala, M., Tomlinson, J. M., Collins, D. R., Cubison, M. J., Dunlea, J., Huffman, J. A., Onasch, T. B., Alfarra, M. R., Williams, P. I., Bower, K., Kondo, Y., Schneider, J., Drewnick, F., Borrmann, S., Weimer, S., Demerjian, K., Salcedo, D., Cottrell, L., Griffin, R., Takami, A., Miyoshi, T., Hatakeyama, S., Shimono, A., Sun, J. Y., Zhang, Y. M., Dzepina, K., Kimmel, J. R., Sueper, D., Jayne, J. T., Herndon, S. C., Trimborn, A. M., Williams, L. R., Wood, E. C., Middlebrook, A. M., Kolb, C. E., Baltensperger, U. and Worsnop, D. R.: Evolution of Organic Aerosols in the Atmosphere, Science (80-.)., 326(5959), 1525–1529, doi:10.1126/science.1180353, 2009.

Jin, X., Wang, Y., Li, Z., Zhang, F., Xu, W., Sun, Y., Fan, X., Chen, G., Wu, H., Ren, J., Wang, Q. and Cribb, M.: Significant contribution of organics to aerosol liquid water content in winter in Beijing, China, Atmos. Chem. Phys., 20(2), 901–914, doi:10.5194/acp-20-901-2020, 2020.

Jones, S. H., Friederich, P. and Donaldson, D. J.: Photochemical Aging of Levitated Aqueous Brown Carbon Droplets, ACS Earth Sp. Chem., 5(4), 749–754, doi:10.1021/acsearthspacechem.1c00005, 2021.

Kanakidou, M., Seinfeld, J. H., Pandis, S. N., Barnes, I., Dentener, F. J., Facchini, M. C., Van Dingenen, R., Ervens, B., Nenes, A., Nielsen, C. J., Swietlicki, E., Putaud, J. P., Balkanski, Y., Fuzzi, S., Horth, J., Moortgat, G. K., Winterhalter, R., Myhre, C. E. L., Tsigaridis, K., Vignati, E., Stephanou, E. G. and Wilson, J.: Organic aerosol and global climate modelling: a review, Atmos. Chem. Phys., 5(4), 1053–1123, doi:10.5194/acp-5-1053-2005, 2005.

Kang, M., Yang, F., Ren, H., Zhao, W., Zhao, Y., Li, L., Yan, Y., Zhang, Y., Lai, S.,

Zhang, Y., Yang, Y., Wang, Z., Sun, Y. and Fu, P.: Influence of continental organic aerosols to the marine atmosphere over the East China Sea: Insights from lipids, PAHs and phthalates, Sci. Total Environ., 607–608, 339–350, doi:10.1016/j.scitotenv.2017.06.214, 2017.

King, M. D., Rennie, A. R., Thompson, K. C., Fisher, F. N., Dong, C. C., Thomas, R. K., Pfrang, C. and Hughes, A. V.: Oxidation of oleic acid at the air-water interface and its potential effects on cloud critical supersaturations, Phys. Chem. Chem. Phys., 11(35), 7699–7707, doi:10.1039/b906517b, 2009.

King, M. D., Jones, S. H., Lucas, C. O. M., Thompson, K. C., Rennie, A. R., Ward, A. D., Marks, A. A., Fisher, F. N., Pfrang, C., Hughes, A. V. and Campbell, R. A.: The reaction of oleic acid monolayers with gas-phase ozone at the air water interface: The effect of sub-phase viscosity, and inert secondary components, Phys. Chem. Chem. Phys., 22(48), 28032–28044, doi:10.1039/d0cp03934a, 2020.

Kirpes, R. M., Bonanno, D., May, N. W., Fraund, M., Barget, A. J., Moffet, R. C., Ault, A. P. and Pratt, K. A.: Wintertime Arctic Sea Spray Aerosol Composition Controlled by Sea Ice Lead Microbiology, ACS Cent. Sci., 5(11), 1760–1767, doi:10.1021/acscentsci.9b00541, 2019.

Köhler, H.: The nucleus in and the growth of hygroscopic droplets, Trans. Faraday Soc., 32, 1152–1161, doi:10.1039/TF9363201152, 1936.

Koop, T., Bookhold, J., Shiraiwa, M. and Pöschl, U.: Glass transition and phase state of organic compounds: Dependency on molecular properties and implications for secondary organic aerosols in the atmosphere, Phys. Chem. Chem. Phys., 13(43), 19238–19255, doi:10.1039/c1cp22617g, 2011.

Krieger, U. K., Marcolli, C. and Reid, J. P.: Exploring the complexity of aerosol particle properties and processes using single particle techniques, Chem. Soc. Rev., 41(19), 6631–6662, doi:10.1039/c2cs35082c, 2012.

Kulkarni, C. V., Wachter, W., Iglesias-Salto, G., Engelskirchen, S. and Ahualli, S.: Monoolein: a magic lipid?, Phys. Chem. Chem. Phys., 13(8), 3004–3021, doi:10.1039/C0CP01539C, 2011.

Lee, J. W. L., Carrascón, V., Gallimore, P. J., Fuller, S. J., Björkegren, A., Spring, D. R., Pope, F. D. and Kalberer, M.: The effect of humidity on the ozonolysis of unsaturated compounds in aerosol particles, Phys. Chem. Chem. Phys., 14(22), 8023–8031, doi:10.1039/c2cp24094g, 2012.

Li, G., Su, H., Ma, N., Tao, J., Kuang, Y., Wang, Q., Hong, J., Zhang, Y., Kuhn, U., Zhang, S., Pan, X., Lu, N., Tang, M., Zheng, G., Wang, Z., Gao, Y., Cheng, P., Xu, W., Zhou, G., Zhao, C., Yuan, B., Shao, M., Ding, A., Zhang, Q., Fu, P., Sun, Y., Pöschl, U. and Cheng, Y.: Multiphase chemistry experiment in Fogs and Aerosols in the North China Plain (McFAN): integrated analysis and intensive winter campaign 2018, Faraday Discuss., 226, doi:10.1039/D0FD00099J, 2021.

Li, W., Li, H., Li, J., Cheng, X., Zhang, Z., Chai, F., Zhang, H., Yang, T., Duan, P., Lu, D. and Chen, Y.: TOF–SIMS surface analysis of chemical components of size–fractioned urban aerosols in a typical heavy air pollution event in Beijing, J. Environ. Sci., 69, 61–76, doi:10.1016/j.jes.2017.04.005, 2018.

Liu, J., Zhang, F., Xu, W., Chen, L., Ren, J., Jiang, S., Sun, Y. and Li, Z.: A Large Impact of Cooking Organic Aerosol (COA) on Particle Hygroscopicity and CCN Activity in Urban Atmosphere, J. Geophys. Res. Atmos., 126(8), 1–11,

doi:10.1029/2020jd033628, 2021.

Lowe, S., Partridge, D. G., Topping, D. and Stier, P.: Inverse modelling of Köhler theory - Part 1: A response surface analysis of CCN spectra with respect to surface-active organic species, Atmos. Chem. Phys., 16(17), 10941–10963, doi:10.5194/acp-16-10941-2016, 2016.

Lyu, X., Huo, Y., Yang, J., Yao, D., Li, K., Lu, H., Zeren, Y. and Guo, H.: Real-time molecular characterization of air pollutants in a Hong Kong residence: Implication of indoor source emissions and heterogeneous chemistry, Indoor Air, (March), 1–13, doi:10.1111/ina.12826, 2021.

Maria, S. F., Russell, L. M., Gilles, M. K. and Myneni, S. C. B.: Organic Aerosol Growth Mechanisms and Their Climate-Forcing Implications, Science, 306(5703), 1921–1924, doi:10.1126/science.1103491, 2004.

Mason, N. J., Drage, E. A., Webb, S. M., Dawes, A., McPheat, R. and Hayes, G.: The spectroscopy and chemical dynamics of microparticles explored using an ultrasonic trap, Faraday Discuss., 137, 367–376, doi:10.1039/b702726p, 2007.

Mattila, J. M., Arata, C., Wang, C., Katz, E. F., Abeleira, A., Zhou, Y., Zhou, S., Goldstein, A. H., Abbatt, J. P. D., Decarlo, P. F. and Farmer, D. K.: Dark Chemistry during Bleach Cleaning Enhances Oxidation of Organics and Secondary Organic Aerosol Production Indoors, Environ. Sci. Technol. Lett., 7(11), 795–801, doi:10.1021/acs.estlett.0c00573, 2020.

Mezzenga, R., Meyer, C., Servais, C., Romoscanu, A. I., Sagalowicz, L. and Hayward, R. C.: Shear rheology of lyotropic liquid crystals: A case study, Langmuir, 21(8), 3322–3333, doi:10.1021/la046964b, 2005.

Mikhailov, E., Vlasenko, S., Martin, S. T., Koop, T. and Pöschl, U.: Amorphous and crystalline aerosol particles interacting with water vapor: Conceptual framework and experimental evidence for restructuring, phase transitions and kinetic limitations, Atmos. Chem. Phys., 9(24), 9491–9522, doi:10.5194/acp-9-9491-2009, 2009.

Milsom, A., Squires, A. M., Woden, B., Terrill, N. J., Ward, A. D. and Pfrang, C.: The persistence of a proxy for cooking emissions in megacities: a kinetic study of the ozonolysis of self-assembled films by simultaneous small and wide angle X-ray scattering (SAXS/WAXS) and Raman microscopy, Faraday Discuss., 226, 364–381, doi:10.1039/D0FD00088D, 2021.

Mu, Q., Shiraiwa, M., Octaviani, M., Ma, N., Ding, A., Su, H., Lammel, G., Pöschl, U. and Cheng, Y.: Temperature effect on phase state and reactivity controls atmospheric multiphase chemistry and transport of PAHs, Sci. Adv., 4(3), eaap7314, doi:10.1126/sciadv.aap7314, 2018.

Narayanan, T. and Konovalov, O.: Synchrotron Scattering Methods for Nanomaterials and Soft Matter Research, Materials (Basel)., 13(3), 752, doi:10.3390/ma13030752, 2020.

Nguyen, Q. T., Kjær, K. H., Kling, K. I., Boesen, T. and Bilde, M.: Impact of fatty acid coating on the CCN activity of sea salt particles, Tellus, Ser. B Chem. Phys. Meteorol., 69(1), 1–15, doi:10.1080/16000889.2017.1304064, 2017.

Or, V. W., Wade, M., Patel, S., Alves, M. R., Kim, D., Schwab, S., Przelomski, H., O'Brien, R., Rim, D., Corsi, R. L., Vance, M. E., Farmer, D. K. and Grassian, V. H.: Glass surface evolution following gas adsorption and particle deposition from indoor cooking events as probed by microspectroscopic analysis, Environ. Sci. Process.

Impacts, 22(8), 1698–1709, doi:10.1039/d0em00156b, 2020.

Ovadnevaite, J., Zuend, A., Laaksonen, A., Sanchez, K. J., Roberts, G., Ceburnis, D., Decesari, S., Rinaldi, M., Hodas, N., Facchini, M. C., Seinfeld, J. H. and O'Dowd, C.: Surface tension prevails over solute effect in organic-influenced cloud droplet activation, Nature, 546(7660), 637–641, doi:10.1038/nature22806, 2017.

Patel, S., Sankhyan, S., Boedicker, E. K., Decarlo, P. F., Farmer, D. K., Goldstein, A. H., Katz, E. F., Nazaroff, W. W., Tian, Y., Vanhanen, J. and Vance, M. E.: Indoor Particulate Matter during HOMEChem: Concentrations, Size Distributions, and Exposures, Environ. Sci. Technol., 54(12), 7107–7116, doi:10.1021/acs.est.0c00740, 2020.

Pauw, B. R.: Everything SAXS: small-angle scattering pattern collection and correction, J. Phys. Condens. Matter, 25(38), 383201, doi:10.1088/0953-8984/25/38/383201, 2013.

Penfold, J. and Thomas, R. K.: The application of the specular reflection of neutrons to the study of surfaces and interfaces, J. Phys. Condens. Matter, 2(6), 1369–1412, doi:10.1088/0953-8984/2/6/001, 1990.

Peng, C., Wang, Y., Wu, Z., Chen, L., Huang, R. J., Wang, W., Wang, Z., Hu, W., Zhang, G., Ge, M., Hu, M., Wang, X. and Tang, M.: Tropospheric aerosol hygroscopicity in China, Atmos. Chem. Phys., 20(22), 13877–13903, doi:10.5194/acp-20-13877-2020, 2020.

Penner, J. E., Xu, L. and Wang, M.: Satellite methods underestimate indirect climate forcing by aerosols, Proc. Natl. Acad. Sci., 108(33), 13404–13408, doi:10.1073/pnas.1018526108, 2011.

Pfrang, C., Shiraiwa, M. and Pöschl, U.: Chemical ageing and transformation of diffusivity in semi-solid multi-component organic aerosol particles, Atmos. Chem. Phys., 11(14), 7343–7354, doi:10.5194/acp-11-7343-2011, 2011.

Pfrang, C., Sebastiani, F., Lucas, C. O. M., King, M. D., Hoare, I. D., Chang, D. and Campbell, R. A.: Ozonolysis of methyl oleate monolayers at the air-water interface: Oxidation kinetics, reaction products and atmospheric implications, Phys. Chem. Chem. Phys., 16(26), 13220–13228, doi:10.1039/c4cp00775a, 2014.

Pfrang, C., Rastogi, K., Cabrera-Martinez, E. R., Seddon, A. M., Dicko, C., Labrador, A., Plivelic, T. S., Cowieson, N. and Squires, A. M.: Complex three-dimensional self-assembly in proxies for atmospheric aerosols, Nat. Commun., 8(1), 1724, doi:10.1038/s41467-017-01918-1, 2017.

Pöschl, U., Rudich, Y. and Ammann, M.: Kinetic model framework for aerosol and cloud surface chemistry and gas-particle interactions - Part 1: General equations, parameters, and terminology, Atmos. Chem. Phys., 7(23), 5989–6023, doi:10.5194/acp-7-5989-2007, 2007.

Prisle, N. L., Asmi, A., Topping, D., Partanen, A.-I., Romakkaniemi, S., Dal Maso, M., Kulmala, M., Laaksonen, A., Lehtinen, K. E. J., McFiggans, G. and Kokkola, H.: Surfactant effects in global simulations of cloud droplet activation, Geophys. Res. Lett., 39(5), doi:10.1029/2011GL050467, 2012.

Prisle, N. L., Lin, J. J., Purdue, S., Lin, H., Meredith, J. C. and Nenes, A.: Cloud condensation nuclei activity of six pollenkitts and the influence of their surface activity, Atmos. Chem. Phys., 19(7), 4741–4761, doi:10.5194/acp-19-4741-2019, 2019.

Putnam, C. D., Hammel, M., Hura, G. L. and Tainer, J. A.: X-ray solution scattering

(SAXS) combined with crystallography and computation: defining accurate macromolecular structures, conformations and assemblies in solution, Q. Rev. Biophys., 40(3), 191–285, doi:10.1017/s0033583507004635, 2007.

Reid, J. P., Bertram, A. K., Topping, D. O., Laskin, A., Martin, S. T., Petters, M. D., Pope, F. D. and Rovelli, G.: The viscosity of atmospherically relevant organic particles, Nat. Commun., 9(1), 1–14, doi:10.1038/s41467-018-03027-z, 2018.

Renbaum-Wolff, L., Grayson, J. W., Bateman, A. P., Kuwata, M., Sellier, M., Murray, B. J., Shilling, J. E., Martin, S. T. and Bertram, A. K.: Viscosity of a-pinene secondary organic material and implications for particle growth and reactivity, Proc. Natl. Acad. Sci., 110(20), 8014–8019, doi:10.1073/pnas.1219548110, 2013.

Reynolds, J. C., Last, D. J., McGillen, M., Nijs, A., Horn, A. B., Percival, C., Carpenter, L. J. and Lewis, A. C.: Structural analysis of oligomeric molecules formed from the reaction products of oleic acid ozonolysis, Environ. Sci. Technol., 40(21), 6674–6681, doi:10.1021/es060942p, 2006.

Richards, D. S., Trobaugh, K. L., Hajek-Herrera, J. and Davis, R. D.: Dual-Balance Electrodynamic Trap as a Microanalytical Tool for Identifying Gel Transitions and Viscous Properties of Levitated Aerosol Particles, Anal. Chem., 92(4), 3086–3094, doi:10.1021/acs.analchem.9b04487, 2020.

Schmedding, R., Rasool, Q. Z., Zhang, Y., Pye, H. O. T., Zhang, H., Chen, Y., Surratt, J. D., Lopez-Hilfiker, F. D., Thornton, J. A., Goldstein, A. H. and Vizuete, W.: Predicting secondary organic aerosol phase state and viscosity and its effect on multiphase chemistry in a regional-scale air quality model, Atmos. Chem. Phys., 20(13), 8201–8225, doi:10.5194/acp-20-8201-2020, 2020.

Schwartz-Narbonne, H. and Donaldson, D. J.: Water uptake by indoor surface films, Sci. Rep., 9(1), 11089, doi:10.1038/s41598-019-47590-x, 2019.

Sebastiani, F., Campbell, R. A., Rastogi, K. and Pfrang, C.: Nighttime oxidation of surfactants at the air-water interface: Effects of chain length, head group and saturation, Atmos. Chem. Phys., 18(5), 3249–3268, doi:10.5194/acp-18-3249-2018, 2018.

Seddon, A. M., Richardson, S. J., Rastogi, K., Plivelic, T. S., Squires, A. M. and Pfrang, C.: Control of Nanomaterial Self-Assembly in Ultrasonically Levitated Droplets, J. Phys. Chem. Lett., 7(7), 1341–1345, doi:10.1021/acs.jpclett.6b00449, 2016.

Seddon, J. M., Bartle, E. A. and Mingins, J.: Inverse cubic liquid-crystalline phases of phospholipids and related lyotropic systems, J. Phys. Condens. Matter, 2, SA285–SA290, doi:10.1088/0953-8984/2/S/043, 1990.

Seinfeld, J. H. and Pandis, S. N.: Atmospheric chemistry and physics: from air pollution to climate change, 2nd ed., John Wiley & Sons, Hoboken., 2006.

Shaw, D. J.: Introduction to Colloid and Surface Chemistry, 1st ed., Elsevier., 1992.

Shiraiwa, M., Pfrang, C. and Pöschl, U.: Kinetic multi-layer model of aerosol surface and bulk chemistry (KM-SUB): The influence of interfacial transport and bulk diffusion on the oxidation of oleic acid by ozone, Atmos. Chem. Phys., 10, 3673–3691, doi:10.5194/acp-10-3673-2010, 2010.

Shiraiwa, M., Ammann, M., Koop, T. and Poschl, U.: Gas uptake and chemical aging of semisolid organic aerosol particles, Proc. Natl. Acad. Sci. U. S. A., 108(27), 11003–11008, doi:10.1073/pnas.1103045108, 2011.

Shiraiwa, M., Li, Y., Tsimpidi, A. P., Karydis, V. A., Berkemeier, T., Pandis, S. N.,

Lelieveld, J., Koop, T. and Pöschl, U.: Global distribution of particle phase state in atmospheric secondary organic aerosols, Nat. Commun., 8, 1–7, doi:10.1038/ncomms15002, 2017.

Shiraiwa, M., Carslaw, N., Tobias, D. J., Waring, M. S., Rim, D., Morrison, G., Lakey, P. S. J., Kruza, M., Von Domaros, M., Cummings, B. E. and Won, Y.: Modelling consortium for chemistry of indoor environments (MOCCIE): Integrating chemical processes from molecular to room scales, Environ. Sci. Process. Impacts, 21(8), 1240–1254, doi:10.1039/c9em00123a, 2019.

Shrivastava, M., Lou, S., Zelenyuk, A., Easter, R. C., Corley, R. A., Thrall, B. D., Rasch, P. J., Fast, J. D., Simonich, S. L. M., Shen, H. and Tao, S.: Global long-range transport and lung cancer risk from polycyclic aromatic hydrocarbons shielded by coatings of organic aerosol, Proc. Natl. Acad. Sci. U. S. A., 114(6), 1246–1251, doi:10.1073/pnas.1618475114, 2017.

Skilling, J.: Nested Sampling, , 395(November 2004), 395–405, doi:10.1063/1.1835238, 2004.

Skilling, J.: Nested sampling for general Bayesian computation, Bayesian Anal., 1(4), 833–860, doi:10.1214/06-BA127, 2006.

Slade, J. H., Shiraiwa, M., Arangio, A., Su, H., Pöschl, U., Wang, J. and Knopf, D. A.: Cloud droplet activation through oxidation of organic aerosol influenced by temperature and particle phase state, Geophys. Res. Lett., 44(3), 1583–1591, doi:10.1002/2016GL072424, 2017.

Slade, J. H., Ault, A. P., Bui, A. T., Ditto, J. C., Lei, Z., Bondy, A. L., Olson, N. E., Cook, R. D., Desrochers, S. J., Harvey, R. M., Erickson, M. H., Wallace, H. W.,

Alvarez, S. L., Flynn, J. H., Boor, B. E., Petrucci, G. A., Gentner, D. R., Griffin, R. J. and Shepson, P. B.: Bouncier Particles at Night: Biogenic Secondary Organic Aerosol Chemistry and Sulfate Drive Diel Variations in the Aerosol Phase in a Mixed Forest, Environ. Sci. Technol., 53(9), 4977–4987, doi:10.1021/acs.est.8b07319, 2019.

Smith, A. J., Alcock, S. G., Davidson, L. S., Emmins, J. H., Hiller Bardsley, J. C., Holloway, P., Malfois, M., Marshall, A. R., Pizzey, C. L., Rogers, S. E., Shebanova, O., Snow, T., Sutter, J. P., Williams, E. P. and Terrill, N. J.: I22: SAXS/WAXS beamline at Diamond Light Source – an overview of 10 years operation, J. Synchrotron Radiat., 28(3), 939–947, doi:10.1107/S1600577521002113, 2021.

Storn, R. and Price, K.: Differential Evolution – A Simple and Efficient Heuristic for global Optimization over Continuous Spaces, J. Glob. Optim., 11, 341–359, doi:10.1023/A1008202821328, 1997.

Tabazadeh, A.: Organic aggregate formation in aerosols and its impact on the physicochemical properties of atmospheric particles, Atmos. Environ., 39(30), 5472–5480, doi:10.1016/j.atmosenv.2005.05.045, 2005.

Tervahattu, H.: Identification of an organic coating on marine aerosol particles by TOF-SIMS, J. Geophys. Res., 107(D16), 4319, doi:10.1029/2001JD001403, 2002.

Tervahattu, H., Juhanoja, J., Vaida, V., Tuck, A. F., Niemi, J. V., Kupiainen, K., Kulmala, M. and Vehkamäki, H.: Fatty acids on continental sulfate aerosol particles, J. Geophys. Res. D Atmos., 110(6), 1–9, doi:10.1029/2004JD005400, 2005.

Tiddy, G. J. T.: Surfactant-water liquid crystal phases, Phys. Rep., 57(1), 1–46, doi:10.1016/0370-1573(80)90041-1, 1980.

Tuckermann, R.: Surface tension of aqueous solutions of water-soluble organic and inorganic compounds, Atmos. Environ., 41(29), 6265–6275, doi:10.1016/j.atmosenv.2007.03.051, 2007.

Vicente, A. M. P., Rocha, S., Duarte, M., Moreira, R., Nunes, T. and Alves, C. A.: Fingerprinting and emission rates of particulate organic compounds from typical restaurants in Portugal, Sci. Total Environ., 778, 146090, doi:10.1016/j.scitotenv.2021.146090, 2021.

Virtanen, A., Joutsensaari, J., Koop, T., Kannosto, J., Yli-Pirilä, P., Leskinen, J., Mäkelä, J. M., Holopainen, J. K., Pöschl, U., Kulmala, M., Worsnop, D. R. and Laaksonen, A.: An amorphous solid state of biogenic secondary organic aerosol particles, Nature, 467(7317), 824–827, doi:10.1038/nature09455, 2010.

Wang, Q., He, X., Zhou, M., Huang, D. D., Qiao, L., Zhu, S., Ma, Y. G., Wang, H. L., Li, L., Huang, C., Huang, X. H. H., Xu, W., Worsnop, D., Goldstein, A. H., Guo, H., Yu, J. Z., Huang, C. and Yu, J. Z.: Hourly Measurements of Organic Molecular Markers in Urban Shanghai, China: Primary Organic Aerosol Source Identification and Observation of Cooking Aerosol Aging, ACS Earth Sp. Chem., 4(9), 1670–1685, doi:10.1021/acsearthspacechem.0c00205, 2020a.

Wang, Q. and Yu, J. Z., Ambient Measurements of Heterogeneous Ozone Oxidation Rates of Oleic, Elaidic, and Linoleic Acid Using a Relative Rate Constant Approach in an Urban Environment, Geophys. Res. Lett., 48 (e2021GL095130), doi: 10.1029/2021GL095130, 2021.

Wang, T., Huang, R. J., Li, Y., Chen, Q., Chen, Y., Yang, L., Guo, J., Ni, H., Hoffmann, T., Wang, X. and Mai, B.: One-year characterization of organic aerosol

markers in urban Beijing: Seasonal variation and spatiotemporal comparison, Sci. Total Environ., 743, 140689, doi:10.1016/j.scitotenv.2020.140689, 2020b.

Wayne, R. P., Barnes, I., Biggs, P., Burrows, J. P., Canosa-Mas, C. E., Hjorth, J., Le Bras, G., Moortgat, G. K., Perner, D., Poulet, G., Restelli, G. and Sidebottom, H.: The nitrate radical: Physics, chemistry, and the atmosphere, Atmos. Environ. Part A, Gen. Top., 25(1), 1–203, doi:10.1016/0960-1686(91)90192-A, 1991.

Weschler, C. J.: Ozone in indoor environments: Concentration and chemistry, Indoor Air, 10(4), 269–288, doi:10.1034/j.1600-0668.2000.010004269.x, 2000.

Westphall, M. S., Jorabchi, K. and Smith, L. M.: Mass spectrometry of acoustically levitated droplets, Anal. Chem., 80(15), 5847–5853, doi:10.1021/ac800317f, 2008.

Woden, B., Skoda, M., Hagreen, M. and Pfrang, C.: Night-Time Oxidation of a Monolayer Model for the Air–Water Interface of Marine Aerosols—A Study by Simultaneous Neutron Reflectometry and in Situ Infra-Red Reflection Absorption Spectroscopy (IRRAS), Atmosphere (Basel)., 9(12), 471, doi:10.3390/atmos9120471, 2018.

Woden, B., Skoda, M. W. A., Milsom, A., Gubb, C., Maestro, A., Tellam, J. and Pfrang, C.: Ozonolysis of fatty acid monolayers at the air–water interface: organic films may persist at the surface of atmospheric aerosols, Atmos. Chem. Phys., 21(2), 1325–1340, doi:10.5194/acp-21-1325-2021, 2021.

Wu, Z. J., Zheng, J., Shang, D. J., Du, Z. F., Wu, Y. S., Zeng, L. M., Wiedensohler, A. and Hu, M.: Particle hygroscopicity and its link to chemical composition in the urban atmosphere of Beijing, China, during summertime, Atmos. Chem. Phys., 16(2), 1123–1138, doi:10.5194/acp-16-1123-2016, 2016.

Xie, W. J. and Wei, B.: Parametric study of single-axis acoustic levitation, Appl. Phys. Lett., 79(6), 881–883, doi:10.1063/1.1391398, 2001.

Zahardis, J. and Petrucci, G. A.: The oleic acid-ozone heterogeneous reaction system: Products, kinetics, secondary chemistry, and atmospheric implications of a model system - A review, Atmos. Chem. Phys., 7(5), 1237–1274, doi:10.5194/acp-7-1237-2007, 2007.

Zahardis, J., LaFranchi, B. W. and Petrucci, G. A.: Direct observation of polymerization in the oleic acid-ozone heterogeneous reaction system by photoelectron resonance capture ionization aerosol mass spectrometry, Atmos. Environ., 40(9), 1661–1670, doi:10.1016/j.atmosenv.2005.10.065, 2006a.

Zahardis, J., LaFranchi, B. W. and Petrucci, G. A.: Photoelectron resonance capture ionization mass spectrometry of fatty acids in olive oil, Eur. J. Lipid Sci. Technol., 108(11), 925–935, doi:10.1002/ejlt.200600143, 2006b.

Zeng, J., Yu, Z., Mekic, M., Liu, J., Li, S., Loisel, G., Gao, W., Gandolfo, A., Zhou, Z., Wang, X., Herrmann, H., Gligorovski, S. and Li, X.: Evolution of Indoor Cooking Emissions Captured by Using Secondary Electrospray Ionization High-Resolution Mass Spectrometry, Environ. Sci. Technol. Lett., 7(2), 76–81, doi:10.1021/acs.estlett.0c00044, 2020.

Zhang, J. M., Wang, T., Ding, A. J., Zhou, X. H., Xue, L. K., Poon, C. N., Wu, W. S., Gao, J., Zuo, H. C., Chen, J. M., Zhang, X. C. and Fan, S. J.: Continuous measurement of peroxyacetyl nitrate (PAN) in suburban and remote areas of western China, Atmos. Environ., 43(2), 228–237, doi:10.1016/j.atmosenv.2008.09.070, 2009.

Zhao, Y., Huang, H., Zhang, Y., Wu, K., Zeng, F., Wang, J., Yu, X., Zhu, Z., Yu, X.-Y.

and Wang, F.: Atmospheric particulate characterization by ToF-SIMS in an urban site in Beijing, Atmos. Environ., 220(June 2019), 117090, doi:10.1016/j.atmosenv.2019.117090, 2020.

Zhou, S., Shiraiwa, M., McWhinney, R. D., Pöschl, U. and Abbatt, J. P. D.: Kinetic limitations in gas-particle reactions arising from slow diffusion in secondary organic aerosol, Faraday Discuss., 165, 391–406, doi:10.1039/c3fd00030c, 2013.

Zhou, S., Hwang, B. C. H., Lakey, P. S. J., Zuend, A., Abbatt, J. P. D. and Shiraiwa, M.: Multiphase reactivity of polycyclic aromatic hydrocarbons is driven by phase separation and diffusion limitations, Proc. Natl. Acad. Sci. U. S. A., 116(24), 11658–11663, doi:10.1073/pnas.1902517116, 2019.

Zobrist, B., Soonsin, V., Luo, B. P., Krieger, U. K., Marcolli, C., Peter, T. and Koop, T.: Ultra-slow water diffusion in aqueous sucrose glasses, Phys. Chem. Chem. Phys., 13(8), 3514–3526, doi:10.1039/c0cp01273d, 2011.

2 CHAPTER 2: THE PERSISTENCE OF A PROXY FOR COOKING EMISSIONS IN MEGACITIES: A KINETIC STUDY OF THE OZONOLYSIS OF SELF-ASSEMBLED FILMS BY SIMULTANEOUS SMALL & WIDE ANGLE X-RAY SCATTERING (SAXS/WAXS) AND RAMAN MICROSCOPY

This study is published in the journal *Faraday Discussions:*

Milsom, A., Squires, A. M., Woden, B., Terrill, N. J., Ward, A. D. and Pfrang, C.: The persistence of a proxy for cooking emissions in megacities: a kinetic study of the ozonolysis of self-assembled films by simultaneous small and wide angle X-ray scattering (SAXS/WAXS) and Raman microscopy, Faraday Discuss., 226, 364–381, doi:10.1039/D0FD00088D, 2021.

2.1 **Abstract**

Cooking emissions account for a significant proportion of the organic aerosol emitted into the urban environment and high pollution events have been linked to an increased organic content on urban particulate matter surfaces. We present a kinetic study on surface coatings of self-assembled (semi-solid) oleic acid-sodium oleate cooking aerosol proxies undergoing ozonolysis. We found a clear film thickness-dependent kinetic behaviour and measured the effect of the organic phase on the reaction kinetics for this system. In addition to the thickness-dependent reaction kinetics, we show that significant fractions of unreacted proxy remain at the end of extensive ozone exposure and that this effect scales approximately linearly with film thickness, suggesting that a late-stage inert reaction product may form to inhibit reaction progress – effectively building up an inert crust. We determine this by using a range of simultaneous analytical techniques; most notably Small-Angle X-ray Scattering (SAXS) has been used for the first time to measure reaction kinetics of films of a wide range of thicknesses from ca. 0.59 to 73 μm with films < 10 μm thick being of potential atmospheric relevance. These observations have implications for the evolution of particulate matter in the urban environment, potentially extending the atmospheric lifetimes of harmful aerosol components and affecting the local urban air quality and climate.

2.2 **Introduction**

Particulate matter is a major contributor to urban air pollution affecting both human health and air quality (Chan and Yao, 2008; Guarnieri and Balmes, 2014; Pöschl, 2005). Organic matter represents a large proportion of urban aerosols (Jimenez et al., 2009). Organic cooking aerosols have been estimated to contribute an additional ca. 10 % to

$PM_{2.5}$ emissions in the UK(Ots et al., 2016), and cooking emissions were recently identified as a major contributor to the organic PM_1 flux in aerosol flux measurements in a Chinese megacity (Squires et al., 2020). Unsaturated fatty acids, such as oleic acid, have been identified as major contributors to urban cooking emissions up to PM_{10} (Allan et al., 2010; Alves et al., 2020; Vicente et al., 2018; Zhao et al., 2015). For this reason, oleic acid has been used as a proxy for the reactive fraction of cooking aerosols and as a representative of unsaturated fatty acids in the atmosphere, which makes it a well-studied model compound (Gallimore et al., 2017; King et al., 2004, 2009, 2010; Morris et al., 2002; Pfrang et al., 2017; Schwier et al., 2011; Shiraiwa et al., 2010, 2012; Zahardis and Petrucci, 2007).

Solid and semi-solid phases have been observed for secondary organic aerosols (Virtanen et al., 2010). In addition to the effects of organic-aqueous phase separation (Freedman, 2020), viscous phases are identified as a key factor in influencing fundamental aerosol processes such as uptake of water and reactive gasses (Reid et al., 2018). In particular, glassy and semi-solid phases have been studied and show drastic differences in their physical properties (Berkemeier et al., 2016; Koop et al., 2011; Mikhailov et al., 2009; Zobrist et al., 2011). Therefore, organic aerosol lifetime can vary significantly depending on temperature and humidity-induced phase changes, which simultaneously alter the viscosity of the aerosol and the diffusion coefficients of key atmospheric species within it (Renbaum-Wolff et al., 2013; Shiraiwa et al., 2011).

Oleic acid is a surfactant and, upon mixing with its salt (sodium oleate) and water, is able to form a range of lyotropic liquid crystalline (LLC) phases (Tiddy, 1980). Oleic acid and its LLC phase behaviour has been studied extensively in biological and cosmetic contexts, exhibiting a range of different 3–D molecular assemblies (Engblom

et al., 1995; Mele et al., 2018; Seddon et al., 1990). More recently, this phase behaviour has been studied in an atmospheric context in levitated droplets (Pfrang et al., 2017). All of these phases exhibit unique physical properties such as viscosity (Mezzenga et al., 2005) and the rate of diffusion of small molecules through them can vary significantly; these are important factors exploited in drug delivery applications that are also applicable to the diffusion of molecules through atmospherically-relevant particles (Zabara and Mezzenga, 2014). In the present study we focus on the lamellar phase formed by the oleic acid-sodium oleate cooking aerosol proxy and explore the impact of this phase on the kinetic behaviour.

Coatings of organic material have been found and characterised on aerosol surfaces, with fatty acids identified as one of the components on sulfate aerosols (Tervahattu, 2002; Tervahattu et al., 2005). Recently, high pollution events have been linked to greater organic content at the surface of urban $PM_{2.5}$ emissions in Beijing, China (Zhao et al., 2020). Urban particulate matter coatings have also been shown to contain harmful species such as Polycyclic Aromatic Hydrocarbons (PAHs) and heavy metals, making these surfaces a potential health hazard in the urban environment (Li et al., 2018). PAHs and oleic acid have been identified in marine aerosols influenced by urban emissions, suggesting a degree of long-range transport from the urban environment (Kang et al., 2017). Long-range transport of PAHs and the link to lung cancer risk has been associated with shielding by organic aerosol coatings and the extent of this effect is attributed to the phase of the PAH-containing aerosol, which is dependent on the surrounding environment (Mu et al., 2018; Shrivastava et al., 2017).

In this work we investigate the effect of film thickness on the reactivity of a self-assembled (semi-solid) form of oleic acid-sodium oleate using simultaneous Small-

Angle X-ray Scattering (SAXS – reaction kinetics and self-assembled structure), Raman microscopy (reaction kinetics) and Wide-Angle X-ray Scattering (WAXS – fatty acid tail packing). These techniques are complemented by Grazing-Incidence SAXS (GI–SAXS – surface orientation). Most notably, we present a novel method of measuring reaction kinetics using SAXS data, taking advantage of the high X-ray flux available at a synchrotron source to enable micron-sized films to be probed – increasing the atmospheric relevance of this proxy compared to large levitated particles in our previous study (Pfrang et al., 2017). We compare the reactivity of oleic acid in the solid, semi-solid and liquid forms under the same conditions, highlighting drastic differences linked to the phase state. Reaction stagnation is observed for the thickest films and we link this to the formation of an inert crust, which has previously been postulated (Pfrang et al., 2011). We associate these findings with the persistence of organic coatings in the atmosphere and potential effects on the urban environment.

2.3 Experimental

2.3.1 Preparation of self-assembled fatty acid coatings inside quartz capillaries

Oleic acid (Sigma-Aldrich, 90 %) and sodium oleate (Sigma-Aldrich, 99 %) were dissolved separately in methanol as 10 wt % solutions. The sodium oleate mixture required gentle heating to ~ 50 ^{o}C for 10 min in order to fully dissolve. These solutions were then mixed together in a 1:1 wt ratio to afford the oleic acid-sodium oleate coating solution.

A 70 µL aliquot of the coating solution was injected inside a quartz capillary tube (Capillary Tube Supplies Ltd., UK, 1.5 ± 0.25 mm diameter, wall thickness 0.010 mm) which was embedded inside a metal holder. The sample solution was passed up and down the tube. Simultaneously, compressed air was passed gently through the tube to

facilitate evaporation of the methanol. Room-temperature compressed air was chosen in order not to risk the breakdown of the possibly temperature-sensitive self-assembled phase. After evaporation, a translucent film of the oleic acid-sodium oleate lamellar phase sample was observed. This method of film coating left a film of unequal thickness along the capillary enabling us to probe sections of the film of different thicknesses under the same conditions (see section 2.4). This coated tube was placed into a sample holder on the I22 beamline at the Diamond Light Source (UK). Dry oxygen was passed through the capillary for ~ 10 min before kinetic experiments began to ensure that all of the methanol had evaporated.

2.3.2 SAXS/WAXS/Raman microscopy during ozonolysis of films coated inside quartz capillaries

SAXS/WAXS is a scattering technique which probes aggregate materials at the nanometre scale (*i.e.* interactions between aggregate structures rather than atoms within molecules) (Li et al., 2016; Pauw, 2013). Scattered intensity is measured against a scattering parameter (q), which is inversely proportional to the spacing between equivalent scattering planes (Fig. 2-1).

SAXS/WAXS patterns were collected as a series of 1 s frames along the length of the coated quartz capillary. We introduced a delay period of 75 s between each set of scans to avoid any possible X-ray beam damage since the signal-to-noise ratios were sufficient at 1-s exposure times. The size of the collimated X-ray beam was approximately 320 μm × 400 μm (FWHM). The film thickness is independent of the size of the X-ray beam. A large X-ray footprint was chosen specifically in order to maximise the signal-to-noise ratios and thus being able to detect micron-sized films, making this a key advantage of the experimental setup. The beam size was determined

by attenuation of the X-rays by the metal capillary holder used during the experiments. By allowing the X-ray beam to hit the metal, a diode close to the detector does not detect the X-ray beam. Moving the beam in small 20 µm steps until the diode detects the full X-ray flux allowed the beam size to be determined (*i.e.* the difference between the stage position at half and full X-ray flux is the radius of the beam in the scanning direction). This was done for the horizontal and vertical directions. Scattering patterns were acquired in the *q*-range 0.008 – 0.6 $Å^{-1}$ by the SAXS detector (*Pilatus P3-2M*) and simultaneously from 0.48 – 5.28 $Å^{-1}$ by the WAXS detector (*Pilatus P3-2M-L*).

Ozone was produced by exposing oxygen (BOC, 99.5 %) to UV radiation through a pen-ray ozoniser (Ultraviolet Products Ltd, Cambridge, UK). The ozone concentration was controlled by exposing the oxygen flow to the desired amount of UV light. The ozone concentration was calibrated offline using UV spectroscopy, monitoring the 254-nm absorption band of ozone using the absorption cross-section for ozone at this wavelength ($(1.14 \pm 0.07) \times 10^{-17}$ cm^2) (Mauersberger et al., 1986). The mixing ratio of ozone used in these experiments was 77 ± 5 ppm. Such a high concentration of ozone was employed as past experience with self-assembled phases suggests that the ozonolysis reaction is very slow (Pfrang et al., 2017). In the timeframe of a synchrotron beamtime experiment, exposing the samples to more atmospherically-relevant ozone mixing ratios (ppb levels) would have resulted in only very few experiments being feasible, thus making a rigorous kinetic study impossible.

60 mL min^{-1} of oxygen/ozone mixture was passed through the fatty acid-coated capillaries. The sample was exposed to X-rays from the synchrotron. Scans across the capillary were carried out with each scan consisting of 11 scattering patterns along the length of the tube, i.e. 11 different sections of the capillary tube.

As the X-ray beam passes through two film surfaces, one surface on the 'beam' side and the other on the 'detector' side of the capillary, the resulting X-ray scattering pattern is two-fold more intense for a particular thickness as would be if the X-ray beam were to pass through just one surface. This is an advantage of using capillary tubes as surfaces to deposit films.

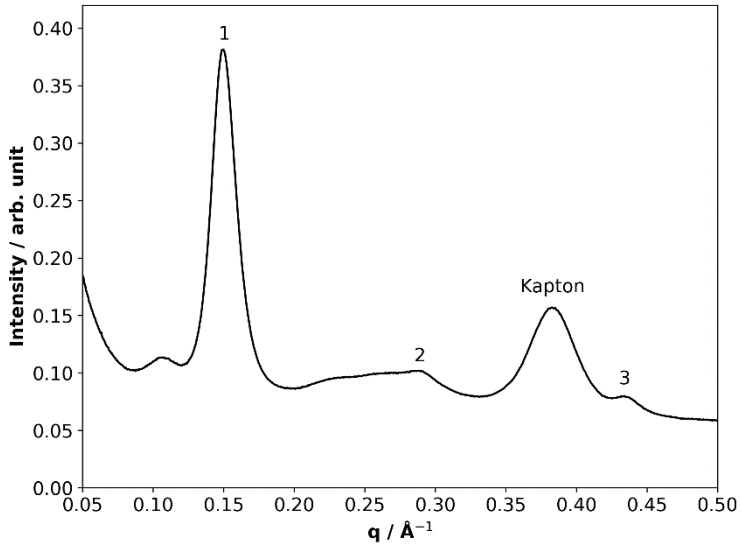

Figure 2-1. The initial SAXS pattern of a 73 ± 2 µm thick film. Numbers indicate the lamellar phase Bragg peaks. The scattering peak from Kapton film on the X-ray detector is also labelled and was used as an internal standard.

For these chosen experimental conditions, the lamellar phase was expected in our fatty acid proxy (Fig. 2-1). Bragg reflections for the lamellar phase were evident in the SAXS patterns. The first Bragg peak ~ 0.15 $Å^{-1}$ was chosen as the peak of interest for the kinetic study. Kapton is a material used in the detector setup at the synchrotron and has a scattering peak at ~ 0.37 $Å^{-1}$. This Kapton peak is not affected by the experiment and was used as an internal standard for the measurement of the lamellar phase peak area.

Normalising to the Kapton peak area has the advantage of accounting for fluctuations in the synchrotron beam intensity and other possible variations in the sample exposure.

The film thickness was determined by measuring the first lamellar peak area (peak "1" in Fig. 2-1) and normalising to the Kapton peak in a quartz capillary of known internal diameter (1.45 mm – measured by attenuation of the X-ray beam while scanning across an empty capillary) entirely filled with the sample. The lamellar peak/Kapton peak ratio of each film was then used to determine the film thickness, taking into account the X-ray beam passing through two films on either side of the capillary. A wide range of film thicknesses (0.59 – 73 µm) were measured. Although organic coatings are known to be present in atmospheric aerosols, to our knowledge there are no explicit studies to date directly characterising organic film thickness in urban particulate matter. However, the morphology of sea spray aerosols with an organic coating has been reported recently, demonstrating that organic films in the order of microns are possible (Kirpes et al., 2019). With particulate matter up to PM_{10} being the most common size observed in the urban environment, we assume that films up to 10 µm thick are thus potentially relevant to the urban environment. The thicker films investigated here together with the atmospherically relevant < 10 µm films are however very useful to demonstrate that the kinetic trends are valid and consistent across more than two orders of magnitude of film thicknesses accessible with our experimental set-up in otherwise identical conditions. Uncertainties associated with these thickness measurements were determined from the error in the intensities recorded over the *q*-range of the lamellar peak. This was done for every peak measurement in order to quantify uncertainty for each point in the decay plots (see Fig. 3(b) below). These numbers are small due to the better statistics

associated with the high-flux synchrotron radiation compared to lab-based X-ray sources. Uncertainties, along with all kinetic data, are listed in Table 10-1 (appendix).

An additional scattering peak at a lower q (~ 0.11 $Å^{-1}$) than the first lamellar scattering peak is likely to be a result of excess oleic acid in the mixture and is observed in the thickest films (Fig. 2-1). This phase is most likely another arrangement of oleic acid, although phase assignment was not possible as more than one peak is required for this.

The peak area of the first lamellar phase reflection was measured as a function of ozone exposure. Measurements of the SAXS patterns were started ~ 3 min after the ozone production was initiated due to the safety procedures necessary at the synchrotron beamline.

As ozone attacks the unsaturated fatty acid double bond, the C=C Raman scattering peak area at ~ 1650 cm^{-1} (normalised to the $–CH_2$ deformation band at ~ 1442 cm^{-1}) was followed during ozonolysis in order to provide complementary kinetic data to the more sensitive SAXS measurements. The reactive decay of disordered oleic acid cannot be measured by SAXS as it does not have a strong SAXS peak due to the lack of self-assembly. For this reason, Raman microscopy is essential to measure reaction kinetics for comparison with the self-assembled samples.

Simultaneous Raman microscopy was possible on the I22 beamline. A 532-nm Raman laser probe with a long working distance objective (numerical aperture: 0.42) and a minimum spot diameter of ~ 1.5 μm was focussed onto the coated film. The laser power emitted from the objective end was between 20 – 50 mW. The focal depth of the Raman probe beam only permitted measurement of the Raman spectrum from the film on one side of the capillary

2.3.3 Challenges associated with the novel SAXS–reaction kinetics method

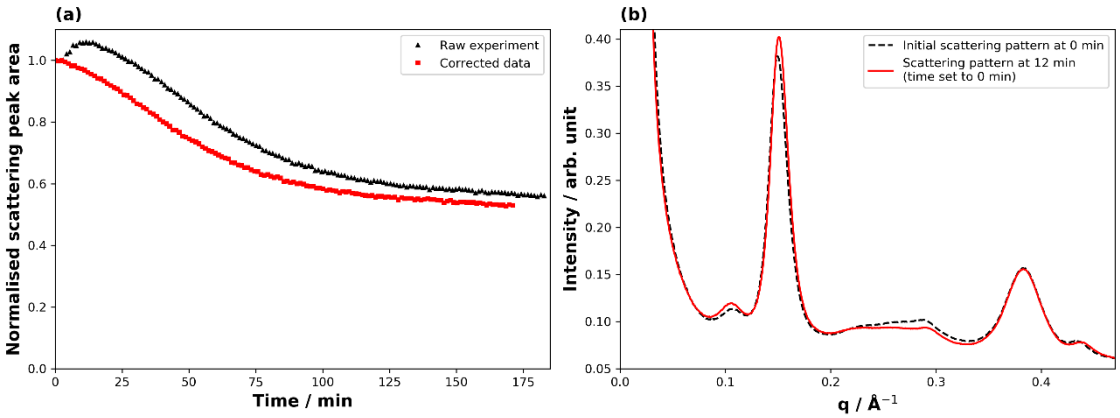

Figure 2-2. Illustration of data correction (film thickness: 73 ± 2 µm). (a) Scattering peak area vs time exposed to ozone, both raw and corrected data plotted. (b) SAXS patterns of the sample at the beginning of the experiment (black dashed line) and at the time (after 12 min) at which the peak scattering area was measured, which was defined as t = 0 for the decay of the lamellar phase (red solid line).

Figure 2-2 illustrates the correction applied to the raw SAXS data for derivation of meaningful kinetic information. At the beginning of the ozonolysis experiment a broad peak arising from a minor co-existent phase (*ca.* 0.20 – 0.25 $Å^{-1}$) decays, accompanied by an increase in the lamellar peak intensity (Fig. 2-2(b)). The measured peak area for the first ~ 10 min of the reaction of the thickest films consequently showed an increase (Fig. 2-2(a)). This was accompanied by a small shift in the peak position (q), corresponding to a decrease in spacing (d) between lamellar sheets ($q \propto 1/d$). It is likely that this minor phase was an inverse micellar arrangement of oleic acid due to the 7.8 % molar excess of oleic acid in the mixture and the dryness of the sample (Mele et al., 2018). The effect was most prominent for the thickest films. To account for this effect, the raw peak area decays were adjusted so that time zero was set as the point at which

the maximum lamellar peak area was measured, with all other peak areas being normalised this new initial value (Fig. 2-2(a)). Adjustments were in the order of *ca.* 0 – 15 min depending on the magnitude of this effect for the different film thicknesses. The observed kinetic decay parameters were calculated from this corrected data. This effect is not dissimilar to overlapping peaks in spectroscopic methods, but if a co-existing phase leading to an interfering peak is not well defined or characterised, corrections can be challenging.

2.4 Results and discussion

2.4.1 Film thickness-dependent reaction kinetics

We were able to take advantage of the smooth decay plots obtained using the synchrotron-SAXS technique and derive observed pseudo-first order decay constants (k_{obs}), measured at the fastest period of the reaction (see Fig. 2-3(b)), for the range of film thicknesses probed in this study (Fig. 2-3).

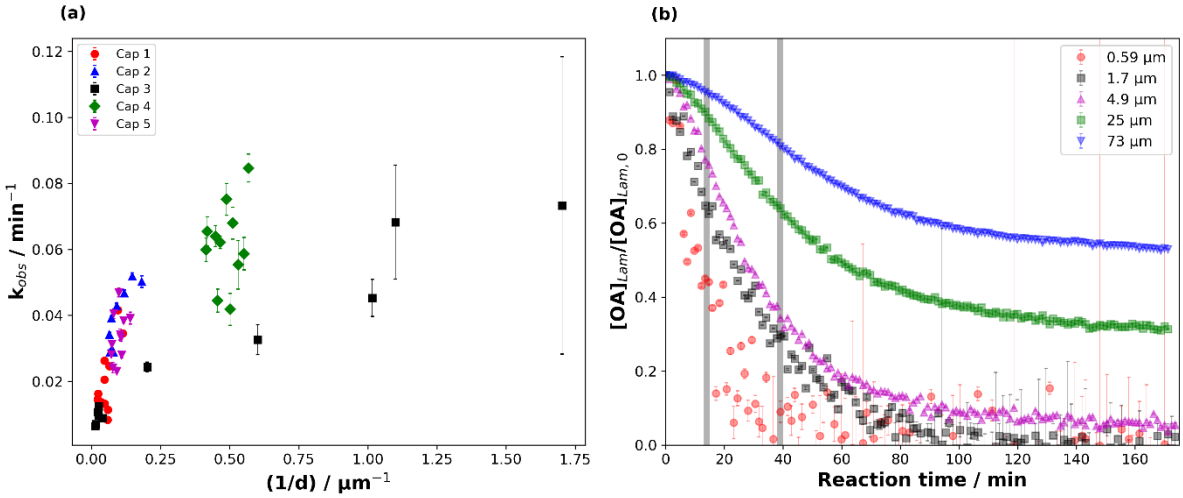

Figure 2-3. The observed pseudo-first order decay constant (k_{obs}) as a function of (a) inverse film thickness (1/d), demonstrating the film-thickness dependence of the reaction kinetics. Different capillary ("Cap") experiments are distinguished by different colours and symbols. (b) Decay plots of the normalised amount of lamellar oleic acid ($[OA]_{Lam}/[OA]_{Lam,0}$) vs reaction time (t) at different thicknesses – data are from one capillary experiment ("Cap 3") and grey bars indicate the reaction times between which k_{obs} was measured for films with d > 2.5 µm. $[O_3]$ is 77 ± 5 ppm.

The data presented in this study come from five different capillary coatings exposed to ozone under the same controlled conditions. Kinetic parameters from different capillaries are highlighted by different colours and symbols in Fig. 2-3. The higher uncertainty in the measured k_{obs} for the thinnest films is derived from fitting fewer points to the decay function and the proximity of the 1st order lamellar peak to the baseline (Fig. 10-1, appendix).

The range of film thicknesses for each coated capillary is generally small (Fig. 2-3(a), with one exception ("Cap 3") showing a range of thicknesses from the thinnest (0.59 ± 0.02 µm) to the thickest (73 ± 2 µm) film (Table 10-1, appendix).

Generally, k_{obs} scales with $1/d$ for the thickest films (Fig. 2-3(a)). However, this trend does not hold as well for the thinner films, though the increase in the uncertainty of k_{obs} at thinner film thicknesses complicates this judgement. This deviation implies that the limiting factors governing k_{obs} change with film thickness (Hearn et al., 2005). The shape of the decay plots changes between the thinnest and thickest films (Fig. 2-3(b)). The decay plot for the thickest film (d = 73 ± 2 μm) reveals an initial slow decay in self-assembled oleic acid-sodium oleate concentration followed by a faster period of decay. Finally, the reaction stagnates with a significant portion of self-assembled oleic acid remaining (this stagnation is discussed in section 2.4.3). A thinner film from the same capillary experiment (d = 0.59 ± 0.02 μm) exhibits a decay profile that has a more "classical" shape following pseudo-first order reaction kinetics with one clear reaction regime similar to experiments performed on liquid oleic acid (Gallimore et al., 2017; He et al., 2017; Hearn et al., 2005; Smith et al., 2002). The reaction does slow down for the thinnest films, but the low signal-to-noise ratio close to the baseline means that there is no clear evidence of stagnation.

It is known that self-assembled phases, such as the lamellar phase studied here, are viscous (Mezzenga et al., 2005); certainly more viscous than pure oleic acid, which is a liquid at room temperature. This means that diffusion throughout a particle of this composition is likely to be hindered for both the reactive gas (ozone) and oleic acid/sodium oleate. The observation that k_{obs} scales with $1/d$ for the thickest films suggests that the reaction is limited to the surface of these particles and/or limited by the diffusion of O_3 through the particle (Hearn et al., 2005; Smith et al., 2002).

The oleic acid–ozone heterogeneous reaction has been shown to be surface-dominated (Hearn et al., 2005). It has been suggested that oleic acid (in the liquid form) can form

ordered structures such as dimers (Iwahashi et al., 1991). Indeed, under certain conditions, oleic acid can even form helices and vesicles (Blöchliger et al., 1998; Ishimaru et al., 2005). Hearn *et al.* suggested that on the particle surface, the alkyl chains in oleic acid are more ordered and that there is an increase in double bond density at the surface, decreasing the rate of ozone diffusion into the bulk and implying that the reaction is surface-dominated (Hearn et al., 2005). Furthermore, they stated that the short spacing between alkyl chains results in reduced diffusion of ozone past them, further limiting bulk uptake of ozone. WAXS patterns obtained simultaneously during our experiments show that the short spacing between oleic acid molecules in the liquid crystalline lamellar phase is 4.41 Å (Fig. 10-2, appendix). This is shorter than the 4.57 Å measured by Iwahashi *et al.*(Iwahashi et al., 1991) and confirmed by our WAXS experiments on liquid oleic acid, indicating that diffusion of ozone past the ordered alkyl chains in our self-assembled case is even slower. Complementary GI-SAXS patterns demonstrate that our lamellar phase sample, deposited on a silicon wafer, shows significant alignment parallel to the silicon surface *i.e.* the alkyl chains are oriented perpendicular to the surface (Fig. 10-3, appendix). Our experiments suggest therefore that the reaction is most likely surface-dominated at the beginning. This is clearly visible for the films thicker than ~ 2 μm, which exhibit an initial slow decay (Fig. 2-3(b)).

There is evidence to suggest that the kinetic regime for the reaction changes after the initial surface-dominated period for the thickest films. The increase in reaction rate after the slow initial reaction period may be due to the initial surface layers of highly ordered oleic acid-sodium oleate having reacted, leaving behind disordered products (and possibly some unreacted oleic acid) which would allow for increased ozone bulk uptake

due to a reduction in steric and diffusional hindrance. We suggest that after the initial surface-limited reaction ozone starts to diffuse further into the bulk layers, forming a concentration gradient along the way. The bulk layers are still composed of the highly viscous lamellar phase with its impaired oleic acid and ozone diffusion. Noting that k_{obs} (calculated from this region) does not scale with $1/d^2$, we conclude that in this reaction period the reaction is limited by ozone diffusion through the bulk and not by oleic acid diffusion. The third part of the decay profile, exhibiting reaction stagnation, will be discussed in section 2.4.3.

Study	Particle or film diameter / µm	k_{obs} / min^{-1}
He *et al.*(He et al., 2017)	50 – 200	(0.036 – 0.135)*
This work	0.59 – 73	0.0064 – 0.085

Table 2-1. Comparison between this work and the work of He et al. on oleic acid particles deposited on ZnSe windows.(He et al., 2017) *[O_3] = 77 ± 5 ppm (this work), [O_3] = 10 ppm (He et al.). *Estimated by us based on graphs published in He et al.*

Kinetic values presented here are comparable to previous kinetic studies on particles or films of oleic acid (Gallimore et al., 2017; González-Labrada et al., 2007; Rosen et al., 2008). In particular an ozonolysis dataset from He *et al.* (He et al., 2017), studying deposited oleic acid particles in the size range of 50 to 200 µm using an IR-based technique, is the most comparable to our study (Table 2-1). Note that the deposited particles of He *et al.* will have a curvature that may affect ozone uptake (Pöschl et al., 2007). Our films are assumed to have a flat geometry on the µm scale (we may also have a slight curvature of the films given the mm-scale round capillaries, but this is not considered significant on the µm scale).

Comparing our film with thickness of $d = 46 \pm 2$ μm to the ~ 50 μm radius oleic acid particle deposited by He *et al.*, we find that k_{obs} is 0.0107 ± 0.0002 min^{-1} and ~ 0.135 min^{-1} for our film and the deposited particle of He *et al.*, respectively. This suggests that our film reacts *ca.* one order of magnitude more slowly than a deposited oleic acid particle of similar size even though we used an ozone concentration nearly 8-fold greater. Despite there being a difference in geometry, this large difference in reactivity is further evidence of the slowing effect our viscous self-assembled phase has on the reaction kinetics.

2.4.2 Quantification of the effect of self-Assembly on reaction kinetics

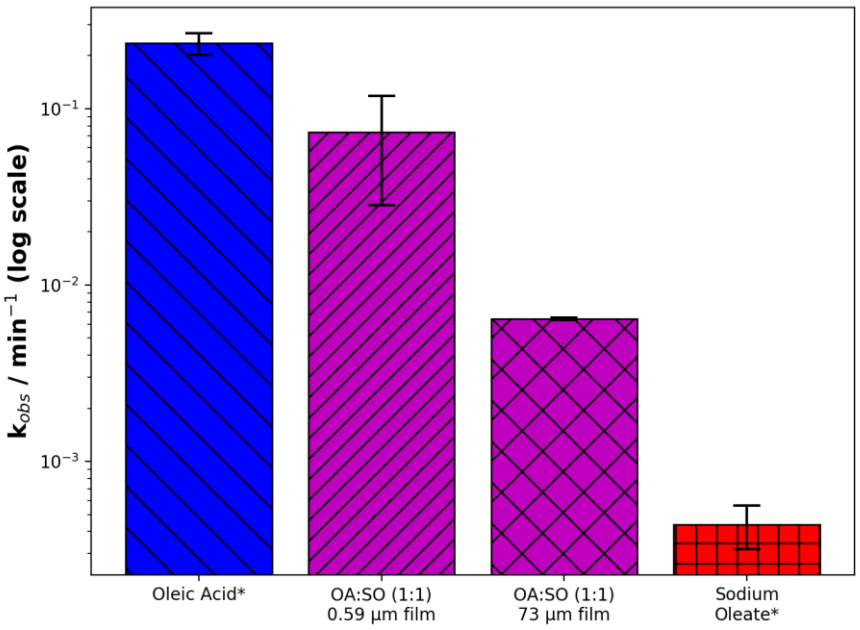

*Figure 2-4. Comparison of k_{obs} between a capillary coating of oleic acid (liquid), two coatings of self-assembled oleic acid-sodium oleate proxy (semi-solid: 0.59 & 73 µm thick) and a coating of sodium oleate (solid). *The oleic acid and sodium oleate decays were followed by Raman microscopy, using the C=C band at 1650 cm^{-1}. The thickness of the oleic acid and sodium oleate coatings was measured to be ~ 50 µm based on the X-ray attenuation of these samples compared to self-assembled coatings of known thickness. (OA: oleic acid; SO: sodium oleate). [O_3] = 77 ± 5 ppm.*

The ability to coat capillaries with oleic acid in various states of solidity under the same laboratory conditions allows us to quantify the effect of phase and, more specifically, of self-assembly on the reaction kinetics of the oleic acid–ozone system.

A comparison of k_{obs} between this self-assembled system and its constituent parts shows a marked difference in reactivity as the system moves from a liquid (oleic acid) via a

semi-solid (self-assembled oleic acid-sodium oleate) to a solid (sodium oleate) phase (Fig. 2-4 – note the log scale). There is approximately an order of magnitude difference in reactivity when going from liquid (~ 10^{-1} min^{-1}), via semi-solid (~ 10^{-2} min^{-1}) to solid (~ 10^{-3} min^{-1}).

This is the first time the effect of self-assembly on reaction kinetics has been quantified. The data also highlight the significance of phase state and viscosity in determining the reactivity of an organic aerosol, which has been the subject of recent discussion in the atmospheric literature (Berkemeier et al., 2016; Marshall et al., 2016; Reid et al., 2018; Shiraiwa et al., 2011). As discussed previously, the same reacto-diffusive arguments related to the viscosity of the lamellar phase provide a reasonable explanation for the much-reduced k_{obs} as the system's solidity is increased.

2.4.3 Reaction stagnation as a function of film thickness

The decay profiles presented in this study show that as film thickness increases, the lamellar SAXS peak area decay slows down significantly by the end of the ~ 3-h experiment (Fig. 2-3(b)) with an increasing fraction of self-assembled material retained, demonstrating an approximately linear relationship (Fig. 2-5).

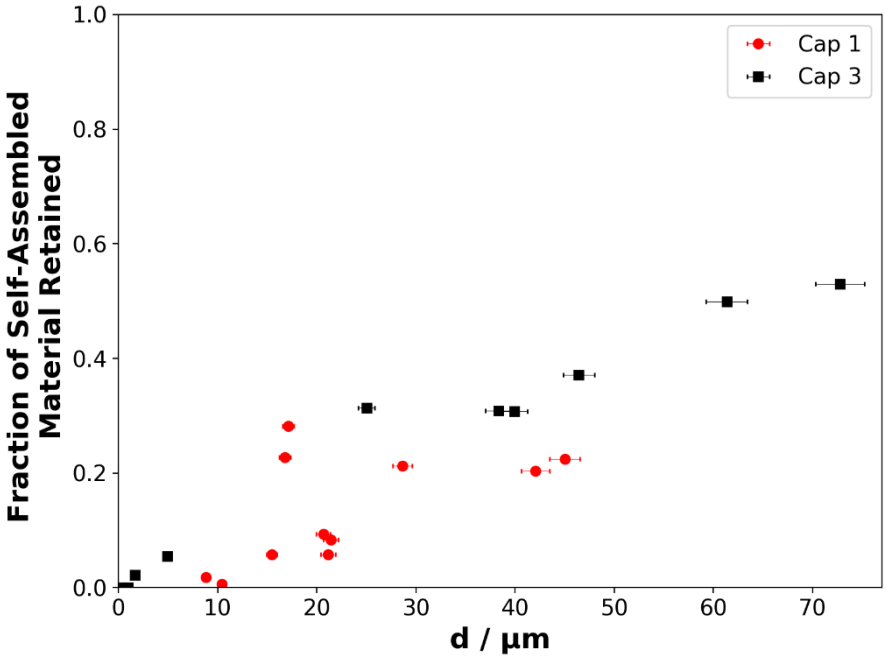

Figure 2-5. The fraction of self-assembled material retained at the end of each experiment (after ~ 175 min of ozonolysis), when the reaction was deemed to have stopped or slowed significantly, as a function of film thickness. Symbols, colours and labels correspond to the same experiments presented in Fig. 2-3. "Cap 1" and "Cap 3"correspond to the "Cap 1" and "Cap 3" experiments presented in Fig. 2-3.

There is a strong correlation between the fraction of self-assembled material left and initial film thickness (Fig. 2-5). We assume that the thinnest films react to completion as no SAXS signal remains and simultaneous Raman microscopy shows that there is no C=C (~ 1650 cm^{-1}) peak remaining by the end of the experiment. Note that Raman

spectra from these coatings were considerably noisier than the SAXS patterns, so that the C=C signal became indistinguishable from the background signal earlier than the SAXS peak.

In this final reaction stage, the reaction has stagnated (Fig. 2-3(b)). The diffusion of ozone and oleic acid is becoming hindered and this must be a result of the ozonolysis reaction. We suggest an inert, highly viscous product is formed. This is likely because whatever is causing this stagnation has to have resulted from the reaction as this is the only process occurring. As the reaction proceeds mainly in the surface layers of the film, with a reacto-diffusive length in the order of ~ 10 nm for oleic acid (Moise and Rudich, 2002; Morris et al., 2002; Smith et al., 2002), it is likely that the outer layers of the film start to form an inert crust of these viscous products. Our results support the idea of an inert crust formation, postulated by Pfrang *et al.* (Pfrang et al., 2011) and suggested by others more recently (Zhou et al., 2019), and are consistent with the notion that viscous phases supress reactive gas uptake (Berkemeier et al., 2016; Marshall et al., 2016; Shiraiwa et al., 2011). High-molecular-weight oligomeric products have been observed in the oleic acid-ozone heterogeneous reaction system (Lee et al., 2012; Reynolds et al., 2006; Wang et al., 2016; Zahardis et al., 2005, 2006). They are formed by the reaction of stabilised Criegee intermediates with other reaction products. Wang *et al.* used a simplified model of this reaction to follow the formation of products as a function of percentage oleic acid conversion (Wang et al., 2016). Their output suggests that at higher oleic acid conversion, there is an increased fraction of high molecular weight product of up to 10 %. This is a result of high-molecular-weight products forming from first-, second- and multi-generational ozonolysis products (Zahardis et al., 2006), inferring a time delay before an appreciable amount of these products is formed.

Our data show that there is indeed a time delay before an appreciable stagnation is observed. Considering the literature and these results, the thickest films would form a greater mass of higher molecular weight products. Therefore a thicker crust with a higher concentration of oligomeric products would be formed compared to the thinnest films, which would not have had the time to form significant concentrations of oligomeric products.

These results are in line with the recent observations of Alpert *et al.* who reported unreacted material remaining after ozonolysis in the cores of viscous particles at low relative humidity, RH (0 – 20 %).(Alpert et al., 2019) In particular, similarities may be drawn between our viscous system and that of Berkemeier *et al.* who also observed changes in kinetic regime and rationalised this using the "kinetic cube" (Berkemeier et al., 2013), demonstrating a transformation from a surface-dominated to a bulk diffusion-limited regime for viscous particles during ozonolysis at low RH (~ 20 %) (Berkemeier et al., 2016). We suggest that a similar reaction regime evolution prevails in our system.

The evolution of the kinetic regime is being explored in an ongoing kinetic modelling study based on the PRA framework (Pöschl et al., 2007; Shiraiwa et al., 2010, 2012) and is suggesting that the additional stagnation is not fully accounted for when evolving particle diffusion using either obstruction theory (*e.g.* Pfrang *et al*.) (Pfrang et al., 2011) or a Vignes-type regime (*e.g.* Zhou *et al*.) (Zhou et al., 2019).

2.4.4 **Implications for the urban atmosphere**

Oleic acid has been measured as a component of cooking emissions in urban areas of the UK and China (Allan et al., 2010; Zhao et al., 2015) and cooking aerosols have been estimated account for an additional 10 % of officially reported $PM_{2.5}$ emissions in the

UK (Ots et al., 2016). Our observations show that the reactive lifetime of oleic acid can vary by orders of magnitude when moving from solid, via self-assembled (semi-solid) to liquid form. In addition, there is a thickness-dependent reactivity associated with these self-assembled films, adding to an increased oleic acid lifetime. This effect suggests that the phase state of organic films formed by cooking emissions, controlled by both the urban environment and aerosol composition, could play a significant part in determining the lifetime of urban particulate matter. Moreover, assuming the thickness of an organic film is related to the amount of cooking activity, the organic film thickness could also vary - implying that the reactivity and persistence of the aerosol could be impacted by the amount of organic emissions. This is likely as high pollution events have been linked to a greater surface organic content in $PM_{2.5}$ emissions in Beijing, China (Zhao et al., 2020).

Heterogeneous reactions of oleic acid with other key initiators of oxidation are possible. Of particular importance at night time is NO_3 (Wayne et al., 1991). It has been shown that unsaturated fatty acid reactivity with NO_3 is ~ 2 orders of magnitude more reactive than ozone (Sebastiani et al., 2018). We suggest that the phase and thickness kinetic effects observed here could be observed for other heterogeneous reactions of this system such as that initiated by NO_3. The oleic acid-ozone reaction is severely impeded by the semi-solid nature of this proxy even at a high ozone concentration. This suggests that a heterogeneous reaction with more reactive species, such as NO_3, would also be impeded by the semi-solid nature of this proxy.

Urban air pollution has been linked to health conditions such as asthma (Guarnieri and Balmes, 2014) and recently a large range of microorganisms have been identified in urban particulate matter emitted in a megacity, implying potential consequences for

human health (Qin et al., 2020). A wide range of compounds emitted into the urban atmosphere are known to have adverse health effects. These include phthalates, which affect male reproductive development (Swan et al., 2005) and are emitted from plastics (Wang et al., 2006); as well as polycyclic aromatic hydrocarbons (PAHs), which have been linked to cancer risk (Boffetta et al., 1997), are emitted by combustion and vehicles (Harrison et al., 1996) and have been observed on the surface of urban particulate matter (Li et al., 2018). Both of these classes of toxic compounds, along with oleic acid, have been found in the same marine aerosols which have been influenced by continental urban emissions (Kang et al., 2017). These compounds therefore survived the journey from the urban to the marine environment. The transport of PAHs in particular has been shown to be highly dependent on aerosol phase, which in turn is dependent on atmospheric conditions (Mu et al., 2018). Coatings of semi-solid organic aerosol are thought to shield PAHs, increasing their global atmospheric transport potential and thus increasing lung cancer risks – again, the effect is highly phase dependent (Shrivastava et al., 2017). The increased reactive lifetime of our self-assembled (semi-solid) films of oleic acid-sodium oleate suggests that the aerosol would travel further, take part in aerosol processes such as cloud nucleation and contribute to the persistence of pollutants in the urban environment and beyond. The fact that all three of these pollutants have been observed in the same urban-influenced marine aerosol samples indicates that viscous forms of oleic acid, such as the form studied here, could contribute to the extended transport distances of the aerosol and the potentially harmful components within it. Additionally, we have demonstrated that there is a film thickness-dependent reactivity and as film thickness increases there is a significant reaction stagnation due to the formation of inert products – this effect is observed down

to d = 4.9 ± 0.2 μm (Table 10-1, the appendix). Unreacted oleic acid, and reaction products, would therefore be protected from further oxidative ageing. This protection is analogous to what has been postulated about the shielding of PAHs by semi-solid organic coatings (Shrivastava et al., 2017). As urban particulate organic content is linked with air quality in $PM_{2.5}$ emissions (Zhao et al., 2020) and cooking aerosols contribute to $PM_{2.5}$ (Zhao et al., 2015) and PM_{10} (Allan et al., 2010; Daellenbach et al., 2017) emissions, the observations for d < 10 μm are most atmospherically relevant and demonstrate that (i) reactivity slows down over the whole film thickness range studied here; and (ii) reaction stagnation is observed only for the thicker films (from d = 4.9 ± 0.2 μm) and is therefore most relevant to PM_{10} emissions – though the effect is not clear for the thinnest films within the limitations of experimental signal-to-noise ratios (Fig. 2-3(b)).

Oleic acid is surface active, along with its primary low-volatility ozonolysis products azelaic (Tuckermann, 2007) and nonanoic acid (King et al., 2009). We suggest that surface-active material is retained after extensive oxidation. This is because low volatility primary products are likely to remain in the surface layers of the film. Surface active organic material affects aerosol hygroscopicity by reducing aqueous droplet surface tension (Bzdek et al., 2020; Facchini et al., 1999; Ovadnevaite et al., 2017). Our findings suggest that surface active components of an organic aerosol could have an increased residence time in the atmosphere, increasing the potential of the aerosol to affect cloud and fog formation in the local urban environment (Facchini et al., 2000). Our results are consistent with organic residues observed in unsaturated organic films at the air–water interface, having similar implications (King et al., 2009; Pfrang et al., 2014; Sebastiani et al., 2018; Woden et al., 2018).

The *e*-folding time (τ_e) can be calculated as the inverse of k_{obs}. These values are valid for the fixed ozone concentration used here, however the general trend is thought to be comparable with what would be observed at ambient ozone concentrations. τ_e ranges from ~ 13 min (d = 0.59 ± 0.02 μm) and ~ 41 min (d = 4.9 ± 0.2 μm) at the lower end of the thickness range to ~ 156 min (d = 73 ± 2 μm) for the thickest film (see Table 10-1, the appendix). Note that k_{obs} was measured at the fastest point in the reaction, meaning that these τ_e values do not take into account the effect of reaction stagnation and the evolution of the kinetic regime observed and discussed here. All τ_e values are longer than that estimated for a film coated with oleic acid, ~ 4 min (d ~ 50 μm – reaction kinetics followed by Raman microscopy). This large range of τ_e values suggests that film thickness and phase state have a significant effect on oleic acid reactivity, implying organic aerosols containing oleic acid in a semi-solid state such as this are likely to persist for longer times in the atmosphere. These experiments provide some explanation for the apparent extended atmospheric lifetime of oleic acid in the atmosphere compared with laboratory observations (Robinson et al., 2006; Rudich et al., 2007).

2.5 **Conclusions**

We have conducted a series of ozonolysis experiments on capillaries coated with self-assembled oleic acid-sodium oleate cooking emission proxies. By taking advantage of the self-assembled nature of these proxies and the high intensity radiation available at a synchrotron X-ray source, we present a novel way of measuring reaction kinetics from time-resolved SAXS data; specifically we measure the rate at which self-assembly disappears during ozonolysis. There is a clear film thickness-dependent reactivity with a significant difference in reactivity between the thickest and thinnest films. We have quantified the effect of phase state on reactivity under the same reaction conditions by

utilising simultaneous Raman microscopy to follow the reaction kinetics of non-self-assembled oleic acid and its salt sodium oleate. Importantly, we have found that the reaction stagnates and there remains a significant amount of unreacted proxy at the end of the experiment. This effect was most pronounced for the thickest films and the fraction of reactant remaining at the end of the experiment exhibited an approximately linear relationship with film thickness.

Our work provides new evidence on the effect of particle phase on atmospheric oxidation processes. We have shown that reactant remains in the particle after ozonolysis down to a film thickness of $d = 4.9 \pm 0.2$ µm and that generally particle phase can alter particle reactivity, which is in line with recent literature highlighting the impact of particle phase on the kinetic regime observed for heterogeneous reaction systems of atmospheric relevance.

We have presented a large dataset of film thickness-dependent kinetic decay parameters for oleic acid in a semi-solid form and have shown how the phase state of this proxy accounts for the reduction in reactivity. The thickness-dependent reaction kinetics trend is consistent with particle size/film thickness studies in the literature and suggests that the reaction is diffusion limited (Al-Kindi et al., 2016; He et al., 2017; Steimer et al., 2014). This diffusion limitation is likely to be enhanced by the formation of inert, viscous oligomeric products which hinder the transport of other molecules in the film. These findings are valid for the range of film thicknesses likely to be found in urban particulate matter ($d < 10$ µm).

In terms of atmospheric implications, our findings demonstrate that both phase state and organic film thickness significantly affect the reactive lifetime of an aerosol particle.

There is clear evidence for reaction stagnation as a result of the formation of an inert crust, contributing to a longer film lifetime. These observed effects would contribute to the protection not only of urban cooking emission surfactant molecules (with implications for cloud/fog droplet formation) but also of potentially harmful compounds associated with aerosols from similar urban sources, enabling extended transport distances and persistence in the atmosphere with associated adverse health implications.

2.6 Acknowledgements

This work was carried out with the support of the Diamond Light Source (DLS), instrument I22 (proposals SM21663 and NT23096). AM wishes to acknowledge funding from NERC SCENARIO DTP award number NE/L002566/1 and CENTA DTP; Eleonore Mason (University of Bath) is thanked for inviting AM/CP to her GI-SAXS beamtime. The authors would like to thank Andy Smith (DLS), Tim Snow (DLS) and Lee Davidson (DLS) for technical support during beamtime experiments; Jacob Boswell is acknowledged for help at beamtimes. The authors are grateful to the Central Laser Facility for access to key equipment for the Raman work simultaneously to the DLS beamtime experiments.

2.6.1 Author contributions

Adam Milsom carried out experiments, processed and analysed and interpreted the data and wrote the manuscript. Christian Pfrang carried out experiments, contributed to data interpretation and to the manuscript. Adam M. Squires carried out experiments, contributed to data interpretation and to the manuscript. Nick J. Terrill setup and provided expertise for the SAXS beamtime. Andy D. Ward setup the Raman microscopy experiment and provided expertise during the beamtime. Ben Woden assisted with experiments at the beamtime and the calibration of the ozoniser.

2.7 **Comment**

This study represents a step forward in the application of SAXS to the study of self-assembled proxies by demonstrating that time-resolved chemical kinetic data could be obtained from SAXS. This is a method applied in chapter 5, where this method is extended to other phases formed by a more complex proxy.

This paper was discussed in a *Faraday Discussion* entitled "Air quality in megacities", hence the weighting of the discussion towards the urban environment. A discussion of this paper is presented in the general discussion published along with this study (Alam et al., 2021).

In the context of this thesis, this study provides a quantification of the effect of surfactant self-assembly on reaction kinetics. Self-assembly into the anhydrous lamellar phase decreases the ozonolysis reaction rate by ~ 1 order of magnitude. The data from this study went on to be used in chapter 3, where a kinetic multi-layer model was applied in order to extract "big picture" atmospheric implications from this work.

2.8 **References**

Al-Kindi, S. S., Pope, F. D., Beddows, D. C., Bloss, W. J. and Harrison, R. M.: Size-dependent chemical ageing of oleic acid aerosol under dry and humidified conditions, Atmos. Chem. Phys., 16(24), 15561–15579, doi:10.5194/acp-16-15561-2016, 2016.

Alam, M. S., Bloss, W., Brean, J., Brimblecombe, P., Chan, C., Chen, Y., Coe, H., Fu, P., Gani, S., Hamilton, J., Harrison, R., Jiang, J., Kulmala, M., Lugon, L., McFiggans, G., Mehra, A., Milsom, A., Nelson, B., Pfrang, C., Sartelet, K., Shi, Z., Srivastava, D., Stewart, G., Styring, P., Su, H., Van Pinxteren, D., Velasco, E. and Yu, J. Z.: General discussion: Aerosol formation and growth; VOC sources and secondary organic

aerosols, Faraday Discuss., 226, 479–501, doi:10.1039/D1FD90011K, 2021.

Allan, J. D., Williams, P. I., Morgan, W. T., Martin, C. L., Flynn, M. J., Lee, J., Nemitz, E. and Phillips, G. J.: and Physics Contributions from transport , solid fuel burning and cooking to primary organic aerosols in two UK cities, Atmos. Chem. Phys., 10, 647–668, 2010.

Alpert, P. A., Arroyo, P. C., Dou, J., Krieger, U. K., Steimer, S. S., Förster, J. D., Ditas, F., Pöhlker, C., Rossignol, S., Passananti, M., Perrier, S., George, C., Shiraiwa, M., Berkemeier, T., Watts, B. and Ammann, M.: Visualizing reaction and diffusion in xanthan gum aerosol particles exposed to ozone, Phys. Chem. Chem. Phys., 21(37), 20613–20627, doi:10.1039/c9cp03731d, 2019.

Alves, C. A., Vicente, E. D., Evtyugina, M., Vicente, A. M., Nunes, T., Lucarelli, F., Calzolai, G., Nava, S., Calvo, A. I., Alegre, C. del B., Oduber, F., Castro, A. and Fraile, R.: Indoor and outdoor air quality: A university cafeteria as a case study, Atmos. Pollut. Res., 11(3), 531–544, doi:10.1016/j.apr.2019.12.002, 2020.

Berkemeier, T., Huisman, A. J., Ammann, M., Shiraiwa, M., Koop, T. and Pöschl, U.: Kinetic regimes and limiting cases of gas uptake and heterogeneous reactions in atmospheric aerosols and clouds: A general classification scheme, Atmos. Chem. Phys., 13(14), 6663–6686, doi:10.5194/acp-13-6663-2013, 2013.

Berkemeier, T., Steimer, S. S., Krieger, U. K., Peter, T., Pöschl, U., Ammann, M. and Shiraiwa, M.: Ozone uptake on glassy, semi-solid and liquid organic matter and the role of reactive oxygen intermediates in atmospheric aerosol chemistry, Phys. Chem. Chem. Phys., 18(18), 12662–12674, doi:10.1039/c6cp00634e, 2016.

Blöchliger, E., Blocher, M., Walde, P. and Luisi, P. L.: Matrix Effect in the Size

Distribution of Fatty Acid Vesicles, J. Phys. Chem. B, 102(50), 10383–10390, doi:10.1021/jp981234w, 1998.

Boffetta, P., Jourenkova, N. and Gustavsson, P.: Cancer risk from occupational and environmental exposure to polycyclic aromatic hydrocarbons, Cancer Causes Control, 8(3), 444–472, doi:10.1023/A:1018465507029, 1997.

Bzdek, B. R., Reid, J. P., Malila, J. and Prisle, N. L.: The surface tension of surfactant-containing, finite volume droplets, Proc. Natl. Acad. Sci. U. S. A., 117(15), 8335–8343, doi:10.1073/pnas.1915660117, 2020.

Chan, C. K. and Yao, X.: Air pollution in mega cities in China, Atmos. Environ., 42(1), 1–42, doi:10.1016/j.atmosenv.2007.09.003, 2008.

Daellenbach, K. R., Stefenelli, G., Bozzetti, C., Vlachou, A., Fermo, P., Gonzalez, R., Piazzalunga, A., Colombi, C., Canonaco, F., Hueglin, C., Kasper-Giebl, A., Jaffrezo, J. L., Bianchi, F., Slowik, J. G., Baltensperger, U., El-Haddad, I. and Prévôt, A. S. H.: Long-term chemical analysis and organic aerosol source apportionment at nine sites in central Europe: Source identification and uncertainty assessment, Atmos. Chem. Phys., 17(21), 13265–13282, doi:10.5194/acp-17-13265-2017, 2017.

Engblom, J., Engström, S. and Fontell, K.: The effect of the skin penetration enhancer Azone® on fatty acid-sodium soap-water mixtures, J. Control. Release, 33(2), 299–305, doi:10.1016/0168-3659(94)00105-4, 1995.

Facchini, M. C., Mircea, M., Fuzzi, S. and Charlson, R. J.: Cloud albedo enhancement by surface-active organic solutes in growing droplets, Nature, 401(6750), 257–259, doi:10.1038/45758, 1999.

Facchini, M. C., Decesari, S., Mircea, M., Fuzzi, S. and Loglio, G.: Surface tension of atmospheric wet aerosol and cloud/fog droplets in relation to their organic carbon content and chemical composition, Atmos. Environ., 34(28), 4853–4857, doi:10.1016/S1352-2310(00)00237-5, 2000.

Freedman, M. A.: Liquid–Liquid Phase Separation in Supermicrometer and Submicrometer Aerosol Particles, Acc. Chem. Res., 53(6), 1102–1110, doi:10.1021/acs.accounts.0c00093, 2020.

Gallimore, P. J., Griffiths, P. T., Pope, F. D., Reid, J. P. and Kalberer, M.: Comprehensive modeling study of ozonolysis of oleic acid aerosol based on real-time, online measurements of aerosol composition, J. Geophys. Res., 122(8), 4364–4377, doi:10.1002/2016JD026221, 2017.

González-Labrada, E., Schmidt, R. and DeWolf, C. E.: Kinetic analysis of the ozone processing of an unsaturated organic monolayer as a model of an aerosol surface, Phys. Chem. Chem. Phys., 9(43), 5814–5821, doi:10.1039/b707890k, 2007.

Guarnieri, M. and Balmes, J. R.: Outdoor air pollution and asthma, Lancet, 383(9928), 1581–1592, doi:10.1016/S0140-6736(14)60617-6, 2014.

Harrison, R. M., Smith, D. I. T. and Luhana, L.: Source apportionment of atmospheric polycyclic aromatic hydrocarbons collected from an urban location in Birmingham, U.K., Environ. Sci. Technol., 30(3), 825–832, doi:10.1021/es950252d, 1996.

He, X., Leng, C., Pang, S. and Zhang, Y.: Kinetics study of heterogeneous reactions of ozone with unsaturated fatty acid single droplets using micro-FTIR spectroscopy, RSC Adv., 7(6), 3204–3213, doi:10.1039/C6RA25255A, 2017.

Hearn, J. D., Smith, G. D. and Lovett, A. J.: Ozonolysis of oleic acid particles: evidence for a surface reaction and secondary reactions involving Criegee intermediates, Phys. Chem. Chem. Phys., 7(3), 501–511, doi:10.1039/b414472d, 2005.

Ishimaru, M., Toyota, T., Takakura, K., Sugawara, T. and Sugawara, Y.: Helical Aggregate of Oleic Acid and Its Dynamics in Water at pH 8, Chem. Lett., 34(1), 46–47, doi:10.1246/cl.2005.46, 2005.

Iwahashi, M., Yamaguchi, Y., Kato, T., Horiuchi, T., Sakurai, I. and Suzuki, M.: Temperature dependence of molecular conformation and liquid structure of cis-9-octadecenoic acid, J. Phys. Chem., 95(1), 445–451, doi:10.1021/j100154a078, 1991.

Jimenez, J. L., Canagaratna, M. R., Donahue, N. M., Prevot, A. S. H., Zhang, Q., Kroll, J. H., DeCarlo, P. F., Allan, J. D., Coe, H., Ng, N. L., Aiken, A. C., Docherty, K. S., Ulbrich, I. M., Grieshop, A. P., Robinson, A. L., Duplissy, J., Smith, J. D., Wilson, K. R., Lanz, V. A., Hueglin, C., Sun, Y. L., Tian, J., Laaksonen, A., Raatikainen, T., Rautiainen, J., Vaattovaara, P., Ehn, M., Kulmala, M., Tomlinson, J. M., Collins, D. R., Cubison, M. J., Dunlea, J., Huffman, J. A., Onasch, T. B., Alfarra, M. R., Williams, P. I., Bower, K., Kondo, Y., Schneider, J., Drewnick, F., Borrmann, S., Weimer, S., Demerjian, K., Salcedo, D., Cottrell, L., Griffin, R., Takami, A., Miyoshi, T., Hatakeyama, S., Shimono, A., Sun, J. Y., Zhang, Y. M., Dzepina, K., Kimmel, J. R., Sueper, D., Jayne, J. T., Herndon, S. C., Trimborn, A. M., Williams, L. R., Wood, E. C., Middlebrook, A. M., Kolb, C. E., Baltensperger, U. and Worsnop, D. R.: Evolution of Organic Aerosols in the Atmosphere, Science, 326(5959), 1525–1529, doi:10.1126/science.1180353, 2009.

Kang, M., Yang, F., Ren, H., Zhao, W., Zhao, Y., Li, L., Yan, Y., Zhang, Y., Lai, S.,

Zhang, Y., Yang, Y., Wang, Z., Sun, Y. and Fu, P.: Influence of continental organic aerosols to the marine atmosphere over the East China Sea: Insights from lipids, PAHs and phthalates, Sci. Total Environ., 607–608, 339–350, doi:10.1016/j.scitotenv.2017.06.214, 2017.

King, M. D., Thompson, K. C. and Ward, A. D.: Laser tweezers raman study of optically trapped aerosol droplets of seawater and oleic acid reacting with ozone: Implications for cloud-droplet properties, J. Am. Chem. Soc., 126(51), 16710–16711, doi:10.1021/ja044717o, 2004.

King, M. D., Rennie, A. R., Thompson, K. C., Fisher, F. N., Dong, C. C., Thomas, R. K., Pfrang, C. and Hughes, A. V.: Oxidation of oleic acid at the air-water interface and its potential effects on cloud critical supersaturations, Phys. Chem. Chem. Phys., 11(35), 7699–7707, doi:10.1039/b906517b, 2009.

King, M. D., Rennie, A. R., Pfrang, C., Hughes, A. V. and Thompson, K. C.: Interaction of nitrogen dioxide (NO2) with a monolayer of oleic acid at the air-water interface - A simple proxy for atmospheric aerosol, Atmos. Environ., 44(14), 1822–1825, doi:10.1016/j.atmosenv.2010.01.031, 2010.

Kirpes, R. M., Bonanno, D., May, N. W., Fraund, M., Barget, A. J., Moffet, R. C., Ault, A. P. and Pratt, K. A.: Wintertime Arctic Sea Spray Aerosol Composition Controlled by Sea Ice Lead Microbiology, ACS Cent. Sci., 5(11), 1760–1767, doi:10.1021/acscentsci.9b00541, 2019.

Koop, T., Bookhold, J., Shiraiwa, M. and Pöschl, U.: Glass transition and phase state of organic compounds: Dependency on molecular properties and implications for secondary organic aerosols in the atmosphere, Phys. Chem. Chem. Phys., 13(43),

19238–19255, doi:10.1039/c1cp22617g, 2011.

Lee, J. W. L., Carrascón, V., Gallimore, P. J., Fuller, S. J., Björkegren, A., Spring, D. R., Pope, F. D. and Kalberer, M.: The effect of humidity on the ozonolysis of unsaturated compounds in aerosol particles, Phys. Chem. Chem. Phys., 14(22), 8023–8031, doi:10.1039/c2cp24094g, 2012.

Li, T., Senesi, A. J. and Lee, B.: Small Angle X-ray Scattering for Nanoparticle Research, Chem. Rev., 116(18), 11128–11180, doi:10.1021/acs.chemrev.5b00690, 2016.

Li, W., Li, H., Li, J., Cheng, X., Zhang, Z., Chai, F., Zhang, H., Yang, T., Duan, P., Lu, D. and Chen, Y.: TOF–SIMS surface analysis of chemical components of size–fractioned urban aerosols in a typical heavy air pollution event in Beijing, J. Environ. Sci., 69, 61–76, doi:10.1016/j.jes.2017.04.005, 2018.

Marshall, F. H., Miles, R. E. H., Song, Y., Ohm, P. B., Power, R. M., Reid, J. P. and Dutcher, C. S.: Diffusion and reactivity in ultraviscous aerosol and the correlation with particle viscosity, Chem. Sci., 7, 1298–1308, doi:10.1039/c5sc03223g, 2016.

Mauersberger, K., Barnes, J., Hanson, D. and Morton, J.: Measurement of the ozone absorption cross-section at the 253.7 nm mercury line, Geophys. Res. Lett., 13(7), 671–673, doi:10.1029/GL013i007p00671, 1986.

Mele, S., Söderman, O., Ljusberg-Wahrén, H., Thuresson, K., Monduzzi, M. and Nylander, T.: Phase behavior in the biologically important oleic acid/sodium oleate/water system, Chem. Phys. Lipids, 211(September 2017), 30–36, doi:10.1016/j.chemphyslip.2017.11.017, 2018.

Mezzenga, R., Meyer, C., Servais, C., Romoscanu, A. I., Sagalowicz, L. and Hayward, R. C.: Shear rheology of lyotropic liquid crystals: A case study, Langmuir, 21(8), 3322–3333, doi:10.1021/la046964b, 2005.

Mikhailov, E., Vlasenko, S., Martin, S. T., Koop, T. and Pöschl, U.: Amorphous and crystalline aerosol particles interacting with water vapor: Conceptual framework and experimental evidence for restructuring, phase transitions and kinetic limitations, Atmos. Chem. Phys., 9(24), 9491–9522, doi:10.5194/acp-9-9491-2009, 2009.

Moise, T. and Rudich, Y.: Reactive uptake of ozone by aerosol-associated unsaturated fatty acids: Kinetics, mechanism, and products, J. Phys. Chem. A, 106(27), 6469–6476, doi:10.1021/jp025597e, 2002.

Morris, J. W., Davidovits, P., Jayne, J. T., Jimenez, J. L., Shi, Q., Kolb, C. E., Worsnop, D. R., Barney, W. S. and Cass, G.: Kinetics of submicron oleic acid aerosols with ozone: A novel aerosol mass spectrometric technique, Geophys. Res. Lett., 29(9), 71-1-71–4, doi:10.1029/2002gl014692, 2002.

Mu, Q., Shiraiwa, M., Octaviani, M., Ma, N., Ding, A., Su, H., Lammel, G., Pöschl, U. and Cheng, Y.: Temperature effect on phase state and reactivity controls atmospheric multiphase chemistry and transport of PAHs, Sci. Adv., 4(3), eaap7314, doi:10.1126/sciadv.aap7314, 2018.

Ots, R., Vieno, M., Allan, J. D., Reis, S., Nemitz, E., Young, D. E., Coe, H., Di Marco, C., Detournay, A., Mackenzie, I. A., Green, D. C. and Heal, M. R.: Model simulations of cooking organic aerosol (COA) over the UK using estimates of emissions based on measurements at two sites in London, Atmos. Chem. Phys., 16(21), 13773–13789, doi:10.5194/acp-16-13773-2016, 2016.

Ovadnevaite, J., Zuend, A., Laaksonen, A., Sanchez, K. J., Roberts, G., Ceburnis, D., Decesari, S., Rinaldi, M., Hodas, N., Facchini, M. C., Seinfeld, J. H. and O'Dowd, C.: Surface tension prevails over solute effect in organic-influenced cloud droplet activation, Nature, 546(7660), 637–641, doi:10.1038/nature22806, 2017.

Pauw, B. R.: Everything SAXS: small-angle scattering pattern collection and correction, J. Phys. Condens. Matter, 25(38), 383201, doi:10.1088/0953-8984/25/38/383201, 2013.

Pfrang, C., Shiraiwa, M. and Pöschl, U.: Chemical ageing and transformation of diffusivity in semi-solid multi-component organic aerosol particles, Atmos. Chem. Phys., 11(14), 7343–7354, doi:10.5194/acp-11-7343-2011, 2011.

Pfrang, C., Sebastiani, F., Lucas, C. O. M., King, M. D., Hoare, I. D., Chang, D. and Campbell, R. A.: Ozonolysis of methyl oleate monolayers at the air-water interface: Oxidation kinetics, reaction products and atmospheric implications, Phys. Chem. Chem. Phys., 16(26), 13220–13228, doi:10.1039/c4cp00775a, 2014.

Pfrang, C., Rastogi, K., Cabrera-Martinez, E. R., Seddon, A. M., Dicko, C., Labrador, A., Plivelic, T. S., Cowieson, N. and Squires, A. M.: Complex three-dimensional self-assembly in proxies for atmospheric aerosols, Nat. Commun., 8(1), 1724, doi:10.1038/s41467-017-01918-1, 2017.

Pöschl, U.: Atmospheric aerosols: Composition, transformation, climate and health effects, Angew. Chemie Int. Ed., 44(46), 7520–7540, doi:10.1002/anie.200501122, 2005.

Pöschl, U., Rudich, Y. and Ammann, M.: Kinetic model framework for aerosol and cloud surface chemistry and gas-particle interactions - Part 1: General equations, parameters, and terminology, Atmos. Chem. Phys., 7(23), 5989–6023, doi:10.5194/acp-

7-5989-2007, 2007.

Qin, N., Liang, P., Wu, C., Wang, G., Xu, Q., Xiong, X., Wang, T., Zolfo, M., Segata, N., Qin, H., Knight, R., Gilbert, J. A. and Zhu, T. F.: Longitudinal survey of microbiome associated with particulate matter in a megacity, Genome Biol., 21(1), 1–11, doi:10.1186/s13059-020-01964-x, 2020.

Reid, J. P., Bertram, A. K., Topping, D. O., Laskin, A., Martin, S. T., Petters, M. D., Pope, F. D. and Rovelli, G.: The viscosity of atmospherically relevant organic particles, Nat. Commun., 9(1), 1–14, doi:10.1038/s41467-018-03027-z, 2018.

Renbaum-Wolff, L., Grayson, J. W., Bateman, A. P., Kuwata, M., Sellier, M., Murray, B. J., Shilling, J. E., Martin, S. T. and Bertram, A. K.: Viscosity of a-pinene secondary organic material and implications for particle growth and reactivity, Proc. Natl. Acad. Sci., 110(20), 8014–8019, doi:10.1073/pnas.1219548110, 2013.

Reynolds, J. C., Last, D. J., McGillen, M., Nijs, A., Horn, A. B., Percival, C., Carpenter, L. J. and Lewis, A. C.: Structural analysis of oligomeric molecules formed from the reaction products of oleic acid ozonolysis, Environ. Sci. Technol., 40(21), 6674–6681, doi:10.1021/es060942p, 2006.

Robinson, A. L., Donahue, N. M. and Rogge, W. F.: Photochemical oxidation and changes in molecular composition of organic aerosol in the regional context, J. Geophys. Res. Atmos., 111(3), 1–15, doi:10.1029/2005JD006265, 2006.

Rosen, E. P., Garland, E. R. and Baer, T.: Ozonolysis of oleic acid adsorbed to polar and nonpolar aerosol particles, J. Phys. Chem. A, 112(41), 10315–10324, doi:10.1021/jp8045802, 2008.

Rudich, Y., Donahue, N. M. and Mentel, T. F.: Aging of Organic Aerosol: Bridging the Gap Between Laboratory and Field Studies, Annu. Rev. Phys. Chem., 58(1), 321–352, doi:10.1146/annurev.physchem.58.032806.104432, 2007.

Schwier, A. N., Sareen, N., Lathem, T. L., Nenes, A. and McNeill, V. F.: Ozone oxidation of oleic acid surface films decreases aerosol cloud condensation nuclei activity, J. Geophys. Res. Atmos., 116(16), D16202, doi:10.1029/2010JD015520, 2011.

Sebastiani, F., Campbell, R. A., Rastogi, K. and Pfrang, C.: Nighttime oxidation of surfactants at the air-water interface: Effects of chain length, head group and saturation, Atmos. Chem. Phys., 18(5), 3249–3268, doi:10.5194/acp-18-3249-2018, 2018.

Seddon, J. M., Bartle, E. A. and Mingins, J.: Inverse cubic liquid-crystalline phases of phospholipids and related lyotropic systems, J. Phys. Condens. Matter, 2, SA285–SA290, doi:10.1088/0953-8984/2/S/043, 1990.

Shiraiwa, M., Pfrang, C. and Pöschl, U.: Kinetic multi-layer model of aerosol surface and bulk chemistry (KM-SUB): The influence of interfacial transport and bulk diffusion on the oxidation of oleic acid by ozone, Atmos. Chem. Phys., 10, 3673–3691, doi:10.5194/acp-10-3673-2010, 2010.

Shiraiwa, M., Ammann, M., Koop, T. and Poschl, U.: Gas uptake and chemical aging of semisolid organic aerosol particles, Proc. Natl. Acad. Sci. U. S. A., 108(27), 11003–11008, doi:10.1073/pnas.1103045108, 2011.

Shiraiwa, M., Pfrang, C., Koop, T. and Pöschl, U.: Kinetic multi-layer model of gas-particle interactions in aerosols and clouds (KM-GAP): Linking condensation, evaporation and chemical reactions of organics, oxidants and water, Atmos. Chem. Phys., 12(5), 2777–2794, doi:10.5194/acp-12-2777-2012, 2012.

Shrivastava, M., Lou, S., Zelenyuk, A., Easter, R. C., Corley, R. A., Thrall, B. D., Rasch, P. J., Fast, J. D., Simonich, S. L. M., Shen, H. and Tao, S.: Global long-range transport and lung cancer risk from polycyclic aromatic hydrocarbons shielded by coatings of organic aerosol, Proc. Natl. Acad. Sci. U. S. A., 114(6), 1246–1251, doi:10.1073/pnas.1618475114, 2017.

Smith, G. D., Woods, E., DeForest, C. L., Baer, T. and Miller, R. E.: Reactive uptake of ozone by oleic acid aerosol particles: Application of single-particle mass spectrometry to heterogeneous reaction kinetics, J. Phys. Chem. A, 106(35), 8085–8095, doi:10.1021/jp020527t, 2002.

Squires, F., Nemitz, E., Langford, B., Wild, O., Drysdale, W., Fu, P., Hamilton, J., Hollaway, M., Kotthaus, S., Lee, J., Metzger, S., Pingintha-Durden, N., Shaw, M., Vaughan, A., Wang, X., Wu, R., Zhang, Q. and Zhang, Y.: Measurements of traffic dominated pollutant emissions in a Chinese megacity, Atmos. Chem. Phys., 20, 8737-8761, doi: 10.5194/acp-20-8737-2020, 2020.

Steimer, S. S., Lampimäki, M., Coz, E., Grzinic, G. and Ammann, M.: The influence of physical state on shikimic acid ozonolysis : a case for in situ microspectroscopy, Atmos. Chem. Phys., 14, 10761–10772, doi:10.5194/acp-14-10761-2014, 2014.

Swan, S. H., Main, K. M., Liu, F., Stewart, S. L., Kruse, R. L., Calafat, A. M., Mao, C. S., Redmon, J. B., Ternand, C. L., Sullivan, S., Teague, J. L., Drobnis, E. Z., Carter, B. S., Kelly, D., Simmons, T. M., Wang, C., Lumbreras, L., Villanueva, S., Diaz-Romero, M., Lomeli, M. B., Otero-Salazar, E., Hobel, C., Brock, B., Kwong, C., Muehlen, A., Sparks, A., Wolf, A., Whitham, J., Hatterman-Zogg, M. and Maifeld, M.: Decrease in anogenital distance among male infants with prenatal phthalate exposure, Environ.

Health Perspect., 113(8), 1056–1061, doi:10.1289/ehp.8100, 2005.

Tervahattu, H.: Identification of an organic coating on marine aerosol particles by TOF-SIMS, J. Geophys. Res., 107(D16), 4319, doi:10.1029/2001JD001403, 2002.

Tervahattu, H., Juhanoja, J., Vaida, V., Tuck, A. F., Niemi, J. V., Kupiainen, K., Kulmala, M. and Vehkamäki, H.: Fatty acids on continental sulfate aerosol particles, J. Geophys. Res. D Atmos., 110(6), 1–9, doi:10.1029/2004JD005400, 2005.

Tiddy, G. J. T.: Surfactant-water liquid crystal phases, Phys. Rep., 57(1), 1–46, doi:10.1016/0370-1573(80)90041-1, 1980.

Tuckermann, R.: Surface tension of aqueous solutions of water-soluble organic and inorganic compounds, Atmos. Environ., 41(29), 6265–6275, doi:10.1016/j.atmosenv.2007.03.051, 2007.

Vicente, E. D., Vicente, A., Evtyugina, M., Carvalho, R., Tarelho, L. A. C., Oduber, F. I. and Alves, C.: Particulate and gaseous emissions from charcoal combustion in barbecue grills, Fuel Process. Technol., 176(April), 296–306, doi:10.1016/j.fuproc.2018.03.004, 2018.

Virtanen, A., Joutsensaari, J., Koop, T., Kannosto, J., Yli-Pirilä, P., Leskinen, J., Mäkelä, J. M., Holopainen, J. K., Pöschl, U., Kulmala, M., Worsnop, D. R. and Laaksonen, A.: An amorphous solid state of biogenic secondary organic aerosol particles, Nature, 467(7317), 824–827, doi:10.1038/nature09455, 2010.

Wang, G., Kawamura, K., Shuncheng, L., Ho, K. and Cao, J.: Molecular , Seasonal , and Spatial Distributions of Organic Aerosols from Fourteen Chinese Cities, Environ. Sci. Technol., 40, 4619–4625, doi:10.1021/es060291x, 2006.

Wang, M., Yao, L., Zheng, J., Wang, X., Chen, J., Yang, X., Worsnop, D. R., Donahue, N. M. and Wang, L.: Reactions of Atmospheric Particulate Stabilized Criegee Intermediates Lead to High-Molecular-Weight Aerosol Components, Environ. Sci. Technol., 50(11), 5702–5710, doi:10.1021/acs.est.6b02114, 2016.

Wayne, R. P., Barnes, I., Biggs, P., Burrows, J. P., Canosa-Mas, C. E., Hjorth, J., Le Bras, G., Moortgat, G. K., Perner, D., Poulet, G., Restelli, G. and Sidebottom, H.: The nitrate radical: Physics, chemistry, and the atmosphere, Atmos. Environ. Part A, Gen. Top., 25(1), 1–203, doi:10.1016/0960-1686(91)90192-A, 1991.

Woden, B., Skoda, M., Hagreen, M. and Pfrang, C.: Night-Time Oxidation of a Monolayer Model for the Air–Water Interface of Marine Aerosols—A Study by Simultaneous Neutron Reflectometry and in Situ Infra-Red Reflection Absorption Spectroscopy (IRRAS), Atmosphere, 9(12), 471, doi:10.3390/atmos9120471, 2018.

Zabara, A. and Mezzenga, R.: Controlling molecular transport and sustained drug release in lipid-based liquid crystalline mesophases, J. Control. Release, 188, 31–43, doi:10.1016/j.jconrel.2014.05.052, 2014.

Zahardis, J. and Petrucci, G. A.: The oleic acid-ozone heterogeneous reaction system: Products, kinetics, secondary chemistry, and atmospheric implications of a model system - A review, Atmos. Chem. Phys., 7(5), 1237–1274, doi:10.5194/acp-7-1237-2007, 2007.

Zahardis, J., LaFranchi, B. W. and Petrucci, G. A.: Photoelectron resonance capture ionization-aerosol mass spectrometry of the ozonolysis products of oleic acid particles: Direct measure of higher molecular weight oxygenates, J. Geophys. Res. D Atmos., 110(8), 1–10, doi:10.1029/2004JD005336, 2005.

Zahardis, J., LaFranchi, B. W. and Petrucci, G. A.: Direct observation of polymerization in the oleic acid-ozone heterogeneous reaction system by photoelectron resonance capture ionization aerosol mass spectrometry, Atmos. Environ., 40(9), 1661–1670, doi:10.1016/j.atmosenv.2005.10.065, 2006.

Zhao, X., Hu, Q., Wang, X., Ding, X., He, Q., Zhang, Z., Shen, R., Lü, S., Liu, T., Fu, X. and Chen, L.: Composition profiles of organic aerosols from Chinese residential cooking: Case study in urban Guangzhou, south China, J. Atmos. Chem., 72(1), 1–18, doi:10.1007/s10874-015-9298-0, 2015.

Zhao, Y., Huang, H., Zhang, Y., Wu, K., Zeng, F., Wang, J., Yu, X., Zhu, Z., Yu, X.-Y. and Wang, F.: Atmospheric particulate characterization by ToF-SIMS in an urban site in Beijing, Atmos. Environ., 220, 117090, doi:10.1016/j.atmosenv.2019.117090, 2020.

Zhou, S., Hwang, B. C. H., Lakey, P. S. J., Zuend, A., Abbatt, J. P. D. and Shiraiwa, M.: Multiphase reactivity of polycyclic aromatic hydrocarbons is driven by phase separation and diffusion limitations, Proc. Natl. Acad. Sci. U. S. A., 116(24), 11658–11663, doi:10.1073/pnas.1902517116, 2019.

Zobrist, B., Soonsin, V., Luo, B. P., Krieger, U. K., Marcolli, C., Peter, T. and Koop, T.: Ultra-slow water diffusion in aqueous sucrose glasses, Phys. Chem. Chem. Phys., 13(8), 3514–3526, doi:10.1039/c0cp01273d, 2011.

3 CHAPTER 3: MODELLNG THE IMPACT OF MOLECULAR SELF-ORGANISATION ON THE REACTIVITY OF A COOKING AEROSOL PROXY

This study is prepared for submission to a journal.

3.1 **Abstract**

Atmospheric aerosols influence the climate via cloud droplet nucleation and can facilitate the long-range transport of harmful pollutants. The lifetime of such aerosols can therefore determine their environmental impact. Fatty acids are found in organic aerosol emissions. Oleic acid, an unsaturated fatty acid, is a large contributor to cooking emissions. As a surfactant, oleic acid can self-organise into nanostructured lamellar bilayers with its sodium salt. We applied a kinetic multi-layer model on decay data obtained from the ozonolysis of coated films of this self-organised proxy, showing a decreased diffusivity for both oleic acid and ozone due to lamellar bilayer formation. Diffusivity was further inhibited by a viscous oligomer product forming in the top layers of the film. Model runs at indoor and outdoor atmospheric ozone concentrations show that nanostructure formation can increase the reactive half-life of oleic acid by an order of days.

3.2 Introduction

Atmospheric aerosols represent a large uncertainty when considering their effect on the climate (Boucher et al., 2013) and can be sources of poor air quality in urban areas (Chan and Yao, 2008). The organic fraction of atmospheric aerosols can include a diverse range of molecules with differing functionalities, varying with season and environment (Jimenez et al., 2009; Wang et al., 2020b).

Cooking emissions are contributors to urban aerosols (Ots et al., 2016; Vicente et al., 2021). Fatty acids are a well-established set of marker compounds used to track cooking emissions due to their relatively high abundance (Wang et al., 2020a; Zhao et al., 2015). In particular oleic acid, an unsaturated fatty acid, has been used to follow the ageing of cooking aerosols (Wang et al., 2020a). The lifetime of oleic acid in the atmosphere is longer compared with laboratory predictions (days compared to hours) (Robinson et al., 2006; Rudich et al., 2007). This is a long-standing discrepancy and suggests that some physical process is inhibiting the ageing of such aerosols. For these reasons, oleic acid has been the compound of choice for laboratory studies into aerosol heterogeneous oxidation (Gallimore et al., 2017; King et al., 2020; Milsom et al., 2021b; Pfrang et al., 2017; Woden et al., 2021; Zahardis and Petrucci, 2007).

The phase state and viscosity of atmospheric aerosols can impact on heterogeneous processes such as reactive gas and water uptake (Reid et al., 2018; Shiraiwa et al., 2011b). Field measurements have shown that semi-solid phase formation takes place in the atmosphere (Virtanen et al., 2010) and that phase state can vary between night and day as well as with organic mass fraction (Slade et al., 2019). The long-range transport of harmful polycyclic aromatic hydrocarbons (PAHs) has been linked with particle phase and the formation of a viscous organic layer, protecting the aerosol's potentially

harmful contents (Mu et al., 2018; Shrivastava et al., 2017). Viscous phase formation is therefore a plausible explanation for the persistence of organic aerosol components in the atmosphere.

As a surfactant, oleic acid can self-assemble into a range of nanostructures, known as lyotropic liquid crystals (LLCs), with its sodium salt and water (Mele et al., 2018; Seddon et al., 1990). The viscosity and the diffusion of small molecules through these phases can vary significantly (Mezzenga et al., 2005; Zabara and Mezzenga, 2014). Some nanostructures, such as the lamellar phase, have highly anisotropic diffusivities resulting in higher diffusivity parallel to the lamellar bilayer compared to the perpendicular direction (Lindblom and Orädd, 1994). This nanostructure formation has been studied in levitated droplets and in coated quartz capillaries (Pfrang et al., 2017; Seddon et al., 2016), where the self-assembly of this proxy system decreased the reactivity of oleic acid by *ca.* an order of magnitude (Milsom et al., 2021b).

In this work, we apply a kinetic multi-layer model to the lamellar phase ozonolysis kinetic data presented by Milsom *et al.* (Milsom et al., 2021b). We determine the effect on particle diffusivity of both nanostructure formation and the formation of a later stage reaction product, which congregates in the surface region of the film. We then apply the optimised model to determine the impact on the atmospheric lifetime of such films, linking this to the discrepancy between measured and predicted atmospheric lifetimes for oleic acid.

3.3 **Methods**

The experimental data used here are from a previous study where small-angle X-ray scattering (SAXS) was used to follow the kinetic decay of the amount of lamellar phase

(nanostructured) fatty acid in films of oleic acid-sodium oleate (Milsom et al., 2021b). In this study, oleic acid refers to both oleic acid and sodium oleate as they are both constituents of the lamellar phase bilayer. The selected decays were from the same experiment carried out simultaneously in the same capillary under the same conditions (77 ppm ozone, dry oxygen-ozone flow).

The kinetic multi-layer model of aerosol surface and bulk chemistry (KM-SUB) was used (Shiraiwa et al., 2010), which is based on the Pöschl-Rudich-Ammann (PRA) framework (Pöschl et al., 2007). An oleic acid ozonolysis reaction scheme was chosen based on that used by Hosny *et al*., where oligomer formation, viscosity and diffusivity were explicitly treated (Hosny et al., 2016). The model uses a flat film geometry. The reaction scheme used and a model description is presented in the appendix (section 10.2.1).

The model was written in the *Python* programming language. A series of ordinary differential equations (ODEs) were written, describing the change in concentration for each model component in each model bulk and surface layer over time. These ODEs were integrated using the *SciPy solve_ivp* solver with a backward differentiation formula (BDF) for stiff ODE solving (Virtanen et al., 2020).

Parameters associated with reaction rate constants, Henry's law coefficient and the gas uptake coefficient for ozone into the organic phase were set to values used for previous oleic acid ozonolysis literature (all model parameters are summarised in the appendix section 10.2.2).

The diffusion of model components throughout the film was made to be composition-dependent. It is known that self-assembled phase formation affects viscosity and

diffusivity (Mezzenga et al., 2005; Zabara and Mezzenga, 2014). Therefore determining the effect of particle diffusivity on reactivity is a key focus of this study. A Vignes-type diffusion regime was employed to account for the effect of composition on molecular diffusivity (Alpert et al., 2019; Zhou et al., 2019). The diffusion of model components was dependent on the fraction of lamellar oleic acid, dimer and trimer oligomers accounted for in the model.

$$D_{Y,i} = (D_{Y,lam})^{1-f_{di,i}-f_{tri,i}} \times (D_{Y,di})^{f_{di,i}} \times (D_{Y,tri})^{f_{tri,i}} \quad (3\text{-}1)$$

$$D_{X,i} = (D_{X,lam})^{1-f_{di,i}-f_{tri,i}} \times (D_{X,di})^{f_{di,i}} \times (D_{X,tri})^{f_{tri,i}} \quad (3\text{-}2)$$

Y in equation 1 refers to oleic acid and 9-carbon products, the diffusion of which in each model layer (*i*) was treated the same. *X* corresponds to the reactive gas, in this case ozone. The fraction of dimer ($f_{di,i}$) and trimer ($f_{tri,i}$) in model layer *i* was used to represent layer composition. The diffusion coefficients of components in the lamellar ($D_{Y,lam}$/ $D_{X,lam}$), dimer ($D_{Y,di}$/ $D_{X,di}$) and trimer ($D_{Y,tri}$/ $D_{X,tri}$) media were allowed to vary during the model fitting procedure.

The diffusion of the dimer and trimer products was treated using power law relationship via a scaling factor (f_{diff}) analogous to an oleic acid ozonolysis modelling study which had access to viscosity data (Hosny et al., 2016). We adapted this parameterisation to define oligomer diffusivity rather than viscosity.

$$D_{tri} = D_{di}\left(\frac{M_{di}}{M_{tri}}\right)^{f_{diff}} \quad (3\text{-}3)$$

D_{tri} and D_{di} are the diffusion coefficients of the trimer and dimer, respectively. D_{di} was allowed to vary during the model fitting procedure. M_{di} and M_{tri} are the respective

molecular masses of the dimer and trimer products. This parameterisation allowed us to reduce the number of free parameters used to fit the model.

The model output was fitted to experimental data using a differential evolution (DE) global optimisation algorithm (Storn and Price, 1997). An initial population of candidate parameter sets was created by Latin Hypercube sampling of the parameter space (McKay et al., 1979). This was carried out in parallel, similar to the procedure described by Berkemeier *et al*., who used Monte Carlo sampling to initialise their candidate parameter sets (Berkemeier et al., 2017). The DE algorithm is a popular one for finding the global minimum of a loss function used to evaluate model fitness, which in this case was the mean-squared error of the model fit. This fitting procedure was implemented using the DE method in the *optimise* module of the *SciPy* package (Virtanen et al., 2020). 20 cpu cores were used for parallelisation of the differential evolution algorithm. In this case a multi-objective optimisation routine was implemented where the model was fit to all the datasets simultaneously. The loss function from each experimental fit was weighted according to the number of data points fitted to.

The sensitivity of the model to the varied parameters was investigated using an Elementary Effects algorithm via the method of Morris implementation of the *SALib Python* package (Campolongo et al., 2007; Herman and Usher, 2018; Morris, 1991). The total loss rate of oleic acid at 50 min reaction time was used as the output variable. Normalised sensitivity coefficients for each varied parameter were then obtained by measuring changes in the total loss rate of oleic acid with changes in each model parameter.

3.4 Results and discussion

3.4.1 Model outputs

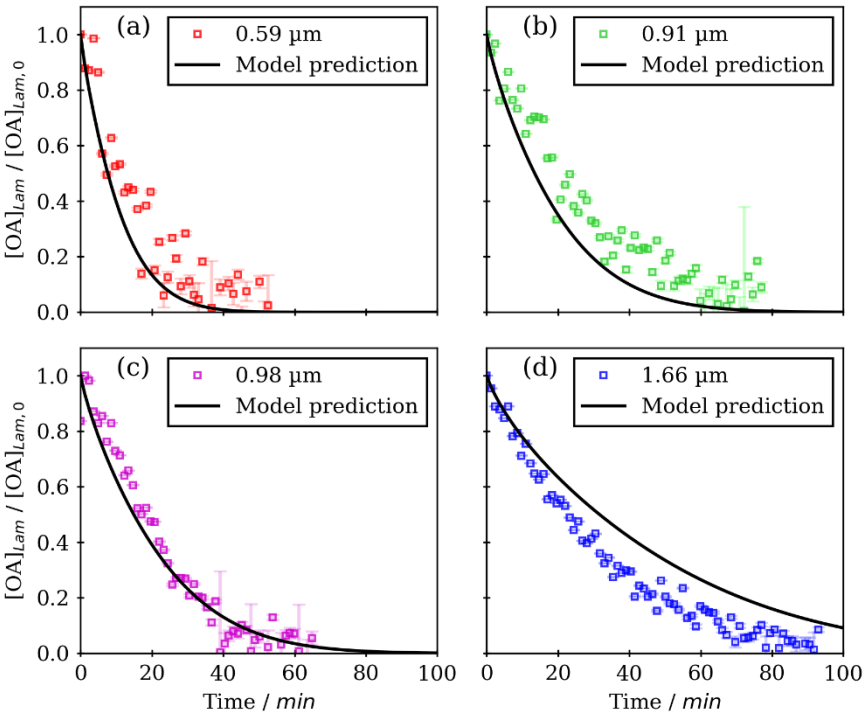

Figure 3-9. Kinetic decay plots of normalised lamellar phase oleic acid concentration ($[OA]_{Lam}/[OA]_{Lam,0}$) vs time data from Milsom et al. and model predictions using the optimised model parameters obtained for this study.

The optimised model parameters returned reasonably good fits with the experimental data over the film thickness range considered here (Fig. 3-1). The 0.91 µm and 1.66 µm films returned slightly poorer fits than the other films. Differences between the model and data arise for a number of reasons: (i) there is an uncertainty associated with the film thickness measurement, in particular the 0.91 and 0.98 µm films are similar when considering their quoted thickness uncertainties representing one standard deviation (0.03 µm) (Milsom et al., 2021b). (ii) If the film structure changes over time exposed to ozone, which has been observed under a microscope (Hung and Tang, 2010), the

surface area available for ozone uptake may also change. This change in surface structure is not considered in the model. (iii) The film may have been slightly thicker on one side of the capillary compared to the other: this technique required the X-ray beam to pass through both sides of a coated quartz capillary. Knowing that film thickness affects reaction kinetics, a difference in film thickness between both sides could impact the experimental result. (iv) The film thickness could have varied over the part of the film illuminated by the X-ray beam: the beam was ~ 320 μm x 400 μm in size, any variation in film thickness within this illuminated area could not be determined with this technique.

We can rule out any variation in sample environment because all four of these datasets were taken from different positions along the same capillary during the same ozonolysis experiment. Thus we are confident that the film structure and morphology must have some impact on reactivity on this thickness scale.

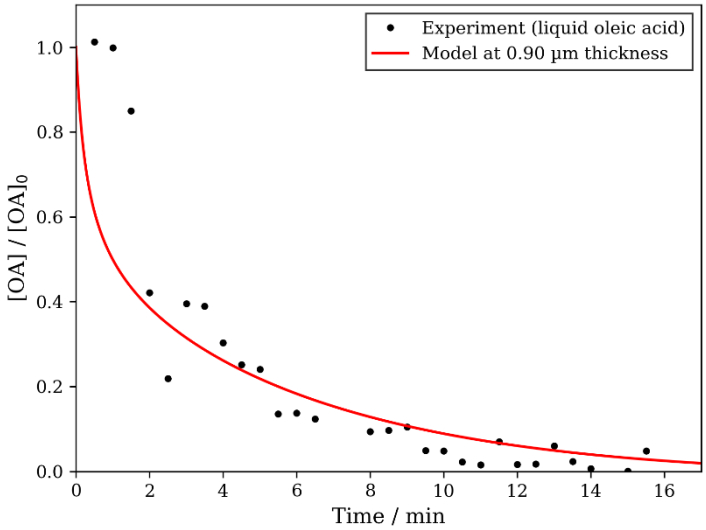

Figure 3-2. Kinetic decay plot of the ozonolysis of liquid oleic acid. Measured by Raman spectroscopy. Model run at 0.90 µm film thickness with liquid oleic acid diffusion parameters ($D_{Y,liq}$ = 1.53 x 10^{-9} cm^2 s^{-1}, $D_{X,liq}$ = 1.00 x 10^{-5} cm^2 s^{-1}, replacing $D_{Y,lam}$ and $D_{X,lam}$). Experimental $[O]_3$ = 77 ± 5 ppm (77 ppm used for the model run).

Encouragingly, the optimised model returned a good fit to ozonolysis decay data obtained by Raman spectroscopy on a film coated with pure oleic acid in the liquid state (Fig. 3-2). This film was prepared in the same way as the semi-solid films, therefore it is not unreasonable to assume a similar film thickness. We found that a model film thickness of 0.90 µm fit well to these data. The concentration evolution of the model components from this fit is presented in the appendix section 10.2.3.

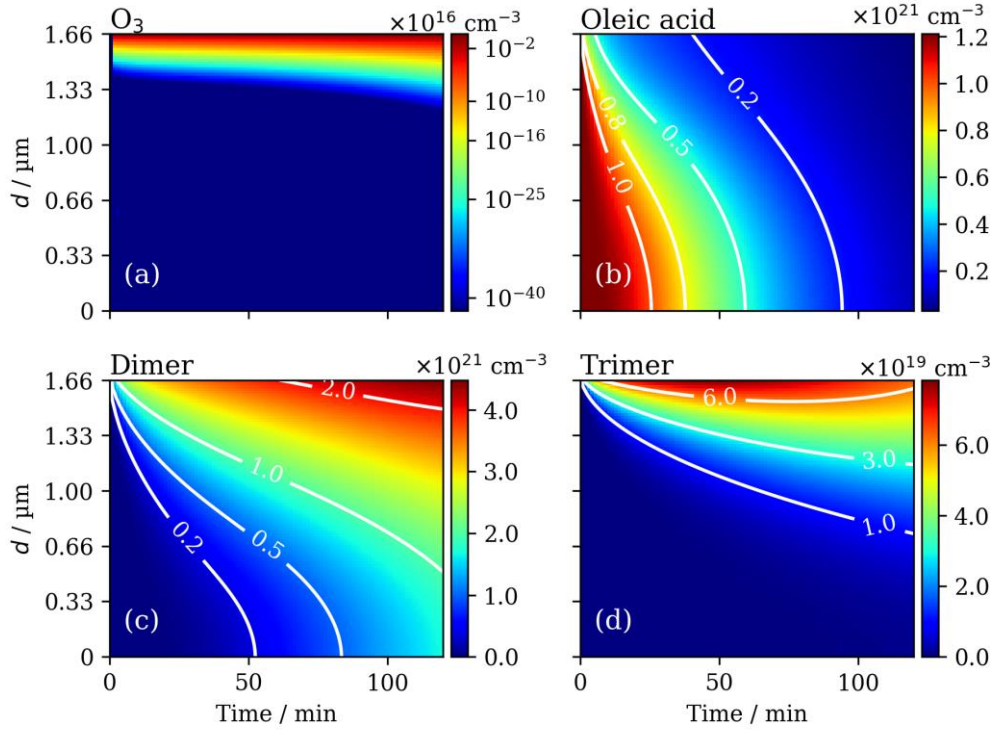

Figure 3-3. Spatially and temporally resolved concentration evolution of ozone (a – Log-scale concentration), oleic acid (b), dimer (c) and trimer (d) model components during ozonolysis for a 1.66 µm film - d: the distance from the core of the film. Contours illustrate the change in concentration gradient over time for the non-reactive gas species. [O_3] = 77 ppm.

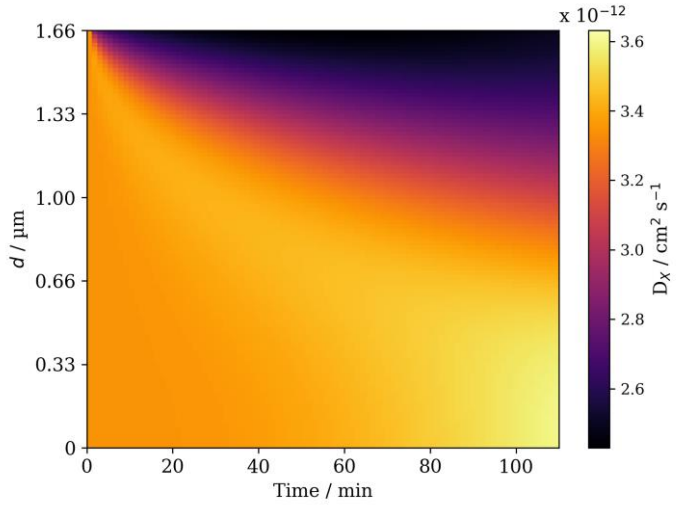

Figure 3-4. The evolution of ozone diffusivity throughout a 1.66 µm film during ozonolysis. [O_3] = 77 ppm. d: the distance from the film core.

$D_{X,lam}$ (3.35 x 10^{-12} cm^2 s^{-1}) is consistent with the diffusion of a reactive gas through a highly viscous matrix (Shiraiwa et al., 2011a). The spacing between lamellar alkyl chains in this system is 4.41 Å (Milsom et al., 2021b), which is close to the molecular diameter of ozone (4 Å used in this study) (Pfrang et al., 2010; Shiraiwa et al., 2010). It has been suggested that the shorter spacing between fatty acid tails on a particle surface could provide steric hindrance to diffusing ozone molecules, limiting access to the double-bond (Hearn et al., 2005; Vieceli et al., 2004). The anhydrous lamellar phase, being viscous and ordered, is likely to present extra steric hindrance compared to surface monolayers because this effect would prevail throughout the film.

Diffusion in the lamellar phase is known to be highly anisotropic, with diffusion parallel to the bilayer plane orders of magnitude higher than perpendicular (Lindblom and Orädd, 1994). We note that the 2-D SAXS patterns obtained from these samples did not exhibit any alignment of the lamellar phase (see Fig. 10-32, appendix). This justifies not considering lamellar phase orientation in this model.

Ozone diffusion in the dimer is ~ 3-fold higher than in the lamellar phase. This is consistent with a steric hindrance argument. Though a molecule with the same number of carbons as oleic acid is formed, the unordered nature of the dimer product suggests that ozone can diffuse past these molecules more easily compared with the restricted bilayers formed by the lamellar phase oleic acid. By contrast, diffusion through the trimer product is slower than in the dimer and lamellar phase. The trimer product in this model lumps together all the higher-order oligomers that can be formed during oleic acid ozonolysis, contributing to an increase in particle viscosity (Hosny et al., 2016). Diffusion of ozone through regions of higher viscosity is expected to be slower and the formation of a crust in the surface layers of the film consisting of the viscous trimer product inhibits the diffusion of ozone through the particle (Fig. 3-2(d) and Fig. 3-3). The formation of a surface crust has been postulated in the literature (Pfrang et al., 2011; Zhou et al., 2013) and direct experimental evidence of surface product aggregation has been presented in a similar proxy (Milsom et al., 2021a) (see chapter 7).

The diffusivity of oleic acid is low in the lamellar phase ($D_{Y,lam}$ = 2.81 x 10^{-12} cm^2 s^{-1}) compared to ~ 1.53 x 10^{-9} cm^2 s^{-1} for pure oleic acid based on its viscosity at 293.15 K (Sagdeev et al., 2019). Experimentally determined lateral diffusion coefficients in hydrated lamellar bilayers are at least four orders of magnitude higher than our model optimisation returned (~10^{-8} – 10^{-7} cm^2 s^{-1}) (Lindblom and Orädd, 1994; Lindblom and Wennerström, 1977). Note that these experimental determinations were on hydrated lamellar phases, which are expected to be less viscous than the anhydrous lamellar phase studied here due to water acting as a plasticiser. The model does not account for directionally dependent diffusion through the lamellar phase because no bilayer

orientation was observed (see previous discussion). These considerations contribute to the difference in experimental and modelled lipid diffusivity.

The diffusivity of oleic acid in the trimer product is within an order of magnitude of the lamellar phase oleic acid diffusivity. After an increase in diffusivity going from the lamellar to the dimer phase ($D_{Y,di}$ = 8.85 x 10^{-11} cm^2 s^{-1}), oleic acid diffusivity decreases in the trimer ($D_{Y,tri}$ = 8.16 x 10^{-11} cm^2 s^{-1}). The model is least sensitive to diffusion coefficients in the dimer phase. Therefore these values are not to be over-interpreted.

The spatial and temporal evolution of ozone concentration is consistent with a bulk diffusion-limited reaction. The concentration of ozone does not reach particularly high levels in the film bulk (Fig. 3-2(a)). The steep ozone concentration gradient developed during the reaction is illustrated by the Log-scale in Fig. 3-2(a).

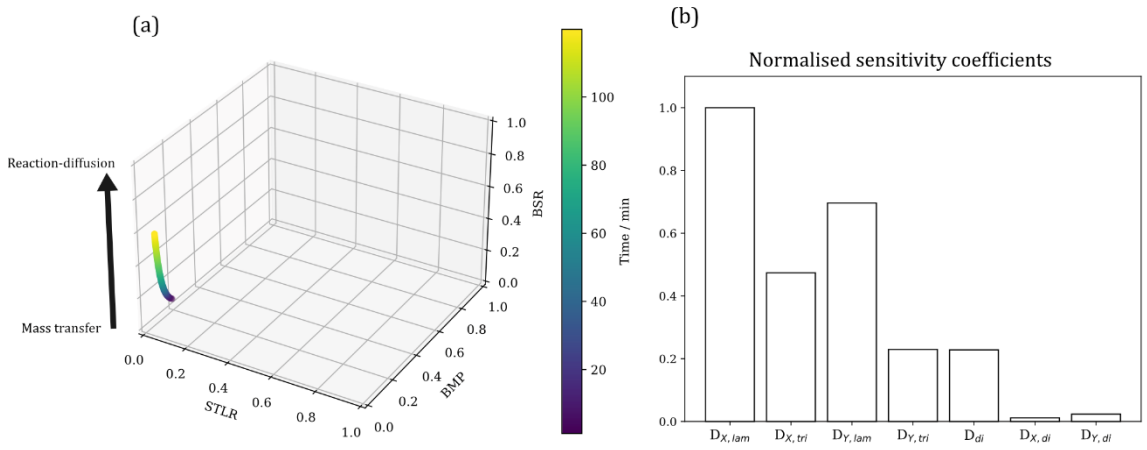

Figure 3-5. (a) A "kinetic cube" plot (described by Berkemeier et al.) (Berkemeier et al., 2013) *of surface-to-total loss ratio (STLR), bulk mixing parameter (BMP) and bulk saturation ratio (BSR) for a model run at 77 ppm ozone and 1.66 µm film thickness. The black arrow illustrates the movement of from the mass transfer to the reaction-diffusion kinetic regimes described by Berkemeier et al.. (b) A summary of the normalised sensitivity coefficients for each varied model parameter.*

The model output was most sensitive to ozone and oleic acid diffusivity, highlighting that film phase heavily influences the lifetime of such a film (Fig. 3-5(b)). From this analysis and the concentration profiles (Fig. 3-2) we can conclude that the reaction is limited both by bulk oleic acid diffusion to the reaction region and by the diffusivity of ozone through the film.

Further analysis using a method described by Berkemeier *et al.* for multi-layer model outputs demonstrates the evolution of kinetic regime as ozonolysis proceeds (Fig. 3-5(a)) (Berkemeier et al., 2013). The surface-to-total loss ratio (STLR) observed throughout the reaction is close to 0, suggesting that reactant loss is not a surface-dominated process. The bulk mixing parameter (BMP) starts at ~ 0.18 and decreases with time. This is a measure of how well mixed the particle is in terms of both the reactive gas and condensed phase reactant – a value of 1 is well-mixed. The film therefore starts poorly mixed and becomes less well-mixed as the reaction progresses. After an initial transient phase, the bulk saturation ratio (BSR) increases steadily over time. This reflects the supply of the reactive gas to the film, which is inhibited by viscous product formation and the viscous lamellar phase.

For an appreciable amount of time the reaction regime lies between a mass-transfer and reaction-diffusion regime, reflecting the importance of both bulk diffusion and accommodation parameters at different times during the reaction (Fig. 3-5(a)). The transient nature of the kinetic regime justifies this more explicit description. Limiting cases based on a resistor model do not account for changes in kinetic regime (Worsnop et al., 2002). This kind of analysis demonstrates the power of spatially and temporally resolved kinetic modelling, enabling us to present a more nuanced picture of the kinetic regimes underpinning this reaction.

There is no experimental information regarding the uptake of reactive gasses to this particular proxy system, therefore parameters such as Henry's law coefficient (H^{cp}) and gas surface accommodation coefficient ($\alpha_{s,0}$) for ozone were set to values used in other literature modelling studies of the oleic acid-ozone system (details of model parameters are presented in the appendix section 10.2.2). We therefore caution the reader not to over-interpret these values as sound experimental determinations.

3.4.2 **Atmospheric implications**

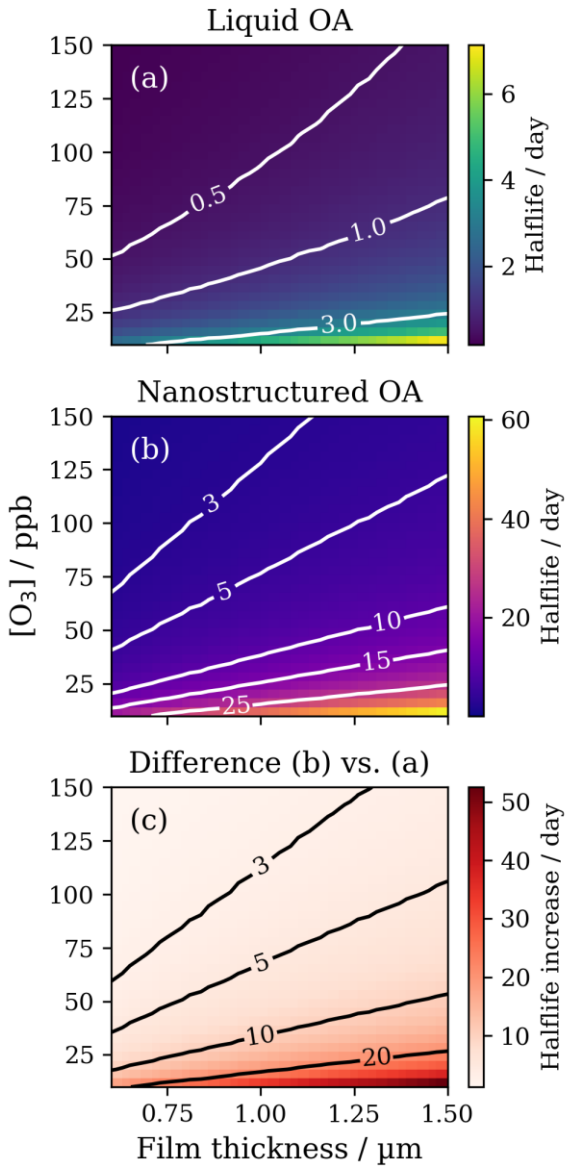

Figure 3-6. Plots of film half-life as a function of ozone concentration ([O_3]) and film thickness. (a) model runs using parameters for liquid oleic acid ($D_{Y,liq}$ = 1.53 x 10^{-9} cm^2 s^{-1}, $D_{X,liq}$ = 1.00 x 10^{-5} cm^2 s^{-1}); (b) model runs using optimised parameters for lamellar phase (nanostructured) oleic acid ($D_{Y,lam}$ = 2.81 x 10^{-12} cm^2 s^{-1}, $D_{X,lam}$ = 3.35 x 10^{-12} cm^2 s^{-1}); (c) The increase in half-life as a result of nanostructure formation. Contours on each plot represent lines of constant half-life.

There is a known discrepancy between laboratory and measured lifetimes of fatty acids, such as oleic acid (Robinson et al., 2006; Rudich et al., 2007). In order to demonstrate the potential impact self-assembly has on the atmospheric lifetime of such organic coatings, the optimised model was run with a film thickness range of 0.60 – 1.50 µm and an ozone concentration range of 10 – 150 ppb, covering pristine (~10 ppb), typical

(20 – 40 ppb) and polluted (> 40 ppb) ozone concentrations in the urban and indoor environment (Fig. 3-6) (Weschler, 2000).

Taking a 1 μm film as an example, where the model agrees the best with the experiment (Fig. 3-1(c)), the half-life increases from ~ 1 to 10 days when moving from the liquid to the nanostructured (lamellar) state at ~ 30 ppb ozone concentration (Fig. 3-6(c)). Such an increase in the apparent lifetime of the unoxidised organic film has implications for the persistence of organic matter in such particles.

These predictions are most likely an upper estimate, especially for the thicker films. The model over-predicts the experiment at 1.66 μm (Fig. 3-1(d)). Phase changes can occur with changes in relative humidity (RH) (Pfrang et al., 2017; Seddon et al., 2016). This particular system is stable below 55 % RH, above which the anhydrous lamellar phase can break down into inverse micelles which are thought to be less viscous. Atmospheric humidity is variable. Therefore any phase transition to a less-viscous phase could enhance ozone uptake and promote a faster reaction, decreasing the half-life. The effect of different molecular arrangements remains to be constrained experimentally.

Organic particulate matter can contain a range of chemical species, some of which are harmful to human health (Chan and Yao, 2008). The long-range transport of carcinogenic PAHs has been linked with particle phase state and the formation of a semi-solid organic coating on PAH-containing particles, increasing the risk of ill-health (Mu et al., 2018; Shrivastava et al., 2017). Our model predictions show that the semi-solidification of this aerosol proxy can increase the lifetime of the organic film substantially. Moreover, the formation of a surface layer of high-molecular-weight

products (represented as the trimer in the model) forms an extra diffusional barrier to oxidants such as ozone.

This lengthening of atmospheric lifetime implies a slower rate of particle oxidation. The degree of oxygenation, measured by the O:C ratio, is linked to aerosol hygroscopicity (Wu et al., 2016). Therefore it is possible that the inhibition of particle oxidation by the formation of this semi-solid phase could have an impact on the CCN ability of the particle and therefore cloud formation and the climate.

The increased lifetime of oleic acid, and therefore the 9-carbon products included in this model, suggests that surface active material can persist for longer times in the atmosphere in a semi-solid organic film. Two of the 9-carbon primary oleic acid ozonolysis products, azelaic acid and nonanoic acid, are also surface active (King et al., 2009; Tuckermann, 2007). Such surface active material has the potential to alter aerosol hygroscopicity by decreasing the surface tension of aqueous droplets, affecting the aerosol's ability to be a cloud condensation nucleus (CCN) (Ovadnevaite et al., 2017). The link between clouds and aerosols is clear and any process affecting the ability of an aerosol to act as a CCN can have an impact on the climate (Boucher et al., 2013).

With cooking aerosols accounting for up to an additional 10 % of reported $PM_{2.5}$ emissions in the UK (Ots et al., 2016) and fatty acids being major contributors to cooking emissions (Wang et al., 2020a), it follows that these effects would most likely be observed in the urban environment.

3.5 Conclusion

The effect of aerosol phase state continues to be a topic of interest for the aerosol community. In this study, a multi-layer kinetic model was fitted to data collected from the ozonolysis of oleic acid coatings in a semi-solid state.

A key advantage of this particular model-experiment approach is that all experimental data fitted to were from samples exposed to exactly the same conditions in the same capillary tube. Therefore differences between model fits and experimental data are most likely from variations in film structure and morphology rather than experimental conditions, which can be uncertainties associated with other kinetic techniques.

The increase in atmospheric lifetime of this proxy from hours to days is consistent with field measurements of oleic acid demonstrating a longer lifetime in comparison to laboratory measurements.

We are now able to place nanostructure formation in an atmospherically meaningful context, contributing to the study of the impact nanostructure formation could have on the atmospheric lifetime of organic aerosol emissions.

3.6 Acknowledgements

AM acknowledges funding by the NERC SCENARIO DTP (NE/L002566/1) and support from the NERC CENTA DTP. This work was carried out with the support of the Diamond Light Source (DLS), instrument I22 (proposal SM21663). The computations described in this paper were performed using the University of Birmingham's BlueBEAR HPC service, which provides a High Performance Computing service to the University's research community.

3.6.1 Contributors

All experimental contributors are the same as in chapter 2. Adam Milsom wrote the manuscript, wrote the model in Python, ran the simulations, optimisation and model analysis. Christian Pfrang and Adam Squires contributed to the interpretation of the results.

3.7 Comment

This chapter and chapter 2 are based on the same set of experiments. The aim of this particular study was to attempt to illustrate the potential effect of self-assembled phase formation on the lifetime of organic films in the atmosphere. Note that only the parameters associated with molecular diffusion were varied, with all other constants associated with reaction rates and gas-particle partitioning constrained to values determined experimentally or optimised in the modelling literature of oleic acid ozonolysis. Increasing the model complexity *e.g.* by explicitly defining each 9-carbon product and including tetra- and penta-mer products may indeed be more realistic. However, this would have created many more uncertain parameters which require optimisation, leading to a number of potential parameter combinations, all fitting equally well to the data – so-called "fitting an elephant". This is a continuous challenge with this kind of modelling.

There is confidence that the optimised parameters presented here are reasonably accurate (see the comparison of $D_{Y,lam}$ with the literature value, which is expected to be higher than the anhydrous lamellar phase studied here). Experimental determination of these key parameters would be ideal for a more accurate model representation and future work should focus on determining these experimentally (see the discussion on future work at the end of this thesis).

3.8 References

Alpert, P. A., Arroyo, P. C., Dou, J., Krieger, U. K., Steimer, S. S., Förster, J. D., Ditas, F., Pöhlker, C., Rossignol, S., Passananti, M., Perrier, S., George, C., Shiraiwa, M., Berkemeier, T., Watts, B. and Ammann, M.: Visualizing reaction and diffusion in xanthan gum aerosol particles exposed to ozone, Phys. Chem. Chem. Phys., 21(37), 20613–20627, doi:10.1039/c9cp03731d, 2019.

Berkemeier, T., Huisman, A. J., Ammann, M., Shiraiwa, M., Koop, T. and Pöschl, U.: Kinetic regimes and limiting cases of gas uptake and heterogeneous reactions in atmospheric aerosols and clouds: A general classification scheme, Atmos. Chem. Phys., 13(14), 6663–6686, doi:10.5194/acp-13-6663-2013, 2013.

Berkemeier, T., Ammann, M., Krieger, U. K., Peter, T., Spichtinger, P., Pöschl, U., Shiraiwa, M. and Huisman, A. J.: Technical note: Monte Carlo genetic algorithm (MCGA) for model analysis of multiphase chemical kinetics to determine transport and reaction rate coefficients using multiple experimental data sets, Atmos. Chem. Phys., 17(12), 8021–8029, doi:10.5194/acp-17-8021-2017, 2017.

Boucher, O., Randall, D., Artaxo, P., Bretherton, C., Feingold, G., Forster, P., Kerminen, V.-M., Kondo, Y., Liao, H., Lohmann, U., Rasch, P., Satheesh, S. K., Sherwood, S., Stevens, B. and Zhang, X. Y.: Clouds and Aerosols, in Climate Change 2013 - The Physical Science Basis, edited by Intergovernmental Panel on Climate Change, pp. 571–658, Cambridge University Press, Cambridge., 2013.

Campolongo, F., Cariboni, J. and Saltelli, A.: An effective screening design for sensitivity analysis of large models, Environ. Model. Softw., 22(10), 1509–1518, doi:10.1016/j.envsoft.2006.10.004, 2007.

Chan, C. K. and Yao, X.: Air pollution in mega cities in China, Atmos. Environ., 42(1), 1–42, doi:10.1016/j.atmosenv.2007.09.003, 2008.

Gallimore, P. J., Griffiths, P. T., Pope, F. D., Reid, J. P. and Kalberer, M.: Comprehensive modeling study of ozonolysis of oleic acid aerosol based on real-time, online measurements of aerosol composition, J. Geophys. Res., 122(8), 4364–4377, doi:10.1002/2016JD026221, 2017.

Hearn, J. D., Smith, G. D. and Lovett, A. J.: Ozonolysis of oleic acid particles: evidence for a surface reaction and secondary reactions involving Criegee intermediates, Phys. Chem. Chem. Phys., 7(3), 501–511, doi:10.1039/b414472d, 2005.

Herman, J. and Usher, W.: SALib : An open-source Python library for Sensitivity Analysis, J. Open Source Softw., 41, 2015–2017, doi:10.1016/S0010-1, 2018.

Hosny, N. A., Fitzgerald, C., Vyšniauskas, A., Athanasiadis, A., Berkemeier, T., Uygur, N., Pöschl, U., Shiraiwa, M., Kalberer, M., Pope, F. D. and Kuimova, M. K.: Direct imaging of changes in aerosol particle viscosity upon hydration and chemical aging, Chem. Sci., 7(2), 1357–1367, doi:10.1039/c5sc02959g, 2016.

Hung, H. and Tang, C.: Effects of Temperature and Physical State on Heterogeneous Oxidation of Oleic Acid Droplets with Ozone, J. Phys. Chem. A, 114, 13104–13112, doi:10.1021/jp105042w, 2010.

Jimenez, J. L., Canagaratna, M. R., Donahue, N. M., Prevot, A. S. H., Zhang, Q., Kroll, J. H., DeCarlo, P. F., Allan, J. D., Coe, H., Ng, N. L., Aiken, A. C., Docherty, K. S., Ulbrich, I. M., Grieshop, A. P., Robinson, A. L., Duplissy, J., Smith, J. D., Wilson, K. R., Lanz, V. A., Hueglin, C., Sun, Y. L., Tian, J., Laaksonen, A., Raatikainen, T., Rautiainen, J., Vaattovaara, P., Ehn, M., Kulmala, M., Tomlinson, J. M., Collins, D. R.,

Cubison, M. J., Dunlea, J., Huffman, J. A., Onasch, T. B., Alfarra, M. R., Williams, P. I., Bower, K., Kondo, Y., Schneider, J., Drewnick, F., Borrmann, S., Weimer, S., Demerjian, K., Salcedo, D., Cottrell, L., Griffin, R., Takami, A., Miyoshi, T., Hatakeyama, S., Shimono, A., Sun, J. Y., Zhang, Y. M., Dzepina, K., Kimmel, J. R., Sueper, D., Jayne, J. T., Herndon, S. C., Trimborn, A. M., Williams, L. R., Wood, E. C., Middlebrook, A. M., Kolb, C. E., Baltensperger, U. and Worsnop, D. R.: Evolution of Organic Aerosols in the Atmosphere, Science, 326(5959), 1525–1529, doi:10.1126/science.1180353, 2009.

King, M. D., Rennie, A. R., Thompson, K. C., Fisher, F. N., Dong, C. C., Thomas, R. K., Pfrang, C. and Hughes, A. V.: Oxidation of oleic acid at the air-water interface and its potential effects on cloud critical supersaturations, Phys. Chem. Chem. Phys., 11(35), 7699–7707, doi:10.1039/b906517b, 2009.

King, M. D., Jones, S. H., Lucas, C. O. M., Thompson, K. C., Rennie, A. R., Ward, A. D., Marks, A. A., Fisher, F. N., Pfrang, C., Hughes, A. V. and Campbell, R. A.: The reaction of oleic acid monolayers with gas-phase ozone at the air water interface: The effect of sub-phase viscosity, and inert secondary components, Phys. Chem. Chem. Phys., 22(48), 28032–28044, doi:10.1039/d0cp03934a, 2020.

Lindblom, G. and Orädd, G.: NMR Studies of translational diffusion in lyotropic liquid crystals and lipid membranes, Prog. Nucl. Magn. Reson. Spectrosc., 26, 483–515, doi:10.1016/0079-6565(94)80014-6, 1994.

Lindblom, G. and Wennerström, H.: Amphiphile diffusion in model membrane systems studied by pulsed NMR, Biophys. Chem., 6(2), 167–171, doi:10.1016/0301-4622(77)87006-3, 1977.

McKay, M. D., Beckman, R. J. and Conover, W. J.: A Comparison of Three Methods for Selecting Values of Input Variables in the Analysis of Output from a Computer Code, Technometrics, 21(2), 239, doi:10.2307/1268522, 1979.

Mele, S., Söderman, O., Ljusberg-Wahrén, H., Thuresson, K., Monduzzi, M. and Nylander, T.: Phase behavior in the biologically important oleic acid/sodium oleate/water system, Chem. Phys. Lipids, 211, 30–36, doi:10.1016/j.chemphyslip.2017.11.017, 2018.

Mezzenga, R., Meyer, C., Servais, C., Romoscanu, A. I., Sagalowicz, L. and Hayward, R. C.: Shear rheology of lyotropic liquid crystals: A case study, Langmuir, 21(8), 3322–3333, doi:10.1021/la046964b, 2005.

Milsom, A., Squires, A. M., Boswell, J. A., Terrill, N. J., Ward, A. D. and Pfrang, C.: An organic crystalline state in ageing atmospheric aerosol proxies : spatially resolved structural changes in levitated fatty acid particles, Atmos. Chem. Phys. Discuss., [preprint], 1–31, doi:https://doi.org/10.5194/acp-2021-270, 2021a.

Milsom, A., Squires, A. M., Woden, B., Terrill, N. J., Ward, A. D. and Pfrang, C.: The persistence of a proxy for cooking emissions in megacities: a kinetic study of the ozonolysis of self-assembled films by simultaneous small and wide angle X-ray scattering (SAXS/WAXS) and Raman microscopy, Faraday Discuss., 226, 364–381, doi:10.1039/D0FD00088D, 2021b.

Morris, M. D.: Factorial Sampling Plans for Preliminary Computational Experiments, Technometrics, 33(2), 161–174, doi:10.1080/00401706.1991.10484804, 1991.

Mu, Q., Shiraiwa, M., Octaviani, M., Ma, N., Ding, A., Su, H., Lammel, G., Pöschl, U. and Cheng, Y.: Temperature effect on phase state and reactivity controls atmospheric

multiphase chemistry and transport of PAHs, Sci. Adv., 4(3), eaap7314, doi:10.1126/sciadv.aap7314, 2018.

Ots, R., Vieno, M., Allan, J. D., Reis, S., Nemitz, E., Young, D. E., Coe, H., Di Marco, C., Detournay, A., Mackenzie, I. A., Green, D. C. and Heal, M. R.: Model simulations of cooking organic aerosol (COA) over the UK using estimates of emissions based on measurements at two sites in London, Atmos. Chem. Phys., 16(21), 13773–13789, doi:10.5194/acp-16-13773-2016, 2016.

Ovadnevaite, J., Zuend, A., Laaksonen, A., Sanchez, K. J., Roberts, G., Ceburnis, D., Decesari, S., Rinaldi, M., Hodas, N., Facchini, M. C., Seinfeld, J. H. and O'Dowd, C.: Surface tension prevails over solute effect in organic-influenced cloud droplet activation, Nature, 546(7660), 637–641, doi:10.1038/nature22806, 2017.

Pfrang, C., Shiraiwa, M. and Pöschl, U.: Coupling aerosol surface and bulk chemistry with a kinetic double layer model (K2-SUB): Oxidation of oleic acid by ozone, Atmos. Chem. Phys., 10(10), 4537–4557, doi:10.5194/acp-10-4537-2010, 2010.

Pfrang, C., Shiraiwa, M. and Pöschl, U.: Chemical ageing and transformation of diffusivity in semi-solid multi-component organic aerosol particles, Atmos. Chem. Phys., 11(14), 7343–7354, doi:10.5194/acp-11-7343-2011, 2011.

Pfrang, C., Rastogi, K., Cabrera-Martinez, E. R., Seddon, A. M., Dicko, C., Labrador, A., Plivelic, T. S., Cowieson, N. and Squires, A. M.: Complex three-dimensional self-assembly in proxies for atmospheric aerosols, Nat. Commun., 8(1), 1724, doi:10.1038/s41467-017-01918-1, 2017.

Pöschl, U., Rudich, Y. and Ammann, M.: Kinetic model framework for aerosol and cloud surface chemistry and gas-particle interactions - Part 1: General equations,

parameters, and terminology, Atmos. Chem. Phys., 7(23), 5989–6023, doi:10.5194/acp-7-5989-2007, 2007.

Reid, J. P., Bertram, A. K., Topping, D. O., Laskin, A., Martin, S. T., Petters, M. D., Pope, F. D. and Rovelli, G.: The viscosity of atmospherically relevant organic particles, Nat. Commun., 9(1), 1–14, doi:10.1038/s41467-018-03027-z, 2018.

Robinson, A. L., Donahue, N. M. and Rogge, W. F.: Photochemical oxidation and changes in molecular composition of organic aerosol in the regional context, J. Geophys. Res. Atmos., 111(3), 1–15, doi:10.1029/2005JD006265, 2006.

Rudich, Y., Donahue, N. M. and Mentel, T. F.: Aging of Organic Aerosol: Bridging the Gap Between Laboratory and Field Studies, Annu. Rev. Phys. Chem., 58(1), 321–352, doi:10.1146/annurev.physchem.58.032806.104432, 2007.

Sagdeev, D., Gabitov, I., Isyanov, C., Khairutdinov, V., Farakhov, M., Zaripov, Z. and Abdulagatov, I.: Densities and Viscosities of Oleic Acid at Atmospheric Pressure, JAOCS, J. Am. Oil Chem. Soc., 96(6), 647–662, doi:10.1002/aocs.12217, 2019.

Seddon, A. M., Richardson, S. J., Rastogi, K., Plivelic, T. S., Squires, A. M. and Pfrang, C.: Control of Nanomaterial Self-Assembly in Ultrasonically Levitated Droplets, J. Phys. Chem. Lett., 7(7), 1341–1345, doi:10.1021/acs.jpclett.6b00449, 2016.

Seddon, J. M., Bartle, E. A. and Mingins, J.: Inverse cubic liquid-crystalline phases of phospholipids and related lyotropic systems, J. Phys. Condens. Matter, 2, SA285–SA290, doi:10.1088/0953-8984/2/S/043, 1990.

Shiraiwa, M., Pfrang, C. and Pöschl, U.: Kinetic multi-layer model of aerosol surface and bulk chemistry (KM-SUB): The influence of interfacial transport and bulk diffusion

on the oxidation of oleic acid by ozone, Atmos. Chem. Phys., 10, 3673–3691, doi:10.5194/acp-10-3673-2010, 2010.

Shiraiwa, M., Ammann, M., Koop, T. and Poschl, U.: Gas uptake and chemical aging of semisolid organic aerosol particles, Proc. Natl. Acad. Sci. U. S. A., 108(27), 11003–11008, doi:10.1073/pnas.1103045108, 2011a.

Shiraiwa, M., Ammann, M., Koop, T. and Pöschl, U.: Gas uptake and chemical aging of semisolid organic aerosol particles -Supporting information, Proc. Natl. Acad. Sci. U. S. A., 108(27), 11003–11008, doi:10.1073/pnas.1103045108, 2011b.

Shrivastava, M., Lou, S., Zelenyuk, A., Easter, R. C., Corley, R. A., Thrall, B. D., Rasch, P. J., Fast, J. D., Simonich, S. L. M., Shen, H. and Tao, S.: Global long-range transport and lung cancer risk from polycyclic aromatic hydrocarbons shielded by coatings of organic aerosol, Proc. Natl. Acad. Sci. U. S. A., 114(6), 1246–1251, doi:10.1073/pnas.1618475114, 2017.

Slade, J. H., Ault, A. P., Bui, A. T., Ditto, J. C., Lei, Z., Bondy, A. L., Olson, N. E., Cook, R. D., Desrochers, S. J., Harvey, R. M., Erickson, M. H., Wallace, H. W., Alvarez, S. L., Flynn, J. H., Boor, B. E., Petrucci, G. A., Gentner, D. R., Griffin, R. J. and Shepson, P. B.: Bouncier Particles at Night: Biogenic Secondary Organic Aerosol Chemistry and Sulfate Drive Diel Variations in the Aerosol Phase in a Mixed Forest, Environ. Sci. Technol., 53(9), 4977–4987, doi:10.1021/acs.est.8b07319, 2019.

Storn, R. and Price, K.: Differential Evolution – A Simple and Efficient Heuristic for global Optimization over Continuous Spaces, J. Glob. Optim., 11, 341–359, doi:10.1023/A1008202821328, 1997.

Tuckermann, R.: Surface tension of aqueous solutions of water-soluble organic and

inorganic compounds, Atmos. Environ., 41(29), 6265–6275, doi:10.1016/j.atmosenv.2007.03.051, 2007.

Vicente, A. M. P., Rocha, S., Duarte, M., Moreira, R., Nunes, T. and Alves, C. A.: Fingerprinting and emission rates of particulate organic compounds from typical restaurants in Portugal, Sci. Total Environ., 778, 146090, doi:10.1016/j.scitotenv.2021.146090, 2021.

Vieceli, J., Ma, O. L. and Tobias, D. J.: Uptake and collision dynamics of gas phase ozone at unsaturated organic interfaces, J. Phys. Chem. A, 108(27), 5806–5814, doi:10.1021/jp0494584, 2004.

Virtanen, A., Joutsensaari, J., Koop, T., Kannosto, J., Yli-Pirilä, P., Leskinen, J., Mäkelä, J. M., Holopainen, J. K., Pöschl, U., Kulmala, M., Worsnop, D. R. and Laaksonen, A.: An amorphous solid state of biogenic secondary organic aerosol particles, Nature, 467(7317), 824–827, doi:10.1038/nature09455, 2010.

Virtanen, P., Gommers, R., Oliphant, T. E., Haberland, M., Reddy, T., Cournapeau, D., Burovski, E., Peterson, P., Weckesser, W., Bright, J., van der Walt, S. J., Brett, M., Wilson, J., Millman, K. J., Mayorov, N., Nelson, A. R. J., Jones, E., Kern, R., Larson, E., Carey, C. J., Polat, İ., Feng, Y., Moore, E. W., VanderPlas, J., Laxalde, D., Perktold, J., Cimrman, R., Henriksen, I., Quintero, E. A., Harris, C. R., Archibald, A. M., Ribeiro, A. H., Pedregosa, F., van Mulbregt, P., Vijaykumar, A., Bardelli, A. Pietro, Rothberg, A., Hilboll, A., Kloeckner, A., Scopatz, A., Lee, A., Rokem, A., Woods, C. N., Fulton, C., Masson, C., Häggström, C., Fitzgerald, C., Nicholson, D. A., Hagen, D. R., Pasechnik, D. V., Olivetti, E., Martin, E., Wieser, E., Silva, F., Lenders, F., Wilhelm, F., Young, G., Price, G. A., Ingold, G. L., Allen, G. E., Lee, G. R., Audren, H., Probst, I.,

Dietrich, J. P., Silterra, J., Webber, J. T., Slavič, J., Nothman, J., Buchner, J., Kulick, J., Schönberger, J. L., de Miranda Cardoso, J. V., Reimer, J., Harrington, J., Rodríguez, J. L. C., Nunez-Iglesias, J., Kuczynski, J., Tritz, K., Thoma, M., Newville, M., Kümmerer, M., Bolingbroke, M., Tartre, M., Pak, M., Smith, N. J., Nowaczyk, N., Shebanov, N., Pavlyk, O., Brodtkorb, P. A., Lee, P., McGibbon, R. T., Feldbauer, R., Lewis, S., Tygier, S., Sievert, S., Vigna, S., Peterson, S., More, S., Pudlik, T., et al.: SciPy 1.0: fundamental algorithms for scientific computing in Python, Nat. Methods, 17(3), 261–272, doi:10.1038/s41592-019-0686-2, 2020.

Wang, Q., He, X., Zhou, M., Huang, D. D., Qiao, L., Zhu, S., Ma, Y. G., Wang, H. L., Li, L., Huang, C., Huang, X. H. H., Xu, W., Worsnop, D., Goldstein, A. H., Guo, H., Yu, J. Z., Huang, C. and Yu, J. Z.: Hourly Measurements of Organic Molecular Markers in Urban Shanghai, China: Primary Organic Aerosol Source Identification and Observation of Cooking Aerosol Aging, ACS Earth Sp. Chem., 4(9), 1670–1685, doi:10.1021/acsearthspacechem.0c00205, 2020a.

Wang, T., Huang, R. J., Li, Y., Chen, Q., Chen, Y., Yang, L., Guo, J., Ni, H., Hoffmann, T., Wang, X. and Mai, B.: One-year characterization of organic aerosol markers in urban Beijing: Seasonal variation and spatiotemporal comparison, Sci. Total Environ., 743, 140689, doi:10.1016/j.scitotenv.2020.140689, 2020b.

Weschler, C. J.: Ozone in indoor environments: Concentration and chemistry, Indoor Air, 10(4), 269–288, doi:10.1034/j.1600-0668.2000.010004269.x, 2000.

Woden, B., Skoda, M. W. A., Milsom, A., Gubb, C., Maestro, A., Tellam, J. and Pfrang, C.: Ozonolysis of fatty acid monolayers at the air–water interface: organic films may persist at the surface of atmospheric aerosols, Atmos. Chem. Phys., 21(2), 1325–1340,

doi:10.5194/acp-21-1325-2021, 2021.

Worsnop, D. R., Morris, J. W., Shi, Q., Davidovits, P. and Kolb, C. E.: A chemical kinetic model for reactive transformations of aerosol particles, Geophys. Res. Lett., 29(20), 19–22, doi:10.1029/2002GL015542, 2002.

Wu, Z. J., Zheng, J., Shang, D. J., Du, Z. F., Wu, Y. S., Zeng, L. M., Wiedensohler, A. and Hu, M.: Particle hygroscopicity and its link to chemical composition in the urban atmosphere of Beijing, China, during summertime, Atmos. Chem. Phys., 16(2), 1123–1138, doi:10.5194/acp-16-1123-2016, 2016.

Zabara, A. and Mezzenga, R.: Controlling molecular transport and sustained drug release in lipid-based liquid crystalline mesophases, J. Control. Release, 188, 31–43, doi:10.1016/j.jconrel.2014.05.052, 2014.

Zahardis, J. and Petrucci, G. A.: The oleic acid-ozone heterogeneous reaction system: Products, kinetics, secondary chemistry, and atmospheric implications of a model system - A review, Atmos. Chem. Phys., 7(5), 1237–1274, doi:10.5194/acp-7-1237-2007, 2007.

Zhao, X., Hu, Q., Wang, X., Ding, X., He, Q., Zhang, Z., Shen, R., Lü, S., Liu, T., Fu, X. and Chen, L.: Composition profiles of organic aerosols from Chinese residential cooking: Case study in urban Guangzhou, south China, J. Atmos. Chem., 72(1), 1–18, doi:10.1007/s10874-015-9298-0, 2015.

Zhou, S., Shiraiwa, M., McWhinney, R. D., Pöschl, U. and Abbatt, J. P. D.: Kinetic limitations in gas-particle reactions arising from slow diffusion in secondary organic aerosol, Faraday Discuss., 165, 391–406, doi:10.1039/c3fd00030c, 2013.

Zhou, S., Hwang, B. C. H., Lakey, P. S. J., Zuend, A., Abbatt, J. P. D. and Shiraiwa, M.: Multiphase reactivity of polycyclic aromatic hydrocarbons is driven by phase separation and diffusion limitations, Proc. Natl. Acad. Sci. U. S. A., 116(24), 11658–11663, doi:10.1073/pnas.1902517116, 2019.

4 CHAPTER 4: PROBING THE SURFACE STRUCTURE RESPONSE TO AGEING IN NANOMETRE-SCALE FILMS OF AN ORGANIC SURFACTANT AEROSOL PROXY

This study is prepared for submission to a journal.

4.1 **Abstract**

Atmospheric aerosol particles can be coated with organic material, impacting on aerosol atmospheric lifetime and urban air quality. Coatings of organic material are also found on indoor surfaces such as window glass. Oleic acid is a fatty acid surfactant which is found in cooking and marine particulate emissions. It can self-assemble into lamellar bilayers (stacks), with its sodium salt, under ambient conditions. We have coated nanometre-scale oleic acid-sodium oleate films onto solid silicon substrates, forming a mixed area consisting of lamellar stacks and an amorphous film. The coatings were subjected to simulated atmospheric ageing (ozonolysis and humidity changes) and changes in the surface structure was followed by neutron reflectometry. The orientation of such lamellar structures is known to affect the diffusivity of small molecules through them. We found that the orientation of lamellar stacks was sensitive to humidity in oxidised and unoxidised films. Complementary analysis by grazing-incidence small-angle X-ray scattering supported these findings. Lamellar stacks, consisting only of starting materials, persist at the end of simulated atmospheric ageing. These nanometre-scale findings corroborate previous work on micrometre-scale films, demonstrating that fatty acid self-assembly could significantly increase the atmospheric lifetime of these molecules. The persistence of such semi-solid surfactant arrangements in the atmosphere has implications for the climate and urban/indoor air pollution.

4.2 Introduction

Aerosols contribute to ambient air pollution and affect processes such as cloud droplet formation, affecting air quality and the climate (Boucher et al., 2013; Pöschl, 2005). Organic compounds can dominate aerosol composition in many parts of the world (Jimenez et al., 2009). This varies with time, location, season and environment (Fu et al., 2008; Li et al., 2021; Wang et al., 2020a, 2020b). Poor air quality has been linked with an increased organic fraction on the surface of urban particulate matter (Zhao et al., 2020) and cooking emissions have been estimated to contribute 10 % more to $PM_{2.5}$ emissions in the UK (Ots et al., 2016). Away from the urban environment, organic compounds have been characterised in particulate matter from biogenic sources such as remote marine (Tervahattu, 2002) and forested (Slade et al., 2019) environments. The study of the effect of organic compounds on aerosol processes is therefore of global importance. Oleic acid is an unsaturated fatty acid commonly found in cooking and marine aerosols (Vicente et al., 2021a; Zeng et al., 2020; Zhao et al., 2015). This makes it an ideal proxy compound for laboratory and model investigations on reactive organic aerosol systems (Gallimore et al., 2017; Milsom et al., 2021; Pfrang et al., 2017; Shiraiwa et al., 2010, 2012; Woden et al., 2021; Zahardis and Petrucci, 2007).

Organic surface coatings on particulate matter have been characterised in field measurements (Mikhailov et al., 2015; Tervahattu, 2002). The reactivity of organic molecules has been shown to proceed faster as a surface coating compared with pure particles, linked with the higher surface area-to-volume ratio associated with such coatings (Lim et al., 2017).

Some organic emissions are surface active, such as fatty acids. Oleic acid has been characterised on the surface of particulate matter (Tervahattu, 2002). As a surfactant, it

can decrease the surface tension of an aqueous particle, affecting the ability of the particle to take up water and form a cloud droplet (Ovadnevaite et al., 2017). Oleic acid molecules, being amphiphilic, can arrange into a range of lyotropic liquid crystal (LLC) phases in contact with water and in the presence of its sodium salt (Mele et al., 2018; Tiddy, 1980). They can also form into anhydrous lamellar bilayers (stacks) at room relative humidity (RH) (~ 50 % RH) (Milsom et al., 2021). These molecular arrangements bring with them differences in viscosity and diffusivity, two factors which impact atmospheric aerosol ageing (Reid et al., 2018; Shiraiwa et al., 2011).

Indoor surfaces can host organic compounds which are emitted by common indoor activities such as cooking, cleaning and ironing (Patel et al., 2020; Vicente et al., 2021b). Organic films were shown to form on glass surfaces after exposure to cooking emissions and qualitatively shown to include oxidised and unoxidised fatty acids (Or et al., 2020). It has been suggested that films collected in a kitchen change surface morphology and/or form viscous phases during humidity changes (Schwartz-Narbonne and Donaldson, 2019). Both hypotheses (morphology change and viscous phase formation) have implications for the uptake of atmospheric oxidants such as ozone due to the implied changes in surface area and film diffusivity. Oleic acid is likely present in such coatings because oleic acid and its reaction products have been followed in real-time during and after simulated cooking (Zeng et al., 2020) and is also used as a tracer for cooking emissions (Wang et al., 2020a). The surface coatings presented here can therefore be a proxy for the surface of atmospheric aerosols and organic coatings on indoor surfaces.

Fatty acid packing has been linked with hygroscopicity (Nguyen et al., 2017; Xiong et al., 1998) and reactivity (Garland et al., 2008; Hearn et al., 2005; Katrib et al., 2005;

Rosen et al., 2008; Vieceli et al., 2004). We have shown previously that the lamellar bilayer formed by the oleic acid-sodium oleate proxy slows down ozonolysis by *ca.* an order of magnitude, depending on the film thickness (Milsom et al., 2021). The orientation of such bilayers is expected to affect the diffusion of small molecules through them. Diffusion perpendicular to the bilayer plane is orders of magnitude smaller than in-plane diffusion (Lindblom and Orädd, 1994). Bilayers are found in the dehydrated upper layer of the skin (*stratum corneum*) along with dead cells. In the context of indoor air quality, models of skin lipid-oxidant reactivity consider diffusion through this layer due to the marked decrease in molecular diffusivity (Lakey et al., 2017), which can be partially attributed to the lipid bilayers present (Wang et al., 2006, 2007). These anisotropic arrangements can therefore have an impact on molecular diffusivity through them. The orientation of such bilayer arrangements is followed in this study.

Neutron and X-ray reflectometry (NR and XR) have been used previously to probe proxy and real organic aerosol material at the air-water interface (Jones et al., 2017; King et al., 2009, 2010, 2020; Pfrang et al., 2014; Sebastiani et al., 2018; Skoda et al., 2017; Woden et al., 2018, 2021). These surface-sensitive techniques allow for the study of organic films down to the monolayer level. NR can be particularly sensitive to a molecule if it is deuterated, due to the much larger neutron scattering power of a deuterium atom compared with a hydrogen atom.

Previous work has focussed on monolayers of deuterated oleic acid on an aqueous sub-phase (King et al., 2020; Sebastiani et al., 2018; Woden et al., 2021), self-assembly in an oleic acid-sodium oleate proxy in large levitated particles (Pfrang et al., 2017) and reaction kinetics in capillaries coated with micron-scale films down to *ca.* 0.5 μm

(Milsom et al., 2021). Many of these studies have suggested the persistence of reacted and/or unreacted organic material after chemical ageing – something we observe and discuss here.

In this study, we spin-coated nanometre-scale films of deuterated oleic acid-sodium oleate on silicon blocks with a native SiO_2 layer. This resulted in a coating with a mixed area composed of lamellar stacks and an amorphous region. We subjected these films to simulated atmospheric ageing by oxidising the sample and changing the humidity. Changes in surface structure were followed by NR and complemented by grazing-incidence small-angle X-ray scattering (GI-SAXS) and optical microscopy. We draw atmospheric implications from these results, which act as a platform for future, more quantitative studies of the reaction kinetics and surface dynamics of such coatings.

4.3 Methods

4.3.1 Preparation of spin-coated films

Spin-coated films of the oleic acid-sodium oleate proxy were prepared for NR/GI-SAXS measurements by first dissolving these components as 1 wt % solutions in methanol. These solutions were then mixed in a 1:1 wt ratio to afford the coating solution. A spin coater (*Laurell WS-650-23*) was set to the desired rpm and a 50 µL aliquot of the coating solution was pipetted onto the centre of the spinning silicon substrate. The silicon surfaces were prepared by exposure to ozone in an ozone surface steriliser (~15 min); then a series of washes with methanol and distilled water, always finishing with a methanol wash and blowing dry nitrogen air over the surface. These surfaces were characterised by NR before films were deposited on them and surface roughness for both the silicon and SiO_2 layers were obtained, along with the thickness of the SiO_2 layer (see appendix section 10.3.1).

Film thickness can be controlled by adjusting the spinning speed during spin coating (Richardson et al., 2015). After the initial coating step, the spin-coater was set to spin at 3000 rpm for 30 s to ensure the solvent had evaporated fully. For GI-SAXS samples, methanol was added to the side of the disks during this additional step in order to remove any ridge formation at the disk's edges – this can affect the GI-SAXS measurement.

Deuterated oleic acid (d_{34}-OA, Sigma-Aldrich 98 % Atom D; 99.9 % purity) was used in order to provide a large contrast between the reflected neutron signal from the deposited film and substrate required for the neutron reflectometry experiment. Sodium oleate (Sigma-Aldrich, 99 % purity) was not deuterated.

4.3.2 **Neutron reflectometry (NR)**

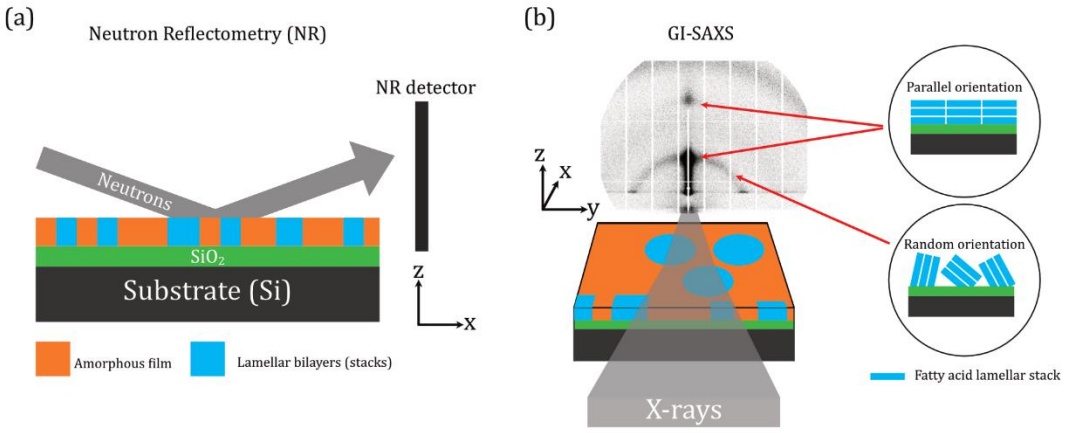

Figure 4-1. Schematic representations of (a) neutron reflectometry (NR) and (b) grazing-incidence small-angle X-ray scattering (GI-SAXS) experiments. The mixed area model is illustrated, showing a mixed area of amorphous film and lamellar bilayers (stacks). The relationship between lamellar stack orientation and scattering pattern is illustrated in (b). The x-z plane is the specular plane.

NR is described in detail elsewhere (Penfold and Thomas, 1990). Here, we summarise the salient points of the technique. All NR was carried out at the ISIS neutron and muon source (UK) on the INTER beamline, which is primarily a specular reflectometer. A schematic of the NR experiment is presented in Fig. 4-1(a) - note the x-z plane is the specular plane.

NR is a technique used to probe the structure of interfaces by providing depth-resolved structural information in the form of a scattering length density (SLD) profile. Different atoms have different neutron scattering lengths. The SLD of a layer is a function of the scattering length and volume fraction of each chemical component in that layer. Layered structures, *e.g.* the oleic acid-sodium oleate films on silicon studied here, give rise to contrasts in SLD. The reflectivity (R – the fraction of neutrons reflected) is related to the SLD and momentum transfer (Q) via the proportionality:

$$\mathrm{R(Q)} \propto \frac{\mathrm{SLD}^2}{\mathrm{Q}^4} \tag{4-1}$$

This relationship is valid above a critical angle, below which all neutrons are reflected. For specular reflectometry, Q is related to the neutron wavelength (λ) and angle of incidence/reflection (θ):

$$\mathrm{Q} = \frac{4\pi}{\lambda}\sin(\theta) \tag{4-2}$$

The INTER NR beamline uses pulsed neutrons of varying wavelengths and the measurement angle is kept constant: this was at 1.4 or 1.6 º for kinetic/water uptake runs and full characterisations were performed by stitching together reflectivity curves measured at 0.5 and 2.3 º. This full Q-range was 0.007 – 0.282 $Å^{-1}$, though little information can be obtained from the higher Q-range (see Eq. 4-1). The measurement

returns a relationship between R and Q. Plots of R vs Q or RQ^4 vs Q are the most common way of presenting NR data and are what will be used in this study.

NR measurements take longer to carry out than similar synchrotron X-ray techniques such as GI-SAXS, where scattering patterns are typically measured in seconds. This is due to the difference in flux between the neutron and X-ray sources. Typical NR measurements for full characterisations were 30-180 min. Data collected at the INTER beamline can be transformed into time slices. The NR data from each time slice and be extracted and fitted to. For kinetic and water uptake runs we chose between 20 – 120 min time slices, which represented a balance between the need for well-resolved NR curves and a decent time resolution to follow structural changes. It follows that this low time resolution compared with GI-SAXS – say, would result in some averaging of the NR curve over that 20 min time period. This would introduce some uncertainty in the model fitting, unavoidable with this experiment. Despite this, changes happened sufficiently slowly so that we could distinguish trends in the fitted parameters (see section 4.4).

The chamber used to control the sample environment during NR experiments is described by Skoda *et al*. (Skoda et al., 2017). In summary, the chamber: has a volume of approximately 1.5 L; has quartz windows at either end which allow the neutrons to pass through, hit the sample and be detected on the other side; and has connectors which allow the chamber to be filled with a gas - such as ozone and water vapour used in this study.

4.3.3 Grazing-incidence small-angle X-ray scattering (GI-SAXS)

GI-SAXS is closely related to NR in that small (grazing) angles of incidence are utilised to probe the surface structure of materials (Narayanan and Konovalov, 2020). The GI-SAXS experiment allows for the measurement of X-ray scattering over a larger angular range and also measures off-specular scattering – this is scattering in the y-direction in Fig. 4-1(b).

The scattered intensity (I) is a function of Q. The spacing between equivalent scattering planes (d) is related to Q by applying Bragg's law ($d = \lambda/2\sin(\theta)$) to Eq. (4-2):

$$d = \frac{2\pi}{Q} \tag{4-3}$$

The d-spacing can be used to determine the spacing between lamellar stacks formed by our samples in this study, as has been done before on a similar system (Milsom et al., 2021).

The orientation of the lamellar stacks can be inferred by variations in the azimuthal intensity profile at the lamellar peak Q position. An increase in I in the specular direction (*i.e.* scattering in the x-z plane in Fig. 4-1) is consistent with a repeating structure that is oriented parallel to the surface. A diffuse scattering ring is consistent with random orientations.

Samples were mounted vertically and measured on the I22 beamline at the Diamond Light Source (UK) with X-rays at 14 keV energy at a 0.4° angle of incidence. Scattering patterns were measured for 1 s per frame over a Q-range of 0.007 – 0.5 $Å^{-1}$.

Offline GI-SAXS measurements were made using a *Xenocs Xeuss 2.0* equipped with a micro-focus Cu Kα source. Each pattern collection was 15 minutes. A more detailed description of the offline GI-SAXS setup is provided in the appendix section 10.3.3.

4.3.4 **Ozonolysis**

Ozonolysis experiments were carried out by passing dry oxygen through a UV pen-ray ozoniser (Ultraviolet Products Ltd, Cambridge, UK) and then to the sample chamber in which the sample was placed. The concentration of ozone was calibrated offline by UV spectroscopy by monitoring the absorption band of ozone at 254 nm and using the absorption cross-section ($(1.14 \pm 0.08) \times 10^{-17}$ cm^2) (Mauersberger et al., 1986). The ozone concentration was in the range of 126 – 4020 ppb and was varied by exposing oxygen to different amounts of UV light and varying the oxygen flow rate (which was varied between 0.4 – 1.2 L min^{-1}). An extra ozoniser was used to reach the highest ozone concentration. Previous experience with this self-assembled system has shown that it is necessary to have a high ozone concentration to observe an appreciable decay in the timeframe of a beamline experiment (Milsom et al., 2021).

4.3.5 **Humidity experiments**

Humidity experiments were carried out using a Raspberry Pi (RPi) humidity control system. The RPi controlled two air pumps – one which pumped air through a bubbler filled with D_2O, the other pumping ambient air. The RPi achieved the target relative humidity (RH) by regulating the wet and dry air pumps. The two air flows were then mixed before entering the sample chamber. D_2O was chosen due to its larger SLD compared to H_2O, this enhances the NR signal.

GI-SAXS humidity experiments differed slightly in that a different sample chamber was used and wet/dry air flows were regulated by mass flow controllers. RH was monitored by an RPi system as for the NR experiments.

4.3.6 NR model fitting

NR data is commonly analysed by fitting interfacial models to the experimental data (Penfold and Thomas, 1990). These models are informed by what the analyst already knows or hypothesises about the system. It is possible that model fits are not unique, motivating the use of complementary techniques (such as GI-SAXS and optical microscopy in this study) to corroborate model selection.

For all fits performed in this study a mixed area model was selected, where the area illuminated by the neutron beam has regions of different interfacial structures (see Fig. 4-1 for a schematic representation). This model, consisting of a lamellar stack region and an amorphous film region, fit the best to all the films probed in this study. This was backed up by determination of the Bayesian evidence for each model, complementary optical microscopy and GI-SAXS (see succeeding discussion).

The lamellar stack model component comprised of two lipid layers (containing d_{34}-OA and sodium oleate) with roughness, number of stacks (lipid bilayers) and SLD allowed to vary during the fitting procedure. An additional D_2O layer between the stacks was included for humidification/dehumidification experiment model fitting. The amorphous film model component was represented as one layer with thickness, roughness and SLD allowed to vary. The relative amount of specular reflection from each of these components is obtained by varying a scale factor applied to each component. The contribution of each model component was scaled by their respective scale factors to

afford the final model reflectivity curve. The overall scale factor was constrained to be approximately what was measured for initial film characterisations (where the critical edge could be seen at low-Q).

The *refnx* Python package was used to create and fit the model with the data, optimising the model parameters with a global optimisation genetic algorithm (Nelson and Prescott, 2019; Virtanen et al., 2020). *refnx* also allowed us to perform Markov Chain Monte Carlo (MCMC) sampling of the parameter space via the *emcee* Python package (Foreman-Mackey et al., 2013). MCMC sampling enabled us to determine the uncertainty in each varied model parameter by estimating a probability distribution for each. We could then illustrate the range of SLD profiles and model fits consistent with the experimental data (see succeeding discussion).

McCluskey *et al.* presented a Bayesian model selection framework in order to maximise the information extractable from NR measurements and to help justify model selection (McCluskey et al., 2020). We have employed this method, which estimates the Bayesian evidence for each model-data combination by sampling from the prior probability distributions for each varying parameter, determined previously by MCMC sampling. This was achieved using the nested sampler available in the *dynesty* Python package (Skilling, 2004, 2006; Speagle, 2020). Details on how this was implemented are available in the appendix section 10.3.4. A summary of this analysis is presented in section 4.4.1.

4.4 **Results and discussion**

4.4.1 **The surface structure of nanometre-scale films**

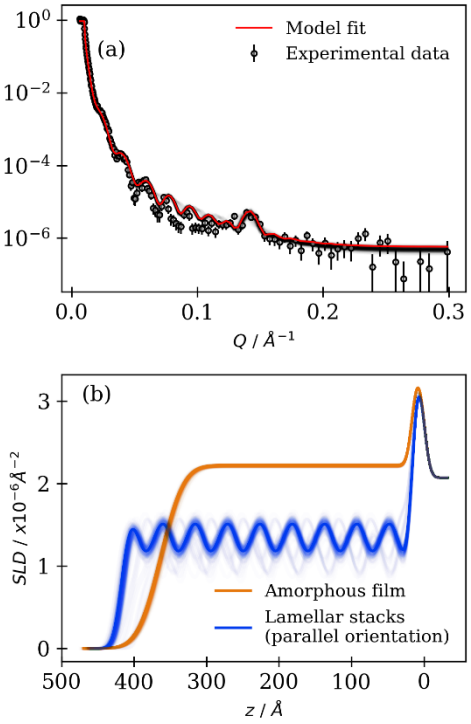

Figure 4-2. (a) R vs Q curve of a film coated at 2000 rpm. Model fit is presented along with 300 curves randomly sampled from the chains stored after MCMC sampling procedure (black curves). (b) SLD profile corresponding to the amorphous film and lamellar stack region. SLD is plotted vs the distance from the substrate surface (z).

Each spin-coated film was characterised before being subjected to simulated ageing. The resulting NR curve and SLD profile for measurements taken at low and high angles (stitched together) are presented in Fig. 4-2 for the film coated at 2000 rpm.

The *R* vs *Q* curve presented in Fig. 4-2(a) is typical of a layered interface. Fringes appear at regular intervals and the spacing between them is inversely proportional to the film thickness (Penfold and Thomas, 1990). A Bragg peak at *ca.* 0.14 $Å^{-1}$ is observed and is consistent with the anhydrous lamellar phase Bragg peak observed in a previous SAXS study on the same non-deuterated proxy, corresponding to a lamellar bilayer thickness of *ca.* 4.5 nm (Milsom et al., 2021).

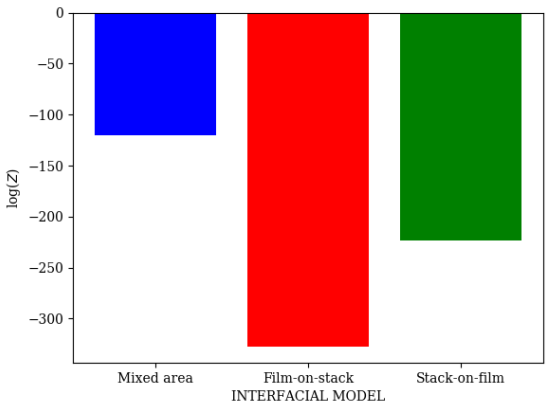

Figure 4-3. The log-evidence (Z) determined for each proposed model for the film coated at 2000 rpm, using the nested sampler available in the dynesty Python package (Speagle, 2020).

In order to quantify our confidence in model selection, Bayesian evidence (*Z*) estimation for a series of plausible model interfacial structures (including the mixed area model) was performed using the nested sampler available in the *dynesty* Python package in combination with *refnx* (Fig. 4-3) (Nelson and Prescott, 2019; Speagle, 2020). It is evident from the plot of log(*Z*) vs interfacial model that the mixed area model is the one most suited to fit these datasets. The mixed area model is further corroborated by the analysis of spin-coated samples prepared offline on ~ 3 cm^2 silicon wafers. Optical microscopy shows a mixed area with islands in the order of ~ 50 - 100 µm diameter and complementary GI-SAXS measurements of those films exhibit lamellar stacks with

both parallel and random orientations (see appendix section 10.3.5). This agrees with NR and synchrotron GI-SAXS measurements on the films that went on to be aged (see later).

The model curve and SLD profile are generated from optimised parameters (Fig. 4-2). Additionally, curves derived from the MCMC sampling procedure that are consistent with the data illustrate the uncertainty associated with the optimised parameters and model fits. Other initial fits are presented in the appendix section 10.3.2.

Spin speed / rpm	Film thickness / nm	Film roughness / nm	No. of parallel lamellar stacks*	Parallel lamellar stack proportion of surface area / %
1000	51.4 ± 0.4	4.6 ± 0.1	11	15
2000	34.5 ± 0.2	2.62 ± 0.05	9	15
4000	23.3 ± 0.2	3.88 ± 0.06	6	12

*Table 4-1. Parameters obtained from initial model fits to NR data from spin-coated samples. *This is the number of repeating lamellar stacks which are oriented parallel to the substrate – only information on the parallel oriented lamellar stacks is available from these specular NR measurements. This number is also the nearest whole number of repeating stacks fitted to due to the MCMC sampling returning the mean number of parallel lamellar stacks consistent with the data.*

The initial proportion of sample area occupied by lamellar stacks oriented parallel to the surface was found to be between 12 and 15 % for the films studied here, the rest of the sample area being the amorphous film (Table. 4-1). This was derived from the scale factors applied to each component of the mixed area model. Note, this does not mean that only 12 to 15 % of the film is self-organised into lamellar stacks. These NR experiments only measured the specular reflected intensity: only reflected neutrons from repeating lamellar stacks that are parallel to the surface are detected. Characterisation of

the same system (with non-deuterated oleic acid) by GI-SAXS revealed a diffuse scattering ring in addition to the specular lamellar stack peak (see Fig. 4-1(b) for an illustration). We are therefore confident that the lamellar stack region of the film is a mixture of both parallel and randomly oriented lamellar stacks. We discuss changes in lamellar stack orientation during simulated ageing in section 4.2.2.

4.4.2 Simulated atmospheric ageing of nanometre-scale films

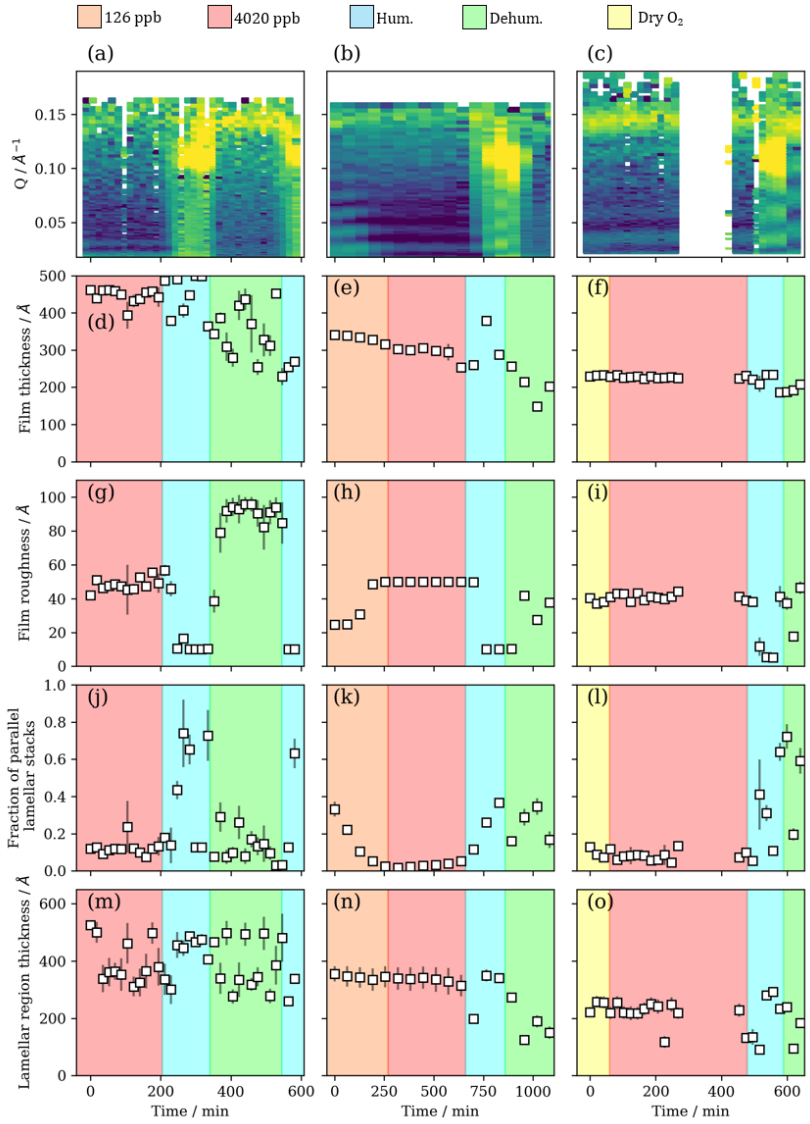

Figure 4-4. Plots of RQ^4 vs Q curves measured during simulated atmospheric ageing of the 3 films studied here: 1000 rpm coating (a), 2000 rpm coating (b) and 4000 rpm coating (c). Optimised parameters from model fits are plotted for each experiment: film thickness (d) – (f), film roughness (g) – (i), fraction of parallel lamellar stacks (j) – (l) and lamellar region thickness (m) – (o). The neutron beam went down for a while during film oxidation of the 4000 rpm coating (c) – parameters generally were unchanged after this period. The coloured regions correspond to ozonolysis at 126 ppb & 4020 ppb, humidification (Hum.), dehumidification (Dehum.) and dry O_2.

We simulated atmospheric ageing by exposing the spin-coated films to ozone (126 – 4020 ppb) and humidity (5 – 90 % RH). Film thickness, roughness and the relative amount (scale factor) of each component can be followed using the NR model fitting procedure.

4.4.2.1 Ozonolysis

Parallel oriented lamellar stacks persist during and after extensive oxidation (see the Bragg peak at ~0.14 $Å^{-1}$ in Fig. 4-4 (a) – (c)). We corroborated this finding with full high and low angle NR measurement on a film after oxidation, showing a Bragg peak (Fig. 10-9, the appendix). The Bragg peak decreased in intensity during ozonolysis (Fig. 4-4(a) – (c)), which is consistent with observations during ozonolysis of micron-scale films of the non-deuterated proxy (Milsom et al., 2021). The implications for the persistence of such surfactant organic material is discussed in section 4.4.3.

A slight decrease in film thickness is observed during the initial stages of ozonolysis, most evident for the film coated at 2000 rpm (Fig. 4-4(g) – (i)). The ozonolysis of oleic acid yields nonanal as one of the primary products. Nonanal is volatile and is assumed to be lost from the film after formation, accounting for the decrease in film thickness (Zahardis and Petrucci, 2007). Generally, the drop in film thickness is small relative to the initial film thickness.

When increasing the ozone concentration, the film thickness remains unchanged for the film coated at 2000 rpm (Fig. 4-4(e)). As ozone exposure continues, non-volatile reaction products are likely to remain in the film. Assuming the small decrease in film thickness is mostly due to the loss of nonanal from the film, the initial ozonolysis reaction is either complete or the formation of inert reaction products hinders further

oleic acid ozonolysis. Note that this would be valid for the amorphous oleic acid film region and not lamellar phase oleic acid region, which is by definition unreacted. High molecular weight products have been observed for the oleic acid-ozone reaction system (Reynolds et al., 2006; Zahardis et al., 2005, 2006b, 2006a). The formation of such crusts has been postulated previously and have implications for the ageing of aerosol particles.(Lee et al., 2012; Pfrang et al., 2011)

A similar trend in thickness is observed for the lamellar phase region during ozonolysis (Fig. 4-4(m) – (o)). This region is modelled as a lipid bilayer, therefore any signal coming from this structure is assumed to be from the oleic acid-sodium oleate bilayer as they are the only molecules in abundance able to form a bilayer. This assumption is valid because if the 9-carbon products from the reaction form bilayers, the associated Bragg peak would appear at a much higher *Q* (shorter *d*-spacing). This has not been observed here nor in SAXS experiments during ozonolysis on the same non-deuterated system (Milsom et al., 2021).

The film roughness increases with exposure to ozone (Fig. 4-4(g) – (i)). This is consistent across all film thicknesses studied here. This implies that the surface area associated with these films also changes with time and that the surface restructures somewhat during ozonolysis. The atmospheric significance of this change in surface roughness is discussed in 4.4.3.

The scale factors applied to the amorphous film and oriented lamellar stacks area change during ozonolysis. They were constrained so that their sum was approximately the original total scale factor before ageing - determined by measuring the critical edge (see Fig. 4-2(a) maximum *R* region at low *Q*). There is an apparent decrease in the

amount of oriented lamellar stacks relative to the amorphous films coated at 2000 and 4000 rpm (Fig. 4-4(k) and (l)), though this effect is less pronounced for the thicker film coated at 1000 rpm (Fig. 4-4(j)). This observation is consistent with the film thickness-dependent decay observed for this system (Milsom et al., 2021). We reiterate that this scale factor is not a measure of how much of the area is covered by lamellar stacks, it only concerns the area covered by parallel oriented lamellar stacks. This is of interest due to the anisotropic diffusion characteristic of such lamellar bilayers (Lindblom and Orädd, 1994), see 4.4.3.

4.4.2.2 Humidification and dehumidification of oxidised and unoxidised films

More changes in surface structure occur when humidifying and dehumidifying the oxidised films. The surface structure changed rapidly with the Bragg peak shifting to a lower *Q* (higher lamellar *d*-spacing) (Fig. 4-4(a) – (c)). This is because the lamellar stacks have taken up water, resulting in a thickening of the lamellar bilayer (Fig. 4-4(m) – (o)). Dehumidification reversed this trend and the Bragg peak moved back to its original position. This movement of the Bragg peak was reversible, suggesting the lamellar stacks can take up water readily and reversibly (Fig. 4-4(a)).

Reorganisation of the film and possible de-wetting from the surface is evidenced by the more scattered nature of the fitted parameters combined with a loss of the critical edge during humidity changes (Fig. 10-9, the appendix). The loss of the critical edge during humidification suggests that in-plane correlations in the surface structure are occurring. This would result in off-specular scattering, decreasing the observed specular NR signal (Dalgliesh, 2002). We carried out an off-specular NR measurement showing evidence of off-specular scattering occurring around the critical edge at high humidity (see the appendix section 10.3.7).

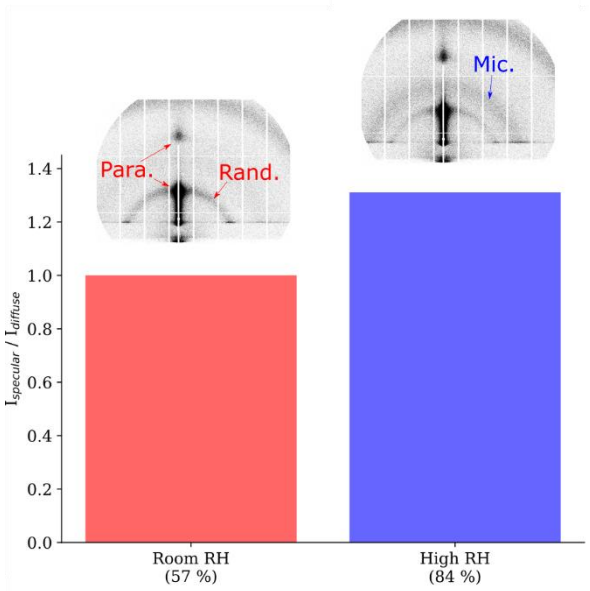

Figure 4-5. A plot of the 1st order lamellar scattering ring specular ($I_{specular}$) and diffuse ($I_{diffuse}$) scattering intensity ratios at 57 and 84 % RH, derived from the corresponding 2-D GI-SAXS patterns presented above the relevant bar. The scattering intensity arising from parallel (Para.) and random (Rand.) lamellar orientations are labelled accordingly in the 57 % RH pattern. The inverse micellar scattering ring (Mic.) present at 84 % RH is also labelled for clarity. The 2-D GI-SAXS patterns are corrected for the incident X-ray intensity and are mapped on the same intensity scale.

GI-SAXS measurements on the non-deuterated and unoxidised form of this proxy at high RH show that an inverse micellar phase forms and exhibits a diffuse scattering peak at a higher Q (~ 0.2 $Å^{-1}$) than what can be distinguishable with these NR measurements. This inverse micellar phase would have different physical properties compared with the lamellar stacks (Tiddy, 1980), adding to the range of factors which change while ageing these organic coatings.

Lamellar stacks reversibly orient themselves parallel to the surface at high RH. This is evidenced by an increase in the proportion of the overall scaling factor arising from the

lamellar stack region and by off-specular NR measurements on an oxidised film at high and low RH (see appendix section 10.3.7). Complementary information was obtained by GI-SAXS experiments on the non-deuterated and non-oxidised form of this proxy. By plotting scattered intensity vs azimuthal angle in the *Q*-range of the first order Bragg peak, a measurement of the degree to which lamellar stacks are either parallel or randomly oriented can be made. This measure is the specular-to-diffuse Bragg peak intensity ratio ($I_{specular}/I_{diffuse}$). The ratio is higher at high RH and the effect is visible in the 2-D GI-SAXS patterns – an increased specular peak intensity and decreased diffuse ring intensity (Fig. 4-5). These observations show that changes in surface structure are possible in both non-oxidised and oxidised films. Note that due to the underlying reflected X-ray signal accompanying the specular Bragg peak, this is not a direct measure of the proportion of parallel and random oriented lamellar stacks.

4.4.3 **Atmospheric implications**

Cooking emissions evolve over time and include fresh and oxidised organic material (including oleic acid) (Zeng et al., 2020) and organic coatings on indoor glass surfaces can contain a mixture of oxidised and non-oxidised compounds (Or et al., 2020). There is a link between fatty acid packing and the key properties of hygroscopicity (Nguyen et al., 2017; Xiong et al., 1998) and reactivity (Garland et al., 2008; Hearn et al., 2005; Rosen et al., 2008; Vieceli et al., 2004). In addition to the effect of lamellar phase formation on reactivity (Milsom et al., 2021), we have shown here that lamellar stacks found in both fresh and oxidised films of our proxy can orient themselves upon humidification. The lamellar phase has directionally dependent diffusion, with diffusion parallel to the bilayer plane orders of magnitude higher than in the perpendicular direction (Lindblom and Orädd, 1994; Lindblom and Wennerström, 1977). This

suggests that lamellar stacks oriented parallel to the surface present an extra steric hindrance to the diffusion of small molecules, such as ozone, through the organic film. Fatty acid packing has been used in the literature to justify the case for a (near) surface reaction between oleic acid and ozone (Hearn et al., 2005). Whether found in organic coatings on indoor surfaces or on aerosol particles, this humidity-dependent change in fatty acid orientation could impact the atmospheric ageing of such films and particles.

The oxidation of organic coatings proceeds rapidly compared to the bulk reaction of the same species as pure particles (Lim et al., 2017). Here, the increase in film roughness observed during oxidation implies that there is an increase in organic surface area. This increase in surface area may facilitate faster uptake of reactive gases such as ozone, though information on reaction kinetics could not be extracted from these NR experiments. Deposited droplets of oleic acid have previously been observed to change morphology during ozone exposure (Hung and Tang, 2010) and floating monolayers of oleic acid-stearic acid can restructure during ozonolysis (Skoda et al., 2017). Such changes in organic film morphology are not currently considered in models of aerosol particle and film reaction kinetics, though changes in film thickness are considered (Shiraiwa et al., 2012). It may therefore be necessary to consider the effect of film morphology on nano-scale films in such kinetic models.

An organic coating consisting of unreacted self-assembled oleic acid and reaction products remains deposited after simulated atmospheric ageing. This is consistent with previous studies on floating monolayers of oleic acid, where surface active products remained at the air-water interface after exposure to ozone (Woden et al., 2021). The residual film is likely to be a mixture of oxidised reaction products (Zahardis and Petrucci, 2007). The lamellar stack Bragg peak also remains, confirming that lamellar

phase oleic acid withstands prolonged exposure to ozone (Milsom et al., 2021) and that this effect is now observed in nanoscale films on a solid surface. If surfactant material persists on particulate matter, the resulting effects on surface tension, water uptake and cloud droplet formation would also be expected to persist (Facchini et al., 1999, 2000; Ovadnevaite et al., 2017).

Viscous organic material in the surface layers of particulate matter has been linked with the increased long-range transport and persistence of harmful compounds found in urban particulate matter, increasing the risk to human health (Mu et al., 2018; Shrivastava et al., 2017). This protection is due to the reduced diffusivity of atmospheric oxidants such as ozone, limiting the extent of particle ageing. Together with our previously determined effect of self-assembly on reactivity in μm films (Milsom et al., 2021), the presence of unreacted semi-solid material (lamellar oleic acid) at the end of simulated ageing suggests that this effect is also valid on nanoscale films. Oleic acid ozonolysis can result in the formation of high-molecular-weight compounds (Reynolds et al., 2006; Zahardis et al., 2006a). The product film that remains after ageing may contain these oligomers, resulting in a more viscous film. An increase in viscosity has been observed experimentally for this reaction system and has been linked with the formation of such oligomers (Hosny et al., 2016).

4.5 **Conclusions**

This study has shown that surface coatings of a semi-solid organic aerosol proxy can undergo changes in morphology during simulated atmospheric ageing. These changes are expected to affect the uptake of trace gases into the condensed phase, especially on the nanoscale due to the increase in surface area-to-volume ratio implied by a film of

increasing roughness. We highlight the importance of considering film morphology in model and experimental studies on nanoscale films.

Lamellar stacks formed by the fatty acid reversibly oriented themselves parallel to the surface with increasing humidity, suggesting that the diffusion of small molecules through the coating could be humidity-dependent due to the anisotropic diffusivity of molecules in lamellar bilayers. This was the case in both oxidised and non-oxidised films.

The lamellar stacks persisted after simulated atmospheric ageing. This is consistent with previous findings on μm-scale films. Additionally, an amorphous film which likely consists of oxidation products also remains – consistent with floating monolayer experiments on this system. We are now confident that the persistence of the semi-solid lamellar phase is valid over the micro-to-nanoscale and that oxidation products persist down to the monolayer scale.

A technique such as NR does not require the sample to be self-assembled. Future experiments on more complex proxies and real atmospheric material deposited on solid surfaces are possible, as long as suitable coatings can be made and challenges associated with non-deuterated samples are overcome – *i.e.* measuring samples for a longer time.

4.6 Acknowledgements

AM acknowledges funding by the NERC SCENARIO DTP (NE/L002566/1) and support from the NERC CENTA DTP. Eleonore Mason (University of Bath) and Nick Terrill (Diamond Light Source) are thanked for inviting AM, CP and AS to the GI-SAXS beamtime at the Diamond Light Source. Jacob Boswell (University of Bath) is acknowledged for helping out at the ISIS beamtime and Ben Woden is acknowledged

for helping to calibrate the ozonisers. We acknowledge the Research England funded TALENT: Technician Led Equipment Fund for enabling the offline GI-SAXS measurements. Steven Huband (University of Warwick) is acknowledged for carrying out these offline GI-SAXS measurements. Experiments at the ISIS Pulsed Neutron and Muon Source were supported by a beamtime allocation from the Science and Technology Facilities Council. This work was carried out with the support of the Diamond Light Source (DLS), instrument I22 (proposal NT23096). The computations described in this paper were performed using the University of Birmingham's BlueBEAR HPC service, which provides a High Performance Computing service to the University's research community.

4.6.1 **Contributors**

Adam Milsom prepared samples, was present at and carried out experiments and wrote the manuscript. Christian Pfrang and Adam M. Squires carried out beamline experiments and contributed to data analysis and interpretation. Maximilian W. A. Skoda contributed to data analysis and interpretation, setup and carried out NR experiments on the INTER beamline at ISIS. Eleonore Mason invited Adam Milsom, Christian Pfrang and Adam M. Squires to her GI-SAXS beamtime on I22 at the Diamond Light Source (DLS), setup and carried out humidity-GI-SAXS measurements. Nick J. Terrill was the beamline scientist responsible for setting up GI-SAXS experiments at DLS and provided expertise. Steven Huband was the technician who carried out the offline GI-SAXS measurements on spin-coated films at the University of Warwick. Jacob Boswell helped out at the NR beamtime. Ben Woden helped to calibrate the ozonisers.

4.7 Comment

Differing from the μm-scale coatings studied in chapter 2 and 5, this study focusses on the surface structural changes which occur when exposing this proxy to simulated atmospheric processing (humidity and ozonolysis). These films returned NR curves with clear fringes and Bragg features which enabled a mixed area model to be fitted to these data – the model being corroborated by Bayesian inference.

The reproducibility of the results was particularly encouraging and gives confidence in the statements made in the discussion. NR still, though, requires some complementary analysis – such as GI-SAXS – to support these results. The persistence of the Bragg peak after simulated atmospheric processing is also consistent with studies presented in chapter 2 and 7, contributing to the idea that self-assembly significantly reduces the reactivity of this proxy.

The results from this study are qualitative and will motivate more quantitative future measurements on similar systems. It also presents the possibility of coating such surfaces with real organic aerosol material, though these measurements would require longer exposure to the neutrons to return acceptable NR curves due to the lack of deuterated material. This is the subject of future work.

4.8 References

Boucher, O., Randall, D., Artaxo, P., Bretherton, C., Feingold, G., Forster, P., Kerminen, V.-M., Kondo, Y., Liao, H., Lohmann, U., Rasch, P., Satheesh, S. K., Sherwood, S., Stevens, B. and Zhang, X. Y.: Clouds and Aerosols, in Climate Change 2013 - The Physical Science Basis, edited by Intergovernmental Panel on Climate Change, pp. 571–658, Cambridge University Press, Cambridge., 2013.

Dalgliesh, R.: Application of off-specular scattering of X-rays and neutrons to the study of soft matter, Curr. Opin. Colloid Interface Sci., 7(3–4), 244–248, doi:10.1016/S1359-0294(02)00054-7, 2002.

Facchini, M. C., Mircea, M., Fuzzi, S. and Charlson, R. J.: Cloud albedo enhancement by surface-active organic solutes in growing droplets, Nature, 401(6750), 257–259, doi:10.1038/45758, 1999.

Facchini, M. C., Decesari, S., Mircea, M., Fuzzi, S. and Loglio, G.: Surface tension of atmospheric wet aerosol and cloud/fog droplets in relation to their organic carbon content and chemical composition, Atmos. Environ., 34(28), 4853–4857, doi:10.1016/S1352-2310(00)00237-5, 2000.

Foreman-Mackey, D., Hogg, D. W., Lang, D. and Goodman, J.: emcee : The MCMC Hammer , Publ. Astron. Soc. Pacific, 125(925), 306–312, doi:10.1086/670067, 2013.

Fu, P., Kawamura, K., Okuzawa, K., Aggarwal, S. G., Wang, G., Kanaya, Y. and Wang, Z.: Organic molecular compositions and temporal variations of summertime mountain aerosols over Mt. Tai, North China Plain, J. Geophys. Res. Atmos., 113(19), 1–20, doi:10.1029/2008JD009900, 2008.

Gallimore, P. J., Griffiths, P. T., Pope, F. D., Reid, J. P. and Kalberer, M.: Comprehensive modeling study of ozonolysis of oleic acid aerosol based on real-time, online measurements of aerosol composition, J. Geophys. Res., 122(8), 4364–4377, doi:10.1002/2016JD026221, 2017.

Garland, E. R., Rosen, E. P., Clarke, L. I. and Baer, T.: Structure of submonolayer oleic acid coverages on inorganic aerosol particles: Evidence of island formation, Phys. Chem. Chem. Phys., 10(21), 3156–3161, doi:10.1039/b718013f, 2008.

Hearn, J. D., Smith, G. D. and Lovett, A. J.: Ozonolysis of oleic acid particles: evidence for a surface reaction and secondary reactions involving Criegee intermediates, Phys. Chem. Chem. Phys., 7(3), 501–511, doi:10.1039/b414472d, 2005.

Hosny, N. A., Fitzgerald, C., Vyšniauskas, A., Athanasiadis, A., Berkemeier, T., Uygur, N., Pöschl, U., Shiraiwa, M., Kalberer, M., Pope, F. D. and Kuimova, M. K.: Direct imaging of changes in aerosol particle viscosity upon hydration and chemical aging, Chem. Sci., 7(2), 1357–1367, doi:10.1039/c5sc02959g, 2016.

Hung, H. and Tang, C.: Effects of Temperature and Physical State on Heterogeneous Oxidation of Oleic Acid Droplets with Ozone, J. Phys. Chem. A, 114, 13104–13112, doi:10.1021/jp105042w, 2010.

Jimenez, J. L., Canagaratna, M. R., Donahue, N. M., Prevot, A. S. H., Zhang, Q., Kroll, J. H., DeCarlo, P. F., Allan, J. D., Coe, H., Ng, N. L., Aiken, A. C., Docherty, K. S., Ulbrich, I. M., Grieshop, A. P., Robinson, A. L., Duplissy, J., Smith, J. D., Wilson, K. R., Lanz, V. A., Hueglin, C., Sun, Y. L., Tian, J., Laaksonen, A., Raatikainen, T., Rautiainen, J., Vaattovaara, P., Ehn, M., Kulmala, M., Tomlinson, J. M., Collins, D. R., Cubison, M. J., Dunlea, J., Huffman, J. A., Onasch, T. B., Alfarra, M. R., Williams, P. I., Bower, K., Kondo, Y., Schneider, J., Drewnick, F., Borrmann, S., Weimer, S., Demerjian, K., Salcedo, D., Cottrell, L., Griffin, R., Takami, A., Miyoshi, T., Hatakeyama, S., Shimono, A., Sun, J. Y., Zhang, Y. M., Dzepina, K., Kimmel, J. R., Sueper, D., Jayne, J. T., Herndon, S. C., Trimborn, A. M., Williams, L. R., Wood, E. C., Middlebrook, A. M., Kolb, C. E., Baltensperger, U. and Worsnop, D. R.: Evolution of Organic Aerosols in the Atmosphere, Science, 326(5959), 1525–1529, doi:10.1126/science.1180353, 2009.

Jones, S. H., King, M. D., Ward, A. D., Rennie, A. R., Jones, A. C. and Arnold, T.: Are organic films from atmospheric aerosol and sea water inert to oxidation by ozone at the air-water interface?, Atmos. Environ., 161, 274–287, doi:10.1016/j.atmosenv.2017.04.025, 2017.

Katrib, Y., Biskos, G., Buseck, P. R., Davidovits, P., Jayne, J. T., Mochida, M., Wise, M. E., Worsnop, D. R. and Martin, S. T.: Ozonolysis of mixed oleic-acid/stearic-acid particles: Reaction kinetics and chemical morphology, J. Phys. Chem. A, 109(48), 10910–10919, doi:10.1021/jp054714d, 2005.

King, M. D., Rennie, A. R., Thompson, K. C., Fisher, F. N., Dong, C. C., Thomas, R. K., Pfrang, C. and Hughes, A. V.: Oxidation of oleic acid at the air-water interface and its potential effects on cloud critical supersaturations, Phys. Chem. Chem. Phys., 11(35), 7699–7707, doi:10.1039/b906517b, 2009.

King, M. D., Rennie, A. R., Pfrang, C., Hughes, A. V. and Thompson, K. C.: Interaction of nitrogen dioxide (NO2) with a monolayer of oleic acid at the air-water interface - A simple proxy for atmospheric aerosol, Atmos. Environ., 44(14), 1822–1825, doi:10.1016/j.atmosenv.2010.01.031, 2010.

King, M. D., Jones, S. H., Lucas, C. O. M., Thompson, K. C., Rennie, A. R., Ward, A. D., Marks, A. A., Fisher, F. N., Pfrang, C., Hughes, A. V. and Campbell, R. A.: The reaction of oleic acid monolayers with gas-phase ozone at the air water interface: The effect of sub-phase viscosity, and inert secondary components, Phys. Chem. Chem. Phys., 22(48), 28032–28044, doi:10.1039/d0cp03934a, 2020.

Lakey, P. S. J., Wisthaler, A., Berkemeier, T., Mikoviny, T., Pöschl, U. and Shiraiwa, M.: Chemical kinetics of multiphase reactions between ozone and human skin lipids:

Implications for indoor air quality and health effects, Indoor Air, 27(4), 816–828, doi:10.1111/ina.12360, 2017.

Lee, J. W. L., Carrascón, V., Gallimore, P. J., Fuller, S. J., Björkegren, A., Spring, D. R., Pope, F. D. and Kalberer, M.: The effect of humidity on the ozonolysis of unsaturated compounds in aerosol particles, Phys. Chem. Chem. Phys., 14(22), 8023–8031, doi:10.1039/c2cp24094g, 2012.

Li, G., Su, H., Ma, N., Tao, J., Kuang, Y., Wang, Q., Hong, J., Zhang, Y., Kuhn, U., Zhang, S., Pan, X., Lu, N., Tang, M., Zheng, G., Wang, Z., Gao, Y., Cheng, P., Xu, W., Zhou, G., Zhao, C., Yuan, B., Shao, M., Ding, A., Zhang, Q., Fu, P., Sun, Y., Pöschl, U. and Cheng, Y.: Multiphase chemistry experiment in Fogs and Aerosols in the North China Plain (McFAN): integrated analysis and intensive winter campaign 2018, Faraday Discuss., 226, 207-222, doi:10.1039/D0FD00099J, 2021.

Lim, C. Y., Browne, E. C., Sugrue, R. A. and Kroll, J. H.: Rapid heterogeneous oxidation of organic coatings on submicron aerosols, Geophys. Res. Lett., 44(6), 2949–2957, doi:10.1002/2017GL072585, 2017.

Lindblom, G. and Orädd, G.: NMR Studies of translational diffusion in lyotropic liquid crystals and lipid membranes, Prog. Nucl. Magn. Reson. Spectrosc., 26, 483–515, doi:10.1016/0079-6565(94)80014-6, 1994.

Lindblom, G. and Wennerström, H.: Amphiphile diffusion in model membrane systems studied by pulsed NMR, Biophys. Chem., 6(2), 167–171, doi:10.1016/0301-4622(77)87006-3, 1977.

Mauersberger, K., Barnes, J., Hanson, D. and Morton, J.: Measurement of the ozone absorption cross-section at the 253.7 nm mercury line, Geophys. Res. Lett., 13(7), 671–

673, doi:10.1029/GL013i007p00671, 1986.

McCluskey, A. R., Cooper, J. F. K., Arnold, T. and Snow, T.: A general approach to maximise information density in neutron reflectometry analysis, Mach. Learn. Sci. Technol., 1(3), 035002, doi:10.1088/2632-2153/ab94c4, 2020.

Mele, S., Söderman, O., Ljusberg-Wahrén, H., Thuresson, K., Monduzzi, M. and Nylander, T.: Phase behavior in the biologically important oleic acid/sodium oleate/water system, Chem. Phys. Lipids, 211(September 2017), 30–36, doi:10.1016/j.chemphyslip.2017.11.017, 2018.

Mikhailov, E. F., Mironov, G. N., Pöhlker, C., Chi, X., Krüger, M. L., Shiraiwa, M., Förster, J. D., Pöschl, U., Vlasenko, S. S., Ryshkevich, T. I., Weigand, M., Kilcoyne, A. L. D. and Andreae, M. O.: Chemical composition, microstructure, and hygroscopic properties of aerosol particles at the Zotino Tall Tower Observatory (ZOTTO), Siberia, during a summer campaign, Atmos. Chem. Phys., 15(15), 8847–8869, doi:10.5194/acp-15-8847-2015, 2015.

Milsom, A., Squires, A. M., Woden, B., Terrill, N. J., Ward, A. D. and Pfrang, C.: The persistence of a proxy for cooking emissions in megacities: a kinetic study of the ozonolysis of self-assembled films by simultaneous small and wide angle X-ray scattering (SAXS/WAXS) and Raman microscopy, Faraday Discuss., 226, 364–381, doi:10.1039/D0FD00088D, 2021.

Mu, Q., Shiraiwa, M., Octaviani, M., Ma, N., Ding, A., Su, H., Lammel, G., Pöschl, U. and Cheng, Y.: Temperature effect on phase state and reactivity controls atmospheric multiphase chemistry and transport of PAHs, Sci. Adv., 4(3), eaap7314, doi:10.1126/sciadv.aap7314, 2018.

Narayanan, T. and Konovalov, O.: Synchrotron Scattering Methods for Nanomaterials and Soft Matter Research, Materials, 13(3), 752, doi:10.3390/ma13030752, 2020.

Nelson, A. R. J. and Prescott, S. W.: Refnx: Neutron and X-ray reflectometry analysis in python, J. Appl. Crystallogr., 52, 193–200, doi:10.1107/S1600576718017296, 2019.

Nguyen, Q. T., Kjær, K. H., Kling, K. I., Boesen, T. and Bilde, M.: Impact of fatty acid coating on the CCN activity of sea salt particles, Tellus, Ser. B Chem. Phys. Meteorol., 69(1), 1–15, doi:10.1080/16000889.2017.1304064, 2017.

Or, V. W., Wade, M., Patel, S., Alves, M. R., Kim, D., Schwab, S., Przelomski, H., O'Brien, R., Rim, D., Corsi, R. L., Vance, M. E., Farmer, D. K. and Grassian, V. H.: Glass surface evolution following gas adsorption and particle deposition from indoor cooking events as probed by microspectroscopic analysis, Environ. Sci. Process. Impacts, 22(8), 1698–1709, doi:10.1039/d0em00156b, 2020.

Ots, R., Vieno, M., Allan, J. D., Reis, S., Nemitz, E., Young, D. E., Coe, H., Di Marco, C., Detournay, A., Mackenzie, I. A., Green, D. C. and Heal, M. R.: Model simulations of cooking organic aerosol (COA) over the UK using estimates of emissions based on measurements at two sites in London, Atmos. Chem. Phys., 16(21), 13773–13789, doi:10.5194/acp-16-13773-2016, 2016.

Ovadnevaite, J., Zuend, A., Laaksonen, A., Sanchez, K. J., Roberts, G., Ceburnis, D., Decesari, S., Rinaldi, M., Hodas, N., Facchini, M. C., Seinfeld, J. H. and O'Dowd, C.: Surface tension prevails over solute effect in organic-influenced cloud droplet activation, Nature, 546(7660), 637–641, doi:10.1038/nature22806, 2017.

Patel, S., Sankhyan, S., Boedicker, E. K., Decarlo, P. F., Farmer, D. K., Goldstein, A. H., Katz, E. F., Nazaroff, W. W., Tian, Y., Vanhanen, J. and Vance, M. E.: Indoor

Particulate Matter during HOMEChem: Concentrations, Size Distributions, and Exposures, Environ. Sci. Technol., 54(12), 7107–7116, doi:10.1021/acs.est.0c00740, 2020.

Penfold, J. and Thomas, R. K.: The application of the specular reflection of neutrons to the study of surfaces and interfaces, J. Phys. Condens. Matter, 2(6), 1369–1412, doi:10.1088/0953-8984/2/6/001, 1990.

Pfrang, C., Shiraiwa, M. and Pöschl, U.: Chemical ageing and transformation of diffusivity in semi-solid multi-component organic aerosol particles, Atmos. Chem. Phys., 11(14), 7343–7354, doi:10.5194/acp-11-7343-2011, 2011.

Pfrang, C., Sebastiani, F., Lucas, C. O. M., King, M. D., Hoare, I. D., Chang, D. and Campbell, R. A.: Ozonolysis of methyl oleate monolayers at the air-water interface: Oxidation kinetics, reaction products and atmospheric implications, Phys. Chem. Chem. Phys., 16(26), 13220–13228, doi:10.1039/c4cp00775a, 2014.

Pfrang, C., Rastogi, K., Cabrera-Martinez, E. R., Seddon, A. M., Dicko, C., Labrador, A., Plivelic, T. S., Cowieson, N. and Squires, A. M.: Complex three-dimensional self-assembly in proxies for atmospheric aerosols, Nat. Commun., 8(1), 1724, doi:10.1038/s41467-017-01918-1, 2017.

Pöschl, U.: Atmospheric aerosols: Composition, transformation, climate and health effects, Angew. Chemie Int. Ed., 44(46), 7520–7540, doi:10.1002/anie.200501122, 2005.

Reid, J. P., Bertram, A. K., Topping, D. O., Laskin, A., Martin, S. T., Petters, M. D., Pope, F. D. and Rovelli, G.: The viscosity of atmospherically relevant organic particles, Nat. Commun., 9(1), 1–14, doi:10.1038/s41467-018-03027-z, 2018.

Reynolds, J. C., Last, D. J., McGillen, M., Nijs, A., Horn, A. B., Percival, C., Carpenter, L. J. and Lewis, A. C.: Structural analysis of oligomeric molecules formed from the reaction products of oleic acid ozonolysis, Environ. Sci. Technol., 40(21), 6674–6681, doi:10.1021/es060942p, 2006.

Richardson, S. J., Staniec, P. A., Newby, G. E., Rawle, J. L., Slaughter, A. R., Terrill, N. J., Elliott, J. M. and Squires, A. M.: Glycerol prevents dehydration in lipid cubic phases, Chem. Commun., 51, 11386–11389, doi:10.1039/c5cc03771a, 2015.

Rosen, E. P., Garland, E. R. and Baer, T.: Ozonolysis of oleic acid adsorbed to polar and nonpolar aerosol particles, J. Phys. Chem. A, 112(41), 10315–10324, doi:10.1021/jp8045802, 2008.

Schwartz-Narbonne, H. and Donaldson, D. J.: Water uptake by indoor surface films, Sci. Rep., 9(1), 11089, doi:10.1038/s41598-019-47590-x, 2019.

Sebastiani, F., Campbell, R. A., Rastogi, K. and Pfrang, C.: Nighttime oxidation of surfactants at the air-water interface: Effects of chain length, head group and saturation, Atmos. Chem. Phys., 18(5), 3249–3268, doi:10.5194/acp-18-3249-2018, 2018.

Shiraiwa, M., Pfrang, C. and Pöschl, U.: Kinetic multi-layer model of aerosol surface and bulk chemistry (KM-SUB): The influence of interfacial transport and bulk diffusion on the oxidation of oleic acid by ozone, Atmos. Chem. Phys., 10, 3673–3691, doi:10.5194/acp-10-3673-2010, 2010.

Shiraiwa, M., Ammann, M., Koop, T. and Pöschl, U.: Gas uptake and chemical aging of semisolid organic aerosol particles -Supporting information, Proc. Natl. Acad. Sci. U. S. A., 108(27), 11003–11008, doi:10.1073/pnas.1103045108, 2011.

Shiraiwa, M., Pfrang, C., Koop, T. and Pöschl, U.: Kinetic multi-layer model of gas-particle interactions in aerosols and clouds (KM-GAP): Linking condensation, evaporation and chemical reactions of organics, oxidants and water, Atmos. Chem. Phys., 12(5), 2777–2794, doi:10.5194/acp-12-2777-2012, 2012.

Shrivastava, M., Lou, S., Zelenyuk, A., Easter, R. C., Corley, R. A., Thrall, B. D., Rasch, P. J., Fast, J. D., Simonich, S. L. M., Shen, H. and Tao, S.: Global long-range transport and lung cancer risk from polycyclic aromatic hydrocarbons shielded by coatings of organic aerosol, Proc. Natl. Acad. Sci. U. S. A., 114(6), 1246–1251, doi:10.1073/pnas.1618475114, 2017.

Skilling, J.: Nested Sampling, , 395(November 2004), 395–405, doi:10.1063/1.1835238, 2004.

Skilling, J.: Nested sampling for general Bayesian computation, Bayesian Anal., 1(4), 833–860, doi:10.1214/06-BA127, 2006.

Skoda, M. W. A., Thomas, B., Hagreen, M., Sebastiani, F. and Pfrang, C.: Simultaneous neutron reflectometry and infrared reflection absorption spectroscopy (IRRAS) study of mixed monolayer reactions at the air-water interface, RSC Adv., 7(54), 34208–34214, doi:10.1039/c7ra04900e, 2017.

Slade, J. H., Ault, A. P., Bui, A. T., Ditto, J. C., Lei, Z., Bondy, A. L., Olson, N. E., Cook, R. D., Desrochers, S. J., Harvey, R. M., Erickson, M. H., Wallace, H. W., Alvarez, S. L., Flynn, J. H., Boor, B. E., Petrucci, G. A., Gentner, D. R., Griffin, R. J. and Shepson, P. B.: Bouncier Particles at Night: Biogenic Secondary Organic Aerosol Chemistry and Sulfate Drive Diel Variations in the Aerosol Phase in a Mixed Forest, Environ. Sci. Technol., 53(9), 4977–4987, doi:10.1021/acs.est.8b07319, 2019.

Speagle, J. S.: DYNESTY: a dynamic nested sampling package for estimating Bayesian posteriors and evidences, Mon. Not. R. Astron. Soc., 493(3), 3132–3158, doi:10.1093/MNRAS/STAA278, 2020.

Tervahattu, H.: Identification of an organic coating on marine aerosol particles by TOF-SIMS, J. Geophys. Res., 107(D16), 4319, doi:10.1029/2001JD001403, 2002.

Tiddy, G. J. T.: Surfactant-water liquid crystal phases, Phys. Rep., 57(1), 1–46, doi:10.1016/0370-1573(80)90041-1, 1980.

Vicente, A. M. P., Rocha, S., Duarte, M., Moreira, R., Nunes, T. and Alves, C. A.: Fingerprinting and emission rates of particulate organic compounds from typical restaurants in Portugal, Sci. Total Environ., 778, 146090, doi:10.1016/j.scitotenv.2021.146090, 2021a.

Vicente, E. D., Evtyugina, M., Vicente, A. M., Calvo, A. I., Oduber, F., Blanco-Alegre, C., Castro, A., Fraile, R., Nunes, T., Lucarelli, F., Calzolai, G. and Alves, C. A.: Impact of ironing on indoor particle levels and composition, Build. Environ., 192, doi:10.1016/j.buildenv.2021.107636, 2021b.

Vieceli, J., Ma, O. L. and Tobias, D. J.: Uptake and collision dynamics of gas phase ozone at unsaturated organic interfaces, J. Phys. Chem. A, 108(27), 5806–5814, doi:10.1021/jp0494584, 2004.

Virtanen, P., Gommers, R., Oliphant, T. E., Haberland, M., Reddy, T., Cournapeau, D., Burovski, E., Peterson, P., Weckesser, W., Bright, J., van der Walt, S. J., Brett, M., Wilson, J., Millman, K. J., Mayorov, N., Nelson, A. R. J., Jones, E., Kern, R., Larson, E., Carey, C. J., Polat, İ., Feng, Y., Moore, E. W., VanderPlas, J., Laxalde, D., Perktold, J., Cimrman, R., Henriksen, I., Quintero, E. A., Harris, C. R., Archibald, A. M., Ribeiro,

A. H., Pedregosa, F., van Mulbregt, P., Vijaykumar, A., Bardelli, A. Pietro, Rothberg, A., Hilboll, A., Kloeckner, A., Scopatz, A., Lee, A., Rokem, A., Woods, C. N., Fulton, C., Masson, C., Häggström, C., Fitzgerald, C., Nicholson, D. A., Hagen, D. R., Pasechnik, D. V., Olivetti, E., Martin, E., Wieser, E., Silva, F., Lenders, F., Wilhelm, F., Young, G., Price, G. A., Ingold, G. L., Allen, G. E., Lee, G. R., Audren, H., Probst, I., Dietrich, J. P., Silterra, J., Webber, J. T., Slavič, J., Nothman, J., Buchner, J., Kulick, J., Schönberger, J. L., de Miranda Cardoso, J. V., Reimer, J., Harrington, J., Rodríguez, J. L. C., Nunez-Iglesias, J., Kuczynski, J., Tritz, K., Thoma, M., Newville, M., Kümmerer, M., Bolingbroke, M., Tartre, M., Pak, M., Smith, N. J., Nowaczyk, N., Shebanov, N., Pavlyk, O., Brodtkorb, P. A., Lee, P., McGibbon, R. T., Feldbauer, R., Lewis, S., Tygier, S., Sievert, S., Vigna, S., Peterson, S., More, S., Pudlik, T., et al.: SciPy 1.0: fundamental algorithms for scientific computing in Python, Nat. Methods, 17(3), 261–272, doi:10.1038/s41592-019-0686-2, 2020.

Wang, Q., He, X., Zhou, M., Huang, D. D., Qiao, L., Zhu, S., Ma, Y. G., Wang, H. L., Li, L., Huang, C., Huang, X. H. H., Xu, W., Worsnop, D., Goldstein, A. H., Guo, H., Yu, J. Z., Huang, C. and Yu, J. Z.: Hourly Measurements of Organic Molecular Markers in Urban Shanghai, China: Primary Organic Aerosol Source Identification and Observation of Cooking Aerosol Aging, ACS Earth Sp. Chem., 4(9), 1670–1685, doi:10.1021/acsearthspacechem.0c00205, 2020a.

Wang, T.-F., Kasting, G. B. and Nitsche, J. M.: A Multiphase Microscopic Diffusion Model for Stratum Corneum permeability. I. Formulation, Solution, and Illustrative Results for Representative Compounds, J. Pharm. Sci., 95(3), 620–648, doi:10.1002/jps.20509, 2006.

Wang, T., Kasting, G. B. and Nitsche, J. M.: A multiphase microscopic diffusion model for stratum corneum permeability. II. estimation of physicochemical parameters, and application to a large permeability database, J. Pharm. Sci., 96(11), 3024–3051, doi:10.1002/jps.20883, 2007.

Wang, T., Huang, R. J., Li, Y., Chen, Q., Chen, Y., Yang, L., Guo, J., Ni, H., Hoffmann, T., Wang, X. and Mai, B.: One-year characterization of organic aerosol markers in urban Beijing: Seasonal variation and spatiotemporal comparison, Sci. Total Environ., 743, 140689, doi:10.1016/j.scitotenv.2020.140689, 2020b.

Woden, B., Skoda, M., Hagreen, M. and Pfrang, C.: Night-Time Oxidation of a Monolayer Model for the Air–Water Interface of Marine Aerosols—A Study by Simultaneous Neutron Reflectometry and in Situ Infra-Red Reflection Absorption Spectroscopy (IRRAS), Atmosphere, 9(12), 471, doi:10.3390/atmos9120471, 2018.

Woden, B., Skoda, M. W. A., Milsom, A., Gubb, C., Maestro, A., Tellam, J. and Pfrang, C.: Ozonolysis of fatty acid monolayers at the air–water interface: organic films may persist at the surface of atmospheric aerosols, Atmos. Chem. Phys., 21(2), 1325–1340, doi:10.5194/acp-21-1325-2021, 2021.

Xiong, J. Q., Zhong, M., Fang, C., Chen, L. C. and Lippmann, M.: Influence of organic films on the hygroscopicity of ultrafine sulfuric acid aerosol, Environ. Sci. Technol., 32(22), 3536–3541, doi:10.1021/es980019q, 1998.

Zahardis, J. and Petrucci, G. A.: The oleic acid-ozone heterogeneous reaction system: Products, kinetics, secondary chemistry, and atmospheric implications of a model system - A review, Atmos. Chem. Phys., 7(5), 1237–1274, doi:10.5194/acp-7-1237-2007, 2007.

Zahardis, J., LaFranchi, B. W. and Petrucci, G. A.: Photoelectron resonance capture ionization-aerosol mass spectrometry of the ozonolysis products of oleic acid particles: Direct measure of higher molecular weight oxygenates, J. Geophys. Res. D Atmos., 110(8), 1–10, doi:10.1029/2004JD005336, 2005.

Zahardis, J., LaFranchi, B. W. and Petrucci, G. A.: Direct observation of polymerization in the oleic acid-ozone heterogeneous reaction system by photoelectron resonance capture ionization aerosol mass spectrometry, Atmos. Environ., 40(9), 1661–1670, doi:10.1016/j.atmosenv.2005.10.065, 2006a.

Zahardis, J., LaFranchi, B. W. and Petrucci, G. A.: Photoelectron resonance capture ionization mass spectrometry of fatty acids in olive oil, Eur. J. Lipid Sci. Technol., 108(11), 925–935, doi:10.1002/ejlt.200600143, 2006b.

Zeng, J., Yu, Z., Mekic, M., Liu, J., Li, S., Loisel, G., Gao, W., Gandolfo, A., Zhou, Z., Wang, X., Herrmann, H., Gligorovski, S. and Li, X.: Evolution of Indoor Cooking Emissions Captured by Using Secondary Electrospray Ionization High-Resolution Mass Spectrometry, Environ. Sci. Technol. Lett., 7(2), 76–81, doi:10.1021/acs.estlett.0c00044, 2020.

Zhao, X., Hu, Q., Wang, X., Ding, X., He, Q., Zhang, Z., Shen, R., Lü, S., Liu, T., Fu, X. and Chen, L.: Composition profiles of organic aerosols from Chinese residential cooking: Case study in urban Guangzhou, south China, J. Atmos. Chem., 72(1), 1–18, doi:10.1007/s10874-015-9298-0, 2015.

Zhao, Y., Huang, H., Zhang, Y., Wu, K., Zeng, F., Wang, J., Yu, X., Zhu, Z., Yu, X.-Y. and Wang, F.: Atmospheric particulate characterization by ToF-SIMS in an urban site in Beijing, Atmos. Environ., 220, 117090, doi:10.1016/j.atmosenv.2019.117090, 2020.

5 CHAPTER 5: THE HYGROSCOPICITY AND REACTIVITY OF FATTY ACID ATMOSPHERIC AEROSOL PROXIES IS AFFECTED BY NANOSTRUCTURE

This study is prepared for submission to a journal.

5.1 **Abstract**

Atmospheric aerosol hygroscopicity and reactivity play a significant role in determining its fate and is affected by aerosol composition and physical properties. Fatty acids are surfactants and are found in organic aerosol emissions. As surfactants they are able to form a range of nanostructures, each of which are formed dependent on water content and mixture composition. In this study we follow nano-structural changes in mixtures of oleic acid, sodium oleate and fructose (another organic aerosol emission) during humidity change and ozone exposure. Addition of fructose altered the nanostructure by acting as a kosmotrope (water-structure-former) and inducing molecular arrangements with increased surfactant-water interface curvature. The hygroscopicity of each nanostructure was derived from time- and humidity-resolved changes in nano-structural parameters, measured by Small-Angle X-ray Scattering (SAXS). We found that hygroscopicity is linked to nanostructure and is dependent on the geometry of the nanostructure. Reaction with ozone, a common atmospheric oxidant, revealed a nanostructure-reactivity trend, with notable differences between nanostructures. Simultaneous Raman spectroscopy complements the SAXS experiment and revealed a persistent signal for oleic acid after extensive oxidation. Our findings suggest that self-assembled fatty acid nanostructures can significantly impact two key atmospheric aerosol processes: water uptake and chemical reactivity, implying that the atmospheric lifetime of these materials would also be affected. This could have impacts on the climate (e.g. cloud formation) and on air urban quality (e.g. protection of harmful urban emissions and their long-range transport).

5.2 **Introduction**

Atmospheric aerosols represent a large uncertainty when considering their impact on the climate (Boucher et al., 2013; Shrivastava et al., 2017b) and urban particulate matter makes a significant contribution to air pollution, affecting air quality and health (Chan and Yao, 2008; Harrison, 2020; Pöschl, 2005; Shrivastava et al., 2017b). Organic matter can account for a large portion of aerosol emissions depending on the emission source (Jimenez et al., 2009) and, recently, environmental conditions have been shown to affect aerosol composition (Li et al., 2021). There are both anthropogenic and biogenic sources of organic aerosols. Activities such as cooking emit a range of organic compounds which can go on to form secondary organic aerosol (SOA) (Zeng et al., 2020) and cooking emissions have been estimated to add *ca*. 10 % to UK $PM_{2.5}$ emissions (Ots et al., 2016).

Oleic acid is a fatty acid and a common organic compound found in both cooking (Alves et al., 2020; Vicente et al., 2018; Zeng et al., 2020) and marine emissions (Fu et al., 2013). It is reactive towards common atmospheric oxidants such as ozone and NO_3, making it a model compound for laboratory studies into aerosol properties (Gallimore et al., 2017; King et al., 2010; Pfrang et al., 2017; Shiraiwa et al., 2010; Zahardis and Petrucci, 2007). Other common organic emissions are saccharides (sugars), which are also found in urban (Wang et al., 2006) and biogenic emissions (Fu et al., 2008, 2013; Kirpes et al., 2019). Sugar emissions such as levoglucosan and glucose have been shown to react readily with Criegee intermediates, which are formed during ozonolysis (Enami et al., 2017). The fact that these two common classes of organic compounds (fatty acids and sugars) are found in the same aerosol samples raises the possibility that they are able to interact; for example by a sugar reacting with oleic acid ozonolysis

Criegee intermediates, potentially altering the product distribution and adding to the complexity of this reaction mechanism – a possibility raised by this study.

Aerosol phase state has been predicted to vary significantly in the atmosphere and is linked to factors such as composition, humidity and temperature (Schmedding et al., 2020; Shiraiwa et al., 2017). One key influence on aerosol multiphase processes is particle viscosity (Reid et al., 2018) and viscous phases have been identified by field measurements of SOA (Virtanen et al., 2010). Particle viscosity can vary by orders of magnitude between phase states, which means the diffusion coefficients of small molecules through the particle phase also vary and heterogeneous processes (*i.e.* oxidation and water uptake) are affected (Koop et al., 2011; Shiraiwa et al., 2011a). Viscous phases can induce diffusion gradients during particle humidification (Hosny et al., 2016; Renbaum-Wolff et al., 2013; Zobrist et al., 2011). Particles of oleic acid have also been observed to increase in viscosity as a result of oxidation (Hosny et al., 2016). The fate of organic atmospheric aerosols is therefore strongly influenced by their phase state.

Organic coatings are present on the surface of marine aerosols, where sugars and fatty acids were found to be major constituents (Kirpes et al., 2019). Poor air quality has been linked to high $PM_{2.5}$ surface organic content in Beijing, China (Zhao et al., 2020) and the long-range transport of harmful substances emitted in the urban environment have been attributed to viscous organic coatings and the phase state of the aerosol (Mu et al., 2018; Shrivastava et al., 2017a). Analysis of marine aerosols heavily influenced by anthropogenic activity found that fatty acids were present along with Polycyclic Aromatic Hydrocarbons (PAHs) and phthalates, which are known to cause poor health (Kang et al., 2017). There is a long-standing discrepancy between the longer lifetime

measured in the field compared to laboratory measurements for oleic acid (Rudich et al., 2007). These observations suggest that aerosols are able to travel far from their sources and that the formation of viscous organic coatings could account for their long-range transport.

Pure oleic acid in the liquid phase exhibits some order by the formation of dimers (Iwahashi et al., 1991). As a surfactant, the addition of its ionic form (sodium oleate) and water can induce the formation of lyotropic liquid crystal (LLC) phases (Tiddy, 1980). These are three-dimensional nanostructures which can vary from spherical and cylindrical micelles to bicontinuous networks and lamellar sheets. These structures can be followed by Small-Angle X-ray Scattering (SAXS), which probes these structures on the nanometre scale. Each of these structures exhibit varying physical properties, the key ones being diffusivity and viscosity. Diffusion coefficients can vary dramatically between micellar, close-packed micellar, hexagonal (cylindrical micellar) and lamellar phases with diffusion in the last two becoming directionally dependent (Lindblom and Orädd, 1994; Orädd et al., 1995). The diffusion of atmospherically relevant small molecules, such as ozone and water, would therefore also be affected by the nanostructure formed in the organic medium, affecting the key aerosol heterogeneous processes of water uptake and chemical reaction.

The feasibility of LLC formation in levitated particles of a fatty acid aerosol proxy has previously been demonstrated (Pfrang et al., 2017) and the SAXS experiment has been exploited to quantify the effect of self-assembly on reaction kinetics (Milsom et al., 2021b). In this study, we coat capillaries with a self-assembled oleic acid-sodium oleate-fructose proxy and take advantage of the nano-structural information provided by SAXS to follow changes in these nanostructures during humidity cycles and exposure to

ozone. We investigate the sensitivity of the nanostructure to proxy composition and humidity and demonstrate that reactivity is affected by nanostructure.

5.3 Methods

5.3.1 Preparation of self-assembled coatings inside quartz capillaries

The method of film preparation is identical to that described in Milsom *et al.* (Milsom et al., 2021b) (see chapter 2). Sample coating solutions were prepared as follows: oleic acid (Sigma-Aldrich, 90 %), sodium oleate (Sigma-Aldrich, 99 %) and fructose (Sigma-Aldrich, 99 %) were dissolved as 10 wt % solutions in methanol and samples weighed to the desired ratio. All coating solutions are weighed as 1:1:x wt ratio mixtures (oleic acid:sodum oleate:fructose), where x is 0.5, 1, 2 corresponding to 20, 33 and 50 wt % fructose compositions.

5.3.2 SAXS experiment and simultaneous Raman microscopy on films coated inside quartz capillaries

SAXS probes aggregates at the nanometre scale, measuring order at the molecular, rather than atomic (X-ray diffraction), scale (Li et al., 2016; Pauw, 2013). The scattered intensity is measured against a scattering parameter (q) which is proportional to the scattering angle. q is inversely proportional to the characteristic spacing between equivalent scattering planes (d) via equation 5-1.

$$\mathrm{d} = \frac{2\pi}{\mathrm{q}} \tag{5-1}$$

This d-spacing can be used to determine a range of nano-structural parameters - for example, the water layer thickness between lamellar sheets (Kulkarni et al., 2011).

This experimental setup is the same as used in our previous capillary film study (Milsom et al., 2021b) (see chapter 2). Key experimental parameters are listed here: SAXS patterns were collected as 1s exposures at different positions along a coated capillary with a delay of 75 s between each scan to avoid any X-ray beam damage; the beam size at the sample was approximately 320 µm x 400 µm (FWHM); SAXS patterns were acquired between q = 0.008 – 0.6 $Å^{-1}$ by a *Pilatus P3-2M* detector.

The Raman microscopy setup is as described in Milsom *et al* (see chapter 2).: A 532-nm Raman laser probe was focussed with a long working distance objective (numerical aperture: 0.42) and a minimum spot diameter of ~ 1.5 µm. The emitted laser power was 20 – 50 mW. By following the oleic acid C=C bond peak at ~ 1650 cm^{-1} and normalising to the $–CH_2$ peak at ~ 1442 cm^{-1}, we were able to follow the progress of the ozonolysis reaction simultaneous to the SAXS measurements.

5.3.3 **Ozonolysis of coated films**

The ozonolysis procedure follows what was set out previously (Milsom et al., 2021b) and is summarised here (see chapter 2): Oxygen (BOC, 99.5 %) was passed through a pen-ray ozoniser (Ultraviolet Products Ltd., Cambridge, UK) which was calibrated offline by UV spectroscopy; the ozone concentration for all ozonolysis experiments was 77 ± 5 ppm at a flow rate of 60 mL min^{-1}. Note that such a high ozone concentration (typical atmospheric concentrations are ppb level) was used as it is known that self-assembled semi-solid phases slow the rate of reaction significantly (Milsom et al., 2021b; Pfrang et al., 2017). The ozone-oxygen mixture was measured to be at < 5 % RH.

Film thickness was determined by X-ray beam attenuation using diodes measuring the incident and transmitted intensities. The maximum attenuation was determined by filling a capillary with sample material. The thickness of each coated film was then calibrated by comparison with the filled capillary's attenuation.

5.3.4 **Controlled humidification of coated films**

Humidity was monitored and controlled using a bespoke Raspberry Pi (RPi) system. Dry (room air) and wet pumps were controlled by the RPi in order to reach the target relative humidity (RH), which was measured by a sensor at the outlet of the coated capillary tube with a precision of 2 %.

After samples were coated they were left for ~ 15 min to equilibrate at room humidity (~ 50 – 60 % RH) before being attached to the humidity control system. The capillary was then humidified to the desired settings using the RPi control programme.

5.4 **Results and Discussion**

5.4.1 **Time- and humidity-resolved nanostructure changes**

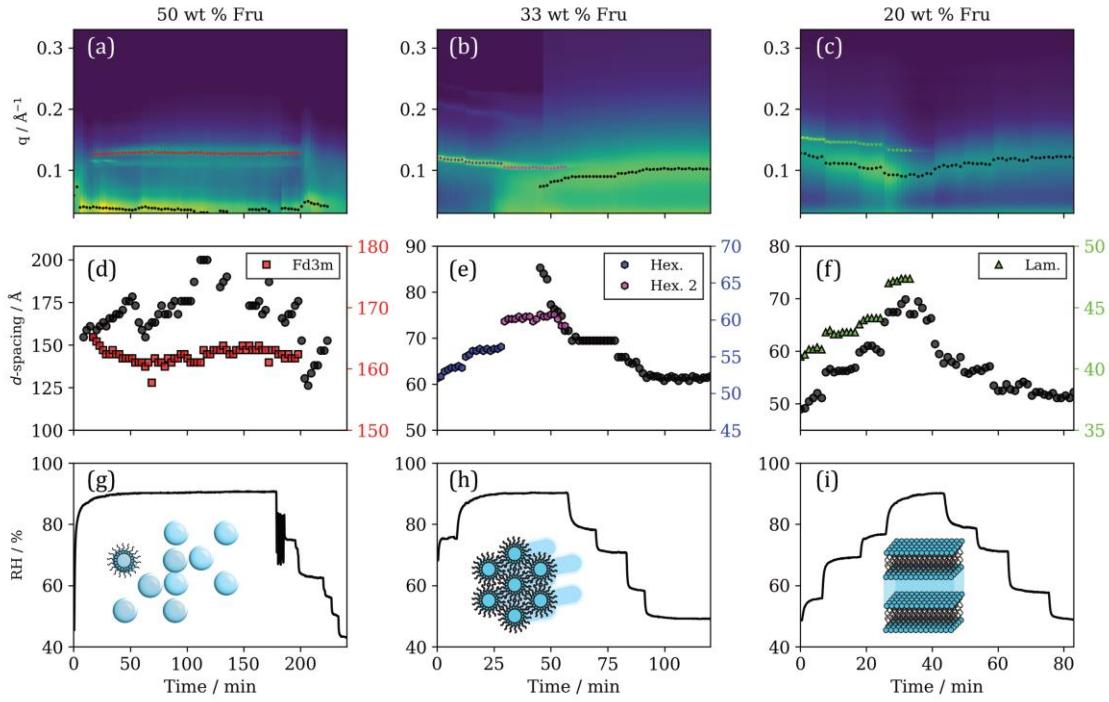

Figure 5-1. (a)-(c) SAXS patterns as a function of time during the humidity cycle. Peak position q-values for inverse micellar (black markers) and specific nanostructures (coloured markers) marker colours correspond to those in (d)-(f), representing the corresponding d-spacings (see Eq. 5-1). (g)-(i) Simultaneous RH measurements during the experiment with cartoons of the observed phases. Each set of SAXS, d-spacing and RH data is presented for each proxy fructose composition labelled as wt % of total organic mass: (a), (d), (g) – 50 wt %; (b), (e), (h) – 33 wt %; (c), (f), (i) – 20 wt % (i.e. 50 wt % fructose is a 1:1:2 oleic acid:sodium oleate:fructose mixture).

Different amounts of fructose in the organic mixture result in different self-assembled nanostructures (Fig. 5-1(a)-(c)). From first principles fructose, as a hydrophilic water-soluble molecule, would be expected to facilitate water uptake into the organic phase

and act as a humectant, analogous to the effect glycerol has on LLC phase boundaries (Richardson et al., 2015). By this logic, larger amounts of fructose should afford more hydrated (lower water-surfactant interfacial curvature) phases at a given humidity. However, an additional effect is observed during our experiments: the water-surfactant interfacial curvature *increases* with increasing fructose concentration. This is clear evidence for fructose acting as a *kosmotrope* – a water-structure-inducing molecule (Koynova et al., 1997; Kulkarni et al., 2011; Libster et al., 2008). As a kosmotrope, fructose removes water from the water-surfactant interface. This reduces the effective surfactant headgroup area, enabling the formation of structures with increased curvature at a given water content (in this case, experimental humidity – see corresponding cartoons of each phase in Fig. 5-1). The phase boundary therefore shifts according to the amount of fructose in the mixture. A set of fructose content-dependent nanostructures are possible as a result. Each one of these nanostructures possesses unique physical properties (as set out in the introduction). The sensitivity of the nanostructure to the amount of fructose in the system suggests that the physical properties, which influence atmospheric trace gas uptake, could also change with similar sensitivity to aerosol composition.

The characteristic *d*-spacing for each of the observed nanostructures increases with increasing RH (Fig. 5-1 (d)-(f)). This is the result of water filing the aqueous cavity in the inverse LLC nanostructures observed here. The time and humidity-resolved SAXS patterns acquired in this study have allowed us to take advantage of this characteristic and observe subtle RH-dependent changes in this parameter and directly measure the water uptake of a specific phase. This analysis can be applied to two coexistent phases,

provided their SAXS peaks do not overlap – as is the case in our study. The effect of these phases on water uptake is explored in section 5.4.2.

The phase change observed when going from low to high RH is not reversible for the two organic compositions which initially formed inverse hexagonal and lamellar phases at < 90 % RH (Fig. 5-1(b) and (c)). There are a few possible explanations for this: (i) there is an entropic effect – both hexagonal and lamellar phases are more ordered than the disordered inverse micellar phases that remain at high RH, resulting in an entropically disfavoured phase transition to a more ordered phase upon dehumidification and therefore slow formation of the more ordered phase; (ii) fructose is a humectant and slows dehydration from the inverse micellar phase, analogous to the effect of glycerol on dehydration from bicontinuous cubic LLC phases (Richardson et al., 2015); (iii) fructose, as a kosmotrope, stabilises the curved inverse micellar structure, making the formation of a less curved phase (*i.e.* the inverse hexagonal or lamellar phase) less thermodynamically favoured. What is certain is that there is no evidence in the SAXS patterns that the original ordered phase returns upon dehumidification. Humidification and dehumidification experiments were on a similar timescale, justifying our suggestion that a reversible phase change, if one occurs, is kinetically limited.

For the 33 wt % fructose mixture, a second hexagonal phase appears at high RH before eventually transitioning to an inverse micellar phase (Fig. 5-1(b) and (e)). Indeed, between ~ 40 – 60 min the inverse micellar and hexagonal phase are observed simultaneously in the mixture. There therefore is a heterogeneity in terms of molecular order and physical properties associated with each of these nanostructures. This coexistent inverse micellar phase is observed for all mixtures studied here.

The 50 wt % fructose mixture exhibits a reversible phase transition from inverse micellar to a close-packed inverse micellar (Fd3m) phase during a humidification-dehumidification cycle (Fig. 5-1(a)). The Fd3m phase appeared only at the highest humidity setting (90 % RH). The phase transition does not involve a significant change in phase topology, making the transition more facile compared with the transition to a hexagonal or lamellar phase - although the Fd3m arrangement is thought to include inverse micelles of differing size (Seddon et al., 1990; Shearman et al., 2010).

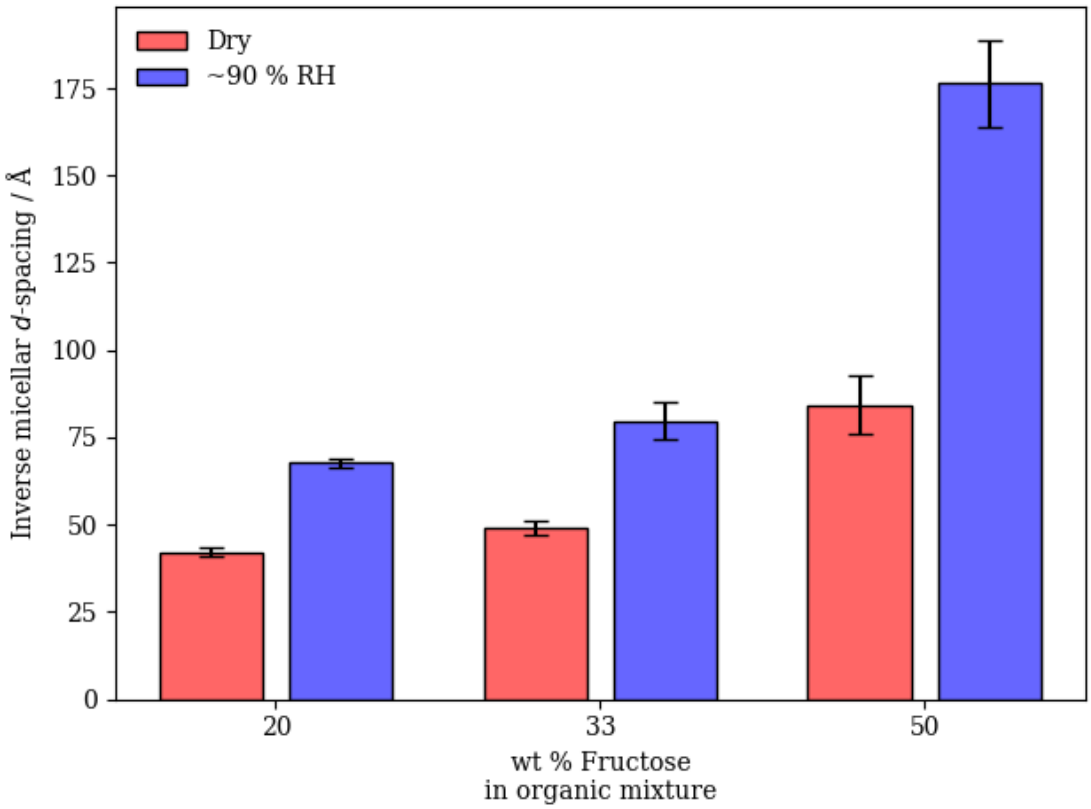

Figure 5-10. Inverse micellar d-spacing vs wt % fructose in the organic mixture under dry (~ 5 % RH) and humid (~ 90 % RH) conditions. A clear increase in d-spacing is visible upon humidification of each organic film.

A coexistent inverse micellar phase is observed for all organic compositions during these humidity experiments (Fig. 5-1(a)-(c) – broad peak at lower *q* values). This

coexistence represents a heterogeneity within the organic film, implying a similar heterogeneity in physical properties. We cannot say for certain whether this phase separation is uniform throughout the film or not using this technique. However, the visible shift in the inverse micellar peak position during humidity changes suggests that the change is happening in the majority of the film *i.e.* the inverse micellar is distributed throughout the film.

The inverse micellar *d*-spacing increases with the amount of fructose in the mixture under dry and humid conditions (Fig. 5-2). The inverse micellar phase observed for all fructose-containing mixtures studied here has a much larger *d*-spacing than mixtures without fructose, where a *d*-spacing of ~28-32 Å is expected (Fig. 10-11, the appendix – SAXS of a hydrated levitated particle of this composition) (Mele et al., 2018). Fructose therefore stabilises larger inverse micelles. Notably, under dry (~5 % RH) conditions fructose seems to have a marked effect on the inverse micellar *d*-spacing. This implies that fructose is collecting within the inverse micellar core and that possibly some water has been accommodated within the structure, explaining the increase in the average repeat distance between inverse micelles.

Increasing the humidity substantially increases the inverse micellar *d*-spacing for all compositions. This effect is most potent for the 50 wt % fructose mixture (Fig. 5-2). This observation highlights the ability of fructose to act as a humectant and stabilise large inverse micelles. It is worth restating that these inverse micellar phases at high RH are coexistent with more ordered phases. A measure of the hygroscopicity for each coexistent phase can be extracted from the SAXS data and is presented in 5.4.2.

5.4.2 Hygroscopicity of observed nanostructures

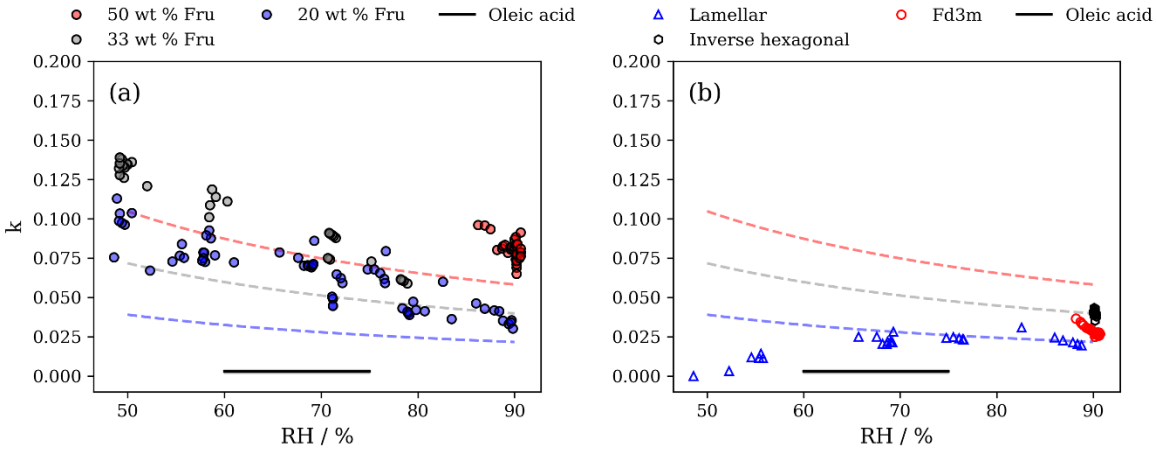

Figure 5-3. Plots of hygroscopicity parameter (κ) derived from d-spacings vs RH for the inverse micellar phases at different weight percentage fructose (wt % Fru) (a) and for other nanostructures including the lamellar phase (at 20 wt % fructose), inverse hexagonal (at 33 wt % fructose) and close-packed inverse micellar (Fd3m, at 50 wt % fructose) (b). Dashed lines on both plots represent κ calculated for the same fructose-lipid ratio based on Raoult's law at a particular RH. The colour of the dashed lines correspond to the wt % fructose in the mixture. The κ value for oleic acid measured by Rickards et al. is also plotted for reference (κ = 0.003 ± 0.001) (*Rickards et al., 2013*).

κ-Köhler theory derives aerosol hygroscopicity from particle sizes at different water activities (a_w) (Petters and Kreidenweis, 2007). The characteristic *d*-spacing calculated for each nanostructure observed here is related to its water content. We have applied κ-Köhler theory by measuring the change in *d*-spacing with a_w to describe the hygroscopicity of each phase. RH was converted to a_w (a_w = RH/100) and it is assumed that the proxy film had equilibrated with the humidity inside the capillary (see the rapid change and equilibration of the *d*-spacing observed when changing RH in Fig. 5-1). Note that κ-Köhler theory is normally applied to aerosol particles, linking particle

growth with humidity. Here we are not measuring individual particles, we are measuring nanoscale changes in structural repeat distances, which are correlated with water content. Equation 5-2 links the dry (V_d) and water (V_w) volumes with a_w and a hygroscopicity parameter (κ) (Petters and Kreidenweis, 2007).

$$\frac{V_w}{V_d} = \frac{a_w}{(1-a_w)} k \tag{5-2}$$

The calculation of κ is based on the geometry of each phase and the information regarding the mass and volume fractions of the lipid and water regions derivable from the equilibrium *d*-spacings obtained by SAXS (Asghar et al., 2015; Kulkarni et al., 2011). An explanation of the calculation of κ is provided in the appendix section 10.4.4.

This parameterisation of hygroscopicity is based on a simplified model which does not account for factors such as the effect of surfactants on surface tension and non-ideal solution behaviour. Also, these experiments are not carried out on particle ensembles or single particles, as has been the application previously (Liu et al., 2021; Rickards et al., 2013). As theories of hygroscopicity are in general agreement at higher a_w (RH) (Clegg et al., 1998; Fredenslund et al., 1975; Rickards et al., 2013; Topping et al., 2005; Wexler and Clegg, 2002; Zuend et al., 2008, 2011), our measurements of κ at high RH (maximum 90 % RH) are the most informative. However, we caution the over-interpretation of these κ values in the context of other hygroscopicity studies due to the experimental differences between this study and others. These κ measurements do however provide a first insight into the hygroscopic behaviour of these nanostructures and comparison between these nanostructures is justified by the same method used to calculate κ.

The κ value for the disordered inverse micellar phase formed at each composition is higher than what is predicted by Raoult's law at that composition and RH (Fig. 5-3(a)). These predictions assume that it is only the fructose that takes up water. Therefore the formation of the inverse micellar nanostructure, in addition to the presence of hygroscopic fructose, increases κ.

The close-packed inverse micellar phase (Fd3m symmetry) appears to be less hygroscopic than the Raoult prediction by a factor of ~ 2 at 90 % RH (Fig. 5-3(b)). This is in contrast to the disordered inverse micelles coexistent with this nanostructure (Fig. 5-3(a)). The key difference between the two nanostructures is that the close-packed inverse micelles are restricted in space. The inverse hexagonal and lamellar phases are in better agreement with Raoult's law predictions at > 85 % RH (Fig. 5-3(b)).

The lamellar phase appears to become much less hygroscopic at low RH. This may be because of an increase in the inter-bilayer attractive forces at lower bilayer separations and/or more restricted alkyl chains resulting from a more crystalline bilayer (Bahadur et al., 2019). A crystalline form of this lamellar bilayer has been observed in similar systems (Milsom et al., 2021a; Tandon et al., 2001).

As a thermodynamic parameter, κ reflects the energy changes involved in changing the nano-structural parameters associated with phase hydration and dehydration. For the lamellar phase, work must be done in order to overcome inter- and intra-bilayer repulsion when increasing and decreasing the volume of water between bilayers (Parsegian et al., 1979). In the inverse hexagonal phase, the elastic free energy change associated with a change in cylindrical radius is related to a bending modulus and the curvature of the cylinder, both of which are associated with the bilayer-forming lipid

and are affected by the addition of other interacting molecules (Chen and Rand, 1997). The close-packed inverse micellar phase is more sterically restricted than the disordered inverse micelles. The disordered inverse micellar phase has the least frustrated hydrocarbon tails out of the nanostructures presented here (*i.e.* they are not constrained close together, as is the case in the hexagonal and lamellar phases). These nanostructure-specific considerations help explain the difference between experiment and prediction.

All κ values derived from our SAXS data are greater than what has been measured for pure oleic acid (Fig. 5-3) (Rickards et al., 2013). The addition of fructose alone does not account for all of the differences in κ observed between pure oleic acid, predictions based on Raoult's law and the nanostructured fatty acid proxy. There must be an effect of the nanostructure formed and this effect is most pronounced for the disordered inverse micellar phase.

5.4.3 **Reactivity-nanostructure relationship**

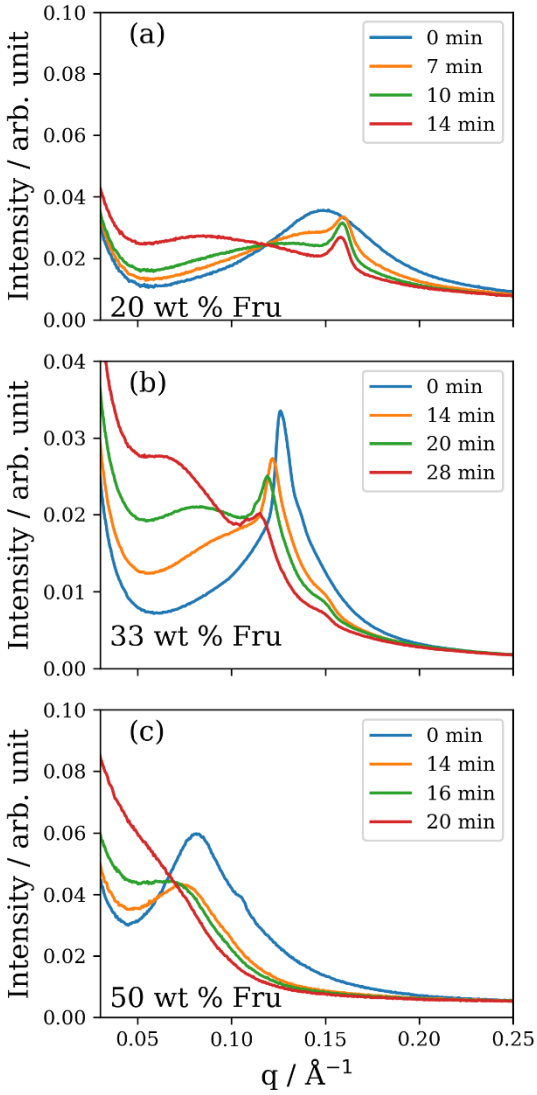

Figure 5-4. 1-D SAXS patterns during ozonolysis of mixtures of: (a) 20 wt % fructose, (b) 33 wt % fructose and (c) 50 wt % fructose. Note the shift to low-q of the broad inverse micellar peak for each composition. An additional phase appears in the first few minutes of reaction for the 20 wt % fructose mixture (a). The additional peaks associated with the ordered inverse micellar ($P6_3/mmc$) are revealed after ~ 20 min for the 33 wt % fructose mixture (b) – these are identified in the appendix section 10.4.3. $[O_3]$ = 77 ± 5 ppm, RH < 5 %.

We subjected proxy coatings of fatty acid-fructose mixtures to ozonolysis under dry conditions analogous to our previous film kinetic study (Milsom et al., 2021b). Figure 5-4 presents the SAXS patterns and phases observed during ozonolysis for the fructose-containing mixtures studied here. There are broad peaks characteristic of the inverse micellar phase in all mixtures, this was the most commonly observed phase under these conditions. An extra feature from an ordered phase appears during ozonolysis for the 20 wt % fructose mixture (Fig. 5-4(a)) – this is discussed in conjunction with simultaneous Raman spectrometry later (see Fig. 5-6). An ordered phase is observed for the 33 wt % fructose film (Fig. 5-4(b)). Initially, the less intense peaks associated with this phase are obscured by the broad overlapping inverse micellar peak. After ~ 20 min of ozonolysis the broad peak has shifted to lower q and the other peaks are visible. These peaks index closest to an ordered micellar phase with $P6_3/mmc$ symmetry, which has been observed before in levitated droplets of a similar proxy (Pfrang et al., 2017) – see the appendix section 10.4.3 for phase indexing. This allowed us to measure the kinetic difference between ordered and disordered inverse micelles.

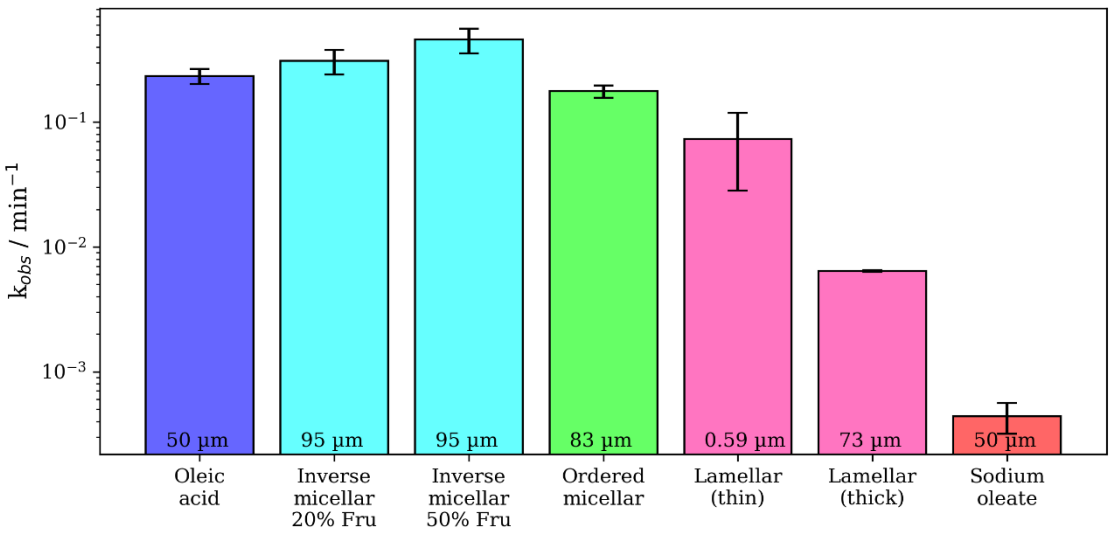

Figure 5-5. Pseudo-first order decay constants (k_{obs}) measured for the oleic acid-ozone reaction carried out on coated films of different compositions and nanostructures. The thickness of each film is displayed at the bottom of each bar (see table 10-3 in the appendix for all kinetic data and associated uncertainties). Oleic acid, sodium oleate and lamellar phase data are reproduced from chapter 2 (Milsom et al., 2021b). The lamellar phase was formed in a dry mixture of oleic acid: sodium oleate (1:1 wt). Oleic acid and sodium oleate decays were measured by following the C=C peak in the Raman spectrum as described in the methods. [O_3] = 77 ± 5 ppm and RH < 5 %.

Reaction kinetics can be followed by SAXS using an analysis technique that we have developed (Milsom et al., 2021b). We took advantage of the time resolution offered by a synchrotron experiment to derive kinetic parameters for coated organic films of different composition and nanostructure (Fig. 5-5). All kinetic data are summarised in Table 10-3 (the appendix) and a description of how these kinetic decay parameters were calculated is presented in the appendix section 10.4.1.

The disordered inverse micellar phase reacts faster than the ordered micellar phase coated at a similar thickness. This is to be expected as the close-packed inverse micelles

are locked into their position, increasing the viscosity of the phase and therefore slowing the diffusion of small molecules such as ozone.

An order of reactivity exists between nanostructures. We are now able to compare the reactivity of different phases formed by this proxy system and the reactivity of its constituent parts (Fig. 5-5). Going from most to least reactive: inverse micellar > close-packed inverse micellar > (dry) lamellar. Note that the lamellar phase in this case is anhydrous. As suggested by Hearn *et al*., diffusion of ozone past the closely packed lamellar chains is likely to be hindered and the rate of reaction reduced as a result, limiting the reaction to the surface of the film (Hearn et al., 2005).

The close-packed (ordered) inverse micellar phase film was ~ 12 μm thinner than the inverse micellar films. We have shown previously that film thickness can affect reactivity (Milsom et al., 2021b), so we cannot rule out the effect of film thickness in these experiments. Though it was not possible to control film thickness, comparisons are still possible and actually reveal some stark differences in reactivity. Most notably is the comparison of the sub-micron lamellar phase film with ~ 95 μm films of inverse micellar phase. The thin lamellar phase film reacts slower than the inverse micellar films despite the ~ 160-fold difference in film thicknesses. There is also about an order of magnitude difference between the thickest lamellar film (73 μm) and the inverse micellar films (95 μm).

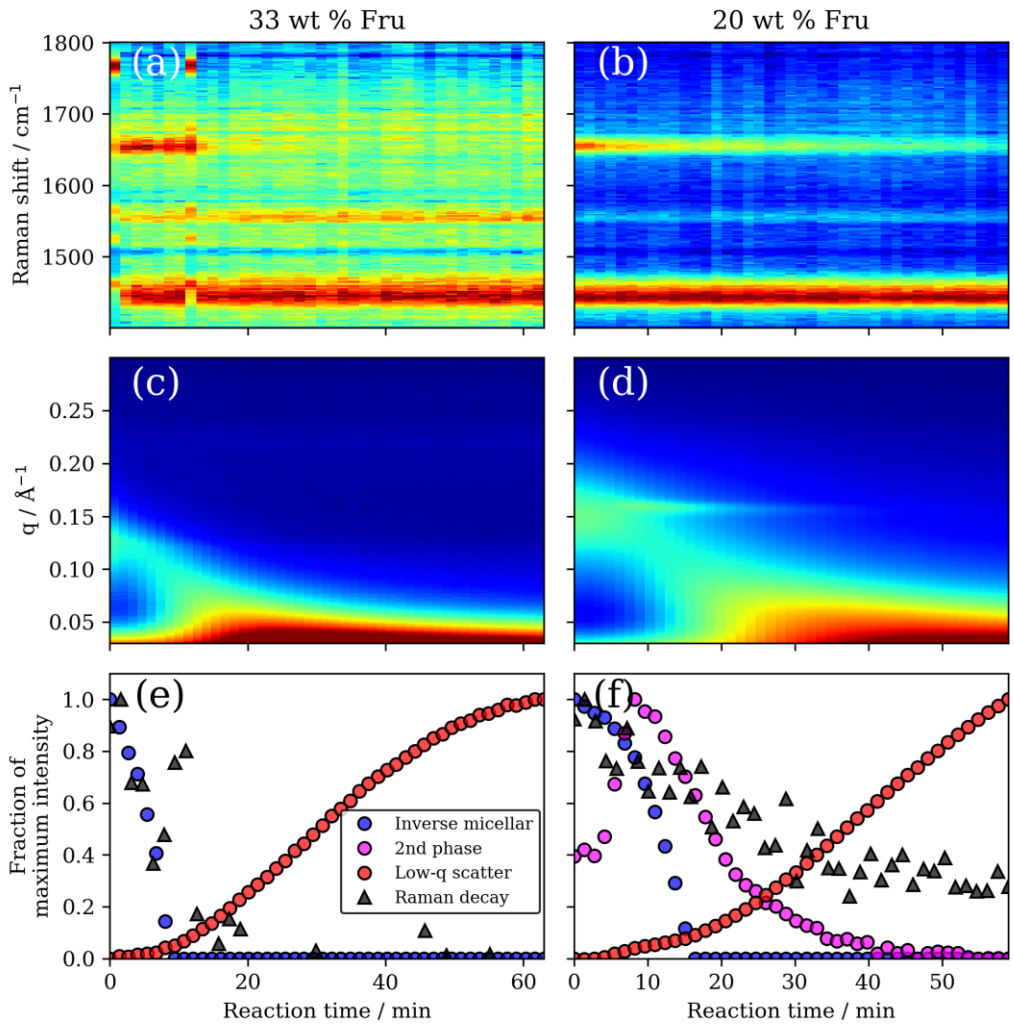

Figure 5-6. (a) and (b) Raman spectra vs reaction time highlighting the disappearance of the oleic acid C=C peak at ~ 1650 cm^{-1} and the persistence of the –CH$_2$ deformation band at ~ 1442 cm^{-1} for the 33 and 20 wt % fructose compositions, respectively. (c) and (d) simultaneous SAXS patterns vs reaction time showing the initial broad inverse micellar peak (0.12-0.15 Å^{-1}) which shifts to lower q and disappears. The increase in low-q scattering is also evident along with the appearance of a 2nd phase peak for the 20 wt % fructose composition (d). (e) and (f) Plots of maximum peak area intensity vs reaction time for key SAXS and Raman peaks. Raman decay is measured by following the C=C/-CH$_2$ peak area ratio.

The inverse micellar *d*-spacing increases (*q* decreases) as ozonolysis progresses (Fig. 5-6). This experiment was carried out under dry conditions, so the increase in spacing must be a result of the reaction rather than any water uptake. We suggest that fructose itself reacts with one of the intermediate products. Common saccharides found in the atmosphere, including glucose (closely related to fructose), have been shown to react readily with Criegee intermediates that are formed as a result of ozonolysis (Enami et al., 2017). This forms ethers of greater mass and therefore products are likely to take up more space, accounting for the increase in *d*-spacing observed during the ozonolysis experiment. Fructose can form an ether with oleic acid, however, to the author's knowledge, this has only been observed as an enzymatic reaction (Ye and Hayes, 2011). Reaction with a Criegee intermediate is therefore the most probable explanation.

Products may themselves self-assemble. The increase in low-*q* scattering observed here was not observed during reactions of similar samples without fructose (Milsom et al., 2021b). This suggests that the species causing the increased low-*q* scatter is associated with the fructose in the system. If high-molecular-weight fructose products are formed, the marked increase in low-*q* scatter suggests that these molecules aggregate into structures with large repeat distances.

A new phase was formed during the ozonolysis of the 20 wt % fructose mixture (Fig. 5-4(a) and Fig. 5-6(d)). This was unexpected as it was assumed that self-assembly would be destroyed by chemical reaction of the constituent fatty acid, as observed previously (Milsom et al., 2021b; Pfrang et al., 2017). This phase took longer to disappear compared with the initial inverse micellar phase. The reaction induced heterogeneity in the film both in the nanostructure and corresponding physical properties. This observation suggests that there is a dynamic relationship between nanostructure and the

chemical reaction of this fatty acid aerosol proxy. The identity of this phase is uncertain due to the lack of a 2nd order peak in the SAXS pattern, however this peak appears where the dry lamellar phase peak is expected to occur (Mele et al., 2018; Milsom et al., 2021b) – this is the most likely arrangement. The atmospheric implications of the effect of nanostructure on reaction kinetics will be discussed in the following section.

There is evidence that the oleic acid double-bond persists at the end of the reaction (Fig. 5-6(b)). Simultaneous Raman spectroscopy on our deposited films shows clearly that the carbon-carbon double-bond peak associated with oleic acid is still present at the end of the reaction even though the initial SAXS peaks are not visible. The increase in inverse micellar *d*-spacing (SAXS peak shift to lower *q*), the notable increase in low-*q* scattering and the persistence of the double-bond suggests that oleic acid may be protected by the increase in viscosity expected by the formation of larger molecular mass molecules, which have been identified as products for the oleic acid-ozone system (Reynolds et al., 2006; Zahardis et al., 2005). This persistence is consistent with recent work on coated capillaries and residues observed after oxidising monolayers of atmospheric surfactants (including oleic acid) coated on water (King et al., 2009; Milsom et al., 2021b; Pfrang et al., 2014; Sebastiani et al., 2018; Woden et al., 2018, 2021). This highlights the utility of a simultaneous technique to measure reaction kinetics (Raman spectroscopy).

5.4.4 **Atmospheric implications**

There is a distribution of aerosol phase states in the atmosphere which has been observed in the field and predicted in global chemistry models (Schmedding et al., 2020; Shiraiwa et al., 2017; Virtanen et al., 2010). This phase state is dependent on the aerosol's environment, which includes humidity and temperature. Aerosol multiphase

processes are affected by the formation of semi-solid and glassy phases due to reduced gas-particle interactions and the effect on particle diffusivity (Berkemeier et al., 2016; Koop et al., 2011; Mikhailov et al., 2009; Zhou et al., 2013, 2019; Zobrist et al., 2011). This in turn leads to a phase-dependent aerosol atmospheric lifetime and can facilitate the long-range transport of an aerosol. Particle phase state and viscous aerosol organic coatings have been linked with the long-range transport of polycyclic aromatic hydrocarbons (PAHs), which are harmful to human health by acting as carcinogens (Mu et al., 2018; Shrivastava et al., 2017a). Our work has demonstrated that changes in the nanostructure, induced by humidity changes, can affect both water uptake and reactivity – two key aerosol ageing processes (Pöschl, 2005). The sensitivity of the nanostructure to changes in RH suggests that aerosol physical properties, such as viscosity and diffusivity, are also as sensitive.

Previously, ozonolysis has been shown to destroy self-assembly in fatty acid aerosol proxies (Milsom et al., 2021b; Pfrang et al., 2017). Now there is evidence that ozonolysis could induce the formation of an intermediate molecular arrangement (Fig. 5-6(d)), demonstrating the possibility that self-assembly could be induced by the chemical reaction of these atmospheric molecules with ozone. This, in combination with humidity-induced phase changes, would lead to a dynamic aerosol phase state which is dependent on the molecular arrangement of the surfactant molecules studied here.

Atmospheric aerosols exhibit heterogeneity both in terms of composition and physical properties such as hygroscopicity (Kirpes et al., 2019; Schill et al., 2015). Particle viscosity can become heterogeneous during chemical reaction and exposure to humidity (Hosny et al., 2016). We have demonstrated that nano-structural heterogeneity exists during humidity change and ozonolysis. There must therefore be a heterogeneity in

hygroscopicity in our proxy films due to the link between nanostructure and κ (Fig. 5-3). Additionally, the formation of an intermediate nanostructure during ozonolysis observed here suggests that viscosity may not be equal throughout the film and that the diffusivity of small molecules such as ozone throughout the particle would also not be even, affecting the lifetime of the proxy (Shiraiwa et al., 2011b). The increase in *d*-spacing observed between inverse micelles during ozonolysis suggests that larger molecules are being formed as a result of the reaction (Fig. 5-4 and Fig. 5-6(c) & (d)). These larger molecules may also contribute to film heterogeneity and affect the reactive lifetime of these molecules.

Sugars and fatty acids, such as fructose and oleic acid, have been identified in aerosols emitted in urban (Wang et al., 2006) and marine (Fu et al., 2013) environments. Specifically, saccharides (sugars) have been identified along with fatty acids as major components of thick (μm-scale) organic coatings observed on sea spray aerosols (Kirpes et al., 2019) and have been also identified in a cafeteria environment (Alves et al., 2020), demonstrating the range of environments our proxy could represent. Their relative abundances can vary depending on season, time of day and location. In this study we have shown that the proxy sugar content can have an impact on aerosol physical properties via a change in nanostructure. We suggest that, as the relative amount of sugar and fatty acid changes between environments, nanostructures could also vary depending on the location and emission type.

We can now demonstrate that the reactivity of surface-active oleic acid not only depends on whether it is self-assembled or not (Milsom et al., 2021b; Pfrang et al., 2017) but that it also depends on the specific nanostructure it adopts (Fig. 5-5). The addition of fructose induces nano-structural changes by acting as a kosmotrope under

humidified conditions. This implies that the lifetime of surfactant material would depend on nanostructure, which in turn is linked to aerosol composition. The persistence of surface-active material has been demonstrated at the air-water interface (King et al., 2009; Pfrang et al., 2014; Sebastiani et al., 2018; Woden et al., 2018, 2021). Simultaneous Raman spectroscopy suggests that oleic acid can persist in the films studied here, a finding consistent with non-fructose-containing films of this proxy (Milsom et al., 2021b). We have shown that the reactive lifetime of oleic acid can vary by orders of magnitude as a result of different molecular arrangements. There is a link between surfactant content and cloud droplet formation potential as a result of a reduction in surface tension (Bzdek et al., 2020; Facchini et al., 1999, 2000; Ovadnevaite et al., 2017); any lengthening of surfactant lifetime would imply a similar lengthening of the cloud formation potential of a surfactant-containing aerosol, such as aerosols containing oleic acid.

5.5 **Conclusions**

This work continues the bottom-up approach to this fatty acid aerosol proxy system by the addition of fructose, another organic aerosol emission. We have demonstrated a link between the nano-structures formed by fructose-containing fatty acid mixtures and the key aerosol properties of hygroscopicity and reactivity by utilising synchrotron SAXS data and complimentary Raman spectroscopy.

Key information relevant to atmospheric aerosol properties has been inferred from the SAXS and Raman data. We were able to extract information from coexistent nanostructures in order to draw comparison between them. As a result, heterogeneity was observed during humidity exposure and ozonolysis, with implications for the atmospheric lifetime of such a system.

The fatty acid nanostructure is sensitive to atmospheric ageing processes. This points towards a system with physical properties of similar sensitivity. We have suggested that a fatty acid atmospheric aerosol, being in a dynamic environment, could undergo significant transformations in terms of key physical properties which are linked to the surfactant nanostructure. If this is the case, the lifetime of such an aerosol would also be sensitive and subject to change, depending on the aerosol's environment.

5.6 Acknowledgements

This work was carried out with the support of the Diamond Light Source (DLS), instrument I22 (proposal SM21663). AM wishes to acknowledge funding from NERC SCENARIO DTP award number NE/L002566/1 and CENTA DTP. The authors would like to thank Andy Smith (DLS), Tim Snow (DLS) and Lee Davidson (DLS) for technical support during beamtime experiments; Jacob Boswell is acknowledged for help at beamtimes. The authors are grateful to the Central Laser Facility for access to key equipment for the Raman work simultaneously to the DLS beamtime experiments. Ben Woden is acknowledged for help at the beamtime and with calibrating the ozoniser. Ben Laurence is acknowledged for developing the RPi humidity control system.

5.6.1 Contributors

Adam Milsom carried out experiments, wrote the manuscript, processed and analysed the data. Christian Pfrang and Adam Squires Carried out experiments and contributed to data analysis and interpretation. Nick Terrill (DLS), Andy Smith (DLS), Tim Snow (DLS) and Lee Davidson (DLS) provided technical support during the SAXS beamtime. Jacob Boswell and Ben Woden helped carry out experiments at the beamtime. Ben Laurence developed the RPi humidity control system. Andy Ward setup and provided support with the simultaneous Raman system.

5.7 **Comment**

This study extends the coated capillary experiments presented in chapter 2 (Milsom et al., 2021b). Here, different nanostructures were targeted and an attempt at quantifying their effect on reaction kinetics and hygroscopicity was presented.

The simultaneous SAXS-Raman experiment was particularly useful in showing that the double-bond for oleic acid persists even after the original nanostructure had broken down, suggesting that the aggregates causing the low-q scattering could be protecting the unreacted oleic acid.

The calculation of the hygroscopicity of each phase was "back-of-the-envelope". However, it is based on sound theory concerning the geometrical parameters extractable from SAXS data. The fundamental relationship between V_w, V_d and a_w is what motivated the use of this method. These κ measurements are at least comparable between nanostructures – a key aim of this work.

5.8 **References**

Alves, C. A., Vicente, E. D., Evtyugina, M., Vicente, A. M., Nunes, T., Lucarelli, F., Calzolai, G., Nava, S., Calvo, A. I., Alegre, C. del B., Oduber, F., Castro, A. and Fraile, R.: Indoor and outdoor air quality: A university cafeteria as a case study, Atmos. Pollut. Res., 11(3), 531–544, doi:10.1016/j.apr.2019.12.002, 2020.

Asghar, K. A., Rowlands, D. A., Elliott, J. M. and Squires, A. M.: Predicting Sizes of Hexagonal and Gyroid Metal Nanostructures from Liquid Crystal Templating, ACS Nano, 9(11), 10970–10978, doi:10.1021/acsnano.5b04176, 2015.

Bahadur, J., Das, A. and Sen, D.: Evaporation-induced structural evolution of the lamellar mesophase: a time-resolved small-angle X-ray scattering study, J. Appl.

Crystallogr., 52(5), 1169–1175, doi:10.1107/S1600576719011671, 2019.

Berkemeier, T., Steimer, S. S., Krieger, U. K., Peter, T., Pöschl, U., Ammann, M. and Shiraiwa, M.: Ozone uptake on glassy, semi-solid and liquid organic matter and the role of reactive oxygen intermediates in atmospheric aerosol chemistry, Phys. Chem. Chem. Phys., 18(18), 12662–12674, doi:10.1039/c6cp00634e, 2016.

Boucher, O., Randall, D., Artaxo, P., Bretherton, C., Feingold, G., Forster, P., Kerminen, V.-M., Kondo, Y., Liao, H., Lohmann, U., Rasch, P., Satheesh, S. K., Sherwood, S., Stevens, B. and Zhang, X. Y.: Clouds and Aerosols, in Climate Change 2013 - The Physical Science Basis, edited by Intergovernmental Panel on Climate Change, pp. 571–658, Cambridge University Press, Cambridge., 2013.

Bzdek, B. R., Reid, J. P., Malila, J. and Prisle, N. L.: The surface tension of surfactant-containing, finite volume droplets, Proc. Natl. Acad. Sci. U. S. A., 117(15), 8335–8343, doi:10.1073/pnas.1915660117, 2020.

Chan, C. K. and Yao, X.: Air pollution in mega cities in China, Atmos. Environ., 42(1), 1–42, doi:10.1016/j.atmosenv.2007.09.003, 2008.

Chen, Z. and Rand, R. P.: The influence of cholesterol on phospholipid membrane curvature and bending elasticity, Biophys. J., 73(1), 267–276, doi:10.1016/S0006-3495(97)78067-6, 1997.

Clegg, S. L., Brimblecombe, P. and Wexler, A. S.: Thermodynamic Model of the System H + −NH 4 + −Na + −SO 4 2- −NO 3 - −Cl - −H 2 O at 298.15 K, J. Phys. Chem. A, 102(12), 2155–2171, doi:10.1021/jp973043j, 1998.

Enami, S., Hoffmann, M. R. and Colussi, A. J.: Criegee Intermediates React with

Levoglucosan on Water, J. Phys. Chem. Lett., 8(16), 3888–3894, doi:10.1021/acs.jpclett.7b01665, 2017.

Facchini, M. C., Mircea, M., Fuzzi, S. and Charlson, R. J.: Cloud albedo enhancement by surface-active organic solutes in growing droplets, Nature, 401(6750), 257–259, doi:10.1038/45758, 1999.

Facchini, M. C., Decesari, S., Mircea, M., Fuzzi, S. and Loglio, G.: Surface tension of atmospheric wet aerosol and cloud/fog droplets in relation to their organic carbon content and chemical composition, Atmos. Environ., 34(28), 4853–4857, doi:10.1016/S1352-2310(00)00237-5, 2000.

Fredenslund, A., Jones, R. L. and Prausnitz, J. M.: Group-contribution estimation of activity coefficients in nonideal liquid mixtures, AIChE J., 21(6), 1086–1099, doi:10.1002/aic.690210607, 1975.

Fu, P., Kawamura, K., Okuzawa, K., Aggarwal, S. G., Wang, G., Kanaya, Y. and Wang, Z.: Organic molecular compositions and temporal variations of summertime mountain aerosols over Mt. Tai, North China Plain, J. Geophys. Res. Atmos., 113(19), 1–20, doi:10.1029/2008JD009900, 2008.

Fu, P. Q., Kawamura, K., Chen, J., Charrière, B. and Sempéré, R.: Organic molecular composition of marine aerosols over the Arctic Ocean in summer: Contributions of primary emission and secondary aerosol formation, Biogeosciences, 10(2), 653–667, doi:10.5194/bg-10-653-2013, 2013.

Gallimore, P. J., Griffiths, P. T., Pope, F. D., Reid, J. P. and Kalberer, M.: Comprehensive modeling study of ozonolysis of oleic acid aerosol based on real-time, online measurements of aerosol composition, J. Geophys. Res., 122(8), 4364–4377,

doi:10.1002/2016JD026221, 2017.

Harrison, R. M.: Airborne particulate matter, Philos. Trans. R. Soc. London A,378, 20190319, doi: 10.1098/rsta.2019.0319, 2020.

Hearn, J. D., Smith, G. D. and Lovett, A. J.: Ozonolysis of oleic acid particles: evidence for a surface reaction and secondary reactions involving Criegee intermediates, Phys. Chem. Chem. Phys., 7(3), 501–511, doi:10.1039/b414472d, 2005.

Hosny, N. A., Fitzgerald, C., Vyšniauskas, A., Athanasiadis, A., Berkemeier, T., Uygur, N., Pöschl, U., Shiraiwa, M., Kalberer, M., Pope, F. D. and Kuimova, M. K.: Direct imaging of changes in aerosol particle viscosity upon hydration and chemical aging, Chem. Sci., 7(2), 1357–1367, doi:10.1039/c5sc02959g, 2016.

Iwahashi, M., Yamaguchi, Y., Kato, T., Horiuchi, T., Sakurai, I. and Suzuki, M.: Temperature dependence of molecular conformation and liquid structure of cis-9-octadecenoic acid, J. Phys. Chem., 95(1), 445–451, doi:10.1021/j100154a078, 1991.

Jimenez, J. L., Canagaratna, M. R., Donahue, N. M., Prevot, A. S. H., Zhang, Q., Kroll, J. H., DeCarlo, P. F., Allan, J. D., Coe, H., Ng, N. L., Aiken, A. C., Docherty, K. S., Ulbrich, I. M., Grieshop, A. P., Robinson, A. L., Duplissy, J., Smith, J. D., Wilson, K. R., Lanz, V. A., Hueglin, C., Sun, Y. L., Tian, J., Laaksonen, A., Raatikainen, T., Rautiainen, J., Vaattovaara, P., Ehn, M., Kulmala, M., Tomlinson, J. M., Collins, D. R., Cubison, M. J., Dunlea, J., Huffman, J. A., Onasch, T. B., Alfarra, M. R., Williams, P. I., Bower, K., Kondo, Y., Schneider, J., Drewnick, F., Borrmann, S., Weimer, S., Demerjian, K., Salcedo, D., Cottrell, L., Griffin, R., Takami, A., Miyoshi, T., Hatakeyama, S., Shimono, A., Sun, J. Y., Zhang, Y. M., Dzepina, K., Kimmel, J. R., Sueper, D., Jayne, J. T., Herndon, S. C., Trimborn, A. M., Williams, L. R., Wood, E. C.,

Middlebrook, A. M., Kolb, C. E., Baltensperger, U. and Worsnop, D. R.: Evolution of Organic Aerosols in the Atmosphere, Science, 326(5959), 1525–1529, doi:10.1126/science.1180353, 2009.

Kang, M., Yang, F., Ren, H., Zhao, W., Zhao, Y., Li, L., Yan, Y., Zhang, Y., Lai, S., Zhang, Y., Yang, Y., Wang, Z., Sun, Y. and Fu, P.: Influence of continental organic aerosols to the marine atmosphere over the East China Sea: Insights from lipids, PAHs and phthalates, Sci. Total Environ., 607–608, 339–350, doi:10.1016/j.scitotenv.2017.06.214, 2017.

King, M. D., Rennie, A. R., Thompson, K. C., Fisher, F. N., Dong, C. C., Thomas, R. K., Pfrang, C. and Hughes, A. V.: Oxidation of oleic acid at the air-water interface and its potential effects on cloud critical supersaturations, Phys. Chem. Chem. Phys., 11(35), 7699–7707, doi:10.1039/b906517b, 2009.

King, M. D., Rennie, A. R., Pfrang, C., Hughes, A. V. and Thompson, K. C.: Interaction of nitrogen dioxide (NO2) with a monolayer of oleic acid at the air-water interface - A simple proxy for atmospheric aerosol, Atmos. Environ., 44(14), 1822–1825, doi:10.1016/j.atmosenv.2010.01.031, 2010.

Kirpes, R. M., Bonanno, D., May, N. W., Fraund, M., Barget, A. J., Moffet, R. C., Ault, A. P. and Pratt, K. A.: Wintertime Arctic Sea Spray Aerosol Composition Controlled by Sea Ice Lead Microbiology, ACS Cent. Sci., 5(11), 1760–1767, doi:10.1021/acscentsci.9b00541, 2019.

Koop, T., Bookhold, J., Shiraiwa, M. and Pöschl, U.: Glass transition and phase state of organic compounds: Dependency on molecular properties and implications for secondary organic aerosols in the atmosphere, Phys. Chem. Chem. Phys., 13(43),

19238–19255, doi:10.1039/c1cp22617g, 2011.

Koynova, R., Brankov, J. and Tenchov, B.: Modulation of lipid phase behavior by kosmotropic and chaotropic solutes, Eur. Biophys. J., 25(4), 261–274, doi:10.1007/s002490050038, 1997.

Kulkarni, C. V., Wachter, W., Iglesias-Salto, G., Engelskirchen, S. and Ahualli, S.: Monoolein: a magic lipid?, Phys. Chem. Chem. Phys., 13(8), 3004–3021, doi:10.1039/C0CP01539C, 2011.

Li, G., Su, H., Ma, N., Tao, J., Kuang, Y., Wang, Q., Hong, J., Zhang, Y., Kuhn, U., Zhang, S., Pan, X., Lu, N., Tang, M., Zheng, G., Wang, Z., Gao, Y., Cheng, P., Xu, W., Zhou, G., Zhao, C., Yuan, B., Shao, M., Ding, A., Zhang, Q., Fu, P., Sun, Y., Pöschl, U. and Cheng, Y.: Multiphase chemistry experiment in Fogs and Aerosols in the North China Plain (McFAN): integrated analysis and intensive winter campaign 2018, Faraday Discuss., 226, 207-222, doi:10.1039/D0FD00099J, 2021.

Li, T., Senesi, A. J. and Lee, B.: Small Angle X-ray Scattering for Nanoparticle Research, Chem. Rev., 116(18), 11128–11180, doi:10.1021/acs.chemrev.5b00690, 2016.

Libster, D., Ishai, P. Ben, Aserin, A., Shoham, G. and Garti, N.: From the microscopic to the mesoscopic properties of lyotropic reverse hexagonal liquid crystals, Langmuir, 24(5), 2118–2127, doi:10.1021/la702570v, 2008.

Lindblom, G. and Orädd, G.: NMR Studies of translational diffusion in lyotropic liquid crystals and lipid membranes, Prog. Nucl. Magn. Reson. Spectrosc., 26, 483–515, doi:10.1016/0079-6565(94)80014-6, 1994.

Liu, J., Zhang, F., Xu, W., Chen, L., Ren, J., Jiang, S., Sun, Y. and Li, Z.: A Large Impact of Cooking Organic Aerosol (COA) on Particle Hygroscopicity and CCN Activity in Urban Atmosphere, J. Geophys. Res. Atmos., 126(8), 1–11, doi:10.1029/2020jd033628, 2021.

Mele, S., Söderman, O., Ljusberg-Wahrén, H., Thuresson, K., Monduzzi, M. and Nylander, T.: Phase behavior in the biologically important oleic acid/sodium oleate/water system, Chem. Phys. Lipids, 211, 30–36, doi:10.1016/j.chemphyslip.2017.11.017, 2018.

Mikhailov, E., Vlasenko, S., Martin, S. T., Koop, T. and Pöschl, U.: Amorphous and crystalline aerosol particles interacting with water vapor: Conceptual framework and experimental evidence for restructuring, phase transitions and kinetic limitations, Atmos. Chem. Phys., 9(24), 9491–9522, doi:10.5194/acp-9-9491-2009, 2009.

Milsom, A., Squires, A. M., Boswell, J. A., Terrill, N. J., Ward, A. D. and Pfrang, C.: An organic crystalline state in ageing atmospheric aerosol proxies : spatially resolved structural changes in levitated fatty acid particles, Atmos. Chem. Phys. Discuss., [preprint], 1–31, doi:https://doi.org/10.5194/acp-2021-270, 2021a.

Milsom, A., Squires, A. M., Woden, B., Terrill, N. J., Ward, A. D. and Pfrang, C.: The persistence of a proxy for cooking emissions in megacities: a kinetic study of the ozonolysis of self-assembled films by simultaneous small and wide angle X-ray scattering (SAXS/WAXS) and Raman microscopy, Faraday Discuss., 226, 364–381, doi:10.1039/D0FD00088D, 2021b.

Mu, Q., Shiraiwa, M., Octaviani, M., Ma, N., Ding, A., Su, H., Lammel, G., Pöschl, U. and Cheng, Y.: Temperature effect on phase state and reactivity controls atmospheric

multiphase chemistry and transport of PAHs, Sci. Adv., 4(3), eaap7314, doi:10.1126/sciadv.aap7314, 2018.

Orädd, G., Lindblom, G., Fontell, K. and Ljusberg-Wahren, H.: Phase diagram of soybean phosphatidylcholine-diacylglycerol-water studied by x-ray diffraction and 31P- and pulsed field gradient 1H-NMR: evidence for reversed micelles in the cubic phase, Biophys. J., 68(5), 1856–1863, doi:10.1016/S0006-3495(95)80362-0, 1995.

Ots, R., Vieno, M., Allan, J. D., Reis, S., Nemitz, E., Young, D. E., Coe, H., Di Marco, C., Detournay, A., Mackenzie, I. A., Green, D. C. and Heal, M. R.: Model simulations of cooking organic aerosol (COA) over the UK using estimates of emissions based on measurements at two sites in London, Atmos. Chem. Phys., 16(21), 13773–13789, doi:10.5194/acp-16-13773-2016, 2016.

Ovadnevaite, J., Zuend, A., Laaksonen, A., Sanchez, K. J., Roberts, G., Ceburnis, D., Decesari, S., Rinaldi, M., Hodas, N., Facchini, M. C., Seinfeld, J. H. and O'Dowd, C.: Surface tension prevails over solute effect in organic-influenced cloud droplet activation, Nature, 546(7660), 637–641, doi:10.1038/nature22806, 2017.

Parsegian, V. A., Fuller, N. and Rand, R. P.: Measured work of deformation and repulsion of lecithin bilayers, Proc. Natl. Acad. Sci. U. S. A., 76(6), 2750–2754, doi:10.1073/pnas.76.6.2750, 1979.

Pauw, B. R.: Everything SAXS: small-angle scattering pattern collection and correction, J. Phys. Condens. Matter, 25(38), 383201, doi:10.1088/0953-8984/25/38/383201, 2013.

Petters, M. D. and Kreidenweis, S. M.: A single parameter representation of hygroscopic growth and cloud condensation nucleus activity, Atmos. Chem. Phys., 7(8), 1961–1971, doi:10.5194/acp-7-1961-2007, 2007.

Pfrang, C., Sebastiani, F., Lucas, C. O. M., King, M. D., Hoare, I. D., Chang, D. and Campbell, R. A.: Ozonolysis of methyl oleate monolayers at the air-water interface: Oxidation kinetics, reaction products and atmospheric implications, Phys. Chem. Chem. Phys., 16(26), 13220–13228, doi:10.1039/c4cp00775a, 2014.

Pfrang, C., Rastogi, K., Cabrera-Martinez, E. R., Seddon, A. M., Dicko, C., Labrador, A., Plivelic, T. S., Cowieson, N. and Squires, A. M.: Complex three-dimensional self-assembly in proxies for atmospheric aerosols, Nat. Commun., 8(1), 1724, doi:10.1038/s41467-017-01918-1, 2017.

Pöschl, U.: Atmospheric aerosols: Composition, transformation, climate and health effects, Angew. Chemie Int. Ed., 44(46), 7520–7540, doi:10.1002/anie.200501122, 2005.

Reid, J. P., Bertram, A. K., Topping, D. O., Laskin, A., Martin, S. T., Petters, M. D., Pope, F. D. and Rovelli, G.: The viscosity of atmospherically relevant organic particles, Nat. Commun., 9(1), 1–14, doi:10.1038/s41467-018-03027-z, 2018.

Renbaum-Wolff, L., Grayson, J. W., Bateman, A. P., Kuwata, M., Sellier, M., Murray, B. J., Shilling, J. E., Martin, S. T. and Bertram, A. K.: Viscosity of a-pinene secondary organic material and implications for particle growth and reactivity, Proc. Natl. Acad. Sci., 110(20), 8014–8019, doi:10.1073/pnas.1219548110, 2013.

Reynolds, J. C., Last, D. J., McGillen, M., Nijs, A., Horn, A. B., Percival, C., Carpenter, L. J. and Lewis, A. C.: Structural analysis of oligomeric molecules formed from the reaction products of oleic acid ozonolysis, Environ. Sci. Technol., 40(21), 6674–6681, doi:10.1021/es060942p, 2006.

Richardson, S. J., Staniec, P. A., Newby, G. E., Rawle, J. L., Slaughter, A. R., Terrill,

N. J., Elliott, J. M. and Squires, A. M.: Glycerol prevents dehydration in lipid cubic phases, Chem. Commun., 51, 11386–11389, doi:10.1039/c5cc03771a, 2015.

Rickards, A. M. J., Miles, R. E. H., Davies, J. F., Marshall, F. H. and Reid, J. P.: Measurements of the Sensitivity of Aerosol Hygroscopicity and the κ Parameter to the O/C Ratio, J. Phys. Chem. A, 117(51), 14120–14131, doi:10.1021/jp407991n, 2013.

Rudich, Y., Donahue, N. M. and Mentel, T. F.: Aging of Organic Aerosol: Bridging the Gap Between Laboratory and Field Studies, Annu. Rev. Phys. Chem., 58(1), 321–352, doi:10.1146/annurev.physchem.58.032806.104432, 2007.

Schill, S. R., Collins, D. B., Lee, C., Morris, H. S., Novak, G. A., Prather, K. A., Quinn, P. K., Sultana, C. M., Tivanski, A. V., Zimmermann, K., Cappa, C. D. and Bertram, T. H.: The impact of aerosol particle mixing state on the hygroscopicity of sea spray aerosol, ACS Cent. Sci., 1(3), 132–141, doi:10.1021/acscentsci.5b00174, 2015.

Schmedding, R., Rasool, Q. Z., Zhang, Y., Pye, H. O. T., Zhang, H., Chen, Y., Surratt, J. D., Lopez-Hilfiker, F. D., Thornton, J. A., Goldstein, A. H. and Vizuete, W.: Predicting secondary organic aerosol phase state and viscosity and its effect on multiphase chemistry in a regional-scale air quality model, Atmos. Chem. Phys., 20(13), 8201–8225, doi:10.5194/acp-20-8201-2020, 2020.

Sebastiani, F., Campbell, R. A., Rastogi, K. and Pfrang, C.: Nighttime oxidation of surfactants at the air-water interface: Effects of chain length, head group and saturation, Atmos. Chem. Phys., 18(5), 3249–3268, doi:10.5194/acp-18-3249-2018, 2018.

Seddon, J. M., Bartle, E. A. and Mingins, J.: Inverse cubic liquid-crystalline phases of phospholipids and related lyotropic systems, J. Phys. Condens. Matter, 2, SA285–SA290, doi:10.1088/0953-8984/2/S/043, 1990.

Shearman, G. C., Tyler, A. I. I., Brooks, N. J., Templer, R. H., Ces, O., Law, R. V. and Seddon, J. M.: Ordered micellar and inverse micellar lyotropic phases, Liq. Cryst., 37(6–7), 679–694, doi:10.1080/02678292.2010.484917, 2010.

Shiraiwa, M., Pfrang, C. and Pöschl, U.: Kinetic multi-layer model of aerosol surface and bulk chemistry (KM-SUB): The influence of interfacial transport and bulk diffusion on the oxidation of oleic acid by ozone, Atmos. Chem. Phys., 10, 3673–3691, doi:10.5194/acp-10-3673-2010, 2010.

Shiraiwa, M., Ammann, M., Koop, T. and Poschl, U.: Gas uptake and chemical aging of semisolid organic aerosol particles, Proc. Natl. Acad. Sci. U. S. A., 108(27), 11003–11008, doi:10.1073/pnas.1103045108, 2011a.

Shiraiwa, M., Ammann, M., Koop, T. and Pöschl, U.: Gas uptake and chemical aging of semisolid organic aerosol particles -Supporting information, Proc. Natl. Acad. Sci. U. S. A., 108(27), 11003–11008, doi:10.1073/pnas.1103045108, 2011b.

Shiraiwa, M., Li, Y., Tsimpidi, A. P., Karydis, V. A., Berkemeier, T., Pandis, S. N., Lelieveld, J., Koop, T. and Pöschl, U.: Global distribution of particle phase state in atmospheric secondary organic aerosols, Nat. Commun., 8, 1–7, doi:10.1038/ncomms15002, 2017.

Shrivastava, M., Lou, S., Zelenyuk, A., Easter, R. C., Corley, R. A., Thrall, B. D., Rasch, P. J., Fast, J. D., Simonich, S. L. M., Shen, H. and Tao, S.: Global long-range transport and lung cancer risk from polycyclic aromatic hydrocarbons shielded by coatings of organic aerosol, Proc. Natl. Acad. Sci. U. S. A., 114(6), 1246–1251, doi:10.1073/pnas.1618475114, 2017a.

Shrivastava, M., Cappa, C. D., Fan, J., Goldstein, A. H., Guenther, A. B., Jimenez, J. L.,

Kuang, C., Laskin, A., Martin, S. T., Ng, N. L., Petaja, T., Pierce, J. R., Rasch, P. J., Roldin, P., Seinfeld, J. H., Shilling, J., Smith, J. N., Thornton, J. A., Volkamer, R., Wang, J., Worsnop, D. R., Zaveri, R. A., Zelenyuk, A. and Zhang, Q.: Recent advances in understanding secondary organic aerosol: Implications for global climate forcing, Rev. Geophys., 55(2), 509–559, doi:10.1002/2016RG000540, 2017b.

Tandon, P., Raudenkolb, S., Neubert, R. H. H., Rettig, W. and Wartewig, S.: X-ray diffraction and spectroscopic studies of oleic acid-sodium oleate, Chem. Phys. Lipids, 109(1), 37–45, doi:10.1016/S0009-3084(00)00207-3, 2001.

Tiddy, G. J. T.: Surfactant-water liquid crystal phases, Phys. Rep., 57(1), 1–46, doi:10.1016/0370-1573(80)90041-1, 1980.

Topping, D. O., McFiggans, G. B. and Coe, H.: A curved multi-component aerosol hygroscopicity model framework: Part 1 - Inorganic compounds, Atmos. Chem. Phys., 5(5), 1205–1222, doi:10.5194/acp-5-1205-2005, 2005.

Vicente, E. D., Vicente, A., Evtyugina, M., Carvalho, R., Tarelho, L. A. C., Oduber, F. I. and Alves, C.: Particulate and gaseous emissions from charcoal combustion in barbecue grills, Fuel Process. Technol., 176, 296–306, doi:10.1016/j.fuproc.2018.03.004, 2018.

Virtanen, A., Joutsensaari, J., Koop, T., Kannosto, J., Yli-Pirilä, P., Leskinen, J., Mäkelä, J. M., Holopainen, J. K., Pöschl, U., Kulmala, M., Worsnop, D. R. and Laaksonen, A.: An amorphous solid state of biogenic secondary organic aerosol particles, Nature, 467(7317), 824–827, doi:10.1038/nature09455, 2010.

Wang, G., Kawamura, K., Shuncheng, L., Ho, K. and Cao, J.: Molecular , Seasonal , and Spatial Distributions of Organic Aerosols from Fourteen Chinese Cities, Environ.

Sci. Technol., 40, 4619–4625, doi:10.1021/es060291x, 2006.

Wexler, A. S. and Clegg, S. L.: Atmospheric aerosol models for systems including the ions H + , NH 4 + , Na + , SO 4 2− , NO 3 − , Cl − , Br − , and H 2 O, J. Geophys. Res., 107(D14), 4207, doi:10.1029/2001JD000451, 2002.

Woden, B., Skoda, M., Hagreen, M. and Pfrang, C.: Night-Time Oxidation of a Monolayer Model for the Air–Water Interface of Marine Aerosols—A Study by Simultaneous Neutron Reflectometry and in Situ Infra-Red Reflection Absorption Spectroscopy (IRRAS), Atmosphere, 9(12), 471, doi:10.3390/atmos9120471, 2018.

Woden, B., Skoda, M. W. A., Milsom, A., Gubb, C., Maestro, A., Tellam, J. and Pfrang, C.: Ozonolysis of fatty acid monolayers at the air–water interface: organic films may persist at the surface of atmospheric aerosols, Atmos. Chem. Phys., 21(2), 1325–1340, doi:10.5194/acp-21-1325-2021, 2021.

Ye, R. and Hayes, D. G.: Optimization of the solvent-free lipase-catalyzed synthesis of fructose-oleic acid ester through programming of water removal, JAOCS, J. Am. Oil Chem. Soc., 88(9), 1351–1359, doi:10.1007/s11746-011-1791-2, 2011.

Zahardis, J. and Petrucci, G. A.: The oleic acid-ozone heterogeneous reaction system: Products, kinetics, secondary chemistry, and atmospheric implications of a model system - A review, Atmos. Chem. Phys., 7(5), 1237–1274, doi:10.5194/acp-7-1237-2007, 2007.

Zahardis, J., LaFranchi, B. W. and Petrucci, G. A.: Photoelectron resonance capture ionization-aerosol mass spectrometry of the ozonolysis products of oleic acid particles: Direct measure of higher molecular weight oxygenates, J. Geophys. Res. D Atmos., 110(8), 1–10, doi:10.1029/2004JD005336, 2005.

Zeng, J., Yu, Z., Mekic, M., Liu, J., Li, S., Loisel, G., Gao, W., Gandolfo, A., Zhou, Z., Wang, X., Herrmann, H., Gligorovski, S. and Li, X.: Evolution of Indoor Cooking Emissions Captured by Using Secondary Electrospray Ionization High-Resolution Mass Spectrometry, Environ. Sci. Technol. Lett., 7(2), 76–81, doi:10.1021/acs.estlett.0c00044, 2020.

Zhao, Y., Huang, H., Zhang, Y., Wu, K., Zeng, F., Wang, J., Yu, X., Zhu, Z., Yu, X.-Y. and Wang, F.: Atmospheric particulate characterization by ToF-SIMS in an urban site in Beijing, Atmos. Environ., 220, 117090, doi:10.1016/j.atmosenv.2019.117090, 2020.

Zhou, S., Shiraiwa, M., McWhinney, R. D., Pöschl, U. and Abbatt, J. P. D.: Kinetic limitations in gas-particle reactions arising from slow diffusion in secondary organic aerosol, Faraday Discuss., 165, 391–406, doi:10.1039/c3fd00030c, 2013.

Zhou, S., Hwang, B. C. H., Lakey, P. S. J., Zuend, A., Abbatt, J. P. D. and Shiraiwa, M.: Multiphase reactivity of polycyclic aromatic hydrocarbons is driven by phase separation and diffusion limitations, Proc. Natl. Acad. Sci. U. S. A., 116(24), 11658–11663, doi:10.1073/pnas.1902517116, 2019.

Zobrist, B., Soonsin, V., Luo, B. P., Krieger, U. K., Marcolli, C., Peter, T. and Koop, T.: Ultra-slow water diffusion in aqueous sucrose glasses, Phys. Chem. Chem. Phys., 13(8), 3514–3526, doi:10.1039/c0cp01273d, 2011.

Zuend, A., Marcolli, C., Luo, B. P. and Peter, T.: A thermodynamic model of mixed organic-inorganic aerosols to predict activity coefficients, Atmos. Chem. Phys., 8(16), 4559–4593, doi:10.5194/acp-8-4559-2008, 2008.

Zuend, A., Marcolli, C., Booth, A. M., Lienhard, D. M., Soonsin, V., Krieger, U. K., Topping, D. O., McFiggans, G., Peter, T. and Seinfeld, J. H.: New and extended

parameterization of the thermodynamic model AIOMFAC: Calculation of activity coefficients for organic-inorganic mixtures containing carboxyl, hydroxyl, carbonyl, ether, ester, alkenyl, alkyl, and aromatic functional groups, Atmos. Chem. Phys., 11(17), 9155–9206, doi:10.5194/acp-11-9155-2011, 2011.

6 CHAPTER 6: EXPLORING THE NANOSTRUCTURES ACCESSIBLE TO AN ORGANIC SURFACTANT ATMOSPHERIC AEROSOL PROXY

This study is prepared for submission to a journal.

6.1 **Abstract**

The composition of atmospheric aerosols can vary with time, season, location and environment. This can affect key aerosol properties such as hygroscopicity and reactivity, influencing the aerosol's impact on the climate and urban environment. The organic fraction of atmospheric aerosol emissions can contain surfactant material, such as fatty acids. These molecules are known to form three-dimensional nanostructures in contact with water. Different nanostructures can have marked differences in viscosity and diffusivity - properties that are essential when considering an aerosol's atmospheric impact. We have explored a range of nanostructures accessible to an organic surfactant, oleic acid (commonly found in cooking emissions), simulating changes that can happen in the atmosphere. This was achieved by changing the amount of aqueous phase, aqueous phase salinity and by addition of other commonly co-emitted compounds: sugars and stearic acid (saturated oleic acid). The nanostructure was followed by laboratory and synchrotron Small Angle X-ray Scattering (SAXS) and was found to be sensitive to the proxy composition. This sensitivity suggests that compositional and subsequent nano-structural changes could affect aerosol processes, leading to an impact on the climate and urban air pollution. We have provided here a composition-nanostructure dataset which enables further study on the impact of these systems in an atmospheric context.

6.2 **Introduction**

Aerosols are emitted into the atmosphere and affect the climate and human health (Boucher et al., 2013; Pöschl, 2005). Their composition can vary with time, season, location and environment (Fu et al., 2008; Jimenez et al., 2009; Li et al., 2021; Wang et al., 2020a, 2020b). Aerosol components can be broadly split into an organic and inorganic fraction. An increased organic mass fraction has been linked with poor air quality (Zhao et al., 2020). Additionally, some organic emissions are surface active and can decrease surface tension and influence water uptake, affecting the ability of a particle to form a cloud droplet and therefore impacting on cloud formation and the climate (Bzdek et al., 2020; Forestieri et al., 2018; Ovadnevaite et al., 2017; Prisle et al., 2012).

Oleic acid is a commonly emitted organic surfactant, with sources including marine (Tervahattu, 2002; Tervahattu et al., 2005) and urban (Alves et al., 2020; Zeng et al., 2020; Zhao et al., 2015) emissions. This has made it the compound of choice for a reactive organic surfactant aerosol proxy (Al-Kindi et al., 2016; King et al., 2009; Milsom et al., 2021; Pfrang et al., 2017; Woden et al., 2021; Zahardis and Petrucci, 2007). Its surface-active nature can cause it to form self-assembled nanostructures when mixed with water and its salt (sodium oleate), these are called lyotropic liquid crystal (LLC) phases (Engblom et al., 1995; Mele et al., 2018; Pfrang et al., 2017). These nanostructures can range from spherical micelles to lamellar multi-layers and cylindrical arrangements with water channels, among others (Tiddy, 1980). Convention dictates that inverse LLC phases are where the surfactant tail is pointing away from the centre of the structure, so-called “water-in-oil” phases. These phases bring with them a unique set of physical characteristics. Viscosity can vary by orders of magnitude when the

surfactant nanostructure changes (Mezzenga et al., 2005). Furthermore, diffusion becomes anisotropic for the inverse hexagonal (an array of cylindrical micelles) and lamellar phase, the latter with lateral diffusion coefficients orders of magnitude higher than in the orthogonal direction (Lindblom and Wennerström, 1977). This has implications for the diffusion of small molecules, such as water and atmospheric oxidants, through these nanostructures.

Aerosol viscosity and the diffusivity of small molecules within aerosol particles have a profound effect on their reactivity and ability to take up water (Berkemeier et al., 2016; Mikhailov et al., 2009; Pfrang et al., 2011; Reid et al., 2018; Shiraiwa et al., 2011a). The phase state of atmospheric aerosols can range from liquid to semi-solid and solid and is dependent on location, season, composition and meteorology (Schmedding et al., 2020; Shiraiwa et al., 2017; Slade et al., 2019; Virtanen et al., 2010). Phase state can also vary in indoor particles, suggesting aerosol viscosity and diffusivity should be considered in such particles (Cummings et al., 2020). Armed with the knowledge that atmospheric aerosol composition and phase state can vary in the atmosphere, it follows that surfactant molecules (such as oleic acid) have the potential to form LLC nanostructures. This was shown to be feasible in a previous studies on a levitated oleic acid-sodium oleate proxy (Pfrang et al., 2017; Seddon et al., 2016) and the effect on reaction kinetics of the formation of one of these semi-solid nanostructures (lamellar) was quantified – lamellar phase formation reduced reactivity by *ca.* an order of magnitude (Milsom et al., 2021) (see chapter 2). Both of these studies contribute to explaining why oleic acid persists longer in the atmosphere compared with laboratory experiments, a long-standing issue in this field (Rudich et al., 2007).

This study seeks a better understanding of the nanostructures accessible to the oleic acid-sodium oleate-water organic surfactant aerosol proxy with the addition of other common atmospheric emissions (sugars and a saturated fatty acid) and by changing the amount and nature of the aqueous phase (*i.e.* changing the amount of aqueous phase and the aqueous phase's salinity). The oleic acid-sodium oleate system has been explored before in a biological context (Engblom et al., 1995; Mele et al., 2018; Seddon et al., 1990) and it has been studied qualitatively in an atmospheric context, demonstrating that nanostructure formation can occur (Pfrang et al., 2017). However, there is a lack of data regarding the systematic addition of atmospherically relevant molecules to the mixture. We do this by using Small Angle X-Ray Scattering (SAXS), a powerful technique used previously to probe aggregate structures on the nanometre scale (Milsom et al., 2021; Pfrang et al., 2017; Seddon et al., 2016). We observe and justify LLC phase changes and link them to variations in aerosol composition that can happen in the atmosphere, drawing atmospheric implications. We intend this to be a resource for subsequent studies on the effect of surfactant (oleic acid) nano-structure on aerosol physical properties, in an atmospheric context.

6.3 **Methods**

All self-assembled mixtures are based on mixtures of oleic acid and sodium oleate, continuing from previous studies on this self-assembled atmospheric aerosol proxy system (Milsom et al., 2021; Pfrang et al., 2017; Seddon et al., 2016). We define a "base" bulk mixture where the organic fraction was made by mixing oleic acid (Sigma-Aldrich, 90 % purity) and sodium oleate (Sigma-Aldrich, 99 % purity) in a 1:1 wt ratio for all mixtures except for where the oleic acid:sodium oleate wt ratio was varied. Aqueous phase (deionised water or NaCl solution) was added to afford a final organic-

aqueous ratio of 1:1 wt for this base mixture. Additional organic molecules (sugars and stearic acid) were added to the base mixture in the desired ratio (relative to the amount of oleic acid/sodium oleate) and the amount of aqueous phase was unchanged, except for where the amount of aqueous phase was varied.

In this study, the wt % quoted when referring to a compound in a sample means the weight percentage of the *organic* fraction of the organic-aqueous mixture (*e.g.* 33 wt % fructose means fructose makes up 33 wt % of the organic fraction). To clarify: an oleic acid-sodium oleate-fructose mixture at 1:1:1 organic wt ratio represents the original base mixture (oleic acid: sodium oleate: water {1:1:2 wt}) plus the additional fructose, representing 33 wt % of the organic fraction.

After weighing out and adding the organic and aqueous components together, the samples were vortex mixed, heated to ~ 50 ^{o}C for 20 min and vortex mixed again before being frozen in a conventional freezer. Samples appeared more homogeneous once frozen and thawed slowly. Before SAXS pattern measurement, samples were allowed to stand at room temperature for at least 1 day and were once again vortex mixed before being put inside X-ray capillary tubes for the SAXS experiment.

SAXS is a technique used to probe aggregate materials on the nanoscale (Pauw, 2013). Self-assembled LLC phases scatter X-rays to small angles and give scattering patterns with characteristic Bragg peaks (Kulkarni et al., 2011). This scattered intensity is measured against a scattering parameter (q), which is inversely proportional to the spacing between equivalent scattering planes (d):

$$q = \frac{2\pi}{d} \tag{6-1}$$

This *d*-spacing can change with increasing/decreasing water content as water is gained/lost from the nanostructure (Rittman et al., 2013). The relative position of each scattering peak for a given nanostructure is known and can be used to determine which nanostructure is present (see Fig. 6-1 for example SAXS patterns for each observed phase and peaks labelled with their corresponding *q* position ratios) (Kulkarni et al., 2011; Shearman et al., 2010).

A combination of synchrotron and laboratory SAXS instrumentation was used to carry out the SAXS experiment. Simultaneous wide-angle X-ray scattering (WAXS) was possible with the synchrotron setup, probing smaller repeat distances.

Synchrotron SAXS/WAXS experiments were carried out on the I22 beamline at the Diamond Light Source (UK). SAXS and WAXS patterns were measured by X-rays of 12.4 keV energy with 0.1 s collection times. The sample-to-detector distance was 3 m. The *q*-range for the SAXS and WAXS measurements were 0.008 – 0.46 and 0.4 – 0.6 $Å^{-1}$, respectively. Samples were mounted in a sample rack enclosed by sticky tape.

An Anton Parr *SAXSpoint 2.0* instrument was used to carry out the laboratory SAXS experiment. A Cu source produced X-rays of 1.54 Å wavelength. The sample-to-detector distance was 0.360 m and patterns were collected for ~ 3 – 5 min for each sample. Samples were enclosed in Kapton tubes and mounted on a sample rack.

Further SAXS/WAXS experiments on mixtures with multiple additives were carried out on a *Xenocs Xeuss 2.0* with a Cu X-ray source and a sample-to-detector distance of 1.185 m. A sample-to-detector distance of 0.162 m was used for WAXS measurements taken after the initial SAXS measurement. Samples were mounted between two Kapton windows.

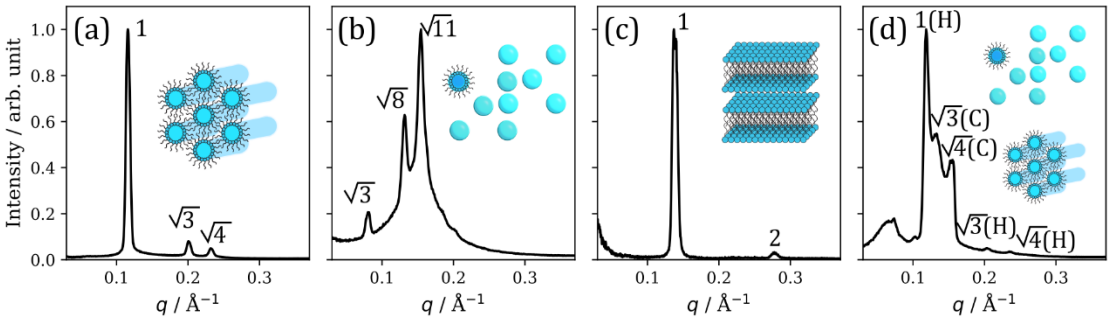

Figure 6-1. Example 1-D SAXS patterns for the fatty acid nanostructures observed in this study. (a) Inverse hexagonal phase; (b) Cubic close-packed inverse micelles (Fd3m symmetry); (c) Lamellar bilayers; (d) Mixture of Cubic close-packed inverse micelles (Fm3m symmetry) and inverse hexagonal phase. Cartoons of each of these phases are also presented (not to scale). Each peak is labelled with the peak position ratio expected for each phase – i.e. *for the lamellar phase in panel (c), the 2nd peak appears at 2 x 1st peak position value (in q). For panel (d), inverse hexagonal and cubic phase peaks are labelled (H) and (C), respectively.*

After collection of the 2-D SAXS pattern from each sample, a radial integration was performed over the *q*-range ~ 0.06 – 0.37 Å^{-1} to afford a 1-D scattering pattern. Examples of scattering patterns for the phases observed in this study are presented in Fig. 6-1. Cartoons of each phase are also presented.

6.4 **Results and discussion**

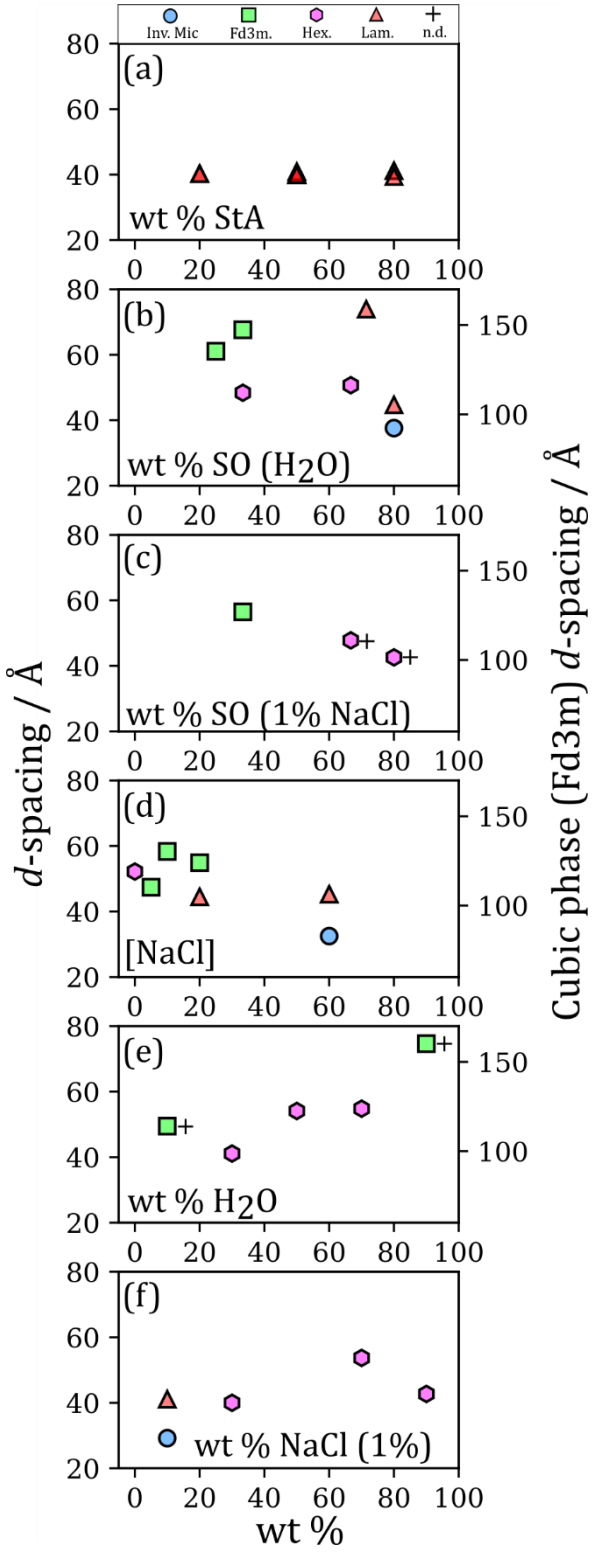

Figure 6-2. Plots of observed nanostructures and their calculated d-spacings vs wt % of each component added to the base mixture: oleic acid:sodium oleate (1:1) 50 % wt in H_2O – exception for the experiment series varying wt % H_2O and wt % NaCl (1%) solution. (a) wt % StA; (b) wt % SO in H_2O; (c) wt % SO in NaCl (1%); (d) [NaCl]; (e) wt % H_2O; (f) wt % NaCl (1%). The d-spacings for the cubic (Fd3m symmetry) nanostructure are placed on a different scale (right-hand side) due to the large difference in values compared to the other nanostructures. StA: Stearic acid (saturated oleic acid analogue); SO: sodium oleate. Phases are abbreviated: Inverse micellar (Inv. Mic.); Fd3m-symmetry cubic close-packed inverse micelles (Fd3m); inverse hexagonal (Hex.); lamellar (Lam.); not determined due to overlapping peaks (n. d.).

6.4.1 **Changing the nature of the surfactant**

Oleic acid is typically found and characterised in organic emissions with its saturated analogue, stearic acid (Alves et al., 2020). The relative proportions of these molecules can vary and can be a measure of how much a sample has aged (Wang et al., 2020a). Figure 6-2(a) shows that the equilibrium phase observed for dry mixtures of oleic acid and stearic acid is the lamellar phase. One can assume that this is a crystalline structure due to the lack of water in the system and peaks observable in the wide-angle X-ray scattering (WAXS) region (see the appendix section 10.5.1). Note that the *d*-spacing for all oleic acid-stearic acid compositions is slightly smaller than that of the dry oleic acid-sodium oleate mixture by 3 – 4 Å. This suggests that the alkyl chain monolayers of the lamellar bilayer are able to pack closer together, presumably due to the lack of a kink in the stearic acid alkyl chain compared to the one induced by the *cis*-double-bond in oleic acid. The presence of WAXS peaks supports this, these peaks arise from well-packed adjacent alkyl chains (see Fig. 10-13, the appendix).

We have noted in previous work that the availability of the double bond to the atmospheric oxidant ozone is likely to be affected by the spacing between alkyl chains by reducing the diffusivity of ozone through the organic phase, limiting the reaction to the surface layers (at least initially) (Milsom et al., 2021) – a theory also described by Hearn *et al*. (Hearn et al., 2005). This may also help explain the trend in reactivity observed by Katrib *et al.* who reacted oleic acid-stearic acid particles with ozone. They observed that ozonolysis was severely reduced at high stearic acid compositions (Katrib et al., 2005). Though explanations were offered, no experiments on the nanostructure of those particles were done and we suggest that the formation of these tightly packed lamellae could play a role in determining reactivity.

Aerosol particle acidity can vary with a typical pH range of ~ 1 – 6, though this is difficult to measure directly and is normally inferred by applying theoretical models (Kakavas et al., 2021; Keene et al., 1998, 2004; Tao et al., 2020). This would affect the degree to which weak acids, such as oleic acid (pK_a ~5), are protonated. The surfactant headgroup charge affects the effective headgroup area which in turn can modify the curvature of a LLC phase (Tiddy, 1980). We simulated a change in headgroup charge by adding increasing amounts of sodium oleate to oleic acid. Figure 6-2(b) demonstrates that increasing the headgroup charge (effective headgroup area) increases the curvature of the headgroup-aqueous phase interface. This results in the following trend from low to high wt % sodium oleate: close-packed inverse micellar phase (Fd3m symmetry), inverse hexagonal phase (array of cylindrical micelles) and the lamellar phase.

Note that coexistent phases were also observed and were determined where more than one SAXS peak clearly indexed to a certain phase. Coexisting phases are a feature of this study and have atmospheric implications (see section 6.5 for a discussion).

6.4.2 **Changing the nature of the aqueous phase**

Soluble inorganic species are components of atmospheric aerosols. Dissolved inorganic species affect the ionic strength of a solution, which in turn can affect the surfactant headgroup-aqueous phase interfacial curvature by shielding headgroup charge. As a result, molecular self-assembly can be influenced by the presence of dissolved inorganic species (Koynova et al., 1997).

Adding 1 wt % NaCl solution to the mixtures of varying sodium oleate content returned phases with higher curvature compared with the non-saline aqueous phase (Fig. 6-2(c)). Even at high sodium oleate content (80 wt %) the hexagonal phase prevailed. This is

due to the NaCl acting as a *kosmotrope* (water structure inducer), removing water from the headgroup-aqueous interface and stabilising higher curvature interfaces (Koynova et al., 1997). Increasing the salt concentration provides additional confirmation of this effect: an inverse hexagonal phase was observed in the salt-free mixture, whereas a more curved ordered inverse micellar phase (Fd3m symmetry) was observed at an aqueous phase salt concentration of 10 wt % NaCl (Fig. 6-2(d)). A change in aqueous phase salinity can therefore have a significant effect on the molecular arrangement of this proxy.

Atmospheric humidity plays a role in determining aerosol properties such as phase state, affecting ageing processes such as multiphase reactions and water uptake (Pajunoja et al., 2016). We varied the water content of the base proxy mixture in order to simulate variations in aerosol water content. Filling the water cavity of an inverse topology phase is expected to induce the formation of phases with lower interfacial curvature – *i.e.* filling a spherical inverse micelle with increasing amounts of water will eventually cause the cylindrical inverse hexagonal phase to form (Engblom et al., 1995; Mele et al., 2018).

Figure 6-2(e) shows the progression from the more-curved close-packed inverse micellar phase to the less-curved inverse hexagonal phase with increasing water content. This is in line with expectations. Furthermore, the hexagonal *d*-spacing (derived from the position of the SAXS peaks) increases with water content (see 30 – 50 wt % data points in Fig. 6-2(e)). Note that the *d*-spacing stays roughly constant past 50 wt %, confirming that phases observed at water contents at or above this value are "excess water" phases. The close-packed inverse micellar phase is a viscous, translucent substance whereas the inverse hexagonal phase is opaque and diffusion of small

molecules through its water channels is directionally dependent (Zabara and Mezzenga, 2014). A relatively small change in water content (from 10 to 30 wt %) resulted in a transition between these two molecular arrangements with quite different physical properties – the atmospheric significance of this is discussed later. A similar trend is observed when adding varying amounts of 1 wt % NaCl solution (Fig. 6-2(f)). The maximum inverse hexagonal *d*-spacing is greater than what was observed for the non-saline aqueous phase, suggesting that the increase in ionic strength stabilises larger water channels.

6.4.3 **Addition of sugars**

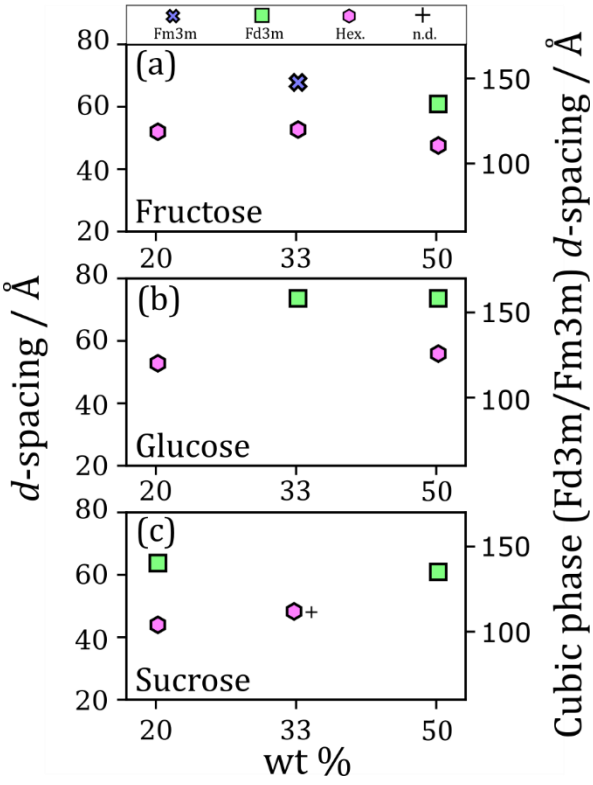

Figure 6-11. Plots of observed nanostructures and their calculated d-spacings vs wt % of each sugar added to the base mixture: oleic acid:sodium oleate (1:1) 50 % wt in H_2O. (a) wt % fructose; (b) wt % glucose; (c) wt % sucrose. The d-spacings for the cubic (Fd3m symmetry) nanostructure are placed on a different scale due to the large difference in values compared to the other nanostructures. Fru: fructose; Glu: glucose; Suc: sucrose. Phases are abbreviated: Fm3m-symmetry cubic close-packed inverse micelles (Fm3m); Fd3m-symmetry cubic close-packed inverse micelles (Fd3m); inverse hexagonal (Hex.); lamellar (Lam.); not determined due to overlapping peaks (n. d.).

Fatty acids and sugars have been identified together as major constituents of particulate matter in both the urban and marine environments (Fu et al., 2013; Kirpes et al., 2019;

Wang et al., 2006, 2020b) and the relative amounts of these molecules can vary on an hourly basis (Wang et al., 2020a). This motivates the study of the effect sugar molecules have on the resulting fatty acid nanostructures observed in this proxy system.

The amount and identity of the sugar affects the fatty acid nanostructure (Fig. 6-3). There is a trend common to all sugars studied: the curvature of the inverse phase increases with increasing sugar concentration – *i.e.* the nanostructure progresses from a cylindrical inverse hexagonal phase to a spherical ordered inverse micellar phase. We ascribe this to the sugars acting as kosmotropes, removing water from the aqueous-surfactant headgroup interface and reducing the effective headgroup area (Koynova et al., 1997).

Fructose and glucose are closely related, having the same molecular mass. Despite this, the 33 wt % glucose and corresponding fructose mixtures returned ordered inverse micellar phases with differing symmetry. This kind of variation in close-packed inverse micellar symmetry has been observed before in levitated particles of this proxy (without sugars), suggesting that these two symmetries are thermodynamically similar (Pfrang et al., 2017). The difference could also arise from the co-existing phases competing for water.

Sucrose, being a disaccharide, has been shown to be a stronger kosmotrope than glucose and fructose (Koynova et al., 1997). This is demonstrated in Fig. 6-3(c), where at 20 wt % sucrose a close-packed inverse micellar phase is observed with a coexisting inverse hexagonal phase. This is not the case for the two monosaccharides (glucose and fructose), even though sucrose is 2-fold more dilute in terms of molarity. Therefore the

nature of the sugar, in addition to the amount of sugar, has a marked effect on nano-structural outcome.

6.4.4 5- and 6-component mixtures

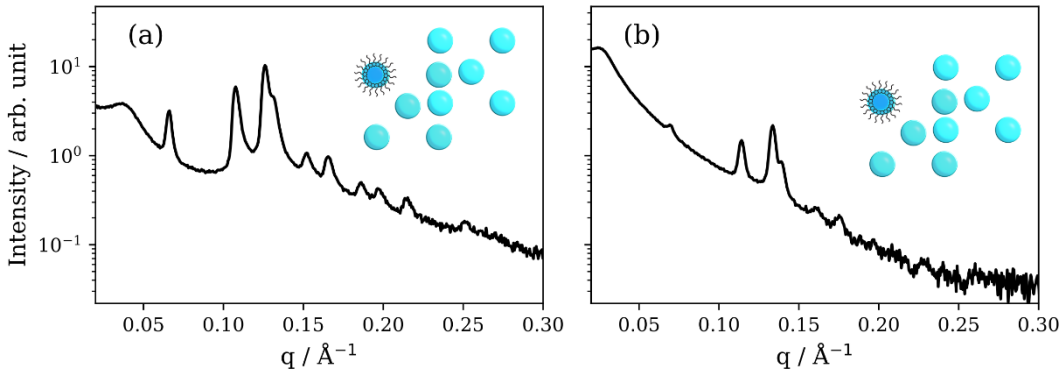

Figure 6-4. SAXS patterns from 5- and 6-component mixtures. (a) Oleic acid-sodium oleate-fructose-glucose (1:1:1:1 wt) 50 wt % H_2O, corresponding to a clear close-packed inverse micellar phase with Fd3m symmetry. (b) oleic acid-sodium-oleate-fructose-glucose-sucrose (1:1:1:1:1 wt) 50 wt % H_2O, corresponding to a close-packed inverse micellar phase with Fd3m symmetry. Cartoons of each phase are presented.

We assessed the effect of adding more than one sugar component to the base organic mixture. An inverse micellar cubic phase with Fd3m symmetry was observed for both mixtures (Fig. 6-4). Details of how this was determined are in the appendix section 10.5.3. The *d*-spacing was 166 Å for the 5-component mixture, decreasing to 157 Å in the 6-component mixture. Adding more components to the aqueous phase therefore decreases the size of the inverse micelles present in this structure.

The dominance of close-packed inverse micelles in these multi-component mixtures was unexpected. A broad peak at low-*q* (~ 0.02 Å^{-1}) is most probably due to a coexistent disordered inverse micellar phase. This inverse micellar phase peak is more prominent

for the 6-component mixture. In both cases the close-packing of these inverse micelles imply an increase in viscosity, potentially by orders of magnitude (Pouzot et al., 2007). This has potential atmospheric implications discussed in the next section.

6.4.5 Atmospheric implications

Atmospheric aerosol composition is dynamic and can change with environment, season, time of day and emission source (Jimenez et al., 2009; Kang et al., 2017; Wang et al., 2006, 2020a, 2020b). In light of this, our results suggest that a variation in aerosol composition could have a marked impact on the resulting molecular arrangements of organic surfactants found in these aerosols - a major class of which being fatty acids, such as oleic acid studied here. These differences in nanostructure bring with them differing properties, two of which are key when considering aerosol processes: viscosity and optical characteristics.

The viscosity of atmospheric aerosol particles affects water uptake and chemical reactivity – two determiners of aerosol persistence and subsequent influence on the atmosphere (Reid et al., 2018). A range of aerosol phase states, from solid to liquid, are possible indoors and outdoors (Cummings et al., 2020; Schmedding et al., 2020; Shiraiwa et al., 2017; Virtanen et al., 2010). Our work shows that changes in organic composition, water content, and salinity can cause LLC phase transitions. Viscosity can vary by orders of magnitude between nanostructures. For example, viscosity is roughly an order of magnitude higher for the inverse hexagonal phase compared with the close-packed inverse micellar (Fd3m) phase (Mezzenga et al., 2005; Pouzot et al., 2007). Additionally, diffusion becomes anisotropic for the lamellar and inverse hexagonal phases – there are orders of magnitude difference between lateral and orthogonal diffusion in the lamellar phase (Lindblom and Wennerström, 1977). These variations in

viscosity and diffusivity have implications for the uptake of trace gases (*e.g.* water vapour and atmospheric oxidants) into aerosol particles and can determine the timescale of bulk diffusion within them, impacting on aerosol persistence and atmospheric lifetime (Berkemeier et al., 2016; Mu et al., 2018; Shiraiwa et al., 2011b; Shrivastava et al., 2017).

Heterogeneity is a feature of many atmospheric aerosols. A range of imaging techniques have demonstrated that atmospheric aerosols are not always well-mixed (Laskin et al., 2019). For example, organic coatings are present on marine aerosols (Tervahattu, 2002), occasionally resulting in an inorganic core-organic shell morphology (Kirpes et al., 2019). Phase separation also happens in liquid particles (Freedman, 2020) and heterogeneities in particle viscosity have been observed to develop during the ozonolysis of an oleic acid aerosol proxy (Hosny et al., 2013, 2016). During this study, an appreciable amount of nano-structural heterogeneity was observed. The most common coexisting phases were the inverse hexagonal and ordered inverse micellar phases. As discussed previously, there are significant differences in physical characteristics between these two phases due to their different geometries. We have shown that composition influences fatty acid nanostructure. If aerosol composition varies within a single aerosol particle, there could be a similar spatial heterogeneity in fatty acid nanostructure, impacting aerosol processes and subsequent effects on urban air pollution and climate.

Aerosol optical properties can vary with environment and over time (Li et al., 2021), with aerosol light scattering and absorption contributing to climatic radiative forcing (Pöschl, 2005). We found visual differences between the optically isotropic phases with cubic symmetry (close-packed inverse micellar) and optically anisotropic phases

(lamellar and inverse hexagonal) (Hyde, 2001): the former being translucent and the latter opaque. This observation suggests that aerosol light scattering could be affected by the optical characteristics of the fatty acid nanostructures, resulting in an indirect effect on the climate.

6.5 **Conclusions**

We have explored the molecular arrangements accessible to the oleic acid-sodium oleate fatty acid aerosol proxy. This was achieved by addition of other common atmospheric emissions (sugars and saturated fatty acids) and by adjusting the amount and salinity of the aqueous phase. Notably, the composition of the proxy heavily influenced the resulting molecular arrangements. Even over a small range of aqueous phase salinity, a phase transition was observed between two nanostructures known to have different physical characteristics.

Bridging the gap between simple aerosol proxy systems and real atmospheric measurements continues to be a challenge. However, this study is a step towards linking the laboratory with the real world when considering the relatively novel proposition of LLC phase formation in the atmosphere.

The potential importance of fatty acid self-organisation in the atmosphere is added to by the demonstration of the range of (often co-existing) nanostructures observed in this study. We now have better knowledge of the phase space accessible to these molecules, providing a basis for future, more quantitative investigations into the physical characteristics of the nanostructures discussed in this study.

6.6 **Acknowledgements**

AM acknowledges funding by the NERC SCENARIO DTP (NE/L002566/1) and support from the NERC CENTA DTP. This work was carried out with the support of the Diamond Light Source (DLS), instrument I22 (proposal SM28020). We acknowledge the help of Olga Shebanova and Andy Smith (DLS) for carrying out the mail-in experiment at DLS. We acknowledge the Research England funded TALENT: Technician Led Equipment Fund for enabling SAXS measurements on the more complex mixtures.

6.6.1 **Contributors**

Adam Milsom carried out SAXS experiments, wrote the manuscript, processed and analysed the data. Christian Pfrang and Adam Squires contributed to the interpretation of the data. Olga Shebanova and Andy Smith (DLS) organised and carried out the mail-in SAXS/WAXS experiments on the stearic acid-containing mixtures. Steve Huband carried out SAXS measurements on the 5- and 6- component mixtures.

6.7 **Comment**

This study looked to explore the phase space accessible to this proxy system. What was surprising was that adding multiple components to the proxy returned clear cubic close-packed inverse micelles. The eternal problem with this kind of proxy is its simplicity. Aerosols are a mixture of many compounds, not all well mixed. This study presents, in a more systematic way than Pfrang *et al*. (Pfrang et al., 2017), what is possible in terms of nanostructures and what composition one would need to achieve such nanostructures. Getting oleic acid into these semi-solid states by following the composition-phase

dataset presented here could help future experimentalists study these phases with their own ideas and techniques.

6.8 References

Al-Kindi, S. S., Pope, F. D., Beddows, D. C., Bloss, W. J. and Harrison, R. M.: Size-dependent chemical ageing of oleic acid aerosol under dry and humidified conditions, Atmos. Chem. Phys., 16(24), 15561–15579, doi:10.5194/acp-16-15561-2016, 2016.

Alves, C. A., Vicente, E. D., Evtyugina, M., Vicente, A. M., Nunes, T., Lucarelli, F., Calzolai, G., Nava, S., Calvo, A. I., Alegre, C. del B., Oduber, F., Castro, A. and Fraile, R.: Indoor and outdoor air quality: A university cafeteria as a case study, Atmos. Pollut. Res., 11(3), 531–544, doi:10.1016/j.apr.2019.12.002, 2020.

Berkemeier, T., Steimer, S. S., Krieger, U. K., Peter, T., Pöschl, U., Ammann, M. and Shiraiwa, M.: Ozone uptake on glassy, semi-solid and liquid organic matter and the role of reactive oxygen intermediates in atmospheric aerosol chemistry, Phys. Chem. Chem. Phys., 18(18), 12662–12674, doi:10.1039/c6cp00634e, 2016.

Boucher, O., Randall, D., Artaxo, P., Bretherton, C., Feingold, G., Forster, P., Kerminen, V.-M., Kondo, Y., Liao, H., Lohmann, U., Rasch, P., Satheesh, S. K., Sherwood, S., Stevens, B. and Zhang, X. Y.: Clouds and Aerosols, in Climate Change 2013 - The Physical Science Basis, edited by Intergovernmental Panel on Climate Change, pp. 571–658, Cambridge University Press, Cambridge., 2013.

Bzdek, B. R., Reid, J. P., Malila, J. and Prisle, N. L.: The surface tension of surfactant-containing, finite volume droplets, Proc. Natl. Acad. Sci. U. S. A., 117(15), 8335–8343, doi:10.1073/pnas.1915660117, 2020.

Cummings, B. E., Li, Y., Decarlo, P. F., Shiraiwa, M. and Waring, M. S.: Indoor aerosol water content and phase state in U.S. residences: Impacts of relative humidity, aerosol mass and composition, and mechanical system operation, Environ. Sci. Process. Impacts, 22(10), 2031–2057, doi:10.1039/d0em00122h, 2020.

Engblom, J., Engström, S. and Fontell, K.: The effect of the skin penetration enhancer Azone® on fatty acid-sodium soap-water mixtures, J. Control. Release, 33(2), 299–305, doi:10.1016/0168-3659(94)00105-4, 1995.

Forestieri, S., Staudt, S. M., Kuborn, T. M., Faber, K., Christopher, R., Bertram, T. H. and Cappa, C. D.: Establishing the Impact of Model Surfactants on Cloud Condensation Nuclei Activity of Sea Spray Aerosols, , 18(15), 10985–11005, doi:10.5194/acp-18-10985-2018, 2018.

Freedman, M. A.: Liquid–Liquid Phase Separation in Supermicrometer and Submicrometer Aerosol Particles, Acc. Chem. Res., 53(6), 1102–1110, doi:10.1021/acs.accounts.0c00093, 2020.

Fu, P., Kawamura, K., Okuzawa, K., Aggarwal, S. G., Wang, G., Kanaya, Y. and Wang, Z.: Organic molecular compositions and temporal variations of summertime mountain aerosols over Mt. Tai, North China Plain, J. Geophys. Res. Atmos., 113(19), 1–20, doi:10.1029/2008JD009900, 2008.

Fu, P. Q., Kawamura, K., Chen, J., Charrière, B. and Sempéré, R.: Organic molecular composition of marine aerosols over the Arctic Ocean in summer: Contributions of primary emission and secondary aerosol formation, Biogeosciences, 10(2), 653–667, doi:10.5194/bg-10-653-2013, 2013.

Hearn, J. D., Smith, G. D. and Lovett, A. J.: Ozonolysis of oleic acid particles: evidence

for a surface reaction and secondary reactions involving Criegee intermediates, Phys. Chem. Chem. Phys., 7(3), 501–511, doi:10.1039/b414472d, 2005.

Hosny, N. A., Fitzgerald, C., Tong, C., Kalberer, M., Kuimova, M. K. and Pope, F. D.: Fluorescent lifetime imaging of atmospheric aerosols: A direct probe of aerosol viscosity, Faraday Discuss., 165, 343–356, doi:10.1039/c3fd00041a, 2013.

Hosny, N. A., Fitzgerald, C., Vyšniauskas, A., Athanasiadis, A., Berkemeier, T., Uygur, N., Pöschl, U., Shiraiwa, M., Kalberer, M., Pope, F. D. and Kuimova, M. K.: Direct imaging of changes in aerosol particle viscosity upon hydration and chemical aging, Chem. Sci., 7(2), 1357–1367, doi:10.1039/c5sc02959g, 2016.

Hyde, S. T.: Identification of Lyotropic Liquid Crystalline Mesophases, in Handbook of Applied Surface and Colloid Chemistry, vol. 2, edited by K. Holmberg, pp. 299–327, John Wiley & Sons, Hoboken., 2001.

Jimenez, J. L., Canagaratna, M. R., Donahue, N. M., Prevot, A. S. H., Zhang, Q., Kroll, J. H., DeCarlo, P. F., Allan, J. D., Coe, H., Ng, N. L., Aiken, A. C., Docherty, K. S., Ulbrich, I. M., Grieshop, A. P., Robinson, A. L., Duplissy, J., Smith, J. D., Wilson, K. R., Lanz, V. A., Hueglin, C., Sun, Y. L., Tian, J., Laaksonen, A., Raatikainen, T., Rautiainen, J., Vaattovaara, P., Ehn, M., Kulmala, M., Tomlinson, J. M., Collins, D. R., Cubison, M. J., Dunlea, J., Huffman, J. A., Onasch, T. B., Alfarra, M. R., Williams, P. I., Bower, K., Kondo, Y., Schneider, J., Drewnick, F., Borrmann, S., Weimer, S., Demerjian, K., Salcedo, D., Cottrell, L., Griffin, R., Takami, A., Miyoshi, T., Hatakeyama, S., Shimono, A., Sun, J. Y., Zhang, Y. M., Dzepina, K., Kimmel, J. R., Sueper, D., Jayne, J. T., Herndon, S. C., Trimborn, A. M., Williams, L. R., Wood, E. C., Middlebrook, A. M., Kolb, C. E., Baltensperger, U. and Worsnop, D. R.: Evolution of

Organic Aerosols in the Atmosphere, Science, 326(5959), 1525–1529, doi:10.1126/science.1180353, 2009.

Kakavas, S., Patoulias, D., Zakoura, M., Nenes, A. and Pandis, S. N.: Size-resolved aerosol pH over Europe during summer, Atmos. Chem. Phys., 21(2), 799–811, doi:10.5194/acp-21-799-2021, 2021.

Kang, M., Yang, F., Ren, H., Zhao, W., Zhao, Y., Li, L., Yan, Y., Zhang, Y., Lai, S., Zhang, Y., Yang, Y., Wang, Z., Sun, Y. and Fu, P.: Influence of continental organic aerosols to the marine atmosphere over the East China Sea: Insights from lipids, PAHs and phthalates, Sci. Total Environ., 607–608, 339–350, doi:10.1016/j.scitotenv.2017.06.214, 2017.

Katrib, Y., Biskos, G., Buseck, P. R., Davidovits, P., Jayne, J. T., Mochida, M., Wise, M. E., Worsnop, D. R. and Martin, S. T.: Ozonolysis of mixed oleic-acid/stearic-acid particles: Reaction kinetics and chemical morphology, J. Phys. Chem. A, 109(48), 10910–10919, doi:10.1021/jp054714d, 2005.

Keene, W. C., Sander, R., Pszenny, A. A. P., Vogt, R., Crutzen, P. J. and Galloway, J. N.: Aerosol pH in the marine boundary layer: A review and model evaluation, J. Aerosol Sci., 29(3), 339–356, doi:10.1016/S0021-8502(97)10011-8, 1998.

Keene, W. C., Pszenny, A. A. P., Maben, J. R., Stevenson, E. and Wall, A.: Closure evaluation of size-resolved aerosol pH in the New England coastal atmosphere during summer, J. Geophys. Res. D Atmos., 109(23), 1–16, doi:10.1029/2004JD004801, 2004.

King, M. D., Rennie, A. R., Thompson, K. C., Fisher, F. N., Dong, C. C., Thomas, R. K., Pfrang, C. and Hughes, A. V.: Oxidation of oleic acid at the air-water interface and its potential effects on cloud critical supersaturations, Phys. Chem. Chem. Phys.,

11(35), 7699–7707, doi:10.1039/b906517b, 2009.

Kirpes, R. M., Bonanno, D., May, N. W., Fraund, M., Barget, A. J., Moffet, R. C., Ault, A. P. and Pratt, K. A.: Wintertime Arctic Sea Spray Aerosol Composition Controlled by Sea Ice Lead Microbiology, ACS Cent. Sci., 5(11), 1760–1767, doi:10.1021/acscentsci.9b00541, 2019.

Koynova, R., Brankov, J. and Tenchov, B.: Modulation of lipid phase behavior by kosmotropic and chaotropic solutes, Eur. Biophys. J., 25(4), 261–274, doi:10.1007/s002490050038, 1997.

Kulkarni, C. V., Wachter, W., Iglesias-Salto, G., Engelskirchen, S. and Ahualli, S.: Monoolein: a magic lipid?, Phys. Chem. Chem. Phys., 13(8), 3004–3021, doi:10.1039/C0CP01539C, 2011.

Laskin, A., Moffet, R. C. and Gilles, M. K.: Chemical Imaging of Atmospheric Particles, Acc. Chem. Res., 52(12), 3419–3431, doi:10.1021/acs.accounts.9b00396, 2019.

Li, G., Su, H., Ma, N., Tao, J., Kuang, Y., Wang, Q., Hong, J., Zhang, Y., Kuhn, U., Zhang, S., Pan, X., Lu, N., Tang, M., Zheng, G., Wang, Z., Gao, Y., Cheng, P., Xu, W., Zhou, G., Zhao, C., Yuan, B., Shao, M., Ding, A., Zhang, Q., Fu, P., Sun, Y., Pöschl, U. and Cheng, Y.: Multiphase chemistry experiment in Fogs and Aerosols in the North China Plain (McFAN): integrated analysis and intensive winter campaign 2018, Faraday Discuss., 226, 207-222, doi:10.1039/D0FD00099J, 2021.

Lindblom, G. and Wennerström, H.: Amphiphile diffusion in model membrane systems studied by pulsed NMR, Biophys. Chem., 6(2), 167–171, doi:10.1016/0301-4622(77)87006-3, 1977.

Mele, S., Söderman, O., Ljusberg-Wahrén, H., Thuresson, K., Monduzzi, M. and Nylander, T.: Phase behavior in the biologically important oleic acid/sodium oleate/water system, Chem. Phys. Lipids, 211, 30–36, doi:10.1016/j.chemphyslip.2017.11.017, 2018.

Mezzenga, R., Meyer, C., Servais, C., Romoscanu, A. I., Sagalowicz, L. and Hayward, R. C.: Shear rheology of lyotropic liquid crystals: A case study, Langmuir, 21(8), 3322–3333, doi:10.1021/la046964b, 2005.

Mikhailov, E., Vlasenko, S., Martin, S. T., Koop, T. and Pöschl, U.: Amorphous and crystalline aerosol particles interacting with water vapor: Conceptual framework and experimental evidence for restructuring, phase transitions and kinetic limitations, Atmos. Chem. Phys., 9(24), 9491–9522, doi:10.5194/acp-9-9491-2009, 2009.

Milsom, A., Squires, A. M., Woden, B., Terrill, N. J., Ward, A. D. and Pfrang, C.: The persistence of a proxy for cooking emissions in megacities: a kinetic study of the ozonolysis of self-assembled films by simultaneous small and wide angle X-ray scattering (SAXS/WAXS) and Raman microscopy, Faraday Discuss., 226, 364–381, doi:10.1039/D0FD00088D, 2021.

Mu, Q., Shiraiwa, M., Octaviani, M., Ma, N., Ding, A., Su, H., Lammel, G., Pöschl, U. and Cheng, Y.: Temperature effect on phase state and reactivity controls atmospheric multiphase chemistry and transport of PAHs, Sci. Adv., 4(3), eaap7314, doi:10.1126/sciadv.aap7314, 2018.

Ovadnevaite, J., Zuend, A., Laaksonen, A., Sanchez, K. J., Roberts, G., Ceburnis, D., Decesari, S., Rinaldi, M., Hodas, N., Facchini, M. C., Seinfeld, J. H. and O'Dowd, C.: Surface tension prevails over solute effect in organic-influenced cloud droplet

activation, Nature, 546(7660), 637–641, doi:10.1038/nature22806, 2017.

Pajunoja, A., Hu, W., Leong, Y. J., Taylor, N. F., Miettinen, P., Palm, B. B., Mikkonen, S., Collins, D. R., Jimenez, J. L. and Virtanen, A.: Phase state of ambient aerosol linked with water uptake and chemical aging in the southeastern US, Atmos. Chem. Phys., 16(17), 11163–11176, doi:10.5194/acp-16-11163-2016, 2016.

Pauw, B. R.: Everything SAXS: small-angle scattering pattern collection and correction, J. Phys. Condens. Matter, 25(38), 383201, doi:10.1088/0953-8984/25/38/383201, 2013.

Pfrang, C., Shiraiwa, M. and Pöschl, U.: Chemical ageing and transformation of diffusivity in semi-solid multi-component organic aerosol particles, Atmos. Chem. Phys., 11(14), 7343–7354, doi:10.5194/acp-11-7343-2011, 2011.

Pfrang, C., Rastogi, K., Cabrera-Martinez, E. R., Seddon, A. M., Dicko, C., Labrador, A., Plivelic, T. S., Cowieson, N. and Squires, A. M.: Complex three-dimensional self-assembly in proxies for atmospheric aerosols, Nat. Commun., 8(1), 1724, doi:10.1038/s41467-017-01918-1, 2017.

Pöschl, U.: Atmospheric aerosols: Composition, transformation, climate and health effects, Angew. Chemie Int. Ed., 44(46), 7520–7540, doi:10.1002/anie.200501122, 2005.

Pouzot, M., Mezzenga, R., Leser, M., Sagalowicz, L., Guillote, S. and Glatter, O.: Structural and rheological investigation of Fd3m inverse micellar cubic phases, Langmuir, 23(19), 9618–9628, doi:10.1021/la701206a, 2007.

Prisle, N. L., Asmi, A., Topping, D., Partanen, A.-I., Romakkaniemi, S., Dal Maso, M., Kulmala, M., Laaksonen, A., Lehtinen, K. E. J., McFiggans, G. and Kokkola, H.:

Surfactant effects in global simulations of cloud droplet activation, Geophys. Res. Lett., 39(5), doi:10.1029/2011GL050467, 2012.

Reid, J. P., Bertram, A. K., Topping, D. O., Laskin, A., Martin, S. T., Petters, M. D., Pope, F. D. and Rovelli, G.: The viscosity of atmospherically relevant organic particles, Nat. Commun., 9(1), 1–14, doi:10.1038/s41467-018-03027-z, 2018.

Rittman, M., Amenitsch, H., Rappolt, M., Sartori, B., Driscoll, B. M. D. O. and Squires, A. M.: Control and Analysis of Oriented Thin Films of Lipid Inverse Bicontinuous Cubic Phases Using Grazing Incidence Small-Angle X - ray Scattering, Langmuir, 29, 9874–9880, doi:10.1021/la401580y, 2013.

Rudich, Y., Donahue, N. M. and Mentel, T. F.: Aging of Organic Aerosol: Bridging the Gap Between Laboratory and Field Studies, Annu. Rev. Phys. Chem., 58(1), 321–352, doi:10.1146/annurev.physchem.58.032806.104432, 2007.

Schmedding, R., Rasool, Q. Z., Zhang, Y., Pye, H. O. T., Zhang, H., Chen, Y., Surratt, J. D., Lopez-Hilfiker, F. D., Thornton, J. A., Goldstein, A. H. and Vizuete, W.: Predicting secondary organic aerosol phase state and viscosity and its effect on multiphase chemistry in a regional-scale air quality model, Atmos. Chem. Phys., 20(13), 8201–8225, doi:10.5194/acp-20-8201-2020, 2020.

Seddon, A. M., Richardson, S. J., Rastogi, K., Plivelic, T. S., Squires, A. M. and Pfrang, C.: Control of Nanomaterial Self-Assembly in Ultrasonically Levitated Droplets, J. Phys. Chem. Lett., 7(7), 1341–1345, doi:10.1021/acs.jpclett.6b00449, 2016.

Seddon, J. M., Bartle, E. A. and Mingins, J.: Inverse cubic liquid-crystalline phases of phospholipids and related lyotropic systems, J. Phys. Condens. Matter, 2, SA285–SA290, doi:10.1088/0953-8984/2/S/043, 1990.

Shearman, G. C., Tyler, A. I. I., Brooks, N. J., Templer, R. H., Ces, O., Law, R. V. and Seddon, J. M.: Ordered micellar and inverse micellar lyotropic phases, Liq. Cryst., 37(6–7), 679–694, doi:10.1080/02678292.2010.484917, 2010.

Shiraiwa, M., Ammann, M., Koop, T. and Poschl, U.: Gas uptake and chemical aging of semisolid organic aerosol particles, Proc. Natl. Acad. Sci. U. S. A., 108(27), 11003–11008, doi:10.1073/pnas.1103045108, 2011a.

Shiraiwa, M., Ammann, M., Koop, T. and Pöschl, U.: Gas uptake and chemical aging of semisolid organic aerosol particles -Supporting information, Proc. Natl. Acad. Sci. U. S. A., 108(27), 11003–11008, doi:10.1073/pnas.1103045108, 2011b.

Shiraiwa, M., Li, Y., Tsimpidi, A. P., Karydis, V. A., Berkemeier, T., Pandis, S. N., Lelieveld, J., Koop, T. and Pöschl, U.: Global distribution of particle phase state in atmospheric secondary organic aerosols, Nat. Commun., 8, 1–7, doi:10.1038/ncomms15002, 2017.

Shrivastava, M., Lou, S., Zelenyuk, A., Easter, R. C., Corley, R. A., Thrall, B. D., Rasch, P. J., Fast, J. D., Simonich, S. L. M., Shen, H. and Tao, S.: Global long-range transport and lung cancer risk from polycyclic aromatic hydrocarbons shielded by coatings of organic aerosol, Proc. Natl. Acad. Sci. U. S. A., 114(6), 1246–1251, doi:10.1073/pnas.1618475114, 2017.

Slade, J. H., Ault, A. P., Bui, A. T., Ditto, J. C., Lei, Z., Bondy, A. L., Olson, N. E., Cook, R. D., Desrochers, S. J., Harvey, R. M., Erickson, M. H., Wallace, H. W., Alvarez, S. L., Flynn, J. H., Boor, B. E., Petrucci, G. A., Gentner, D. R., Griffin, R. J. and Shepson, P. B.: Bouncier Particles at Night: Biogenic Secondary Organic Aerosol Chemistry and Sulfate Drive Diel Variations in the Aerosol Phase in a Mixed Forest,

Environ. Sci. Technol., 53(9), 4977–4987, doi:10.1021/acs.est.8b07319, 2019.

Tao, W., Su, H., Zheng, G., Wang, J., Wei, C., Liu, L., Ma, N., Li, M., Zhang, Q., Pöschl, U. and Cheng, Y.: Aerosol pH and chemical regimes of sulfate formation in aerosol water during winter haze in the North China Plain, Atmos. Chem. Phys., 20(20), 11729–11746, doi:10.5194/acp-20-11729-2020, 2020.

Tervahattu, H.: Identification of an organic coating on marine aerosol particles by TOF-SIMS, J. Geophys. Res., 107(D16), 4319, doi:10.1029/2001JD001403, 2002.

Tervahattu, H., Juhanoja, J., Vaida, V., Tuck, A. F., Niemi, J. V., Kupiainen, K., Kulmala, M. and Vehkamäki, H.: Fatty acids on continental sulfate aerosol particles, J. Geophys. Res. D Atmos., 110(6), 1–9, doi:10.1029/2004JD005400, 2005.

Tiddy, G. J. T.: Surfactant-water liquid crystal phases, Phys. Rep., 57(1), 1–46, doi:10.1016/0370-1573(80)90041-1, 1980.

Virtanen, A., Joutsensaari, J., Koop, T., Kannosto, J., Yli-Pirilä, P., Leskinen, J., Mäkelä, J. M., Holopainen, J. K., Pöschl, U., Kulmala, M., Worsnop, D. R. and Laaksonen, A.: An amorphous solid state of biogenic secondary organic aerosol particles, Nature, 467(7317), 824–827, doi:10.1038/nature09455, 2010.

Wang, G., Kawamura, K., Shuncheng, L., Ho, K. and Cao, J.: Molecular , Seasonal , and Spatial Distributions of Organic Aerosols from Fourteen Chinese Cities, Environ. Sci. Technol., 40, 4619–4625, doi:10.1021/es060291x, 2006.

Wang, Q., He, X., Zhou, M., Huang, D. D., Qiao, L., Zhu, S., Ma, Y. G., Wang, H. L., Li, L., Huang, C., Huang, X. H. H., Xu, W., Worsnop, D., Goldstein, A. H., Guo, H., Yu, J. Z., Huang, C. and Yu, J. Z.: Hourly Measurements of Organic Molecular Markers

in Urban Shanghai, China: Primary Organic Aerosol Source Identification and Observation of Cooking Aerosol Aging, ACS Earth Sp. Chem., 4(9), 1670–1685, doi:10.1021/acsearthspacechem.0c00205, 2020a.

Wang, T., Huang, R. J., Li, Y., Chen, Q., Chen, Y., Yang, L., Guo, J., Ni, H., Hoffmann, T., Wang, X. and Mai, B.: One-year characterization of organic aerosol markers in urban Beijing: Seasonal variation and spatiotemporal comparison, Sci. Total Environ., 743, 140689, doi:10.1016/j.scitotenv.2020.140689, 2020b.

Woden, B., Skoda, M. W. A., Milsom, A., Gubb, C., Maestro, A., Tellam, J. and Pfrang, C.: Ozonolysis of fatty acid monolayers at the air–water interface: organic films may persist at the surface of atmospheric aerosols, Atmos. Chem. Phys., 21(2), 1325–1340, doi:10.5194/acp-21-1325-2021, 2021.

Zabara, A. and Mezzenga, R.: Controlling molecular transport and sustained drug release in lipid-based liquid crystalline mesophases, J. Control. Release, 188, 31–43, doi:10.1016/j.jconrel.2014.05.052, 2014.

Zahardis, J. and Petrucci, G. A.: The oleic acid-ozone heterogeneous reaction system: Products, kinetics, secondary chemistry, and atmospheric implications of a model system - A review, Atmos. Chem. Phys., 7(5), 1237–1274, doi:10.5194/acp-7-1237-2007, 2007.

Zeng, J., Yu, Z., Mekic, M., Liu, J., Li, S., Loisel, G., Gao, W., Gandolfo, A., Zhou, Z., Wang, X., Herrmann, H., Gligorovski, S. and Li, X.: Evolution of Indoor Cooking Emissions Captured by Using Secondary Electrospray Ionization High-Resolution Mass Spectrometry, Environ. Sci. Technol. Lett., 7(2), 76–81, doi:10.1021/acs.estlett.0c00044, 2020.

Zhao, X., Hu, Q., Wang, X., Ding, X., He, Q., Zhang, Z., Shen, R., Lü, S., Liu, T., Fu, X. and Chen, L.: Composition profiles of organic aerosols from Chinese residential cooking: Case study in urban Guangzhou, south China, J. Atmos. Chem., 72(1), 1–18, doi:10.1007/s10874-015-9298-0, 2015.

Zhao, Y., Huang, H., Zhang, Y., Wu, K., Zeng, F., Wang, J., Yu, X., Zhu, Z., Yu, X.-Y. and Wang, F.: Atmospheric particulate characterization by ToF-SIMS in an urban site in Beijing, Atmos. Environ., 220, 117090, doi:10.1016/j.atmosenv.2019.117090, 2020.

7 CHAPTER 7: AN ORGANIC CRYSTALLINE STATE IN AGEING ATMOSPHERIC AEROSOL PROXIES: SPATIALLY RESOLVED STRUCTURAL CHANGES IN LEVITATED FATTY ACID PARTICLES

This study is published in the journal *Atmospheric Chemistry and Physics:*

Milsom, A., Squires, A. M., Boswell, J. A., Terrill, N. J., Ward, A. D. and Pfrang, C.: An organic crystalline state in ageing atmospheric aerosol proxies: spatially resolved structural changes in levitated fatty acid particles, Atmos. Chem. Phys. Discuss., 21, doi: 10.5194/acp-21-15003-2021, 2021.

7.1 **Abstract**

Organic aerosols are key components of the Earth's atmospheric system. The phase state of organic aerosols is known to be a significant factor in determining aerosol reactivity, water uptake and atmospheric lifetime - with wide implications for cloud formation, climate, air quality and human health. Unsaturated fatty acids contribute to urban cooking emissions and sea spray aerosols. These compounds, exemplified by oleic acid and its sodium salt, are surface active and have been shown to self-assemble into a variety of liquid-crystalline phases upon addition of water. Here we observe a crystalline acid–soap complex in acoustically levitated oleic acid–sodium oleate particles. We developed a synchrotron-based simultaneous Small-Angle & Wide-Angle X-ray Scattering (SAXS/WAXS)/Raman microscopy system to probe physical and chemical changes in the proxy during exposure to humidity and the atmospheric oxidant ozone. We present a spatially resolved structural picture of a levitated particle during humidification, revealing a phase gradient consisting of a disordered liquid crystalline shell and crystalline core. Ozonolysis is significantly slower in the crystalline phase compared with the liquid phase and a significant portion (34 ± 8 %) of unreacted material remains after extensive oxidation. We present experimental evidence of inert surface layer formation during ozonolysis, taking advantage of spatially resolved simultaneous SAXS/WAXS experiments. These observations suggest atmospheric lifetimes of surface-active organic species in aerosols are highly phase dependent, potentially impacting on climate, urban air quality and long-range transport of pollutants such as Polycyclic Aromatic Hydrocarbons (PAHs).

7.2 Introduction

Aerosols are ubiquitous in the atmosphere and are key components of the climate system (Pöschl, 2005; Stevens and Feingold, 2009). They present a large uncertainty when it comes to predicting their effect on the global climate (Boucher et al., 2013). Aerosols can act as pollutants and affect air quality and human health, especially when considering the urban environment (Chan and Yao, 2008; Guarnieri and Balmes, 2014). A large proportion of atmospheric aerosols are organic, (Jimenez et al., 2009) some of which are surface-active (Cheng et al., 2004). Unsaturated fatty acids are a major class of surface-active organic compounds found in the atmosphere with oleic acid (18-carbon backbone) as a widely-studied example (Gallimore et al., 2017; King et al., 2010; Zahardis and Petrucci, 2007). Sources of atmospheric oleic acid include marine (Fu et al., 2013; Osterroht, 1993) and cooking emissions (Allan et al., 2010; Alves et al., 2020; Ots et al., 2016; Vicente et al., 2018; Zhao et al., 2015). The reaction of organic compounds with the key initiators of atmospheric oxidation: hydroxyl radicals (OH), nitrate radicals (NO_3) and ozone (O_3) is an important factor in the evolution of these aerosols (Estillore et al., 2016). Oleic acid, along with the other unsaturated fatty acids, can be oxidised by these species and its reaction with O_3 in particular is well-studied and has made it the model system for both theoretical and experimental studies (Gallimore et al., 2017; King et al., 2004, 2009; Last et al., 2009; Milsom et al., 2021; Morris et al., 2002; Pfrang et al., 2017; Schwier et al., 2011; Shiraiwa et al., 2010; Zahardis and Petrucci, 2007).

The phase state of organic aerosols can vary significantly and has been identified as an important factor in determining atmospheric lifetimes (Shiraiwa et al., 2017; Slade et al., 2019; Virtanen et al., 2010) with particle viscosity being a key property (Reid et al.,

2018). Indeed, the chemical lifetime of an organic species in the atmosphere could increase from seconds to days due to temperature and humidity-induced changes in particle viscosity and the diffusion coefficient of molecules through the particle (Shiraiwa et al., 2010, 2011a). Glassy and semi-solid states of organic aerosols have been postulated and studies have shown that a phase transition causes a drastic change in physical properties such as the uptake of water and reactive gases (Berkemeier et al., 2016; Knopf et al., 2005; Koop et al., 2011; Mikhailov et al., 2009; Zobrist et al., 2011). Diffusion gradients may arise within a viscous organic aerosol particle being exposed to humidity changes and are due to the kinetic limitation of water uptake and loss to and from the viscous particle (Bastelberger et al., 2018; Zobrist et al., 2011). The long equilibration times for these viscous aerosols imply similarly long evolutions in key aerosol properties. Oleic acid, harmful Polycyclic Aromatic Hydrocarbons (PAHs) and phthalates have been identified in marine aerosols that have been heavily influenced by urban emissions (Kang et al., 2017), suggesting that long-range transport of these molecules does happen. PAH reactivity has been shown to be strongly affected by interactions with particle surfaces (Chu et al., 2010). It has also been indicated that coatings of organic aerosol shield PAHs, increasing their ability to be transported and cause harm and this has been linked to the phase state of the aerosol (Mu et al., 2018; Shrivastava et al., 2017).

As a surface-active molecule oleic acid is able to form, in contact with water, complex self-assembled structures such as organogels (in organic solvents) (Nikiforidis et al., 2015), vesicles (Blöchliger et al., 1998) and even helices (Ishimaru et al., 2005). Mixed with its sodium salt (sodium oleate) and water, oleic acid can also form lyotropic liquid crystalline (LLC) phases (Tiddy, 1980). These phases bring with them a range of

different physical properties such as directionally dependent water diffusion, viscosity differences and different optical characteristics. The LLC phase behaviour of oleic acid–sodium oleate has been extensively studied in a biological and cosmetic context and has been shown to have a diverse set of accessible phases ranging from a simple micellar solution through to hexagonal arrays of water channels formed by cylindrical assemblies of the fatty acid (Engblom et al., 1995; Mele et al., 2018; Seddon et al., 1990).

Fatty acids, mixed with their fatty acid soap (salt), can form another set of unique structures called acid–soap complexes (Lynch, 1997). These complexes result from the strong hydrogen bonding between the carboxylate head group of the soap and the carboxylic acid group of the fatty acid and the interactions between the fatty acid alkyl chains. They are stoichiometrically discrete compounds. For the palmitic acid–sodium palmitate acid–soap complex, the sodium ion is shared between adjacent carboxylate anions. Carboxylic acid groups are associated mainly via hydrogen bonding to the carboxylate anions (Lynch et al., 2002). Key properties of acid–soap complexes include: (i) crystallinity: in an atmospheric context this is important, as discussed previously there is a strong link between phase state and the atmospheric properties of an aerosol particle; (ii) unique hydrogen bonding exhibited by their distinct IR spectra (compared to their constituent parts); and (iii) ordered alkyl chain packing deduced spectroscopically and using X-ray techniques such as Small-Angle/Wide-Angle X-ray Scattering (SAXS/WAXS). They are also known to form a range of LLC phases upon addition of water, further demonstrating the versatile nature of the oleic acid–sodium oleate system (Cistola et al., 1986).

Previous work has demonstrated that these LLC phases were present in a levitated unsaturated fatty acid aerosol proxy (Seddon et al., 2016) and that self-assembly drastically reduces the oleic acid ozonolysis reaction rate (Pfrang et al., 2017). The formation of one of these phases (lamellar phase) was found to decrease the ozonolysis reaction rate by *ca.* an order of magnitude (Milsom et al., 2021).

In this work, the importance of the oleic acid–sodium oleate acid–soap complex in atmospheric conditions is investigated. This complex has previously been studied in a biological context (Ananthapadmanabhan and Somasundaran, 1988; Tandon et al., 2001). The hydrocarbon chain and head group of the fatty acid can be characterised by complementary Raman and IR spectroscopy: the acid–soap complex has characteristic peaks both in the IR and Raman spectra, allowing confirmation of the structure of the complex (Lynch et al., 1996; Tandon et al., 2001). SAXS and WAXS have also been used to confirm the lamellar packing of the acid–soap complex and to reveal the sub-cell packing arrangement of the alkyl chains unique to the acid–soap complex (Tandon et al., 2001). We also employed Polarising Optical Microscopy (POM) in order to visualise structural changes with temperature and humidity.

The oleic acid–sodium oleate acid–soap complex is studied in acoustically levitated droplets and analysed by simultaneous SAXS/WAXS and Raman microscopy. Ozonolysis is followed by Raman, while the effect of oxidative ageing on self-assembly is investigated using SAXS/WAXS. We first carried out a detailed structural characterisation of the acid–soap complex to confirm its presence in the levitated particles. We then probed the effects of exposure to humidity and ozone. We employed a micron-sized X-ray beam (16 μm x 12 μm) available on the I22 beamline at the Diamond Light Source (UK) to follow structural changes throughout the particle during

controlled humidity changes and atmospheric ageing. This enabled us to build a spatially resolved SAXS/WAXS picture of the particle as a function of time exposed to humidity and ozone. Using this technique, we observed the emergence of a diffusion gradient across the humidifying/dehumidifying acid–soap particle and described this effect. We also investigated if exposure to ozone destroys the acid–soap structure and if the crystalline structure affects the reaction kinetics, drawing atmospheric implications.

7.3 Methodology

A 1:1 wt ratio of oleic acid and sodium oleate was chosen to afford a system with a molar excess (7.8 %) of oleic acid, simulating the acidic nature of urban (Zhang et al., 2007) and marine (Keene et al., 2004) aerosols.

7.3.1 Sample preparation

Oleic acid ((Z)-octadec-9-enoic acid, 90 %) and sodium oleate (sodium (Z)-octadec-9-enoate, 99 %) were purchased from Sigma-Aldrich (UK) and used as received. Oleic acid and sodium oleate were weighed in a 1:1 wt ratio and dissolved as an ethanolic solution in a minimum of hot ethanol. This solution was allowed to cool to room temperature (~ 22 ^{o}C). The ethanol in the sample was evaporated before being placed into an acoustic node for the study of levitated particles. Samples were alternatively deposited on glass microscope slides for offline Raman Microscopy and POM.

7.3.2 Preparation of the bulk oleic acid/sodium oleate/water mixture

Oleic acid and sodium oleate were weighed and mixed in a 1:1 wt ratio with addition of water in order to afford a final mixture which is 70 % aqueous phase. The mixture was homogenised first by sonicating in a heated ultrasonicator (~ 40–50 ^{o}C) for 30 min, followed by vortexing for 1 min. The sample was then placed in a freezer for storage

and further homogenisation. Upon defrosting, the sample was observed to be homogeneous, as subsequently confirmed by the SAXS pattern.

The sample was then placed inside a poly-imide tube. The tube was sealed at both ends with heat-shrink tubing. The sample was then placed in the beam path of an *Anton Paar SAXSpoint 2.0* instrument at the University of Bath. The sample was irradiated by X-rays with a 1.54 Å (Cu source) wavelength for 3 min at a 360 mm sample-detector distance.

7.3.3 Simultaneous Raman microscopy and small-angle/wide-angle X-ray scattering (SAXS/WAXS) of levitated particles during exposure to humidity and ozone

A modified commercial levitator (tec5, Oberursel, Germany) with a fixed transducer frequency (100 kHz) and variable HF power (0.65–5 W) was used to levitate the atmospheric aerosol proxies. A concave reflector was positioned above the transducer and was fitted with a micrometre screw to adjust the reflector–transducer distance. The reflector–transducer distance was generally in the range of 20–30 mm. The levitator was enclosed in a 3–D-printed chamber equipped with X-ray transparent Mica windows and access ports for injection, Raman probe and gas in- and outlets.

The levitated particles were analysed on the I22 beamline at the Diamond Light Source (UK). Solid samples, crystallised from ethanolic solutions, were placed into a node of the acoustic levitator. The particles had vertical radii of ~ 90–150 µm and horizontal radii of ~ 500 µm (determined using the attenuation of the X-ray beam). One particle of proxy mixture was levitated subjected to the humidity change experiment. Two particles of the proxy mixture and one pure oleic acid particle were levitated and subjected to

ozonolysis experiments. Once the particle stabilised, a 532-nm Raman laser probe with a 12 mm focal length and ~ 4 μm focal point spot diameter (minimum) was focussed onto the particle. The laser power delivered to the particle was determined to be ~ 20 mW (source power up to 450 mW).

A dry flow of oxygen was passed through a commercial pen-ray ozoniser (Ultraviolet Products Ltd, Cambridge, UK). The ozone concentration was kept constant at 51.9 ± 0.5 ppm and was calibrated offline by UV/Vis spectroscopy at the outlet of the ozoniser using a *PerkinElmer Lambda 465 Spectrophotometer* and the ozone absorption band at 254 nm and the absorption cross-section for ozone at this wavelength (1.137 ± 0.070 $x10^{-17}$ cm^2) (Mauersberger et al., 1986). The high ozone concentration was chosen to observe an appreciable decay within the limited timescale of a synchrotron experiment.

SAXS/WAXS patterns were collected as a series of 1 s frame vertical scans across the particle. There was an intentional delay of 15 s between each set of scans to avoid any potential X-ray beam damage. A micro-focus X-ray beam was used to enable sufficient spatial resolution of the SAXS patterns within the particle. The size of the micro-focus beam was approximately 16 μm x 12 μm (FWHM). Scattering patterns up to q = 0.58 $Å^{-1}$ were recorded by the SAXS detector (*Pilatus P3-2M*) and from 0.50–4.45 $Å^{-1}$ by the WAXS detector (*Pilatus P3-2M-L*). The scattering intensity is related to the momentum transfer (q), which is a function of scattering angle and is related to the spacing (d) between scattering planes via Eq. (6-1) (Putnam et al., 2007).

$$q = \frac{2\pi}{d} \qquad (7\text{-}1)$$

A bespoke relative humidity (RH) control system, using a Raspberry Pi with air pumps and RH sensor, was used to monitor and control RH in real-time. The line of humidified air was passed into the levitation chamber. An RH/temperature sensor was placed inside the chamber for real-time monitoring of the chamber RH and temperature.

7.3.4 Offline Raman microscopy

A *Renishaw InVia* Raman microscope was used to analyse samples deposited onto microscope slides. This was achieved by placing a drop of ethanolic solution on the slide and allowing it to evaporate in air. Cool air was passed over the sample to aid evaporation. A film was left deposited on the microscope slide. A 532-nm laser was focussed onto the sample using a 20x objective lens and Raman spectra were acquired in the range 100–3500 cm^{-1} with two acquisitions.

7.3.5 Polarising optical microscopy (POM)

All POM was performed using a *Carl Zeiss Axioskop 40* fitted with removable polarising filters. Samples were prepared as for the Raman microscope. Visualisation was accomplished using either 5x or 10x objective lenses. A Peltier heating stage was used to control the temperature of samples under the microscope.

Samples for humidity experiments were deposited on microscope slides and allowed to dry at ~ 50 % RH over 6 days. Samples were then humidified by suspending the slides above distilled water inside a small, sealed, container. This provided a saturated environment for the samples to equilibrate with for 7 days. Samples for temperature experiments were prepared in the same way but without any humidification.

7.3.6 **Infrared spectroscopy (IR)**

Infrared spectroscopy was carried out on a *PerkinElmer Spectrum 100* FTIR spectrometer with an ATR attachment. Measurements comprised of 32 scans at a resolution of 4 cm^{-1}. This technique required more material to analyse, therefore a small amount of ethanolic sample solution was left to evaporate to leave behind crystals. The quantitative evaporation of ethanol in the samples was confirmed by IR spectroscopy. All samples were analysed at room RH of ~ 50 %.

7.4 **Results and discussion**

7.4.1 **Characterisation of the acid–soap complex by SAXS/WAXS**

The dry acid–soap complex was probed by simultaneous SAXS/WAXS and Raman in acoustically levitated droplets. SAXS allows investigation of the long-scale order (repeated structures). The regular interval between each SAXS peak in Fig. 7-1(a) is characteristic of a lamellar system with a *d*-spacing of 4.5773 ± 0.0001 nm between repeat structures (see Table 10-5).

The WAXS data (Fig. 7-1(b)) reveal information about the packing of the alkyl chains in particular and are consistent with the literature data at a lower temperature (Tandon et al., 2001). A table of WAXS data and a comparison with the literature is presented in the appendix section 10.6.1. They also confirm the crystallinity of the sample. Note the broad peak underneath the sharp WAXS peaks in Fig. 7-1(b) is due to the 7.8 % molar excess of oleic acid (with its own WAXS peak – see section 7.4.2) in the sample. A fuller characterisation involving Raman microscopy, IR spectroscopy and polarising optical microscopy (POM) is presented in the appendix section 10.6.1.

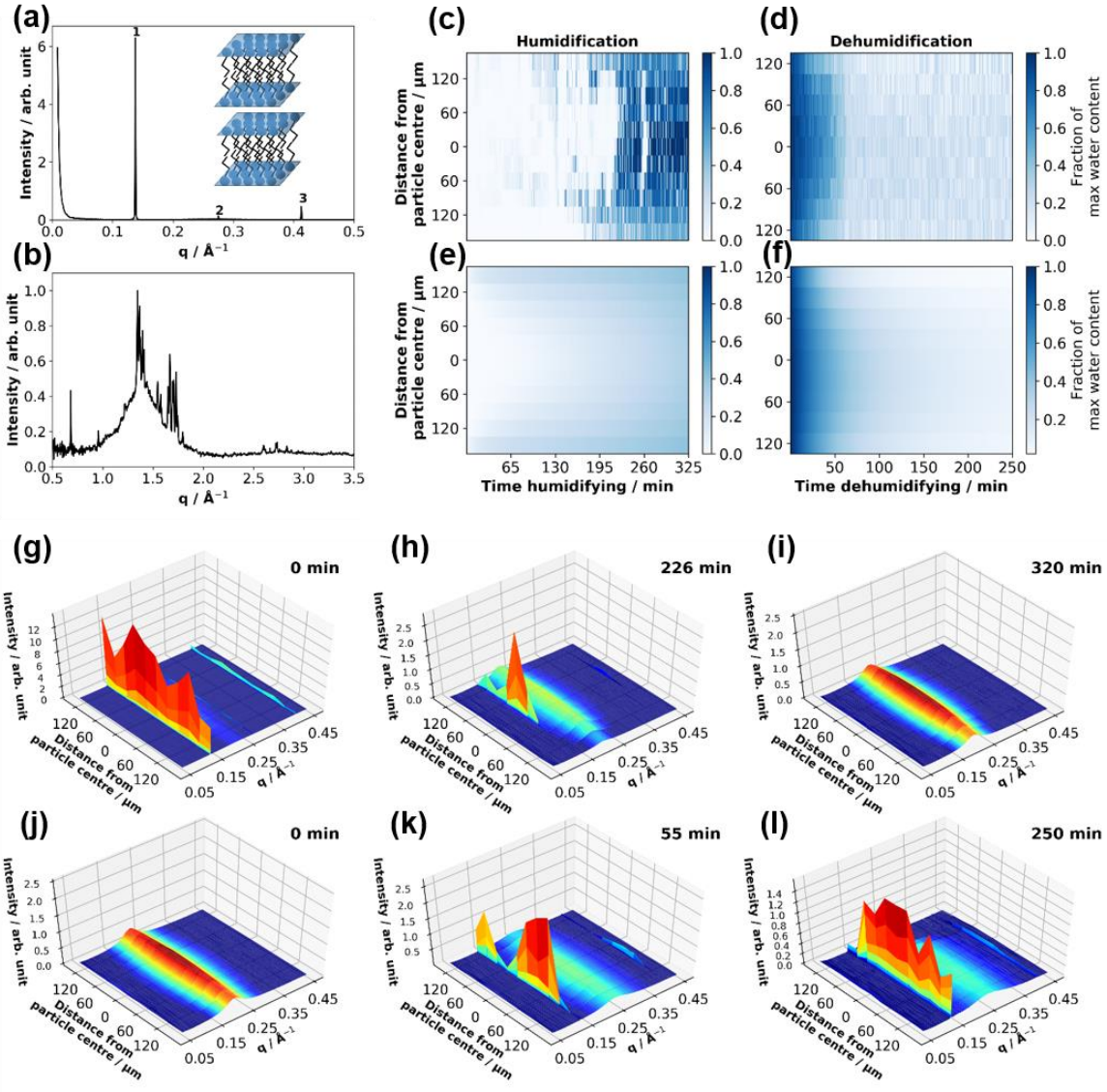

Figure 7-1. ((a) and (b)) 1-D SAXS and WAXS patterns obtained from a dry levitated particle of the acid–soap complex – 1st, 2nd and 3rd lamellar peaks are labelled and a cartoon of the lamellar phase is presented (a). ((c) and (d)) experimental fraction of maximum water content as a function of distance from particle centre and time humidifying/dehumidifying. ((e) and (f)) modelled fraction of maximum water content – best fits to experimental data for humidification and dehumidification. 3–D surface plots of 1–D SAXS patterns plotted against distance from the particle centre for the same particle humidifying ((g) – (i)) and dehumidifying ((j) – (l)) with time humidifying/dehumidifying presented at the top right of each plot (particle size: ~ 150 µm (vertical radius) x 500 µm (horizontal radius); humidification experiment: ~ 38 % (room RH) ((g)) to 90 % ((h) and (i)) RH, dehumidification experiment: 90 % (j) to ~ 38 % ((k) and (l)) RH).

7.4.2 Atmospheric processing: (i) exposure to humidity changes

Field measurements have shown atmospheric aerosols to be often in a highly viscous state (Virtanen et al., 2010). Aerosol particle viscosity is dependent on water content, which in turn is controlled by its chemical nature and the variable surrounding relative humidity (Fitzgerald et al., 2016; Hosny et al., 2016; Renbaum-Wolff et al., 2013; Shiraiwa et al., 2011a). Changing the humidity of the sample environment effectively controls how much water is taken up by the particle. Therefore it is necessary to build an understanding of this system's behaviour when subjected to atmospherically relevant humidity changes.

The acid–soap complex studied here is crystalline and as such, may have different hygroscopic properties compared to liquid aerosols. The literature presents a conceptual framework for the interaction of amorphous and crystalline aerosol particles with water (Koop et al., 2011; Mikhailov et al., 2009). It suggests that crystalline particles deliquesce promptly whereas amorphous particles gradually absorb water and deliquesce at a slower rate due to limited water diffusion through the amorphous phase.

7.4.2.1 Structural changes during humidification and dehumidification

Our humidity–SAXS/WAXS experiments on levitated acid–soap complex particles presented here suggest that these particles do take up water at high humidity. The levitated particle exhibited reversible structural changes as a result of one humidification–dehumidification cycle, illustrated in Fig. 7-1(g)-(l) by the disappearance and reappearance of the acid–soap complex SAXS peaks during humidification and dehumidification. Simultaneous SAXS/WAXS data from the particle centre are presented in the appendix (Fig. 10-19). The horizontal position was changed by 15 µm between the humidification and dehumidification runs in order to

check for beam damage, of which there was no evidence (see Fig. 7-1(g)-(l) and Fig. 10-19, the appendix – SAXS patterns are identical between the last humidification and first dehumidification runs).

The particles were exposed to an RH of 90 % and SAXS/WAXS patterns were collected. Water uptake changes the physical characteristics of the droplet and therefore small size and shape changes would occur (Mikhailov et al., 2009), resulting in some destabilisation of the levitated particle. Such physical changes were observed visually for a particle of sodium oleate offline (Fig. 10-22, the appendix).

The acid–soap complex breaks down when exposed to a high-humidity environment. The dry acid–soap sample has a lamellar SAXS pattern with characteristic peaks in the WAXS (Fig. 7-1(b)). Upon adding humid air, a small broad peak at ~ 0.2 $Å^{-1}$ appeared almost immediately (Fig. 7-1(g) and Fig. 10-19, the appendix). This broad peak is caused by the formation of a disordered inverse micellar phase. This phase becomes more prominent during continuous exposure to 90 % RH. Eventually, there is a decrease and then disappearance of the acid–soap lamellar phase signal in the SAXS data. This is also true for the WAXS peaks (Fig. 10-19, the appendix).

Dehumidification mostly reversed this trend, though a broad inverse micellar peak still remained present by the end of the experiment – evident in the SAXS pattern (see Fig. 7-1(l) and succeeding discussion).

This experiment demonstrates that the acid–soap complex can form from an inverse micellar phase of this particular composition in water. As it is highly unlikely for there to be enough ethanol in the atmosphere to form this complex by evaporation from an

ethanolic solution, the most likely atmospheric formation pathway is from an aqueous inverse micellar phase of this composition, as presented here.

Spatially resolved 1–D SAXS patterns were acquired whilst scanning through the particle during exposure of the acid–soap complex to high RH (Fig. 7-1(g)-(l)). At the beginning of the humidification experiment, sharp, evenly spaced peaks were visible in the SAXS (Fig. 7-1(g)). This is consistent with the lamellar packing of the acid–soap complex. Moving through the particle, the broad inverse micellar peak is approximately the same intensity relative to the most intense first order lamellar peak. The increase in overall intensity approaching the centre of the particle is expected as the X-ray beam travels through more material and therefore more scattering occurs. In general, the particle shows a consistent composition throughout. The characteristic acid–soap complex WAXS peaks are also observed and confirm the crystalline nature of the particle at the beginning of the experiment (Fig. 10-19, the appendix).

During humidification the broad inverse micellar peak present at the beginning of the experiment becomes more intense and the sharp lamellar signal starts to disappear, starting from the edges of the particle (Fig. 7-1(h)). For example after 226 min, there is an apparent difference in SAXS patterns between the edge and centre of the particle. The edge region exhibits only the broad disordered inverse micellar peak, suggesting that the uptake of water breaks the acid–soap complex down into this disordered phase. By the end of the hydration experiment the SAXS pattern throughout the particle consisted of one broad inverse micellar peak (Fig. 7-1(i)). This shows that the particle had taken up water throughout and that the acid–soap complex was no longer present. A similar change was seen in the WAXS pattern (Fig. 10-19, the appendix).

The reverse trend is observed during dehumidification, though the phase change from inverse micellar to lamellar particle happens markedly faster (Fig. 7-1(j)-(l)) and Fig. 10-19, the appendix). It is clear that the crystalline lamellar phase signal is most intense in the centre of the particle during dehumidification. There is evidence of the lamellar phase forming on the outside of the particle, suggesting that the phase change is spatially more uniform than during humidification (Fig. 7-1(k)).

Figure 7-1(h) illustrates the presence of a viscous (crystalline lamellar) core with a less viscous (inverse micellar) shell, inferring that a diffusion gradient is established during particle humidification (see section 7.4.2.2). Diffusion gradients have been theorised in the past when humidifying atmospherically relevant viscous systems (Bastelberger et al., 2018; Zobrist et al., 2011). This kind of core-shell morphology is plausible for particles of this size (Veghte et al., 2013).

The inverse micellar phase and acid–soap complex will have different viscosities and as such, reactive gas and water uptake may be significantly affected. The literature suggests that at high RH, moisture-induced phase transitions could increase reactive gas uptake by reducing the viscosity of the aerosol particle (Shiraiwa et al., 2011). Hosny *et al.* visualised this viscosity gradient using a fluorescence-based technique to probe the viscosity response of oxidised organic aerosols to a step change in RH (Hosny et al., 2016). See section 7.6 for further discussion.

The acid–soap complex scattering pattern was observed after dehumidification (Fig. 7-1(j)–(l)). There was, however, a broad inverse micellar peak present at the end of dehumidification. The suggestion is that a phase separation took place within the particle – the two phases being the crystalline acid–soap complex and an inverse

micellar phase. Previous work has focussed on liquid–liquid phase separations at high RH in organic aerosols (Freedman, 2017, 2020; Liu et al., 2018). In this study, a water-containing inverse micellar phase forms initially on the outside, creating a clear phase gradient during humidification. Upon dehumidification of the levitated particle from 90 % RH to ~ 38 % RH, some of the inverse micellar phase remains in the particle. The SAXS pattern is consistent throughout the particle which suggests that this phase separation is not due to some inverse micellar phase being trapped within the particle as a result of the rapid dehumidification. Rather, the dehumidified particle may have the two phases evenly distributed throughout.

Long-term humidity exposure experiments were performed on acid–soap complex samples deposited on microscope slides. POM of these samples revealed an eventual transition to the inverse hexagonal phase after a week of humidification followed by phase separation to an acid–soap complex and a non-birefringent (not lamellar or inverse hexagonal) phase after removal from the humid environment (Fig. 10-24, the appendix).

7.4.2.2 The water diffusion gradient during humidity change

In order to estimate the water diffusion gradient between the inverse micellar and crystalline lamellar phase during humidification and dehumidification, a suitable parameter corresponding to water content was required. The position (in q) of the micellar peak centre in the SAXS pattern was chosen for the dehumidification experiment as this is inversely proportional to the micellar d-spacing *i.e.* the average distance between inverse micelles (Eq. 7-1), which is determined by the water content of the inverse micellar phase. For humidification, the micellar-lamellar peak area ratio was chosen as a suitable measure of water content. In this case q is not a good measure

due to the peak position stabilising after ~ 50 min (Fig. 10-19, the appendix), implying that water uptake finishes at that time when it is clear from the micellar-lamellar peak area ratio data that water uptake had not finished (Fig. 10-25, the appendix). This is due to the inverse micellar phase reaching an equilibrium *d*-spacing, from that point onward the peak area increases while the peak position stays the same.

Water concentration was not quantified as this would have required determining the dependence of *d*-spacing on water content, which was not practicable during a beamtime experiment and would require water content to be measured over a very small range – increasing the amount of water can also change the self-assembled phase (Engblom et al., 1995; Mele et al., 2018). However, there is confidence that the water content is ~ 5 wt % at high RH as previous literature (in dilute salt solution) suggests the inverse micellar phase forms at this water content before becoming an ordered inverse micellar phase at 10 wt % (Mele et al., 2018). Water content was measured as a fraction of the maximum micellar-lamellar/*d*-spacing peak area ratio observed in the particle during the entire humidification/dehumidification experiment.

A simple model of water uptake and loss was created to account for experimental observations. The particle was split into layers, equivalent to the number of positions probed across the particle. Water uptake into/out of the particle and water diffusion between model layers were described by two parameters: rate in/out of the particle ($k_{in/out}$) and rate of internal diffusion ($k_{internal}$), which was split into the rate of water diffusion in the inverse micellar phase ($k_{micellar}$) and crystalline lamellar phase ($k_{lamellar}$). Splitting $k_{internal}$ in this way, and assuming the direct proportionality of $k_{micellar}$ and $k_{lamellar}$ with their respective diffusion coefficients, allowed parameters for internal diffusion to be evolved as a function of layer composition using a Vignes-type equation

(see the appendix section 10.6.8) (Davies and Wilson, 2016; Price et al., 2015). See the appendix for a schematic representation of the model (Fig. 10-26, the appendix).

As actual water content data were not available for these experiments, water content as a fraction of maximum water content was used in the model in order to fit with the experimental data. Note that water content data derived from micellar–lamellar peak area ratios is noisier than those derived from *d*-spacing measurements.

During humidification the model first overpredicts then underpredicts the amount of water in the particle (Fig. 7-1(c) and (e)). Clearly there is very little water observed experimentally in the centre of the particle at ~ 200 min (~ 1 % maximum water content), whereas the model returns ~ 16 % maximum water content. After ~ 230 min humidification the water content of the whole particle increases sharply, in line with the crystalline model for water uptake (Mikhailov et al., 2009). The model now underpredicts the experiment, peaking at ~ 40 % maximum water content whereas the experimental data tends to 100 %. The uptake model does not capture this sudden jump in water content. We suggest that this is due to the restructuring and prompt deliquescence of our crystalline particle, not accounted for in the model and described by Mikhailov *et al.* (Mikhailov et al., 2009). This finding supports the crystalline lamellar core–inverse micellar shell observed in the corresponding spatially resolved SAXS patterns (Fig. 7-1(h)).

During dehumidification the model agrees well with the experiment for the first ~ 65 min (Fig. 7-1(d) and (f)). After ~ 65 min the acid–soap complex signal starts to dominate the SAXS pattern (Fig. 7-1(k) and Fig. 10-19, the appendix). The more viscous acid–soap complex phase slows down water diffusion. The final experimental

and model water contents are ~ 17 % and ~ 5 % maximum water content, respectively. There is still an appreciable difference between model and experiment, likely reflecting the irreducible noise in the experimental data.

The model was parameterised in order to estimate the relative water diffusivity in the inverse micellar phase compared with the crystalline lamellar phase. We used the dehumidification experiment and model fit to estimate these values as this experiment returned the least noisy data and the lowest fitting error (see the appendix section 10.6.8). Water diffusivity was found to be ~ 33-fold greater in the inverse micellar phase. We stress that this is an estimation based on our simplified model of water uptake and diffusion with limited knowledge of the actual water content. Increasing the complexity of the model would introduce too many unknowns that cannot be constrained with currently existing experimental data. This does however open the door to future, more explicit, descriptions of water diffusivity changes in self-assembled systems, analogous to studies of ultraviscous aerosols (Davies and Wilson, 2016; Price et al., 2015; Zobrist et al., 2011). See section 7.5 for a discussion of the significance of these findings.

7.4.3 **Atmospheric processing: (ii) exposure to ozone**

Levitated particles of the acid–soap complex were exposed to ozone in order to simulate chemical ageing of the particle in the atmosphere. Ozone attacks the carbon–carbon double bond found half way along the alkyl chain. A complex reaction mechanism ensues involving Criegee intermediates. Major products include nonanal, nonanoic acid, 9-oxo-nonanoic acid and azaleic acid (Gallimore et al., 2017; Hung et al., 2005; Zahardis and Petrucci, 2007). Oligomeric products have also been observed and result

from the reaction of Criegee intermediates with the reaction products mentioned above (Reynolds et al., 2006; Zahardis et al., 2006).

Of the reaction products, only nonanal is known to be volatile enough to evaporate appreciably (Vesna et al., 2009). The rest of the ozonolysis products are assumed to remain in the particle phase. There is evidence that particles of oleic acid lose a small proportion of mass during ozonolysis (~ 6 % mass loss after 20 h at 2 ppm), probably due to nonanal loss (Lee et al., 2012). If this is the case, a size change in these particles is likely to be smaller than can be resolved by the X-ray beam in these experiments (~ 15 μm in diameter). Being in an open system with a constant flow of oxygen and ozone, we cannot rule out any mass loss occurring during these experiments. Compared with the effect of particle phase state, we do not expect nonanal loss to impact significantly on the reaction rate.

Water is known to affect the reaction mechanism of ozonolysis and affect the product distribution in oxidised oleic acid particles (Al-Kindi et al., 2016; Vesna et al., 2009). In our experiments, ozonolysis was carried out under dry conditions (< 5 % RH) in order to negate any effect the presence of water might have on the ozone uptake and reaction rate (Berkemeier et al., 2016; He et al., 2017; Nájera et al., 2015).

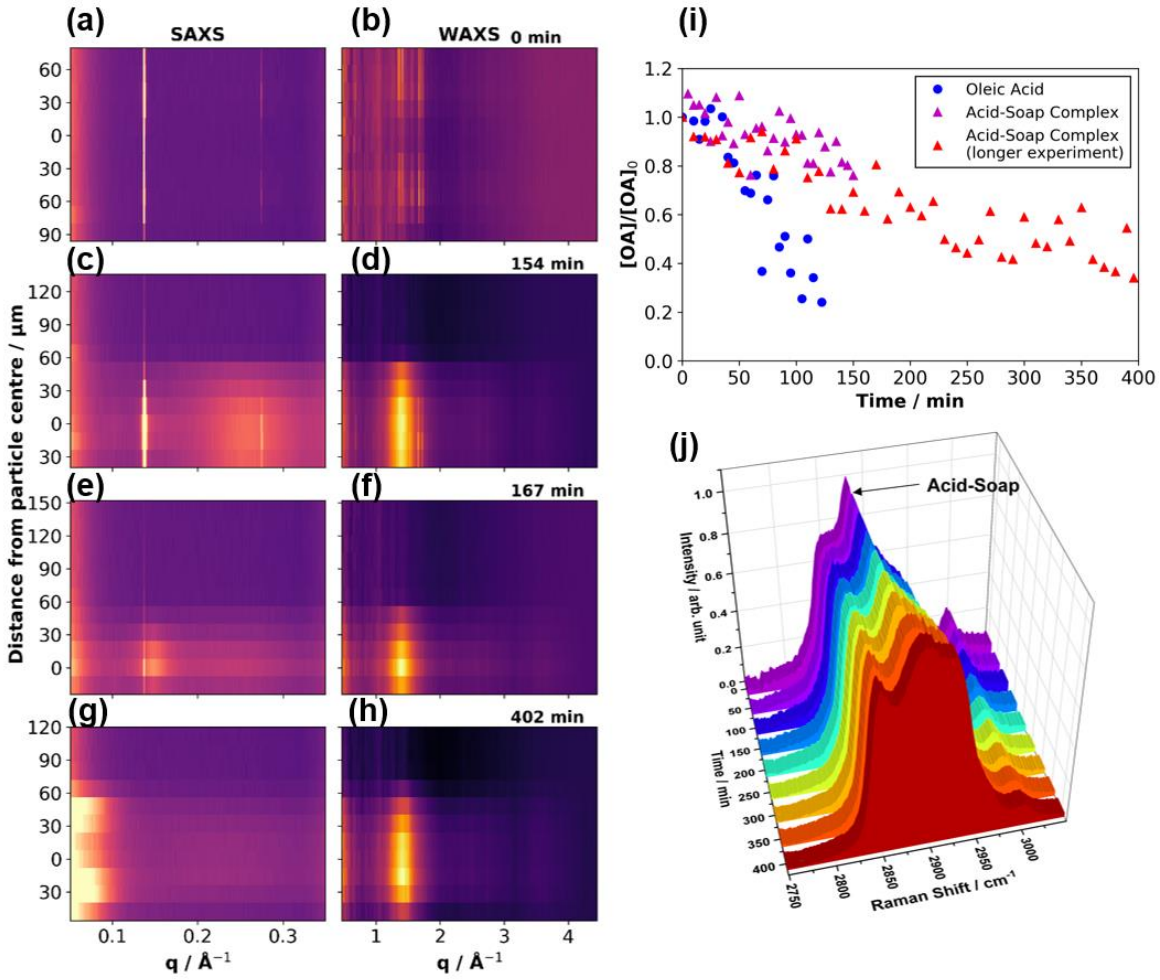
(a)
SAXS
(b)
WAXS 0 min
(c)
(d)
154 min
(e)
(f)
167 min
(g)
(h)
402 min
Distance from particle centre / µm
q / Å^{-1}
q / Å^{-1}
(i)
Oleic Acid
Acid-Soap Complex
Acid-Soap Complex (longer experiment)
[OA]/[OA]$_0$
Time / min
(j)
Acid-Soap
Intensity / arb. unit
Time / min
Raman Shift / cm^{-1}

Figure 7-2. Vertical scans through the particle showing the effect of ozonolysis on self-assembly. Each row of plots ((a) and (b), (c) and (d), (e) and (f), (g) and (h)) shows simultaneous 1–D SAXS and WAXS scattering patterns vs. distance from the particle centre (measured in µm from what was deemed the particle centre from attenuation data) at increasing time exposed to ozone (labelled at the top-right of every WAXS plot). The particle moved and possibly changed shape during the experiment, vertical movement is apparent from the SAXS and WAXS patterns. (i) Comparison of a levitated pure oleic acid droplet vs. a levitated acid–soap complex particle undergoing ozonolysis, measured by Raman microscopy - A longer ozonolysis experiment on a different levitated acid–soap complex particle is also presented, totalling two ozonolysis experiments on this proxy. (j) Evolution of the Raman spectra between 2750 and 3050 cm^{-1} of a levitated acid–soap complex during ozonolysis. (Particle size: ~ 85 µm (vertical radius) x ~ 500 µm (horizontal radius); $[O_3]$ = 51.9 ± 0.5 ppm).

7.4.3.1 The effect of the crystalline phase on reactivity

After considering the effect of humidity, we now explore specifically the effect of phase on chemical kinetics in dry conditions with a focus on spatial resolution of the phase evolution across individual droplets, which is the key strength of our experimental approach. The impact of humidity on chemical ageing will be discussed in the *Atmospheric Implications* and explored by follow-on modelling work since it cannot be de-convoluted by experimental work alone given the complex interplay of humidity, phase and chemistry.

Kinetics are followed by Raman microscopy. The area of the C=C peak (~ 1650 cm^{-1}) is integrated and normalised against the $–CH_2$ deformation band (~ 1442 cm^{-1}). A decay plot (Fig. 7-2(i)) is then created normalising to the starting C=C/$–CH_2$ ratio. The Raman

spectra from these beamline experiments had a high and varying background and as such the signal-to-noise ratio was poorer compared to experiments carried out offline (Fig. 10-21).

The two particles used for ozonolysis experiments were non-spherical with vertical and horizontal diameters of ~ 170 x 1000 μm and ~ 225 x 1000 μm as determined from our SAXS data. An optical picture (taken offline) of a levitated particle of sodium oleate is presented in the appendix as an illustration of the particle shape (Fig. 10-22, the appendix).

Figure 7-2(i) demonstrates that the levitated particles of the acid–soap complex are much less reactive than droplets of oleic acid. The ratio of reactivity between oleic acid vs the acid–soap complex is 4.95 ± 0.40, suggesting that oleic acid in the crystalline acid–soap complex form reacts significantly slower than in the liquid form. This is consistent with observations previously made on levitated complex 3–D self-assembled aerosol proxies (Pfrang et al., 2017). We are now able to quantify impact of phase on the reactivity of oleic acid.

The C=C peak at ~ 1650 cm^{-1} does not disappear entirely by the end of the reaction and 34 ± 8 % of oleic acid remains in the particle, suggesting there is still unreacted oleic acid at the end of the experiment despite being exposed to a high [O_3] (51.9 ± 0.5 ppm) for more than 6 hours (Fig. 7-2(i)).

7.4.3.2 Evolution of the SAXS pattern during ozonolysis

The SAXS pattern of the levitated acid–soap complex during ozonolysis evolved slowly thoroughout the particle. Initially, the particle is lamellar throughout and the characteristic acid–soap complex WAXS peaks are present (Fig. 7-2(a) and (b)). As the

reaction progresses, broad features start to appear in the SAXS pattern at ~ 0.15 $Å^{-1}$ and 0.27 $Å^{-1}$ close to the original lamellar peaks and the original WAXS signals start to fade, with a new broad peak starting to appear at ~ 1.4 $Å^{-1}$ (Fig. 7-2(c) and (d), (e) and (f)). These features are due to the gradual disordering of the crystalline lamellar structure. The broad WAXS peak corresponds to an average spacing between alkyl chains of ~ 4.52 Å which is similar to the value we obtained for pure oleic acid at ~ 4.57 Å (Fig. 10-28, the appendix). There is also a similarity to the value measured by Iwahashi *et al.* (4.58 Å) (Iwahashi et al., 1991) which is associated with dimer formation in "free" oleic acid. By the end of the reaction the lamellar phase signal in the SAXS pattern has disappeared and the broad WAXS peak associated with oleic acid remains (Fig. 7-2(g) and (h)).

An increasing amount of low-*q* SAXS scattering is observed by the end of the reaction (Fig. 7-2(g)). *q* is inversely proportional to the distance between equivalent scattering locales. Low-*q* scattering therefore implies that molecules which exhibit some order with relatively large repeat distances have been formed (note there is always some background scattering at low-*q* close to the X-ray beamstop). This low-*q* scattering may come from material such as an oligomeric/high-molecular-weight product, which has been observed as a result of oleic acid ozonolysis (Lee et al., 2012; Reynolds et al., 2006; Wang et al., 2016; Zahardis et al., 2005, 2006). Water reacts with Criegee intermediates (Vesna et al., 2009), which are involved in the formation of these high molecular weight oligomers. These ozonolysis experiments were carried out under dry (< 5 % RH) conditions, raising the probablility of oligomer formation. Further discussion of the evidence for oligomer formation is presented in Sect. 6 of the Supplement. It is evident from the vertical SAXS/WAXS profile (Fig. 7-2(g) and (h))

that the oleic acid WAXS signal was most intense at the centre of the particle and least intense at the edges. Significantly, low-*q* SAXS signals are more intense towards the edges of the particle, suggesting that there is a shell of oligomeric/high-molecular-weight material encompassing a free oleic acid core – though weaker WAXS signals are still observable at the edges, which suggests that free oleic acid is also present there to some degree - diffusion of which would be impeded by the viscous layer. Raman spectra suggest that a significant amount of oleic acid does indeed remain after oxidation, supporting the structural findings presented here (see Sect. 7.4.3.3). The significance of this core–shell finding is discussed in 7.5.

These experiments provided ~ 16 x 12 μm resolution SAXS images across the particle. This is the first time that spatially resolved structural changes have been measured in acoustically levitated particles during ozonolysis. This resolution gives a structural insight into the evolution of a particle during ozonolysis, allowing for the first time to draw a time-resolved self-assembled phase picture across a particle.

7.4.3.3 Evolution of the Raman spectrum during ozonolysis

Three key changes in the Raman spectrum are observed during ozonolysis. First, there is a clear shift of the strong acid–soap peak from ~ 2887 cm^{-1} (-CH_2 asymmetric stretching band) to ~ 2897 cm^{-1} accompanied by some broadening. This is indicative of the loss of alkyl chain order upon degradation of the acid–soap complex (Tandon et al., 2001). Secondly, the weak shoulder at ~ 2854 cm^{-1} (-CH_2 symmetric stretch) becomes a more defined peak during oxidation. This region of the Raman spectrum resembles that of oleic acid (Fig. 10-16(c)). This is further evidence, in combination with SAXS observations (Fig. 7-2(j)), that the oleic acid left in the system is not involved in an acid–soap structure after ozonolysis. This also stresses the importance of the

simultaneous SAXS/Raman technique for time-resolved structural and chemical analysis. Similar changes in the Raman spectra were observed during week-long high humidity experiments, in which the acid–soap complex also breaks down due to the formation of liquid crystalline phases in which the hydrophobic tails are not well-packed (Fig. 10-24, the appendix). Finally, the C=C-H peak at ~ 3000 cm^{-1} decreases in intensity due to the loss of unsaturation and removal of oleic acid from the system. It is important to note that this peak, along with the C=C peak at ~ 1650 cm^{-1} does not disappear entirely by the end of the reaction.

The observed evolution of the SAXS/WAXS and Raman data during ozonolysis coincide with each other and are complementary to one another since they follow structural and chemical changes simultaneously, demonstrating the power of the SAXS/WAXS/Raman technique for investigation of levitated particles. Note that the spatial scale is different between the techniques: micro-focus SAXS/WAXS experiments used a beam width and height of ~ 16 x 12 μm whereas the Raman laser spot diameter was ~ 4 μm focussed on the bulk of the particle. Both techniques concurrently confirm that the acid–soap complex breaks down as a result of simulated atmospheric ageing by ozone, however the Raman spectrum clearly demonstrates that 34 ± 8 % of oleic acid -generally assumed to be broken down efficiently by ozone- remains after the oxidation process. The significance of this is discussed in the following section.

7.4.4 **Atmospheric implications**

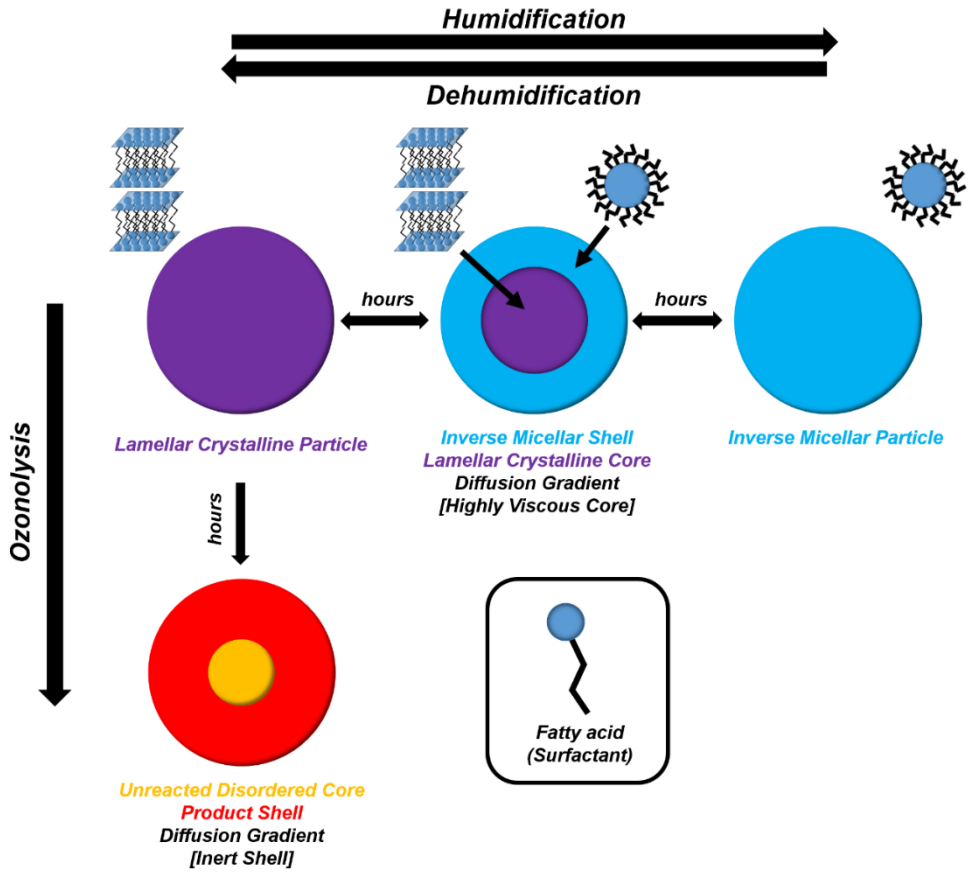

Figure 7-3. A schematic summarising the findings of this study. Particle humidification-dehumidification and ozonolysis are represented showing core–shell behaviour. Cartoons of SAXS-observed phases are labelled for clarity.

The acid–soap complex reported here is a crystalline organic material that is made up of surface-active molecules. The observations in this study suggest that water uptake is in line with the crystalline water uptake model described in the literature (Koop et al., 2011; Mikhailov et al., 2009). The addition of water gradually broke down the acid–soap complex and created a majority inverse micellar phase initially on the outside of the particle, then throughout the particle by the end of the experiment. This inverse micellar phase will have a different bulk diffusion coefficient compared to the

crystalline solid (Shiraiwa et al., 2011a). Our results suggest that water uptake into these separate crystalline and liquid crystalline phases is markedly different due to viscosity-related differences in diffusivity. Equilibration times are longer than what would be expected for a well-mixed liquid particle, explaining the observation of a water diffusion and particle phase gradient throughout the humidifying/dehumidifying particle (Fig. 7-1(c)-(f) and (g)-(l)). A similar trend is expected for other atmospheric trace gases such as ozone, implying the reactive lifetime of this aerosol would be affected by water uptake. These observations were backed up by the use of a simple model of water uptake and loss, which revealed that water diffusivity is reduced by ~ 33-fold in the crystalline lamellar phase compared with the inverse micellar phase.

Previous work has not considered the formation of inverse micelles, though there has been a theoretical study on aggregate formation in organic aerosols where the formation of micelles was postulated (Tabazadeh, 2005). However, recent atmospheric (Pfrang et al., 2017) and biological (Mele et al., 2018) studies into the oleic acid/sodium oleate/water self-assembled system have shown that the *inverse* micellar phase can form for this system due to a significant non-polar "oily" fraction in the mixture (*i.e.* oleic acid). This is because the majority of head groups in the mixture are protonated (*i.e.* uncharged). The larger hydrophobic tail region of the oleic acid molecule compared with its hydrophilic head drives interface curvature towards water, and therefore the formation of inverse phases, even in excess water. Inverted micellar and other inverted topology phases have been observed for oleic acid–sodium oleate mixtures in excess water (Seddon et al., 1990). Normal topology micelles (polar head groups at the micelle surface) form in systems with larger/charged headgroups, and are only observed within the sodium oleate–oleic acid system at high sodium oleate content (> 80 wt %) (Seddon

et al., 1990). It is therefore likely that the micellar phase observed in this system has an inverse rather than normal topology suggested in the preceding atmospheric literature (see Fig. 7-3 for a cartoon representation). Further addition of water to this phase would decrease the oil fraction in the mixture to a point where the water cavities, formed inside the inverse micelles, transform into hexagonal arrays of cylindrical water channels (Lisiecki et al., 1999). Our week-long humidity experiments, which revealed this inverse hexagonal phase, suggest that the inverse micellar phase observed in these levitated particles is a transient phase on its way to becoming the inverse hexagonal phase observed under the polarising microscope – consistent with the excess water phase observed in bulk mixtures with water of the same organic composition (Fig. 10-24 and 10-27, the appendix, which includes a cartoon of the inverse hexagonal phase). These phases are known to have differing physical characteristics such as viscosities (Mezzenga et al., 2005; Tiddy, 1980), which have a significant effect on diffusion through the particle phase, affecting reactive gas and water uptake and the rate of these processes (Koop et al., 2011; Marshall et al., 2016; Mikhailov et al., 2009; Reid et al., 2018; Shiraiwa et al., 2011).

There are implications for the atmospheric lifetime of such particles in locations where oleic acid is likely to be found such as in cooking emissions in urban areas of the UK (Allan et al., 2010) and China (Zhao et al., 2015), even emissions from a university cafeteria (Alves et al., 2020). We have shown that the dry acid–soap complex is much more stable towards ozonolysis than liquid oleic acid (Fig. 7-2(i)), having an ~ 80 % lower reactivity. If humidity-dependent phase changes take *ca.* a few hours to occur (~ 4 h for the large particle studied here), viscosity and diffusion through the particle would also change on a similar timescale. Reactive uptake of oxidants such as ozone would

therefore evolve slowly, resulting in a varying particle lifetime in the atmosphere that is dependent on its surrounding humidity - one of the uncertainties that need to be considered in atmospheric models (Abbatt et al., 2012; Gallimore et al., 2011; Liao et al., 2004).

Ozonolysis eventually breaks down the acid–soap complex. The reaction was stopped after 6+ h (400 min) exposure to a high ozone concentration (Fig. 7-2(i)). 34 ± 8 % of the double bonds remain in the particle as demonstrated by simultaneous Raman microscopy, while the acid–soap structure was no longer observable by SAXS from ~ 300 min onwards with 59 ± 8 % of the double bonds still remaining at that point. Atmospheric ageing thus changes the relative amounts of oleic acid and sodium oleate in the particle, limiting the ability of the acid–soap to remain stable and slowly breaking down the structure. The fact that the reaction remains slow after the acid–soap complex has disappeared indicates that the diffusivity of oleic acid and ozone continues to be severely impeded, thus maintaining the low reaction rate.

The aged particle is a more complicated mixture of reactants and products, some of which could be surface active and affect the phases observed within the particle. The presence of surface-active organic material in atmospheric aerosols is known to affect aerosol hygroscopicity by affecting properties such as the surface tension of aqueous droplets (Bzdek et al., 2020; Facchini et al., 1999, 2000; Ovadnevaite et al., 2017). Two of the primary products of oleic acid ozonolysis have been reported to be surface active: azelaic acid (Tuckermann, 2007) and nonanoic acid (King et al., 2009). If a significant portion of oleic acid remains in the particle as we have reported, it is likely that some of these surface-active products also remain in the viscous particle, although formation of high molecular weight products derived from these molecules would act as a sink

(Zahardis et al., 2006). This implies that in addition to the preservation of oleic acid in the particle, other surface-active products could also be preserved. Increasing the residence time of these surfactant molecules could have significant effects on cloud formation (Facchini et al., 1999; Prisle et al., 2012). These findings are also consistent with organic residues observed after oxidation of unsaturated organic films at the air–water interface, with similar implications (King et al., 2009; Pfrang et al., 2014; Sebastiani et al., 2018; Woden et al., 2018, 2021).

Products from oleic acid ozonolysis are known to take part in oligomerisation reactions with Criegee intermediates (Lee et al., 2012; Reynolds et al., 2006; Wang et al., 2016; Zahardis et al., 2006). These high molecular weight species are likely to have different physical characteristics, *e.g.* lower bulk diffusion coefficients and higher viscosities, compared to their precursors and other components in the particle. The higher molecular weight products may therefore impede reactant diffusion and act as a "crust", as proposed in previous modelling studies (Pfrang et al., 2011; Zhou et al., 2019). This is consistent with the continued slow ozonolysis after the acid–soap complex degradation we report here.

We suggest that there is a phase separation between viscous products and unreacted oleic acid at the end of the ozonolysis experiment, as suggested in the schematic Fig. 7-3. This separation is in the form of a core–shell arrangement where the shell consists of a majority high-molecular-weight, viscous product phase (evidenced by the low-q scattering observed in the oxidised particle, Fig. 7-2(g) and Fig. 10-13, the appendix) and the core is a majority unreacted disordered oleic acid phase. This is opposite to the viscous core-less viscous shell behaviour observed during humidification. Unlike the core–shell behaviour observed during humidification, where both phases are observable

by SAXS, the unreacted (and disordered) oleic acid is not detectable by SAXS. However, simultaneous WAXS has enabled us to determine that unreacted free oleic acid (with a characteristic WAXS peak, Fig. 10-28, the appendix) does exist both in the core and the shell of the particle at the end of ozonolysis (Fig. 7-2(h)). The fact that: (i) the Raman laser was focussed on the bulk of the sample, showing only disordered oleic acid by the end of the reaction; and (ii) ozonolysis does not speed up after the acid–soap SAXS signal has gone means it is most likely that a core–shell morphology prevails and that the reaction becomes limited by this inert shell (Pfrang et al., 2011). This also fits with the previous suggestion that viscous and large particles are not well-mixed and that the reaction occurs primarily in the surface layers of the particle (Moise and Rudich, 2002). The boundary between these phases is not thought to be as distinct as in the core–shell system observed during humidification due to the presence of oleic acid WAXS signal both in the centre and the edge of the particle.

The phase state of organic aerosols has been shown to affect the chemistry and transport of harmful pollutants, such as Polycyclic Aromatic Hydrocarbons (PAHs) (Mu et al., 2018). A coating of organic material on an aerosol particle has been used to explain the long-range atmospheric transport of toxic PAHs, which are products of combustion, increasing lung cancer risks (Shrivastava et al., 2017). The authors stated that the shielding was viscosity-dependent, therefore depending on the on the phase of the organic layer. In this study, atmospheric processing of the proxy (whether by humidity change or oxidation) significantly affects the phase of the particle by either changing the 3–D molecular arrangement or destroying the self-assembly altogether. Additionally, an inert crust layer formed as a result of oxidation may contribute to the shielding effect. As oleic acid has been observed in the urban environment, viscous oleic acid-derived

phases (including the acid–soap complex) could contribute to the effect organic films have on the shielding and transport of pollutants and thus on public health. Indeed, oleic acid has been observed in PAH-containing marine organic aerosols with significant urban influences, suggesting that this shielding effect could contribute to the transport of such aerosols (Kang et al., 2017).

Temperature has been identified as a key factor in determining phase state, reactivity and atmospheric transport of a reactive aerosol species (Mu et al., 2018). The acid–soap complex is stable at room temperature (~ 22 ^{o}C). Our POM temperature experiments also show that the acid–soap complex is thermally stable until degradation at ~ 32 ^{o}C, i.e. in the atmospherically relevant range (Fig. S5) consistent with the literature (Tandon et al., 2001). This suggests that this crystalline phase could exist in warm and dry environments. Although temperature would affect key parameters such as reaction rate constants and reactive gas surface accommodation times, the observation of a crystalline phase of oleic acid up to ~ 32 ^{o}C implies that reactant diffusion arguments made here are valid in many atmospheric temperature conditions.

Heterogeneous oleic acid ozonolysis has been reported to be a surface reaction with a small reacto-diffusive length of ~ 10–20 nm (Mendez et al., 2014; Moise and Rudich, 2002; Morris et al., 2002; Smith et al., 2002). A study on a different solid (in this case frozen) form of oleic acid showed that the reactive uptake of ozone is significantly decreased due to its solidity - the reaction happens only at the surface and diffusion to and from the near-surface and bulk layers is severely impeded (Moise and Rudich, 2002). The same argument can be applied to the acid–soap complex, which is stable at significantly higher temperatures than the frozen oleic acid investigated previously.

These observations emphasise the importance of the effect that solid/semi-solid species have on the viscosity and diffusion of reactants, and therefore oxidation kinetics. Atmospheric lifetimes of organic aerosols can be significantly increased as a result of viscous phase formation (Shiraiwa et al., 2010, 2011a; Virtanen et al., 2010). Here, in addition to previously-reported liquid crystalline phases (Pfrang et al., 2017), a solid crystalline state of an unsaturated fatty acid aerosol proxy was oxidised and results clearly show that the crystalline nature of the particle is the reason for the retardation of the reaction rate, which we estimate as being ~ 80 % slower for the acid–soap complex compared to an oleic acid droplet of similar size.

Atmospheric particulate matter is not always well mixed and their composition can be rather heterogeneous (Laskin et al., 2019). Fatty acids, including oleic acid, have been characterised on the surface of marine aerosols (Kirpes et al., 2019; Tervahattu et al., 2002, 2005). This therefore means that they can concentrate in a specific region of a particle, and we suggest that 1:1 acid soap complexes can exist in some regions, in coexistence with other sections of different compositions. The fact that this acid-soap complex still forms at a molar excess of oleic acid shows that the sample does not need to be at an exact 1:1 composition, and that there is a composition window where it can form, where the 1:1 molar complex coexists with the excess component. Our results suggest that it is possible to form such a phase at room humidity (~ 50 % RH). Formation of this phase could contribute to an explanation for the extended lifetime of oleic acid in the atmosphere compared with laboratory investigations (Robinson et al., 2006; Rudich et al., 2007).

As pH is variable in atmospheric aerosols (Paglione et al., 2021), so too would the ratio of oleic acid and sodium oleate. SAXS data from a 2:1 wt (oleic acid : sodium oleate)

levitated particle, representing more acidic conditions, demonstrate that an inverse micellar phase forms at ~ 50 % RH (Fig. 10-29, the appendix). Where exactly in the phase diagram this transition would occur is difficult to determine, requiring small changes in composition not practicable for a beamline experiment. This observation shows that a change in aerosol pH could affect particle viscosity via a change in nanostructure. The addition of other molecules does not prevent self-assembled phase formation and composition-dependent phase changes have been qualitatively observed (Pfrang et al., 2017) and are explored in follow-on work.

We are now able to spatially resolve SAXS/WAXS patterns through an acoustically levitated particle during humidity changes, revealing structural and physical changes as a result. This has provided a droplet-level picture of a diffusion front forming in a humidifying particle whereby an inverse micellar phase starts to form on the outside of the particle before eventually forming the dominant particle phase. This is in line with literature observations of diffusion fronts in highly viscous aerosol particles (Bastelberger et al., 2018; Zobrist et al., 2011). If diffusion varies across a particle, it follows that the diffusion coefficients of atmospheric trace gases would also vary throughout the particle. Some gases, such as ozone, are more soluble in hydrophobic than hydrophilic solvents (Panich and Ershov, 2019). The inverse micellar phase is a "water-in-oil" phase – where pockets of water are enclosed by surfactant molecules with their hydrophobic chains forming the majority hydrophobic "oil" domain (see Fig. 7-3). This means that ozone uptake is expected to increase upon inverse micelle formation for two reasons: (i) the phase is less viscous than the solid acid–soap complex, increasing the rate of ozone dissolution; and (ii) the majority of the particle is hydrophobic (water-

in-oil), suggesting ozone is more likely to dissolve and diffuse through the hydrophobic region of the particle rather than being constrained inside pockets of water.

7.5 Conclusion

The oleic acid/sodium oleate acid–soap complex has been identified in an unsaturated fatty acid aerosol proxy. Raman and IR spectroscopy, along with SAXS/WAXS, were used to confirm the formation of the acid–soap complex in acoustically levitated particles. The acid–soap complex was also identified by Raman microscopy on microscope slide deposits.

We observed a clear phase gradient in a humidifying levitated acid–soap complex consistent with impeded diffusion of water through highly viscous (in this case, solid and semi-solid) aerosols (Koop et al., 2011; Mikhailov et al., 2009; Pfrang et al., 2011; Reid et al., 2018). This is the first time that a spatially resolved phase gradient throughout a levitated humidifying aerosol particle has been reported using an X-ray-based technique. While we are unable to quantify the viscosity of the particle directly, it is possible to probe changes at the molecular organisational level, identifying clear differences in the way oleic acid moieties organise themselves during atmospheric processing. Preceding literature has reported mapped viscosity changes across a humidifying and oxidising aerosol particle using a fluorescence-based technique: Fluorescence Lifetime Imaging Microscopy (FLIM) (Hosny et al., 2013, 2016), with some experiments on optically-levitated particles (Athanasiadis et al., 2016; Fitzgerald et al., 2016). An advantage of an X-ray-based technique in comparison to FLIM is that there is no need to add a molecular marker to the sample in order to measure physical changes. This is especially important when considering self-assembled systems as adding other molecules to the system is likely to change the self-assembled structure

(Salentinig et al., 2010). The SAXS/WAXS experiment can also be used on samples in any physical state found in the atmosphere, allowing for phase changes to be monitored under a variety of conditions. Signals in the WAXS pattern correlate with crystallinity for this system and also contain information about the packing of alkyl chains via characteristic scattering peaks (Fig. 7-1(b)). We have also shown that it is possible to observe product formation via low-*q* scattering intensity increases, opening a new avenue of inquiry.

An aerosol particle will experience changes in humidity during its lifetime in the atmosphere. A gradual phase change throughout the humidifying acid–soap complex suggests that the particle may rarely be in a homogeneous state; rather, there would likely be humidity-dependent physical differences within the particle as its atmospheric environment is changing.

Week-long exposure to high humidity revealed the inverse hexagonal liquid crystal phase observed under the polarising microscope, correlating with the inverse hexagonal phase observed in bulk mixtures of oleic acid/sodium oleate with excess water. This is therefore believed to be the equilibrium phase at saturated humidity. Molecular diffusion through liquid crystal phases, such as the inverse hexagonal phase, can vary significantly and has been used for this reason with regard to drug delivery (Zabara and Mezzenga, 2014). Analogy can be drawn with the dissolution of atmospheric species whereby uptake of atmospheric trace gases could vary significantly depending on the 3–D organisation of the surfactant molecules.

The present study demonstrates that oleic acid will have a longer atmospheric lifetime if incorporated in an acid–soap complex. Aerosols have significant impacts on urban air

pollution with organic aerosol emissions as key components (Chan and Yao, 2008). In the UK, cooking organic aerosols have been estimated as an additional 10 % of anthropogenic $PM_{2.5}$ emissions (Ots et al., 2016). As previously discussed, phase-dependent viscous organic coatings have been reported to shield harmful carcinogenic combustion products (Shrivastava et al., 2017). Inert organic layer formation, such as what was observed in this study, may therefore contribute to this shielding effect, since a gas-phase oxidant cannot reach even highly reactive compounds in our particles.

The modelling of organic atmospheric aerosols and their effect on the climate is of great importance to the climate community (Jimenez et al., 2009; Kanakidou et al., 2005). If an aerosol has an extended atmospheric lifetime, it is more likely to affect the climate and urban environment. The physical state-dependent reactivity of the unsaturated fatty acid aerosol proxy presented here suggests that its atmospheric lifetime is variable and that this variance is significant. The addition of the humidity-dependent phase changes observed in the levitated proxy further enhances the dynamic nature of this system, highlighting how physical state is of utmost importance when considering reactivity and atmospheric lifetimes.

In summary, we have shown that the acid–soap complex is formed in an unsaturated fatty acid atmospheric aerosol proxy. This acid–soap complex is stable under atmospheric conditions and can be formed from an inverse micellar phase as demonstrated by reversible phase changes during a humidification–dehumidification cycle. A core–shell effect was observed during this cycle and phase-dependent diffusivity was estimated with ~ 33-fold difference between crystalline core and liquid crystalline shell. The proxy's ozone reactivity reduces significantly in the acid–soap complex state, and this remained so even after the acid–soap complex broke down.

Ozonolysis does not go to completion after the reaction was allowed to continue for ~ 6 h at a high ozone concentration: 34 ± 8 % of initial oleic acid remains in the particle and low-q scattering is observed in the SAXS pattern, suggesting that high-molecular-weight/oligomeric products are present and these products exhibit some order. This is evidence for an inert crust formation, inhibiting particle reactivity and protecting surface-active molecules from ageing with implications for aerosol processes such as cloud formation. This layer may also help protect toxic aerosol components such as PAHs, enabling them to travel further. This study presents a novel way of obtaining a spatially resolved phase picture of single aerosol particles, with the addition of WAXS to the list of simultaneous experiments possible on an acoustically levitated particle. We continue to demonstrate the versatile nature of oleic acid as an unsaturated fatty acid aerosol proxy.

7.6 Acknowledgements

AM wishes to thank NERC SCENARIO DTP award number NE/L002566/1 and CENTA DTP; CP wishes to thank the Royal Society (2007/R2) and NERC (grants NE/G000883/1 and NE/G019231/1) for support to develop the acoustic levitation system; JB was funded by the EPSRC Centre for Doctoral Training in Sustainable Chemical Technologies EP/L016354/1; Staff on the I22 beamline at the Diamond Light Source including Andy Smith and Tim Snow are acknowledged; Niclas Johansson and Esko Kokkonen are acknowledged for their help at beamtime experiments. Ben Woden is acknowledged for helping to calibrate the ozoniser. This work was carried out with the support of the Diamond Light Source, instrument I22 (proposals SM20541 and SM21663). Joanne M. Elliott is acknowledged for providing access to the polarising microscope.

7.6.1 **Author contributions**

AM carried out experiments, processed/analysed the data and co-wrote the manuscript; CP led the design and development of the acoustic levitator, initiated and co-designed the research project, carried out experiments, contributed to data analysis and co-wrote the manuscript; AMS co-designed the research project, carried out experiments, contributed to data analysis and co-wrote the manuscript; NJT set up and provided support during experiments on the I22 beamline at the Diamond Light Source; ADW set up and coupled the Raman experiment with the acoustic levitator and provided support during beamtime experiments. JB helped at beamtime experiments and contributed to sample preparation.

7.7 **Comment**

This study showcases the utility of a range of simultaneous techniques used on a levitated particle. It is the first time that spatially resolved nano-structural changes have been followed in such a proxy and there is good agreement between SAXS and Raman data regarding when self-assembly is destroyed by ozonolysis.

In the context of this thesis, the observation of low-q scattering from larger aggregates after extensive oxidation is similar to that observed in chapter 5, where fructose was added to the mixture. In this chapter, there is evidence that these aggregates concentrate at the surface of the particle, contributing to the product “crust” notion presented in chapter 2 and modelled in chapter 3.

A further experimental development is presented in the following chapter, where acoustic levitation was combined with polarising optical microscopy to follow structural changes with increasing humidity.

7.8 References

Abbatt, J. P. D., Lee, A. K. Y. and Thornton, J. A.: Quantifying trace gas uptake to tropospheric aerosol: Recent advances and remaining challenges, Chem. Soc. Rev., 41(19), 6555–6581, doi:10.1039/c2cs35052a, 2012.

Al-Kindi, S. S., Pope, F. D., Beddows, D. C., Bloss, W. J. and Harrison, R. M.: Size-dependent chemical ageing of oleic acid aerosol under dry and humidified conditions, Atmos. Chem. Phys., 16(24), 15561–15579, doi:10.5194/acp-16-15561-2016, 2016.

Allan, J. D., Williams, P. I., Morgan, W. T., Martin, C. L., Flynn, M. J., Lee, J., Nemitz, E. and Phillips, G. J.: and Physics Contributions from transport , solid fuel burning and cooking to primary organic aerosols in two UK cities, Atmos. Chem. Phys., 10, 647–668, 2010.

Alves, C. A., Vicente, E. D., Evtyugina, M., Vicente, A. M., Nunes, T., Lucarelli, F., Calzolai, G., Nava, S., Calvo, A. I., Alegre, C. del B., Oduber, F., Castro, A. and Fraile, R.: Indoor and outdoor air quality: A university cafeteria as a case study, Atmos. Pollut. Res., 11(3), 531–544, doi:10.1016/j.apr.2019.12.002, 2020.

Ananthapadmanabhan, K. P. and Somasundaran, P.: Acid-soap formation in aqueous oleate solutions, J. Colloid Interface Sci., 122(1), 104–109, doi:10.1016/0021-9797(88)90293-7, 1988.

Athanasiadis, A., Fitzgerald, C., Davidson, N. M., Giorio, C., Botchway, S. W., Ward, A. D., Kalberer, M., Pope, F. D. and Kuimova, M. K.: Dynamic viscosity mapping of the oxidation of squalene aerosol particles, Phys. Chem. Chem. Phys., 18(44), 30385–30393, doi:10.1039/c6cp05674a, 2016.

Bastelberger, S., Krieger, U. K., Luo, B. P. and Peter, T.: Time evolution of steep diffusion fronts in highly viscous aerosol particles measured with Mie resonance spectroscopy, J. Chem. Phys., 149(24), 244506, doi:10.1063/1.5052216, 2018.

Berkemeier, T., Steimer, S. S., Krieger, U. K., Peter, T., Pöschl, U., Ammann, M. and Shiraiwa, M.: Ozone uptake on glassy, semi-solid and liquid organic matter and the role of reactive oxygen intermediates in atmospheric aerosol chemistry, Phys. Chem. Chem. Phys., 18(18), 12662–12674, doi:10.1039/c6cp00634e, 2016.

Blöchliger, E., Blocher, M., Walde, P. and Luisi, P. L.: Matrix Effect in the Size Distribution of Fatty Acid Vesicles, J. Phys. Chem. B, 102(50), 10383–10390, doi:10.1021/jp981234w, 1998.

Boucher, O., Randall, D., Artaxo, P., Bretherton, C., Feingold, G., Forster, P., Kerminen, V.-M., Kondo, Y., Liao, H., Lohmann, U., Rasch, P., Satheesh, S. K., Sherwood, S., Stevens, B. and Zhang, X. Y.: Clouds and Aerosols, in Climate Change 2013 the Physical Science Basis: Working Group I Contribution to the Fifth Assessment Report of the Intergovernmental Panel on Climate Change, edited by T. F. Stocker, D. Qin, G.-K. Plattner, M. Tignor, S. K. Allen, J. Boschung, A. Nauels, Y. Xia, V. Bex, and P. M. Midgley, pp. 571–658, Cambridge University Press, Cambridge, United Kingdom and New York, NY, USA., 2013.

Bzdek, B. R., Reid, J. P., Malila, J. and Prisle, N. L.: The surface tension of surfactant-containing, finite volume droplets, Proc. Natl. Acad. Sci. U. S. A., 117(15), 8335–8343, doi:10.1073/pnas.1915660117, 2020.

Chan, C. K. and Yao, X.: Air pollution in mega cities in China, Atmos. Environ., 42(1), 1–42, doi:10.1016/j.atmosenv.2007.09.003, 2008.

Cheng, Y., Li, S. M., Leithead, A., Brickell, P. C. and Leaitch, W. R.: Characterizations of cis-pinonic acid and n-fatty acids on fine aerosols in the Lower Fraser Valley during Pacific 2001 Air Quality Study, Atmos. Environ., 38(34), 5789–5800, doi:10.1016/j.atmosenv.2004.01.051, 2004.

Chu, S. N., Sands, S., Tomasik, M. R., Lee, P. S. and McNeill, V. F.: Ozone oxidation of surface-adsorbed polycyclic aromatic hydrocarbons: Role of PAH-surface interaction, J. Am. Chem. Soc., 132(45), 15968–15975, doi:10.1021/ja1014772, 2010.

Cistola, D. P., Atkinson, D., Hamilton, J. A. and Small, D. M.: Phase Behavior and Bilayer Properties of Fatty Acids: Hydrated 1:1 Acid-Soaps, Biochemistry, 25(10), 2804–2812, doi:10.1021/bi00358a011, 1986.

Davies, J. F. and Wilson, K. R.: Raman Spectroscopy of Isotopic Water Diffusion in Ultraviscous, Glassy, and Gel States in Aerosol by Use of Optical Tweezers, Anal. Chem., 88(4), 2361–2366, doi:10.1021/acs.analchem.5b04315, 2016.

Engblom, J., Engström, S. and Fontell, K.: The effect of the skin penetration enhancer Azone® on fatty acid-sodium soap-water mixtures, J. Control. Release, 33(2), 299–305, doi:10.1016/0168-3659(94)00105-4, 1995.

Estillore, A. D., Trueblood, J. V. and Grassian, V. H.: Atmospheric chemistry of bioaerosols: Heterogeneous and multiphase reactions with atmospheric oxidants and other trace gases, Chem. Sci., 7(11), 6604–6616, doi:10.1039/c6sc02353c, 2016.

Facchini, M. C., Mircea, M., Fuzzi, S. and Charlson, R. J.: Cloud albedo enhancement by surface-active organic solutes in growing droplets, Nature, 401(6750), 257–259, doi:10.1038/45758, 1999.

Facchini, M. C., Decesari, S., Mircea, M., Fuzzi, S. and Loglio, G.: Surface tension of atmospheric wet aerosol and cloud/fog droplets in relation to their organic carbon content and chemical composition, Atmos. Environ., 34(28), 4853–4857, doi:10.1016/S1352-2310(00)00237-5, 2000.

Fitzgerald, C., Hosny, N. A., Tong, H., Seville, P. C., Gallimore, P. J., Davidson, N. M., Athanasiadis, A., Botchway, S. W., Ward, A. D., Kalberer, M., Kuimova, M. K. and Pope, F. D.: Fluorescence lifetime imaging of optically levitated aerosol: A technique to quantitatively map the viscosity of suspended aerosol particles, Phys. Chem. Chem. Phys., 18(31), 21710–21719, doi:10.1039/c6cp03674k, 2016.

Freedman, M. A.: Phase separation in organic aerosol, Chem. Soc. Rev., 46(24), 7694–7705, doi:10.1039/c6cs00783j, 2017.

Freedman, M. A.: Liquid–Liquid Phase Separation in Supermicrometer and Submicrometer Aerosol Particles, Acc. Chem. Res., 53(6), 1102–1110, doi:10.1021/acs.accounts.0c00093, 2020.

Fu, P. Q., Kawamura, K., Chen, J., Charrière, B. and Sempéré, R.: Organic molecular composition of marine aerosols over the Arctic Ocean in summer: Contributions of primary emission and secondary aerosol formation, Biogeosciences, 10(2), 653–667, doi:10.5194/bg-10-653-2013, 2013.

Gallimore, P. J., Achakulwisut, P., Pope, F. D., Davies, J. F., Spring, D. R. and Kalberer, M.: Importance of relative humidity in the oxidative ageing of organic aerosols: Case study of the ozonolysis of maleic acid aerosol, Atmos. Chem. Phys., 11(23), 12181–12195, doi:10.5194/acp-11-12181-2011, 2011.

Gallimore, P. J., Griffiths, P. T., Pope, F. D., Reid, J. P. and Kalberer, M.: Comprehensive modeling study of ozonolysis of oleic acid aerosol based on real-time, online measurements of aerosol composition, J. Geophys. Res., 122(8), 4364–4377, doi:10.1002/2016JD026221, 2017.

Guarnieri, M. and Balmes, J. R.: Outdoor air pollution and asthma, Lancet, 383(9928), 1581–1592, doi:10.1016/S0140-6736(14)60617-6, 2014.

He, X., Leng, C., Pang, S. and Zhang, Y.: Kinetics study of heterogeneous reactions of ozone with unsaturated fatty acid single droplets using micro-FTIR spectroscopy, RSC Adv., 7(6), 3204–3213, doi:10.1039/C6RA25255A, 2017.

Hosny, N. A., Fitzgerald, C., Tong, C., Kalberer, M., Kuimova, M. K. and Pope, F. D.: Fluorescent lifetime imaging of atmospheric aerosols: A direct probe of aerosol viscosity, Faraday Discuss., 165, 343–356, doi:10.1039/c3fd00041a, 2013.

Hosny, N. A., Fitzgerald, C., Vyšniauskas, A., Athanasiadis, A., Berkemeier, T., Uygur, N., Pöschl, U., Shiraiwa, M., Kalberer, M., Pope, F. D. and Kuimova, M. K.: Direct imaging of changes in aerosol particle viscosity upon hydration and chemical aging, Chem. Sci., 7(2), 1357–1367, doi:10.1039/c5sc02959g, 2016.

Hung, H. M., Katrib, Y. and Martin, S. T.: Products and mechanisms of the reaction of oleic acid with ozone and nitrate radical, J. Phys. Chem. A, 109(20), 4517–4530, doi:10.1021/jp0500900, 2005.

Ishimaru, M., Toyota, T., Takakura, K., Sugawara, T. and Sugawara, Y.: Helical Aggregate of Oleic Acid and Its Dynamics in Water at pH 8, Chem. Lett., 34(1), 46–47, doi:10.1246/cl.2005.46, 2005.

Iwahashi, M., Yamaguchi, Y., Kato, T., Horiuchi, T., Sakurai, I. and Suzuki, M.: Temperature dependence of molecular conformation and liquid structure of cis-9-octadecenoic acid, J. Phys. Chem., 95(1), 445–451, doi:10.1021/j100154a078, 1991.

Jimenez, J. L., Canagaratna, M. R., Donahue, N. M., Prevot, A. S. H., Zhang, Q., Kroll, J. H., DeCarlo, P. F., Allan, J. D., Coe, H., Ng, N. L., Aiken, A. C., Docherty, K. S., Ulbrich, I. M., Grieshop, A. P., Robinson, A. L., Duplissy, J., Smith, J. D., Wilson, K. R., Lanz, V. A., Hueglin, C., Sun, Y. L., Tian, J., Laaksonen, A., Raatikainen, T., Rautiainen, J., Vaattovaara, P., Ehn, M., Kulmala, M., Tomlinson, J. M., Collins, D. R., Cubison, M. J., Dunlea, J., Huffman, J. A., Onasch, T. B., Alfarra, M. R., Williams, P. I., Bower, K., Kondo, Y., Schneider, J., Drewnick, F., Borrmann, S., Weimer, S., Demerjian, K., Salcedo, D., Cottrell, L., Griffin, R., Takami, A., Miyoshi, T., Hatakeyama, S., Shimono, A., Sun, J. Y., Zhang, Y. M., Dzepina, K., Kimmel, J. R., Sueper, D., Jayne, J. T., Herndon, S. C., Trimborn, A. M., Williams, L. R., Wood, E. C., Middlebrook, A. M., Kolb, C. E., Baltensperger, U. and Worsnop, D. R.: Evolution of Organic Aerosols in the Atmosphere, Science (80-.)., 326(5959), 1525–1529, doi:10.1126/science.1180353, 2009.

Kanakidou, M., Seinfeld, J. H., Pandis, S. N., Barnes, I., Dentener, F. J., Facchini, M. C., Van Dingenen, R., Ervens, B., Nenes, A., Nielsen, C. J., Swietlicki, E., Putaud, J. P., Balkanski, Y., Fuzzi, S., Horth, J., Moortgat, G. K., Winterhalter, R., Myhre, C. E. L., Tsigaridis, K., Vignati, E., Stephanou, E. G. and Wilson, J.: Organic aerosol and global climate modelling: a review, Atmos. Chem. Phys., 5(4), 1053–1123, doi:10.5194/acp-5-1053-2005, 2005.

Kang, M., Yang, F., Ren, H., Zhao, W., Zhao, Y., Li, L., Yan, Y., Zhang, Y., Lai, S., Zhang, Y., Yang, Y., Wang, Z., Sun, Y. and Fu, P.: Influence of continental organic aerosols to the marine atmosphere over the East China Sea: Insights from lipids, PAHs and phthalates, Sci. Total Environ., 607–608, 339–350, doi:10.1016/j.scitotenv.2017.06.214, 2017.

Keene, W. C., Pszenny, A. A. P., Maben, J. R., Stevenson, E. and Wall, A.: Closure evaluation of size-resolved aerosol pH in the New England coastal atmosphere during summer, J. Geophys. Res. D Atmos., 109(23), 1–16, doi:10.1029/2004JD004801, 2004.

King, M. D., Thompson, K. C. and Ward, A. D.: Laser tweezers raman study of optically trapped aerosol droplets of seawater and oleic acid reacting with ozone: Implications for cloud-droplet properties, J. Am. Chem. Soc., 126(51), 16710–16711, doi:10.1021/ja044717o, 2004.

King, M. D., Rennie, A. R., Thompson, K. C., Fisher, F. N., Dong, C. C., Thomas, R. K., Pfrang, C. and Hughes, A. V.: Oxidation of oleic acid at the air-water interface and its potential effects on cloud critical supersaturations, Phys. Chem. Chem. Phys., 11(35), 7699–7707, doi:10.1039/b906517b, 2009.

King, M. D., Rennie, A. R., Pfrang, C., Hughes, A. V. and Thompson, K. C.: Interaction of nitrogen dioxide (NO2) with a monolayer of oleic acid at the air-water interface - A simple proxy for atmospheric aerosol, Atmos. Environ., 44(14), 1822–1825, doi:10.1016/j.atmosenv.2010.01.031, 2010.

Kirpes, R. M., Bonanno, D., May, N. W., Fraund, M., Barget, A. J., Moffet, R. C., Ault, A. P. and Pratt, K. A.: Wintertime Arctic Sea Spray Aerosol Composition Controlled by

Sea Ice Lead Microbiology, ACS Cent. Sci., 5(11), 1760–1767, doi:10.1021/acscentsci.9b00541, 2019.

Knopf, D. A., Anthony, L. M. and Bertram, A. K.: Reactive uptake of O3 by multicomponent and multiphase mixtures containing oleic acid, J. Phys. Chem. A, 109(25), 5579–5589, doi:10.1021/jp0512513, 2005.

Koop, T., Bookhold, J., Shiraiwa, M. and Pöschl, U.: Glass transition and phase state of organic compounds: Dependency on molecular properties and implications for secondary organic aerosols in the atmosphere, Phys. Chem. Chem. Phys., 13(43), 19238–19255, doi:10.1039/c1cp22617g, 2011.

Laskin, A., Moffet, R. C. and Gilles, M. K.: Chemical Imaging of Atmospheric Particles, Acc. Chem. Res., 52(12), 3419–3431, doi:10.1021/acs.accounts.9b00396, 2019.

Last, D. J., Nájera, J. J., Wamsley, R., Hilton, G., McGillen, M., Percival, C. J. and Horn, A. B.: Ozonolysis of organic compounds and mixtures in solution. Part I: Oleic, maleic, nonanoic and benzoic acids, Phys. Chem. Chem. Phys., 11(9), 1427–1440, doi:10.1039/b815425b, 2009.

Lee, J. W. L., Carrascón, V., Gallimore, P. J., Fuller, S. J., Björkegren, A., Spring, D. R., Pope, F. D. and Kalberer, M.: The effect of humidity on the ozonolysis of unsaturated compounds in aerosol particles, Phys. Chem. Chem. Phys., 14(22), 8023–8031, doi:10.1039/c2cp24094g, 2012.

Liao, H., Seinfeld, J. H., Adams, P. J. and Mickley, L. J.: Global radiative forcing of coupled tropospheric ozone and aerosols in a unified general circulation model, J. Geophys. Res. Atmos., 109(16), 1–33, doi:10.1029/2003JD004456, 2004.

Lisiecki, I., André, P., Filankembo, A., Petit, C., Tanori, J., Gulik-Krzywicki, T., Ninham, B. W. and Pileni, M. P.: Mesostructured fluids. 1. Cu(AOT)2-H2O-isooctane in oil rich regions, J. Phys. Chem. B, 103(43), 9168–9175, doi:10.1021/jp991242s, 1999.

Liu, P., Song, M., Zhao, T., Gunthe, S. S., Ham, S., He, Y., Qin, Y. M., Gong, Z., Amorim, J. C., Bertram, A. K. and Martin, S. T.: Resolving the mechanisms of hygroscopic growth and cloud condensation nuclei activity for organic particulate matter, Nat. Commun., 9(1), 4076, doi:10.1038/s41467-018-06622-2, 2018.

Lynch, M. L.: Acid-soaps, Curr. Opin. Colloid Interface Sci., 2(5), 495–500, doi:10.1016/S1359-0294(97)80097-0, 1997.

Lynch, M. L., Pan, Y. and Laughlin, R. G.: Spectroscopic and thermal characterization of 1:2 sodium soap/fatty acid acid-soap crystals, J. Phys. Chem., 100(1), 357–361, doi:10.1021/jp952124h, 1996.

Lynch, M. L., Wireko, F., Tarek, M. and Klein, M.: Intermolecular Interactions and the Structure of Fatty Acid−Soap Crystals, J. Phys. Chem. B, 105(2), 552–561, doi:10.1021/jp002602a, 2002.

Marshall, F. H., Miles, R. E. H., Song, Y., Ohm, P. B., Power, R. M., Reid, J. P. and Dutcher, C. S.: Diffusion and reactivity in ultraviscous aerosol and the correlation with particle viscosity, Chem. Sci., 7, 1298–1308, doi:10.1039/c5sc03223g, 2016.

Mauersberger, K., Barnes, J., Hanson, D. and Morton, J.: Measurement of the ozone absorption cross-section at the 253.7 nm mercury line, Geophys. Res. Lett., 13(7), 671–673, doi:10.1029/GL013i007p00671, 1986.

Mele, S., Söderman, O., Ljusberg-Wahrén, H., Thuresson, K., Monduzzi, M. and Nylander, T.: Phase behavior in the biologically important oleic acid/sodium oleate/water system, Chem. Phys. Lipids, 211(September 2017), 30–36, doi:10.1016/j.chemphyslip.2017.11.017, 2018.

Mendez, M., Visez, N., Gosselin, S., Crenn, V., Riffault, V. and Petitprez, D.: Reactive and nonreactive ozone uptake during aging of oleic acid particles, J. Phys. Chem. A, 118(40), 9471–9481, doi:10.1021/jp503572c, 2014.

Mezzenga, R., Meyer, C., Servais, C., Romoscanu, A. I., Sagalowicz, L. and Hayward, R. C.: Shear rheology of lyotropic liquid crystals: A case study, Langmuir, 21(8), 3322–3333, doi:10.1021/la046964b, 2005.

Mikhailov, E., Vlasenko, S., Martin, S. T., Koop, T. and Pöschl, U.: Amorphous and crystalline aerosol particles interacting with water vapor: Conceptual framework and experimental evidence for restructuring, phase transitions and kinetic limitations, Atmos. Chem. Phys., 9(24), 9491–9522, doi:10.5194/acp-9-9491-2009, 2009.

Milsom, A., Squires, A. M., Woden, B., Terrill, N. J., Ward, A. D. and Pfrang, C.: The persistence of a proxy for cooking emissions in megacities: a kinetic study of the ozonolysis of self-assembled films by simultaneous small and wide angle X-ray scattering (SAXS/WAXS) and Raman microscopy, Faraday Discuss., (Accepted Manuscript), doi:10.1039/D0FD00088D, 2021.

Moise, T. and Rudich, Y.: Reactive uptake of ozone by aerosol-associated unsaturated fatty acids: Kinetics, mechanism, and products, J. Phys. Chem. A, 106(27), 6469–6476, doi:10.1021/jp025597e, 2002.

Morris, J. W., Davidovits, P., Jayne, J. T., Jimenez, J. L., Shi, Q., Kolb, C. E., Worsnop, D. R., Barney, W. S. and Cass, G.: Kinetics of submicron oleic acid aerosols with ozone: A novel aerosol mass spectrometric technique, Geophys. Res. Lett., 29(9), 71-1-71–4, doi:10.1029/2002gl014692, 2002.

Mu, Q., Shiraiwa, M., Octaviani, M., Ma, N., Ding, A., Su, H., Lammel, G., Pöschl, U. and Cheng, Y.: Temperature effect on phase state and reactivity controls atmospheric multiphase chemistry and transport of PAHs, Sci. Adv., 4(3), eaap7314, doi:10.1126/sciadv.aap7314, 2018.

Nájera, J. J., Percival, C. J. and Horn, A. B.: Infrared spectroscopic evidence for a heterogeneous reaction between ozone and sodium oleate at the gas-aerosol interface: Effect of relative humidity, Int. J. Chem. Kinet., 47(4), 277–288, doi:10.1002/kin.20907, 2015.

Nikiforidis, C. V., Gilbert, E. P. and Scholten, E.: Organogel formation via supramolecular assembly of oleic acid and sodium oleate, RSC Adv., 5(59), 47466–47475, doi:10.1039/c5ra05336f, 2015.

Osterroht, C.: Extraction of dissolved fatty acids from sea water, Fresenius. J. Anal. Chem., 345(12), 773–779, doi:10.1007/BF00323009, 1993.

Ots, R., Vieno, M., Allan, J. D., Reis, S., Nemitz, E., Young, D. E., Coe, H., Di Marco, C., Detournay, A., Mackenzie, I. A., Green, D. C. and Heal, M. R.: Model simulations of cooking organic aerosol (COA) over the UK using estimates of emissions based on measurements at two sites in London, Atmos. Chem. Phys., 16(21), 13773–13789, doi:10.5194/acp-16-13773-2016, 2016.

Ovadnevaite, J., Zuend, A., Laaksonen, A., Sanchez, K. J., Roberts, G., Ceburnis, D., Decesari, S., Rinaldi, M., Hodas, N., Facchini, M. C., Seinfeld, J. H. and O'Dowd, C.: Surface tension prevails over solute effect in organic-influenced cloud droplet activation, Nature, 546(7660), 637–641, doi:10.1038/nature22806, 2017.

Panich, N. M. and Ershov, B. G.: Solubility of Ozone in Organic Solvents, Russ. J. Gen. Chem., 89(2), 185–189, doi:10.1134/S1070363219020026, 2019.

Paglione, M., Decesari, S., Rinaldi, M., Tarozzi, L., Manarini, F., Gilardoni, S., Facchini, M. C., Fuzzi, S., Bacco, D., Trentini, A., Pandis, S. N. and Nenes, A.: Historical Changes in Seasonal Aerosol Acidity in the Po Valley (Italy) as Inferred from Fog Water and Aerosol Measurements, Environ. Sci. Technol., acs.est.1c00651, doi:10.1021/acs.est.1c00651, 2021.

Pfrang, C., Shiraiwa, M. and Pöschl, U.: Chemical ageing and transformation of diffusivity in semi-solid multi-component organic aerosol particles, Atmos. Chem. Phys., 11(14), 7343–7354, doi:10.5194/acp-11-7343-2011, 2011.

Pfrang, C., Sebastiani, F., Lucas, C. O. M., King, M. D., Hoare, I. D., Chang, D. and Campbell, R. A.: Ozonolysis of methyl oleate monolayers at the air-water interface: Oxidation kinetics, reaction products and atmospheric implications, Phys. Chem. Chem. Phys., 16(26), 13220–13228, doi:10.1039/c4cp00775a, 2014.

Pfrang, C., Rastogi, K., Cabrera-Martinez, E. R., Seddon, A. M., Dicko, C., Labrador, A., Plivelic, T. S., Cowieson, N. and Squires, A. M.: Complex three-dimensional self-assembly in proxies for atmospheric aerosols, Nat. Commun., 8(1), 1724, doi:10.1038/s41467-017-01918-1, 2017.

Pöschl, U.: Atmospheric aerosols: Composition, transformation, climate and health effects, Angew. Chemie Int. Ed., 44(46), 7520–7540, doi:10.1002/anie.200501122, 2005.

Price, H. C., Mattsson, J., Zhang, Y., Bertram, A. K., Davies, J. F., Grayson, J. W., Martin, S. T., O'Sullivan, D., Reid, J. P., Rickards, A. M. J. and Murray, B. J.: Water diffusion in atmospherically relevant α-pinene secondary organic material, Chem. Sci., 6(8), 4876–4883, doi:10.1039/c5sc00685f, 2015.

Prisle, N. L., Asmi, A., Topping, D., Partanen, A.-I., Romakkaniemi, S., Dal Maso, M., Kulmala, M., Laaksonen, A., Lehtinen, K. E. J., McFiggans, G. and Kokkola, H.: Surfactant effects in global simulations of cloud droplet activation, Geophys. Res. Lett., 39(5), n/a-n/a, doi:10.1029/2011GL050467, 2012.

Putnam, C. D., Hammel, M., Hura, G. L. and Tainer, J. A.: X-ray solution scattering (SAXS) combined with crystallography and computation: defining accurate macromolecular structures, conformations and assemblies in solution, Q. Rev. Biophys., 40(3), 191–285, doi:10.1017/s0033583507004635, 2007.

Reid, J. P., Bertram, A. K., Topping, D. O., Laskin, A., Martin, S. T., Petters, M. D., Pope, F. D. and Rovelli, G.: The viscosity of atmospherically relevant organic particles, Nat. Commun., 9(1), 1–14, doi:10.1038/s41467-018-03027-z, 2018.

Renbaum-Wolff, L., Grayson, J. W., Bateman, A. P., Kuwata, M., Sellier, M., Murray, B. J., Shilling, J. E., Martin, S. T. and Bertram, A. K.: Viscosity of a-pinene secondary organic material and implications for particle growth and reactivity, Proc. Natl. Acad. Sci., 110(20), 8014–8019, doi:10.1073/pnas.1219548110, 2013.

Reynolds, J. C., Last, D. J., McGillen, M., Nijs, A., Horn, A. B., Percival, C., Carpenter, L. J. and Lewis, A. C.: Structural analysis of oligomeric molecules formed from the reaction products of oleic acid ozonolysis, Environ. Sci. Technol., 40(21), 6674–6681, doi:10.1021/es060942p, 2006.

Robinson, A. L., Donahue, N. M. and Rogge, W. F.: Photochemical oxidation and changes in molecular composition of organic aerosol in the regional context, J. Geophys. Res. Atmos., 111(3), 1–15, doi:10.1029/2005JD006265, 2006.

Rudich, Y., Donahue, N. M. and Mentel, T. F.: Aging of Organic Aerosol: Bridging the Gap Between Laboratory and Field Studies, Annu. Rev. Phys. Chem., 58(1), 321–352, doi:10.1146/annurev.physchem.58.032806.104432, 2007.

Salentinig, S., Sagalowicz, L. and Glatter, O.: Self-Assembled Structures and pKa Value of Oleic Acid in Systems of Biological Relevance, Langmuir, 26(14), 11670–11679, doi:10.1021/la101012a, 2010.

Schwier, A. N., Sareen, N., Lathem, T. L., Nenes, A. and McNeill, V. F.: Ozone oxidation of oleic acid surface films decreases aerosol cloud condensation nuclei activity, J. Geophys. Res. Atmos., 116(16), D16202, doi:10.1029/2010JD015520, 2011.

Sebastiani, F., Campbell, R. A., Rastogi, K. and Pfrang, C.: Nighttime oxidation of surfactants at the air-water interface: Effects of chain length, head group and saturation, Atmos. Chem. Phys., 18(5), 3249–3268, doi:10.5194/acp-18-3249-2018, 2018.

Seddon, A. M., Richardson, S. J., Rastogi, K., Plivelic, T. S., Squires, A. M. and Pfrang, C.: Control of Nanomaterial Self-Assembly in Ultrasonically Levitated Droplets, J. Phys. Chem. Lett., 7(7), 1341–1345, doi:10.1021/acs.jpclett.6b00449, 2016.

Seddon, J. M., Bartle, E. A. and Mingins, J.: Inverse cubic liquid-crystalline phases of phospholipids and related lyotropic systems, J. Phys. Condens. Matter, 2, SA285–SA290, doi:10.1088/0953-8984/2/S/043, 1990.

Shiraiwa, M., Pfrang, C. and Pöschl, U.: Kinetic multi-layer model of aerosol surface and bulk chemistry (KM-SUB): The influence of interfacial transport and bulk diffusion on the oxidation of oleic acid by ozone, Atmos. Chem. Phys., 10, 3673–3691, doi:10.5194/acp-10-3673-2010, 2010.

Shiraiwa, M., Ammann, M., Koop, T. and Poschl, U.: Gas uptake and chemical aging of semisolid organic aerosol particles, Proc. Natl. Acad. Sci. U. S. A., 108(27), 11003–11008, doi:10.1073/pnas.1103045108, 2011.

Shiraiwa, M., Li, Y., Tsimpidi, A. P., Karydis, V. A., Berkemeier, T., Pandis, S. N., Lelieveld, J., Koop, T. and Pöschl, U.: Global distribution of particle phase state in atmospheric secondary organic aerosols, Nat. Commun., 8, 1–7, doi:10.1038/ncomms15002, 2017.

Shrivastava, M., Lou, S., Zelenyuk, A., Easter, R. C., Corley, R. A., Thrall, B. D., Rasch, P. J., Fast, J. D., Simonich, S. L. M., Shen, H. and Tao, S.: Global long-range transport and lung cancer risk from polycyclic aromatic hydrocarbons shielded by coatings of organic aerosol, Proc. Natl. Acad. Sci. U. S. A., 114(6), 1246–1251, doi:10.1073/pnas.1618475114, 2017.

Slade, J. H., Ault, A. P., Bui, A. T., Ditto, J. C., Lei, Z., Bondy, A. L., Olson, N. E., Cook, R. D., Desrochers, S. J., Harvey, R. M., Erickson, M. H., Wallace, H. W., Alvarez, S. L., Flynn, J. H., Boor, B. E., Petrucci, G. A., Gentner, D. R., Griffin, R. J. and Shepson, P. B.: Bouncier Particles at Night: Biogenic Secondary Organic Aerosol

Chemistry and Sulfate Drive Diel Variations in the Aerosol Phase in a Mixed Forest, Environ. Sci. Technol., 53(9), 4977–4987, doi:10.1021/acs.est.8b07319, 2019.

Smith, G. D., Woods, E., DeForest, C. L., Baer, T. and Miller, R. E.: Reactive uptake of ozone by oleic acid aerosol particles: Application of single-particle mass spectrometry to heterogeneous reaction kinetics, J. Phys. Chem. A, 106(35), 8085–8095, doi:10.1021/jp020527t, 2002.

Stevens, B. and Feingold, G.: Untangling aerosol effects on clouds and precipitation in a buffered system, Nature, 461(7264), 607–613, doi:10.1038/nature08281, 2009.

Tabazadeh, A.: Organic aggregate formation in aerosols and its impact on the physicochemical properties of atmospheric particles, Atmos. Environ., 39(30), 5472–5480, doi:10.1016/j.atmosenv.2005.05.045, 2005.

Tandon, P., Raudenkolb, S., Neubert, R. H. H., Rettig, W. and Wartewig, S.: X-ray diffraction and spectroscopic studies of oleic acid-sodium oleate, Chem. Phys. Lipids, 109(1), 37–45, doi:10.1016/S0009-3084(00)00207-3, 2001.

Tervahattu, H.: Identification of an organic coating on marine aerosol particles by TOF-SIMS, J. Geophys. Res., 107(D16), 4319, doi:10.1029/2001JD001403, 2002.

Tervahattu, H., Juhanoja, J., Vaida, V., Tuck, A. F., Niemi, J. V., Kupiainen, K., Kulmala, M. and Vehkamäki, H.: Fatty acids on continental sulfate aerosol particles, J. Geophys. Res. D Atmos., 110(6), 1–9, doi:10.1029/2004JD005400, 2005.

Tiddy, G. J. T.: Surfactant-water liquid crystal phases, Phys. Rep., 57(1), 1–46, doi:10.1016/0370-1573(80)90041-1, 1980.

Tuckermann, R.: Surface tension of aqueous solutions of water-soluble organic and inorganic compounds, Atmos. Environ., 41(29), 6265–6275, doi:10.1016/j.atmosenv.2007.03.051, 2007.

Veghte, D. P., Altaf, M. B. and Freedman, M. A.: Size dependence of the structure of organic aerosol, J. Am. Chem. Soc., 135(43), 16046–16049, doi:10.1021/ja408903g, 2013.

Vesna, O., Sax, M., Kalberer, M., Gaschen, A. and Ammann, M.: Product study of oleic acid ozonolysis as function of humidity, Atmos. Environ., 43(24), 3662–3669, doi:10.1016/j.atmosenv.2009.04.047, 2009.

Vicente, E. D., Vicente, A., Evtyugina, M., Carvalho, R., Tarelho, L. A. C., Oduber, F. I. and Alves, C.: Particulate and gaseous emissions from charcoal combustion in barbecue grills, Fuel Process. Technol., 176(April), 296–306, doi:10.1016/j.fuproc.2018.03.004, 2018.

Virtanen, A., Joutsensaari, J., Koop, T., Kannosto, J., Yli-Pirilä, P., Leskinen, J., Mäkelä, J. M., Holopainen, J. K., Pöschl, U., Kulmala, M., Worsnop, D. R. and Laaksonen, A.: An amorphous solid state of biogenic secondary organic aerosol particles, Nature, 467(7317), 824–827, doi:10.1038/nature09455, 2010.

Wang, M., Yao, L., Zheng, J., Wang, X., Chen, J., Yang, X., Worsnop, D. R., Donahue, N. M. and Wang, L.: Reactions of Atmospheric Particulate Stabilized Criegee Intermediates Lead to High-Molecular-Weight Aerosol Components, Environ. Sci. Technol., 50(11), 5702–5710, doi:10.1021/acs.est.6b02114, 2016.

Woden, B., Skoda, M., Hagreen, M. and Pfrang, C.: Night-Time Oxidation of a Monolayer Model for the Air–Water Interface of Marine Aerosols—A Study by

Simultaneous Neutron Reflectometry and in Situ Infra-Red Reflection Absorption Spectroscopy (IRRAS), Atmosphere (Basel)., 9(12), 471, doi:10.3390/atmos9120471, 2018.

Woden, B., Skoda, M. W. A., Milsom, A., Gubb, C., Maestro, A., Tellam, J. and Pfrang, C.: Ozonolysis of fatty acid monolayers at the air–water interface: organic films may persist at the surface of atmospheric aerosols, Atmos. Chem. Phys., 21(2), 1325–1340, doi:10.5194/acp-21-1325-2021, 2021.

Zabara, A. and Mezzenga, R.: Controlling molecular transport and sustained drug release in lipid-based liquid crystalline mesophases, J. Control. Release, 188, 31–43, doi:10.1016/j.jconrel.2014.05.052, 2014.

Zahardis, J. and Petrucci, G. A.: The oleic acid-ozone heterogeneous reaction system: Products, kinetics, secondary chemistry, and atmospheric implications of a model system - A review, Atmos. Chem. Phys., 7(5), 1237–1274, doi:10.5194/acp-7-1237-2007, 2007.

Zahardis, J., LaFranchi, B. W. and Petrucci, G. A.: Photoelectron resonance capture ionization-aerosol mass spectrometry of the ozonolysis products of oleic acid particles: Direct measure of higher molecular weight oxygenates, J. Geophys. Res. D Atmos., 110(8), 1–10, doi:10.1029/2004JD005336, 2005.

Zahardis, J., LaFranchi, B. W. and Petrucci, G. A.: Direct observation of polymerization in the oleic acid-ozone heterogeneous reaction system by photoelectron resonance capture ionization aerosol mass spectrometry, Atmos. Environ., 40(9), 1661–1670, doi:10.1016/j.atmosenv.2005.10.065, 2006.

Zhang, Q., Jimenez, J. L., Worsnop, D. R. and Canagaratna, M.: A case study of urban particle acidity and its influence on secondary organic aerosol, Environ. Sci. Technol., 41(9), 3213–3219, doi:10.1021/es061812j, 2007.

Zhao, X., Hu, Q., Wang, X., Ding, X., He, Q., Zhang, Z., Shen, R., Lü, S., Liu, T., Fu, X. and Chen, L.: Composition profiles of organic aerosols from Chinese residential cooking: Case study in urban Guangzhou, south China, J. Atmos. Chem., 72(1), 1–18, doi:10.1007/s10874-015-9298-0, 2015.

Zhou, S., Hwang, B. C. H., Lakey, P. S. J., Zuend, A., Abbatt, J. P. D. and Shiraiwa, M.: Multiphase reactivity of polycyclic aromatic hydrocarbons is driven by phase separation and diffusion limitations, Proc. Natl. Acad. Sci. U. S. A., 116(24), 11658–11663, doi:10.1073/pnas.1902517116, 2019.

Zobrist, B., Soonsin, V., Luo, B. P., Krieger, U. K., Marcolli, C., Peter, T. and Koop, T.: Ultra-slow water diffusion in aqueous sucrose glasses, Phys. Chem. Chem. Phys., 13(8), 3514–3526, doi:10.1039/c0cp01273d, 2011.

8 CHAPTER 8: COUPLING LEVITATION WITH POLARISING OPTICAL MICROSCOPY: WATER UPTAKE IN A NANOSTRUCTURED ATMOSPHERIC AEROSOL PROXY

This study is prepared as a research letter for submission to a journal.

8.1 **Abstract**

Laboratory studies on levitated particles of atmospheric aerosol proxies have provided significant contributions to our understanding of aerosol processes. We present an experimental setup combining acoustic levitation with polarising optical microscopy to probe optically birefringent particles, such as the nanostructured surfactant atmospheric aerosol proxy presented here. Birefringent particles were subjected to a step increase in humidity. A decrease in birefringence was measured over time as a result of a nanostructure change, confirmed by complementary X-ray scattering. A multi-layer water uptake model was created and fitted to the experimental data, revealing a water diffusion coefficient increase by *ca.* 5 – 6 orders of magnitude upon phase transition. This has implications for the timescale of water uptake in surfactant-containing aerosols and their subsequent atmospheric lifetimes. This experimental setup has the potential to be used with other methods of levitation and in different contexts concerning birefringent material.

8.2 Introduction

A range of techniques have been combined with single particle levitation including Raman spectroscopy (Davies and Wilson, 2016; Gallimore et al., 2018), mass spectrometry (Westphall et al., 2008), X-ray scattering (Seddon et al., 2016), Mie scattering (Zobrist et al., 2011) and various other spectroscopic techniques (Cohen et al., 2020; Mason et al., 2007). The contactless environment afforded by single particle levitation has made it of particular interest to the atmospheric aerosol community (Krieger et al., 2012). The focus of this study is on acoustic levitation (Santesson and Nilsson, 2004).

Atmospheric aerosols facilitate cloud droplet formation (Boucher et al., 2013) and make a significant contribution to urban air quality (Kulmala et al., 2021). The organic fraction of atmospheric aerosols can include a diverse range of molecules from alkanes to harmful polycyclic aromatic hydrocarbons (PAHs). This organic composition varies over time and between environments (Jimenez et al., 2009; Wang et al., 2020).

Fatty acids are organic surfactants commonly observed in cooking and marine aerosol emissions (Alves et al., 2020; Tervahattu et al., 2005). Organic surfactant material affects cloud droplet nucleation by decreasing surface tension (Ovadnevaite et al., 2017). Oleic acid, a fatty acid surfactant and cooking emission marker (Wang et al., 2020), has been shown to form a range of lyotropic liquid crystal (LLC) phases in contact with water (Mele et al., 2018; Pfrang et al., 2017). The diffusion of small molecules through these phases is known to vary considerably due to the variable viscosities of these phases, compared with the free fatty acid (Zabara and Mezzenga, 2014). Water uptake and diffusion through viscous particles has been an important topic of study due to the implications for cloud droplet nucleation (Davies and Wilson, 2016;

Price et al., 2015; Zobrist et al., 2011). We have previously shown that unsaturated fatty acid self-assembly can decrease reactivity with ozone by *ca.* an order of magnitude (Milsom et al., 2021b).

We present a new experimental approach to following water diffusion through LLC phases by coupling acoustic levitation with polarising optical microscopy (POM). We followed the change from an optically birefringent (lamellar) to non-birefringent (close-packed inverse micellar) phase during humidification in a controlled gas-phase environment. A multi-layer water uptake model was created to reveal how water diffusivity changes during humidification, depending on the fatty acid molecular arrangement.

8.3 Methods

8.3.1 Preparation of the fatty acid aerosol proxy

Oleic acid (Sigma-Aldrich, 90 % purity) and sodium oleate (Sigma-Aldrich, 99 % purity) were dissolved as 10 wt % solutions in methanol, with gentle heating at ~ 50 ^{o}C until fully dissolved. Equal volumes of each solution were mixed to afford a 1:1 wt ratio solution of oleic acid and sodium oleate. This mixture was used throughout this study and is analogous to the mixture used for kinetic experiments on this proxy system (Milsom et al., 2021b).

8.3.2 **Acoustic levitation-polarising optical microscopy**

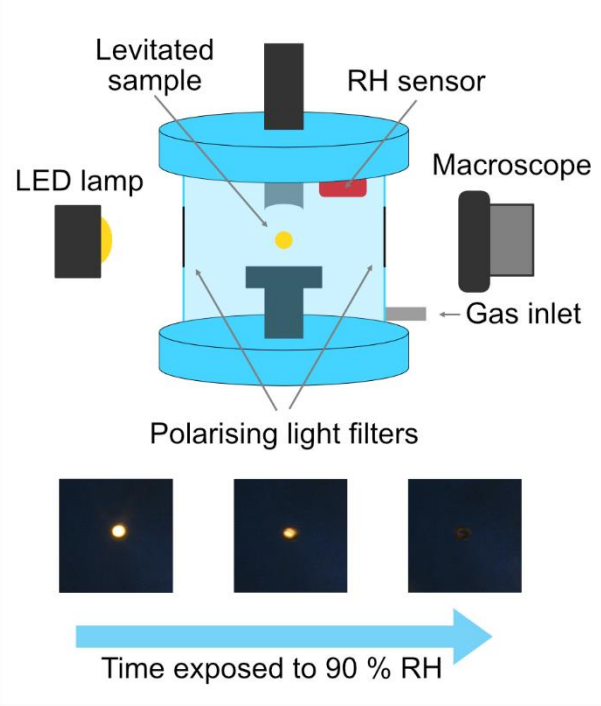

Figure 8-1. Schematic representation of the POM setup with example images of a levitated sample during a humidity experiment, showing a reduction and disappearance of particle birefringence.

Acoustic levitation of the fatty acid aerosol proxy was achieved by injecting ~ 20 µL of the proxy solution into the node of a modified commercial acoustic levitator (tec5, Oberursel, Germany) and allowing the solvent to evaporate, leaving behind the levitated sample. More than one droplet can be levitated simultaneously. This levitator has a fixed transducer frequency (100 kHz) and variable HF power (0.65 – 5 W). A concave reflector was positioned above the transducer and the transducer-reflector distance (typically 20 – 30 mm) was adjusted with a micrometre screw. The levitator was contained in a bespoke 3-D-printed chamber with ports to allow gas flow and viewing windows for optical and X-ray experiments (Fig. 8-1).

A cross-polarised optical system was established by attaching two light polarising filters on two opposing viewing windows of the levitation chamber. These filters were aligned in order to extinguish the light passing through both filters. An LED lamp was used as the light source. Only birefringent material placed between these filters would allow light to pass through, allowing us to detect a birefringent levitated particle (see images in Fig. 8-1). A macroscope with a digital camera attached (*Leica MC190 HD*) was used to take images of the levitated particles from the side opposite to the incoming light. One image was taken every minute. A magnification of x 3.2 was used and the working distance was ~ 100 mm. The image analysis procedure is described in the appendix section 10.7.1.

Humidity was controlled using a bespoke Raspberry Pi (RPi) mini-computer system. This system controlled an air pump which pumped air through a glass humidifier. A humidity sensor was placed inside the levitation chamber and was read by an Arduino mini-computer, which fed into the RPi humidity control software. For all experiments the starting relative humidity (RH) was ~ 50 %. The levitation chamber was humidified to 90 % RH for each experiment.

8.3.3 Acoustic levitation Small-angle X-ray Scattering (SAXS)

SAXS probes samples on the nanoscale to reveal how molecules aggregate together (Li et al., 2016). The nanostructured sample is illuminated by X-rays, some of which are scattered. Plots of scattered intensity vs q (momentum transfer – related to scattering angle) allow for determination of which (if any) arrangement is present in a sample by identifying Bragg scattering peak positions (Kulkarni et al., 2011).

SAXS measurements were carried out on levitated particles on the I22 beamline at the Diamond Light Source synchrotron X-ray facility. Levitated particles were exposed to X-rays of 12.4 keV energy in 1 s frames using a *Pilatus P3-2M* detector. The size of the X-ray beam used was ~ 22 x 19 μm^2.

8.3.4 Multi-layer water uptake model

We have devised a multi-layer approach to spatially and temporally resolve the uptake and diffusion of water through a self-assembled particle, incorporating changes in diffusivity caused by water content-dependent phase changes. This modelling approach is similar to those which resolve aerosol and surface and bulk chemistry (Shiraiwa et al., 2010) and ones which consider water uptake into viscous particles (Lienhard et al., 2014; Price et al., 2015; Zobrist et al., 2011). The multi-layer model is described in detail in the appendix section 10.7.2.

Water diffusion was made to be composition-dependent and is related to the fraction of lamellar phase in layer *i* ($f_{lam,i}$) by a Vignes-type relationship (Vignes, 1966):

$$D_{w,i} = (D_{w,lam})^{f_{lam,i}} + (D_{w,mic})^{(1-f_{lam,i})} \quad (8\text{-}1)$$

Where $D_{b,w,lam}$ and $D_{b,w,mic}$ are the diffusivities of water in the lamellar phase and close-packed inverse micellar phase, respectively.

We could not directly determine D^o_w in these phases with this experiment, though there have been NMR-based diffusion measurements on similar systems (Hendrikx et al., 1994). We use this literature value of D^o_w in order to place the model results in a physically meaningful context (see later).

The model parameters were optimised using a differential evolution algorithm available in the *Scipy* package in *Python* (Storn and Price, 1997; Virtanen et al., 2020). The initial

population of parameter sets were sampled using a latin hypercube, which ensures the initial population evenly covers the available parameter space. The resulting population was evolved in parallel over 20 cpu cores. This approach to global optimisation is similar to that of Berkemeier *et al*., who used an initial Monte Carlo sampling method (Berkemeier et al., 2017). The number of model layers was adjusted to maintain the same spatial resolution for each particle (*i.e.* 200 layers for the 220 µm diameter particle; 236 layers for the 260 µm particle).

8.4 Results and Discussion

8.4.1 Identification of surfactant arrangements at low and high humidity

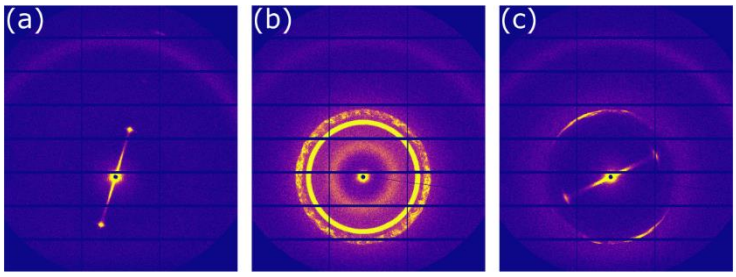

Figure 8-2. 2-D SAXS patterns from a levitated oleic acid-sodium oleate particle. (a) The edge of the particle at the beginning of the experiment, showing a highly oriented lamellar phase. (b) The centre of the same particle at high humidity (90 % RH), showing the Fd3m close-packed inverse micellar phase. (c) The edge of the same particle at high humidity showing some orientation of the Fd3m phase.

In order to confirm which molecular arrangements were present at room (~ 50 % RH) and high (~90 % RH) humidity, samples were levitated and SAXS patterns were taken. Figure 8-2(a) shows the 2-D scattering pattern from the top edge of a levitated particle ~ 3 min after levitation at room humidity. This scattering pattern corresponds to the

lamellar phase. This lamellar phase is highly oriented due to the lack of a diffuse scattering ring for each lamellar Bragg peak (see the appendix section 10.7.3 for a scattering pattern from a randomly oriented lamellar phase showing diffuse scattering rings). This kind of surface orientation has been observed previously in levitated droplets of LLC phases (Seddon et al., 2016).

Diffusion is highly anisotropic in the lamellar phase (Lindblom and Orädd, 1994; Lindblom and Wennerström, 1977). If lamellar bilayers are highly aligned parallel to the droplet surface (as observed here), water uptake is likely to be affected. This justifies the explicit separation of water uptake into the lamellar and inverse micellar phase in the surface layer of the model (see the appendix section 10.7.2).

At high humidity, we observed the ordered inverse micellar phase with Fd3m symmetry after ~ 10 min (Fig. 8-2(b)). The close-packed inverse micelles present in this phase have varying sizes and restricted water mobility (Hendrikx et al., 1994; Pouzot et al., 2007).

The close-packed inverse micellar phase is isotropic and is not observable by POM. This is in agreement with the levitation-POM humidity experiment: where an optically anisotropic (lamellar) phase transformed into an optically isotropic phase (close-packed inverse micellar) (Fig. 8-1).

8.4.2 Following water uptake during humidification

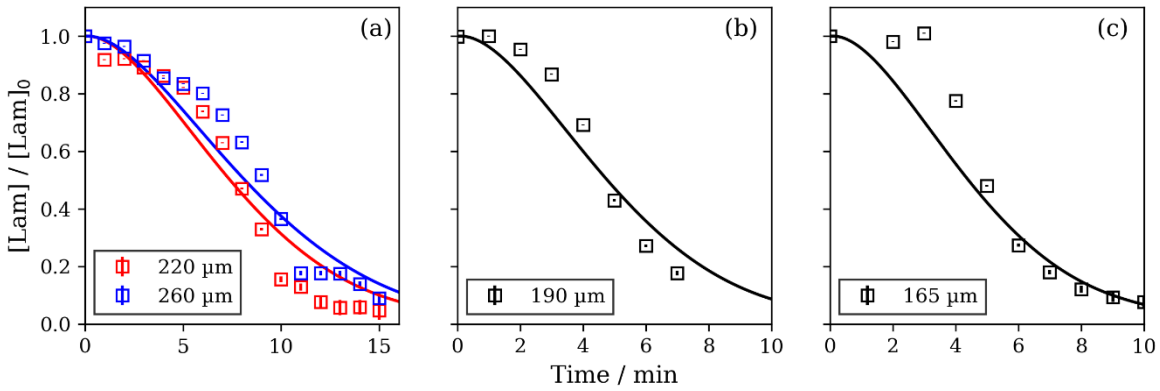

Figure 8-3. Plots of the normalised amount of lamellar phase ([Lam]/[Lam]$_0$) vs time with corresponding model fits (solid lines) for each particle diameter. (a) an experiment where two particles were levitated simultaneously. (b) & (c) two particles levitated separately – the optimised model fits for these two experiments returned slightly different parameters to the ones optimised in panel (a).

We levitated two particles of 220 and 260 µm diameter simultaneously and followed their respective water uptakes with the levitation-POM experiment. A single set of optimised model parameters fit reasonably well with these data (Fig. 8-3(a)). A separate model optimisation using the data from a 190 µm particle returned optimised parameters which were similar to those obtained by the simultaneous particle optimisation (Fig. 8-3(b) & (c)). This set of parameters fit well to both the 190 and 165 µm particles, which were levitated in separate experiments. Optimised model parameters are presented in the appendix 10.7.4.

The water uptake model did not account for any intermediate phases that could have formed when transitioning from the anhydrous lamellar to the close-packed inverse micellar phase. It is possible that a disordered (rather than close-packed) inverse

micellar phase forms as an intermediate phase (Seddon et al., 1990). This has been observed in experiments on a crystalline form of this proxy (Milsom et al., 2021a) (see chapter 7). The less viscous nature of the disordered inverse micellar phase, which is also non-birefringent, could account for some of the difference between the model fits and experimental data.

The diffusion coefficient of water in the oleic acid-sodium oleate close-packed inverse micellar phase has been experimentally determined to be 2.4×10^{-8} cm^2 s^{-1} (Hendrikx et al., 1994). We used this to convert model diffusion coefficients to physically meaningful values. The water diffusion coefficient in the lamellar phase was determined from the model fit as 7.0×10^{-14} cm^2 s^{-1}. This puts water diffusivity in these observed phases in the semi-solid regime (Shiraiwa et al., 2011). This value was obtained from the set of model parameters fitting to the 220 and 260 μm diameter particles (Fig. 8-3(a)), which were levitated simultaneously and had the most experimental measurements to fit to.

Water diffusion through the anhydrous lamellar phase is *ca.* 5 – 6 orders of magnitude slower than in the close-packed inverse micellar phase, demonstrating the sensitivity of water diffusion to particle nanostructure and viscosity. Note that the lamellar phase studied here is anhydrous and not a lyotropic system (*i.e.* it is without a solvent). Without water acting as a plasticiser, anhydrous lamellar bilayers are more restricted in their movement, increasing their rigidity and viscosity (Youssry et al., 2008). The spacing between fatty acid chains in this lamellar phase has been measured to be 0.441 nm (Milsom et al., 2021b). This is within double the molecular diameter of water (*ca.* 0.27 nm) (Schatzberg, 1967). The steric restriction imposed by the spacing between

fatty acid alkyl chains helps explain why water diffusion through the anhydrous lamellar phase is so much slower than in the close-packed inverse micellar phase.

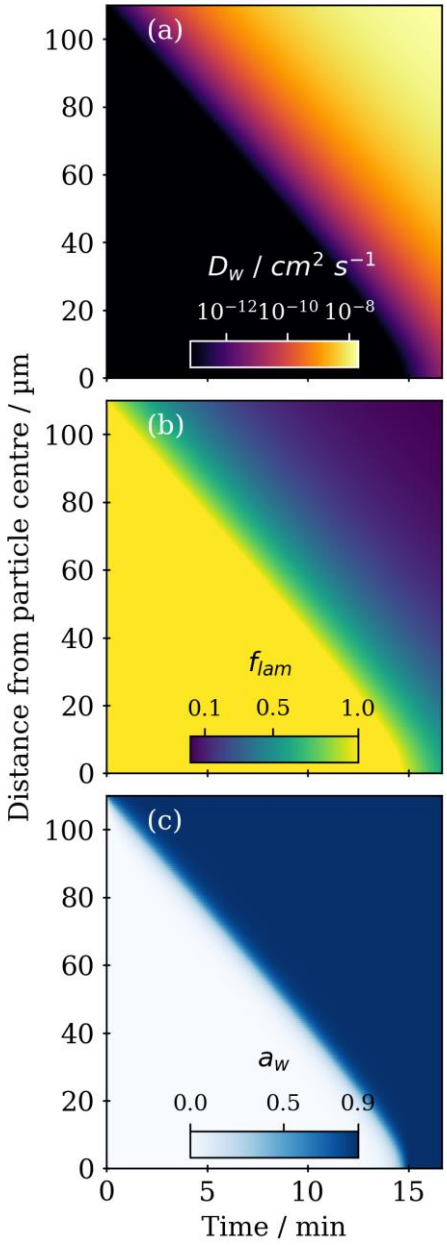

Figure 8-4. Model outputs for a 110 µm radius particle exposed to 90 % RH. (a) Evolution of the water diffusion coefficient (D_w) throughout a humidifying particle. (b) Evolution of the fraction of lamellar phase (f_{lam}) throughout the particle. (c) Evolution of water activity (a_w) throughout the particle.

A steep water diffusion gradient is established within the particle during humidification (Fig. 8-4(a)). As more water is taken up, the lamellar phase transitions to the close-packed inverse micellar phase, affecting D_w via the Vignes-type relationship described earlier. Particle water and lamellar phase content follow a similar trend, highlighting the link between water content, phase transition and water diffusivity (Fig 8-4(b) & (c)).

8.4.3 **Atmospheric implications**

The D_w range derived from our model (~ 10^{-14} – 10^{-8} cm^2 s^{-1}) is similar to measurements of D_w in water-sucrose mixtures (~ 10^{-13} – 10^{-6} cm^2 s^{-1}), placing this nanostructured proxy system in a similar water diffusion regime.

There is a strong dependence of D_w on molecular arrangement, with D_w increasing by *ca.* 5 – 6 orders of magnitude upon the lamellar-to-ordered inverse micellar phase transition. We can therefore say that water diffusion is affected by molecular arrangement, similar to the effect that nanostructure formation has on the oxidation reactivity of the same proxy system (Milsom et al., 2021b).

The link between aerosol phase state and atmospheric lifetime is well-established and has implications for the long-range transport of aerosols and their impact on the climate and pollution (Mu et al., 2018; Slade et al., 2017; Zhou et al., 2019). We have shown here that the diffusivity of water though a nanostructured surfactant aerosol proxy is impacted by the arrangement of these surfactant molecules, which itself is determined by the amount of water in the system.

8.5 **Conclusions**

The simple composition-dependent parameterisation of water diffusivity, along with the inclusion and parameterisation of phase transition boundaries in the model, means that the model could be applied to more complex systems such as the inverse micellar (non-birefringent)-hydrated lamellar(birefringent)-inverse cubic (non-birefringent) phase transitions observed for the phytantriol-glycerol system (Richardson et al., 2015). With prior knowledge of the diffusion coefficient of water through at least one of these phases, predictions could be made regarding the diffusivity of water through such

phases – the diffusion of small molecules through LLC phases is also of importance to the drug delivery community (Zabara and Mezzenga, 2014).

This work has shown that a facile laboratory-based setup consisting of polarising filters, an acoustic levitator, a camera and a light source can return physically meaningful results provided the sample environment can be controlled. LLC phase transitions have previously been followed in acoustically levitated droplets when coupled with X-ray scattering techniques, providing a more detailed insight into the nanostructure of the particle (Milsom et al., 2021a; Pfrang et al., 2017; Seddon et al., 2016). However, this requires rather specialist instrumentation and time applied for and spent at a synchrotron light source. This experimental setup is possible in a standard chemistry laboratory and could be coupled with other forms of levitation such as an Electro-Dynamic Balance (EDB). The quality of the camera need not be high, the phase transition observed during this study is still observable with a standard computer webcam (demonstrated in the appendix section 10.7.5).

8.6 Acknowledgements

AM acknowledges funding by the NERC SCENARIO DTP (NE/L002566/1) and support from the NERC CENTA DTP. Chris Brasnett and Annela Seddon are acknowledged for allowing AM to levitate samples during their beamtime at the Diamond Light Source (DLS). This work was carried out with the support of the DLS, instrument I22 (proposals SM23852 and SM17791). Nick Terrill, Andy Smith, Tim Snow and Olga Shebanova (DLS) are acknowledged for their support during experiments at the DLS. The computations described in this paper were performed using the University of Birmingham's BlueBEAR HPC service, which provides a High Performance Computing service to the University's research community.

8.6.1 Contributors

Adam Milsom developed/carried out the levitation-polarising optical microscopy experiments and wrote the manuscript. Christian Pfrang and Adam Squires contributed to the interpretation of the results. Chris Brasnett and Dr Annela Seddon invited AM, CP and AS to their SAXS-levitation beamtime.

8.7 Comment

This study presents the development and application of a simple experiment, coupling polarising optical microscopy with acoustic levitation. In contrast to the specialist techniques presented in chapter 7, this experiment is relatively facile to carry out and I have shown that something physically meaningful can be extracted from it.

8.8 References

Alves, C. A., Vicente, E. D., Evtyugina, M., Vicente, A. M., Nunes, T., Lucarelli, F., Calzolai, G., Nava, S., Calvo, A. I., Alegre, C. del B., Oduber, F., Castro, A. and Fraile, R.: Indoor and outdoor air quality: A university cafeteria as a case study, Atmos. Pollut. Res., 11(3), 531–544, doi:10.1016/j.apr.2019.12.002, 2020.

Berkemeier, T., Ammann, M., Krieger, U. K., Peter, T., Spichtinger, P., Pöschl, U., Shiraiwa, M. and Huisman, A. J.: Technical note: Monte Carlo genetic algorithm (MCGA) for model analysis of multiphase chemical kinetics to determine transport and reaction rate coefficients using multiple experimental data sets, Atmos. Chem. Phys., 17(12), 8021–8029, doi:10.5194/acp-17-8021-2017, 2017.

Boucher, O., Randall, D., Artaxo, P., Bretherton, C., Feingold, G., Forster, P., Kerminen, V.-M., Kondo, Y., Liao, H., Lohmann, U., Rasch, P., Satheesh, S. K., Sherwood, S., Stevens, B. and Zhang, X. Y.: Clouds and Aerosols, in Climate Change

2013 - The Physical Science Basis, edited by Intergovernmental Panel on Climate Change, pp. 571–658, Cambridge University Press, Cambridge., 2013.

Cohen, L., Quant, M. I., Quant, M. I., Donaldson, D. J. and Donaldson, D. J.: Real-Time Measurements of pH Changes in Single, Acoustically Levitated Droplets Due to Atmospheric Multiphase Chemistry, ACS Earth Sp. Chem., 4(6), 854–861, doi:10.1021/acsearthspacechem.0c00041, 2020.

Davies, J. F. and Wilson, K. R.: Raman Spectroscopy of Isotopic Water Diffusion in Ultraviscous, Glassy, and Gel States in Aerosol by Use of Optical Tweezers, Anal. Chem., 88(4), 2361–2366, doi:10.1021/acs.analchem.5b04315, 2016.

Gallimore, P. J., Davidson, N. M., Kalberer, M., Pope, F. D. and Ward, A. D.: 1064 nm Dispersive Raman Microspectroscopy and Optical Trapping of Pharmaceutical Aerosols, Anal. Chem., 90(15), 8838–8844, doi:10.1021/acs.analchem.8b00817, 2018.

Hendrikx, Y., Sotta, P., Seddon, J. M., Dutheillet, Y. and Bartle, E. A.: NMR self-diffusion measurements in inverse micellar cubic phases, Liq. Cryst., 16(5), 893–903, doi:10.1080/02678299408027860, 1994.

Jimenez, J. L., Canagaratna, M. R., Donahue, N. M., Prevot, A. S. H., Zhang, Q., Kroll, J. H., DeCarlo, P. F., Allan, J. D., Coe, H., Ng, N. L., Aiken, A. C., Docherty, K. S., Ulbrich, I. M., Grieshop, A. P., Robinson, A. L., Duplissy, J., Smith, J. D., Wilson, K. R., Lanz, V. A., Hueglin, C., Sun, Y. L., Tian, J., Laaksonen, A., Raatikainen, T., Rautiainen, J., Vaattovaara, P., Ehn, M., Kulmala, M., Tomlinson, J. M., Collins, D. R., Cubison, M. J., Dunlea, J., Huffman, J. A., Onasch, T. B., Alfarra, M. R., Williams, P. I., Bower, K., Kondo, Y., Schneider, J., Drewnick, F., Borrmann, S., Weimer, S., Demerjian, K., Salcedo, D., Cottrell, L., Griffin, R., Takami, A., Miyoshi, T.,

Hatakeyama, S., Shimono, A., Sun, J. Y., Zhang, Y. M., Dzepina, K., Kimmel, J. R., Sueper, D., Jayne, J. T., Herndon, S. C., Trimborn, A. M., Williams, L. R., Wood, E. C., Middlebrook, A. M., Kolb, C. E., Baltensperger, U. and Worsnop, D. R.: Evolution of Organic Aerosols in the Atmosphere, Science, 326(5959), 1525–1529, doi:10.1126/science.1180353, 2009.

Krieger, U. K., Marcolli, C. and Reid, J. P.: Exploring the complexity of aerosol particle properties and processes using single particle techniques, Chem. Soc. Rev., 41(19), 6631–6662, doi:10.1039/c2cs35082c, 2012.

Kulkarni, C. V., Wachter, W., Iglesias-Salto, G., Engelskirchen, S. and Ahualli, S.: Monoolein: a magic lipid?, Phys. Chem. Chem. Phys., 13(8), 3004–3021, doi:10.1039/C0CP01539C, 2011.

Kulmala, M., Dada, L., Daellenbach, K. R., Yan, C., Stolzenburg, D., Kontkanen, J., Ezhova, E., Hakala, S., Tuovinen, S., Kokkonen, T. V., Kurppa, M., Cai, R., Zhou, Y., Yin, R., Baalbaki, R., Chan, T., Chu, B., Deng, C., Fu, Y., Ge, M., He, H., Heikkinen, L., Junninen, H., Liu, Y., Lu, Y., Nie, W., Rusanen, A., Vakkari, V., Wang, Y., Yang, G., Yao, L., Zheng, J., Kujansuu, J., Kangasluoma, J., Petäjä, T., Paasonen, P., Järvi, L., Worsnop, D., Ding, A., Liu, Y., Wang, L., Jiang, J., Bianchi, F. and Kerminen, V.-M.: Is reducing new particle formation a plausible solution to mitigate particulate air pollution in Beijing and other Chinese megacities?, Faraday Discuss., 226, 334–347, doi:10.1039/d0fd00078g, 2021.

Li, T., Senesi, A. J. and Lee, B.: Small Angle X-ray Scattering for Nanoparticle Research, Chem. Rev., 116(18), 11128–11180, doi:10.1021/acs.chemrev.5b00690, 2016.

Lienhard, D. M., Huisman, A. J., Bones, D. L., Te, Y. F., Luo, B. P., Krieger, U. K. and Reid, J. P.: Retrieving the translational diffusion coefficient of water from experiments on single levitated aerosol droplets, Phys. Chem. Chem. Phys., 16(31), 16677–16683, doi:10.1039/c4cp01939c, 2014.

Lindblom, G. and Orädd, G.: NMR Studies of translational diffusion in lyotropic liquid crystals and lipid membranes, Prog. Nucl. Magn. Reson. Spectrosc., 26, 483–515, doi:10.1016/0079-6565(94)80014-6, 1994.

Lindblom, G. and Wennerström, H.: Amphiphile diffusion in model membrane systems studied by pulsed NMR, Biophys. Chem., 6(2), 167–171, doi:10.1016/0301-4622(77)87006-3, 1977.

Mason, N. J., Drage, E. A., Webb, S. M., Dawes, A., McPheat, R. and Hayes, G.: The spectroscopy and chemical dynamics of microparticles explored using an ultrasonic trap, Faraday Discuss., 137, 367–376, doi:10.1039/b702726p, 2007.

Mele, S., Söderman, O., Ljusberg-Wahrén, H., Thuresson, K., Monduzzi, M. and Nylander, T.: Phase behavior in the biologically important oleic acid/sodium oleate/water system, Chem. Phys. Lipids, 211, 30–36, doi:10.1016/j.chemphyslip.2017.11.017, 2018.

Milsom, A., Squires, A. M., Boswell, J. A., Terrill, N. J., Ward, A. D. and Pfrang, C.: An organic crystalline state in ageing atmospheric aerosol proxies : spatially resolved structural changes in levitated fatty acid particles, Atmos. Chem. Phys. Discuss., [preprint], 1–31, doi:https://doi.org/10.5194/acp-2021-270, 2021a.

Milsom, A., Squires, A. M., Woden, B., Terrill, N. J., Ward, A. D. and Pfrang, C.: The persistence of a proxy for cooking emissions in megacities: a kinetic study of the

ozonolysis of self-assembled films by simultaneous small and wide angle X-ray scattering (SAXS/WAXS) and Raman microscopy, Faraday Discuss., 226, 364–381, doi:10.1039/D0FD00088D, 2021b.

Mu, Q., Shiraiwa, M., Octaviani, M., Ma, N., Ding, A., Su, H., Lammel, G., Pöschl, U. and Cheng, Y.: Temperature effect on phase state and reactivity controls atmospheric multiphase chemistry and transport of PAHs, Sci. Adv., 4(3), eaap7314, doi:10.1126/sciadv.aap7314, 2018.

Ovadnevaite, J., Zuend, A., Laaksonen, A., Sanchez, K. J., Roberts, G., Ceburnis, D., Decesari, S., Rinaldi, M., Hodas, N., Facchini, M. C., Seinfeld, J. H. and O'Dowd, C.: Surface tension prevails over solute effect in organic-influenced cloud droplet activation, Nature, 546(7660), 637–641, doi:10.1038/nature22806, 2017.

Pfrang, C., Rastogi, K., Cabrera-Martinez, E. R., Seddon, A. M., Dicko, C., Labrador, A., Plivelic, T. S., Cowieson, N. and Squires, A. M.: Complex three-dimensional self-assembly in proxies for atmospheric aerosols, Nat. Commun., 8(1), 1724, doi:10.1038/s41467-017-01918-1, 2017.

Pouzot, M., Mezzenga, R., Leser, M., Sagalowicz, L., Guillote, S. and Glatter, O.: Structural and rheological investigation of Fd3m inverse micellar cubic phases, Langmuir, 23(19), 9618–9628, doi:10.1021/la701206a, 2007.

Price, H. C., Mattsson, J., Zhang, Y., Bertram, A. K., Davies, J. F., Grayson, J. W., Martin, S. T., O'Sullivan, D., Reid, J. P., Rickards, A. M. J. and Murray, B. J.: Water diffusion in atmospherically relevant α-pinene secondary organic material, Chem. Sci., 6(8), 4876–4883, doi:10.1039/c5sc00685f, 2015.

Richardson, S. J., Staniec, P. A., Newby, G. E., Rawle, J. L., Slaughter, A. R., Terrill,

N. J., Elliott, J. M. and Squires, A. M.: Glycerol prevents dehydration in lipid cubic phases, Chem. Commun., 51, 11386–11389, doi:10.1039/c5cc03771a, 2015.

Santesson, S. and Nilsson, S.: Airborne chemistry: Acoustic levitation in chemical analysis, Anal. Bioanal. Chem., 378(7), 1704–1709, doi:10.1007/s00216-003-2403-2, 2004.

Schatzberg, P.: Molecular diameter of water from solubility and diffusion measurements, J. Phys. Chem., 71(13), 4569–4570, doi:10.1021/j100872a075, 1967.

Seddon, A. M., Richardson, S. J., Rastogi, K., Plivelic, T. S., Squires, A. M. and Pfrang, C.: Control of Nanomaterial Self-Assembly in Ultrasonically Levitated Droplets, J. Phys. Chem. Lett., 7(7), 1341–1345, doi:10.1021/acs.jpclett.6b00449, 2016.

Seddon, J. M., Bartle, E. A. and Mingins, J.: Inverse cubic liquid-crystalline phases of phospholipids and related lyotropic systems, J. Phys. Condens. Matter, 2, SA285–SA290, doi:10.1088/0953-8984/2/S/043, 1990.

Shiraiwa, M., Pfrang, C. and Pöschl, U.: Kinetic multi-layer model of aerosol surface and bulk chemistry (KM-SUB): The influence of interfacial transport and bulk diffusion on the oxidation of oleic acid by ozone, Atmos. Chem. Phys., 10, 3673–3691, doi:10.5194/acp-10-3673-2010, 2010.

Shiraiwa, M., Ammann, M., Koop, T. and Poschl, U.: Gas uptake and chemical aging of semisolid organic aerosol particles, Proc. Natl. Acad. Sci. U. S. A., 108(27), 11003–11008, doi:10.1073/pnas.1103045108, 2011.

Slade, J. H., Shiraiwa, M., Arangio, A., Su, H., Pöschl, U., Wang, J. and Knopf, D. A.: Cloud droplet activation through oxidation of organic aerosol influenced by temperature

and particle phase state, Geophys. Res. Lett., 44(3), 1583–1591, doi:10.1002/2016GL072424, 2017.

Storn, R. and Price, K.: Differential Evolution – A Simple and Efficient Heuristic for global Optimization over Continuous Spaces, J. Glob. Optim., 11, 341–359, doi:10.1023/A1008202821328, 1997.

Tervahattu, H., Juhanoja, J., Vaida, V., Tuck, A. F., Niemi, J. V., Kupiainen, K., Kulmala, M. and Vehkamäki, H.: Fatty acids on continental sulfate aerosol particles, J. Geophys. Res. D Atmos., 110(6), 1–9, doi:10.1029/2004JD005400, 2005.

Vignes, A.: Variation in Diffusion Coefficient with Composition, Ind. Eng. Chem. Fundam., 5(2), 189–199, 1966.

Virtanen, P., Gommers, R., Oliphant, T. E., Haberland, M., Reddy, T., Cournapeau, D., Burovski, E., Peterson, P., Weckesser, W., Bright, J., van der Walt, S. J., Brett, M., Wilson, J., Millman, K. J., Mayorov, N., Nelson, A. R. J., Jones, E., Kern, R., Larson, E., Carey, C. J., Polat, İ., Feng, Y., Moore, E. W., VanderPlas, J., Laxalde, D., Perktold, J., Cimrman, R., Henriksen, I., Quintero, E. A., Harris, C. R., Archibald, A. M., Ribeiro, A. H., Pedregosa, F., van Mulbregt, P., Vijaykumar, A., Bardelli, A. Pietro, Rothberg, A., Hilboll, A., Kloeckner, A., Scopatz, A., Lee, A., Rokem, A., Woods, C. N., Fulton, C., Masson, C., Häggström, C., Fitzgerald, C., Nicholson, D. A., Hagen, D. R., Pasechnik, D. V., Olivetti, E., Martin, E., Wieser, E., Silva, F., Lenders, F., Wilhelm, F., Young, G., Price, G. A., Ingold, G. L., Allen, G. E., Lee, G. R., Audren, H., Probst, I., Dietrich, J. P., Silterra, J., Webber, J. T., Slavič, J., Nothman, J., Buchner, J., Kulick, J., Schönberger, J. L., de Miranda Cardoso, J. V., Reimer, J., Harrington, J., Rodríguez, J. L. C., Nunez-Iglesias, J., Kuczynski, J., Tritz, K., Thoma, M., Newville, M., Kümmerer,

M., Bolingbroke, M., Tartre, M., Pak, M., Smith, N. J., Nowaczyk, N., Shebanov, N., Pavlyk, O., Brodtkorb, P. A., Lee, P., McGibbon, R. T., Feldbauer, R., Lewis, S., Tygier, S., Sievert, S., Vigna, S., Peterson, S., More, S., Pudlik, T., et al.: SciPy 1.0: fundamental algorithms for scientific computing in Python, Nat. Methods, 17(3), 261–272, doi:10.1038/s41592-019-0686-2, 2020.

Wang, Q., He, X., Zhou, M., Huang, D. D., Qiao, L., Zhu, S., Ma, Y. G., Wang, H. L., Li, L., Huang, C., Huang, X. H. H., Xu, W., Worsnop, D., Goldstein, A. H., Guo, H., Yu, J. Z., Huang, C. and Yu, J. Z.: Hourly Measurements of Organic Molecular Markers in Urban Shanghai, China: Primary Organic Aerosol Source Identification and Observation of Cooking Aerosol Aging, ACS Earth Sp. Chem., 4(9), 1670–1685, doi:10.1021/acsearthspacechem.0c00205, 2020.

Westphall, M. S., Jorabchi, K. and Smith, L. M.: Mass spectrometry of acoustically levitated droplets, Anal. Chem., 80(15), 5847–5853, doi:10.1021/ac800317f, 2008.

Youssry, M., Coppola, L., Nicotera, I. and Morán, C.: Swollen and collapsed lyotropic lamellar rheology, J. Colloid Interface Sci., 321(2), 459–467, doi:10.1016/j.jcis.2008.02.023, 2008.

Zabara, A. and Mezzenga, R.: Controlling molecular transport and sustained drug release in lipid-based liquid crystalline mesophases, J. Control. Release, 188, 31–43, doi:10.1016/j.jconrel.2014.05.052, 2014.

Zhou, S., Hwang, B. C. H., Lakey, P. S. J., Zuend, A., Abbatt, J. P. D. and Shiraiwa, M.: Multiphase reactivity of polycyclic aromatic hydrocarbons is driven by phase separation and diffusion limitations, Proc. Natl. Acad. Sci. U. S. A., 116(24), 11658–11663, doi:10.1073/pnas.1902517116, 2019.

Zobrist, B., Soonsin, V., Luo, B. P., Krieger, U. K., Marcolli, C., Peter, T. and Koop, T.: Ultra-slow water diffusion in aqueous sucrose glasses, Phys. Chem. Chem. Phys., 13(8), 3514–3526, doi:10.1039/c0cp01273d, 2011.

9 SUMMARY AND FUTURE WORK

This thesis has explored the potential atmospheric impact of surfactant self-assembly. It has demonstrated the power of simultaneous experimental techniques by offering complementary ways of probing the same phenomena – *i.e.* simultaneous SAXS and Raman experiments that follow reaction kinetics.

Generally, self-assembled phase formation slows heterogeneous processes (chemical reaction and water uptake). Compared with liquid oleic acid, reactivity is significantly decreased upon self-assembled phase formation due to an increase in organic phase viscosity. Moreover, water uptake appears to be affected not only by this formation, but also by the specific nanostructure formed.

The potential atmospheric implications of these findings focus on the extended lifetime of fatty acid molecules, something observed in the literature (Rudich et al., 2007). This is also interesting because oleic acid is a surfactant, which can impact on the CCN ability of a cloud droplet (Ovadnevaite et al., 2017). Indeed, the persistence of surface-active molecules at the air-water interface has been observed in work related to this thesis (Woden et al., 2021).

Though the studies presented in this thesis are on a proxy system, this bottom-up approach provides an assessment of this specific phenomenon in an atmospheric context. One suggestion is that future proxy studies should look at other fatty acids. Especially compounds such as stearic and linoleic acids, also commonly found in cooking emissions (Wang et al., 2020).

Experimental determination of the viscosity of these nanostructured systems would be a valuable resource for future research, constraining these parameters for future modelling work.

Of course, studies on real atmospheric material would be ideal and are suggested for future work once possible. The synchrotron techniques used here could be used to assess whether aggregate formation occurs in real organic aerosol material. SAXS patterns are unlikely to return clear well-defined peaks, but with the high-intensity X-ray beam available at a synchrotron light source it may be possible to distinguish scattering to small angles consistent with aggregate formation. Neutron and X-ray reflectometry have the added advantage that aggregates need not form to give a signal. Chapter 4 demonstrated that useful information can be obtained by such measurements on films coated on solid substrates.

Modelling the reactivity of the proxy based on experimental results became a focus in the later stages of the work on this thesis. This provided an overview of the potential impact on the atmospheric lifetime of such material. Atmospherically relevant ozone concentrations were used in the optimised model. These conditions would not have been practicable in the context of a beamline experiment, demonstrating the power of numerical modelling.

Challenges still exist with multi-layer modelling regarding the selection of a model reaction scheme, model complexity (number of layers, components etc.) and model optimisation. This should be the subject of future work, looking at how to optimise these kinds of models efficiently and with extra information regarding optimised parameter uncertainty. Of particular interest is using Bayesian methods such as MCMC

and nested sampling (outlined in chapter 4) to estimate model parameters, their uncertainties and the appropriateness of a selected model. Work is ongoing on creating a *Python* package which would build a multi-layer model for the user, compare the model with an experiment, optimise the model and analyse the model output. There is an opening for such a tool in the current research environment. Developing this code in the future as an open-source project would enable greater collaboration and further the research of those who are not primarily computational researchers.

References

Ovadnevaite, J., Zuend, A., Laaksonen, A., Sanchez, K. J., Roberts, G., Ceburnis, D., Decesari, S., Rinaldi, M., Hodas, N., Facchini, M. C., Seinfeld, J. H. and O'Dowd, C.: Surface tension prevails over solute effect in organic-influenced cloud droplet activation, Nature, 546(7660), 637–641, doi:10.1038/nature22806, 2017.

Rudich, Y., Donahue, N. M. and Mentel, T. F.: Aging of Organic Aerosol: Bridging the Gap Between Laboratory and Field Studies, Annu. Rev. Phys. Chem., 58(1), 321–352, doi:10.1146/annurev.physchem.58.032806.104432, 2007.

Wang, Q., He, X., Zhou, M., Huang, D. D., Qiao, L., Zhu, S., Ma, Y. G., Wang, H. L., Li, L., Huang, C., Huang, X. H. H., Xu, W., Worsnop, D., Goldstein, A. H., Guo, H., Yu, J. Z., Huang, C. and Yu, J. Z.: Hourly Measurements of Organic Molecular Markers in Urban Shanghai, China: Primary Organic Aerosol Source Identification and Observation of Cooking Aerosol Aging, ACS Earth Sp. Chem., 4(9), 1670–1685, doi:10.1021/acsearthspacechem.0c00205, 2020.

Woden, B., Skoda, M. W. A., Milsom, A., Gubb, C., Maestro, A., Tellam, J. and Pfrang, C.: Ozonolysis of fatty acid monolayers at the air–water interface: organic films may persist at the surface of atmospheric aerosols, Atmos. Chem. Phys., 21(2), 1325–1340, doi:10.5194/acp-21-1325-2021, 2021.

10 APPENDIX

10.1 Supporting information for chapter 2

10.1.1 Kinetic data

Cap	*d / µm*	*d (uncert.) / µm*	*kobs* / x 10^{-2} min^{-1}*	*kobs (uncert.) / x 10^{-2} min^{-1}*	*e-folding time / min*	*Fraction remaining***
1	8.8	0.3	3.45	0.09	28.95	0.02
1	10.4	0.4	4.16	0.08	24.06	0.01
1	15.5	0.5	2.46	0.04	40.58	0.06
1	16.8	0.6	1.14	0.05	87.78	0.23
1	17.1	0.6	0.84	0.05	119.30	0.29
1	20.7	0.7	1.32	0.04	75.82	0.10
1	21.1	0.7	2.63	0.08	38.09	0.06
1	21.4	0.7	2.05	0.04	48.77	0.09
1	29	1	1.38	0.03	72.72	0.22
1	42	1	1.63	0.02	61.33	0.21
1	45	2	1.45	0.02	68.87	0.23
2	5.5	0.2	5.0	0.2	19.91	N/A
2	6.8	0.2	5.2	0.1	19.28	N/A
2	8.5	0.3	4.7	0.1	21.40	N/A
2	11.0	0.4	4.28	0.09	23.34	N/A
2	12.6	0.4	2.89	0.08	34.58	N/A
2	14.0	0.5	3.91	0.07	25.56	N/A
2	14.2	0.5	2.92	0.07	34.28	N/A
2	15.0	0.5	2.88	0.08	34.69	N/A
2	15.4	0.5	3.42	0.07	29.23	N/A
3	0.59	0.02	7	5	13.64	0.00
3	0.91	0.03	7	2	14.65	0.00
3	0.98	0.03	4.5	0.6	22.08	0.00
3	1.66	0.06	3.3	0.5	30.63	0.00
3	4.9	0.2	2.4	0.2	40.99	0.05
3	25.0	0.9	0.89	0.04	112.74	0.31
3	38	1	1.24	0.02	80.68	0.31
3	40	1	0.97	0.02	103.12	0.31
3	46	2	1.07	0.02	93.53	0.37
3	61	2	0.71	0.01	141.73	0.50
3	73	2	0.64	0.01	155.57	0.53
4	1.76	0.06	8.5	0.4	11.82	N/A
4	1.81	0.06	5.9	0.5	17.04	N/A
4	1.89	0.06	5.5	0.7	18.07	N/A
4	1.96	0.07	6.8	0.5	14.72	N/A
4	1.99	0.07	4.2	0.5	23.91	N/A
4	2.05	0.07	7.5	0.5	13.30	N/A
4	2.15	0.07	6.2	0.2	16.10	N/A
4	2.19	0.07	4.5	0.4	22.47	N/A

4	2.23	0.08	6.4	0.3	15.62	N/A
4	2.39	0.08	6.5	0.4	15.28	N/A
4	2.41	0.08	6.0	0.4	16.70	N/A
5	7.1	0.2	3.9	0.2	25.53	N/A
5	8.6	0.3	3.85	0.07	25.99	N/A
5	9.2	0.3	2.8	0.1	35.66	N/A
5	9.3	0.3	3.3	0.1	30.07	N/A
5	9.6	0.3	3.4	0.2	29.26	N/A
5	10.1	0.3	4.7	0.1	21.32	N/A
5	10.9	0.4	2.32	0.04	43.16	N/A
5	12.5	0.4	4.0	0.2	24.64	N/A
5	13.0	0.4	2.4	0.2	41.35	N/A
5	13.5	0.5	3.1	0.1	31.96	N/A
5	13.8	0.5	2.82	0.06	35.47	N/A

Table 10-1. Collection of measured first order decay constants (k_{obs}) for differing film thicknesses (d) observed along coated capillaries. Sorted by capillary number (Cap) and d. Uncertainties *in r and k_{obs} (d(uncert.) & k_{obs}(uncert.)) are quoted in their respective adjacent columns. *Measurement of the fastest stage of reactive decay (explanation in the main text section 2.4.1). **Fraction remaining after ~ 175 min when the reaction was deemed to have stagnated significantly for the thickest films and when the experiments were stopped – only values from experiments which were allowed to continue to 175 min are presented. Note that this is ~ 175 min experiment time, not the corrected reaction time explained in the main text.*

10.1.2 **SAXS patterns before and after ozonolysis**

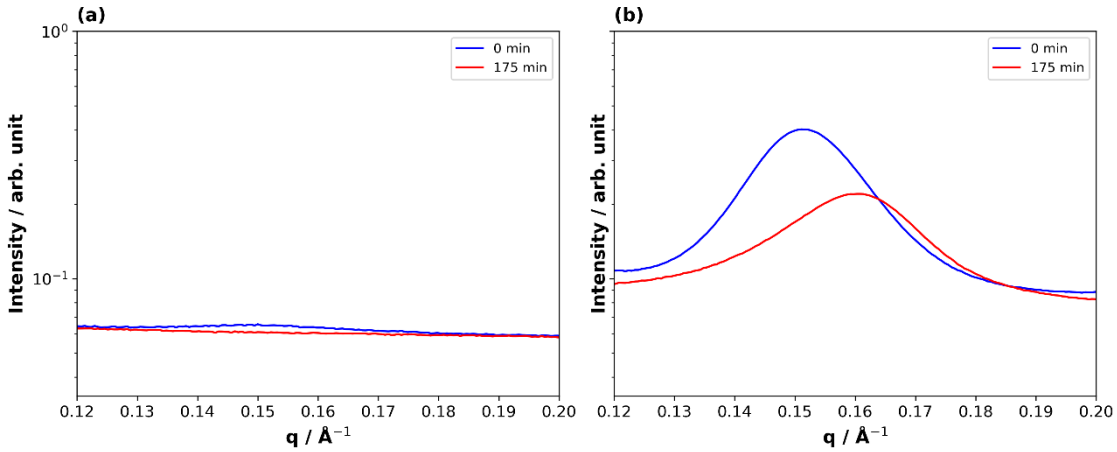

Figure 10-1. SAXS patterns showing the lamellar peak (~ 0.15 Å^{-1}) at the start and after 175 min of ozonolysis: (a) d = 0.59 ± 0.02 µm, (b) d = 73 ± 2 µm. [O_3] = 77 ± 5 ppm.

The initial SAXS patterns collected for the thinnest and thickest films (Fig. 10-1) probed in this study show a large difference in peak intensity. The main source of error in kinetic values measured in this study arises when, for the thinnest films, the lamellar peak approached the background signal making peak integration less accurate. This is reflected in the errors associated with k_{obs} (see Table 10-1) and peak area measurements in the decay plots presented in the main text (Fig. 2-3(b) – chapter 2). Note the change in lamellar peak position and peak broadening as a result of the disordering of the lamellar structure during ozonolysis (Fig. 10-1(b)).

10.1.3 **WAXS pattern of the self-assembled proxy**

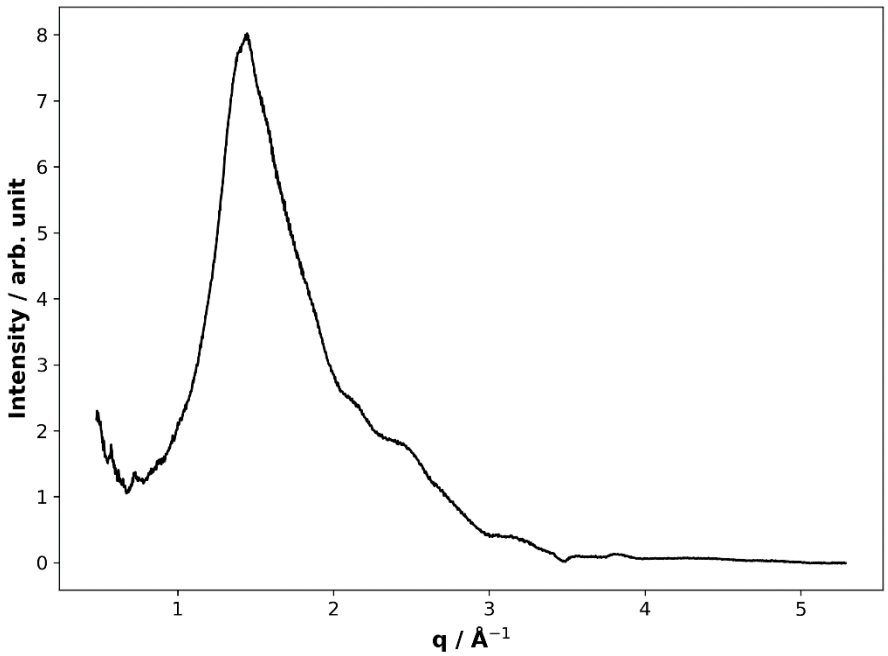

Figure 10-2. The WAXS pattern of the lamellar phase oleic acid:sodium oleate (1:1 wt) proxy which exhibits a clear peak at ~ 1.43 Å^{-1} which corresponds to a 4.41 Å spacing between alkyl chains in the lamellar structure.

10.1.4 **Grazing-incidence (GI)-SAXS image of the self-assembled proxy**

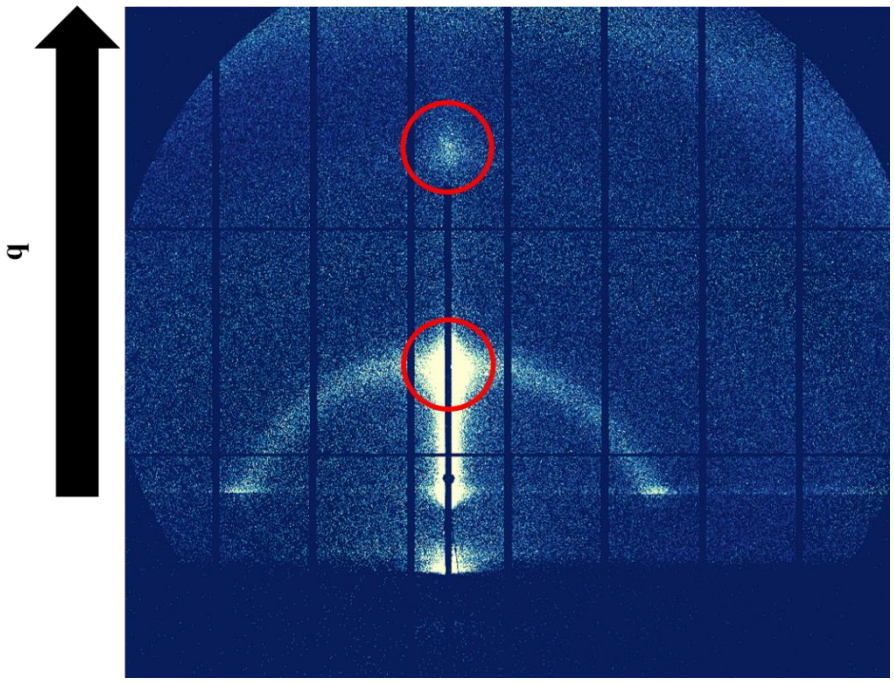

Figure 10-3. 2D GI-SAXS pattern of the lamellar phase oleic acid:sodium oleate (1:1 wt) proxy coated on a silicon wafer. Direction of q is indicated and aligned lamellar peaks are highlighted by red circles.

The proxy was deposited onto a silicon wafer by spin coating of the solution prepared as described in the main text. The sample was then exposed to X-rays at a 0.4 ^{o} angle of incidence (grazing incidence) in order to determine the alignment of the lamellar sheets in the proxy. Note that in GI-SAXS experiments only "half" of the scattering pattern is observed due to only the X-rays scattered from the sample side of the silicon wafer being detected. Areas of increased intensity aligned with the reflected X-ray signal (the bright streak starting from the beamstop to the first lamellar ring) indicate that there is a degree of alignment of the lamellar sheets parallel to the silicon surface, meaning that the alkyl chains in the lamellar structure are perpendicular to the surface. There is, however, a broad ring most prominent for the first lamellar reflection, suggesting that there is also a degree of random orientation.

10.2 Supporting information for chapter 3

10.2.1 Model reaction scheme

(R1) O_3 + oleic acid → c(NN + CI) + (1-c)(C_9 + CI)

(R2) CI + C9 → dimer

(R3) CI + dimer → trimer

A simplified form of the reaction scheme used by Hosny et al has been used (Hosny et al., 2016). The initial reaction of oleic acid with ozone (O_3) forms nonanal (NN) or a 9-carbon (C_9) product (nonanoic acid, 9-oxononanoic acid or azelaic acid) plus a Criegee intermediate (CI). The relative amount of NN and C_9 products is determined by the branching ratio (c). We have also included the loss of NN from the surface due to its high volatility. The CI then goes onto react with a C_9 product to form the dimer. This dimer then reacts with another CI to form the trimer, which represents all higher order products in this model scheme.

Since this is a simplified reaction scheme and we assume that diffusion parameters dominate the reaction kinetics, we have held all reaction rates to those optimised by Hosny et al. (Hosny et al., 2016) (see next section). These values should not be over-interpreted.

10.2.2 **Model parameters**

Parameter	***Description***	***Value***	***Units***
$k_{BR,1}$	Bulk reaction rate coefficient for R1	1.13×10^{-18}	$cm^3\ s^{-1}$
$k_{BR,2}$	Bulk reaction rate coefficient for R2	1.86×10^{-17}	$cm^3\ s^{-1}$
$k_{BR,3}$	Bulk reaction rate coefficient for R3	1.99×10^{-16}	$cm^3\ s^{-1}$
c	Stoichiometric coefficient (branching ratio)	0.454	
$H_{cp,O3}$	Henry's law coefficient of O3 in organics	6.66×10^{-4}	mol cm^{-1} atm
$T_{d,O3}$	Surface desorption lifetime of O3	1.67×10^{-7}	s
$\alpha_{s,0}$	Surface accommodation coefficient of O3	0.13	
D_{dimer}	Bulk diffusion coefficient of the dimer	$[1.03 \times 10^{-12}]$	$cm^2\ s^{-1}$
f_{diff}	Power law scaling factor for oligomer viscosity	3.96	
$D_{X,lam}$	Bulk diffusion coefficient of ozone in the lamellar phase	$[3.35 \times 10^{-12}]$	$cm^2\ s^{-1}$
$D_{Y,lam}$	Bulk diffusion coefficient of oleic acid in the lamellar phase	$[2.81 \times 10^{-12}]$	$cm^2\ s^{-1}$
$D_{X,di}$	Bulk diffusion coefficient of O3 in the dimer	$[4.66 \times 10^{-9}]$	$cm^2\ s^{-1}$
$D_{Y,di}$	Bulk diffusion coefficient of oleic acid in the dimer	$[8.85 \times 10^{-11}]$	$cm^2\ s^{-1}$
$D_{X,tri}$	Bulk diffusion coefficient of O3 in the trimer	$[1.49 \times 10^{-12}]$	$cm^2\ s^{-1}$
$D_{y,tri}$	Bulk diffusion coefficient of oleic acid in the trimer	$[8.16 \times 10^{-11}]$	$cm^2\ s^{-1}$
f_{slr}	Scaling factor for surface reaction rates	4.41×10^{-6}	cm^{-1}
$k_{loss,NN}$	Rate of nonanal loss from particle surface	1.4	s^{-1}

Table 10-2. Parameters used in the model. Parameters in square brackets were optimised using the differential evolution global optimisation algorithm.

All unvaried parameters are constrained to the values reported by Hosny *et al.* (Hosny et al., 2016) except for the rate of nonanal loss from the particle surface ($k_{loss,NN}$), which was found not to affect the model output in this regime and set to a value of 1.4 s^{-1}.

10.2.3 **Film composition evolution for liquid oleic acid model run**

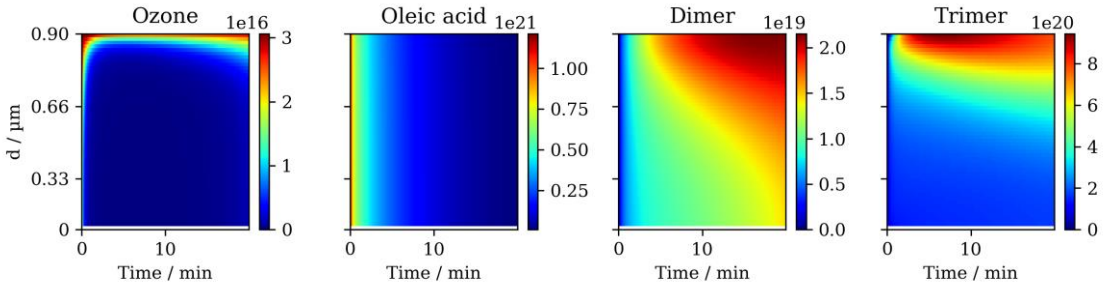

Figure 10-4. Evolution of component concentration for model runs using liquid oleic acid diffusivity parameters described in section 3.4.1. d: distance from the film core. $[O_3]$ = 77. ppm. Concentrations are in cm^{-3}.

10.3 Supporting information for chapter 4

10.3.1 Neutron reflectometry of bare silicon substrates

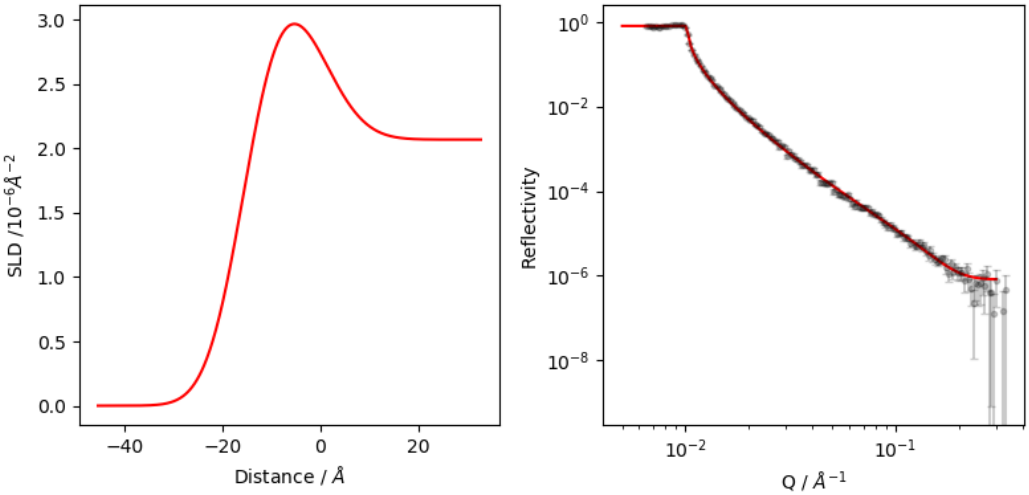

Figure 10-5. The NR curve and resulting SLD profile of one of the bare substrates (disk A) deposited on for the films presented in chapter 4.

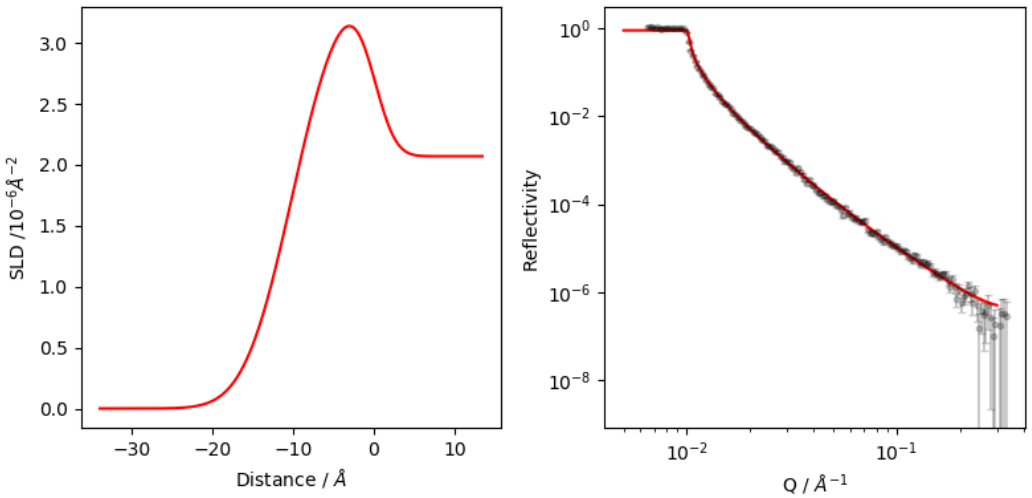

Figure 10-6. The NR curve and resulting SLD profile of one of the bare substrates (block P60) deposited on for the films presented in chapter 4.

The silicon substrate roughness and the native SiO_2 layer thickness and roughness were determined by measuring an NR curve and fitting an interfacial model to it.

Si substrate roughness for one of the disks (disk A) was 6.95 Å and the thickness and roughness of the SiO_2 layer was 15.33 Å and 6.26 Å, respectively (Fig. 10-6).

Si substrate roughness for the other substrate (block P60) was 2.11 Å and the thickness and roughness of the SiO_2 layer was 10.14 Å and 4.70 Å, respectively (Fig. 10-7).

10.3.2 **Initial fits of other spin-coated films**

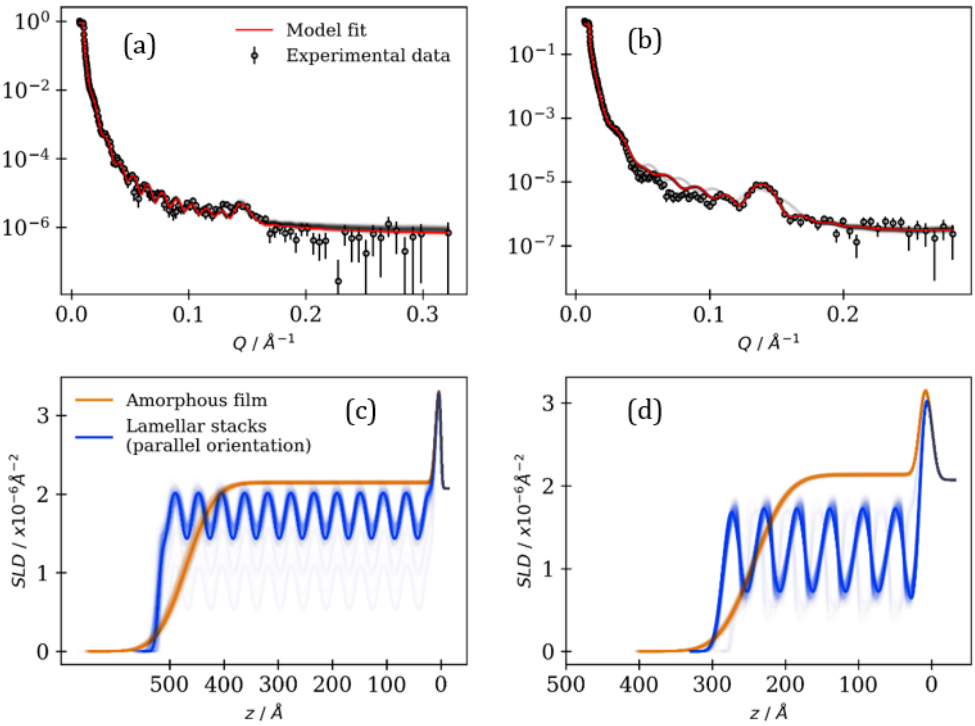

Figure 10-7. R vs Q curves of films coated at 1000 (a) and 4000 (b) rpm. Model fits are presented along with 200 curves randomly sampled from the Markov Chains stored after the MCMC sampling procedure (black curves). SLD profiles corresponding to the amorphous film and lamellar stack region are presented below their relevant R vs Q curve ((c) and (d)). z is the distance from the substrate. 200 samples from the MCMC sampling procedure are presented.

The model fits presented in Fig. 10-7 correspond to the 1000 and 4000 rpm coatings summarised in table 4-1 in section 4.4.1.

10.3.3 Further details of the offline GI-SAXS experiment

The scattering pattern was measured using a Pilatus 300k detector with a pixel size of 0.172 mm x 0.172 mm mounted on a translatable stage. The sample to detector distance for these samples 1.185 m and the detector was translated vertically and the images combined to form a virtual detector without gaps between the detector chips. Each image collection was 15 minutes. The sample chamber was filled with flowing dry nitrogen.

10.3.4 Details of the nested sampling procedure

The principles behind the use of the *dynesty* python package are presented in detail by Speagle *et al.* (Speagle, 2020). Essentially, a number of live points (parameter sets) are drawn from the prior probability distribution of each parameter. In this case, we used 500 live points. Each point has a likelihood function (goodness-of-fit) evaluated. The point with the lowest likelihood is discarded and a new point with a higher likelihood is sampled. This is iterated until some stopping criterion is achieved. The stopping criterion in this case is when the contribution to the evidence of the remaining parameter volume compared to the total evidence from all samples is less than a threshold value. In this case, a value of 0.01 was used (*dlogz* argument in the *run_nested* function of the *NestedSampler* object).

10.3.5 Offline GI-SAXS pattern and microscopy of a spin-coated film

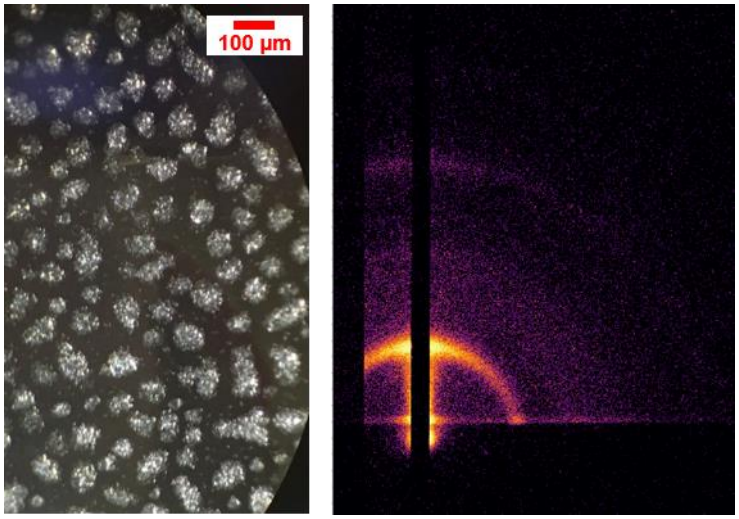

Figure 10-8. Optical microscopy image (left) and 2-D GI-SAXS pattern (right) of a film deposited on a silicon substrate.

A separate film was spin-coated offline (away from the beamline) and a GI-SAXS measurement taken (Fig. 10-8). This pattern exhibited a diffuse scattering ring corresponding to a lamellar phase bilayer. Scattering in the specular direction (vertical direction in Fig. 10-8 (right)) is more intense compared to the rest of the scattering peak. This means that there is a degree of parallel orientation of lamellar stacks, as demonstrated by synchrotron GI-SAXS and NR experiments in chapter 4.

10.3.6 **Changes to the NR curve during ageing**

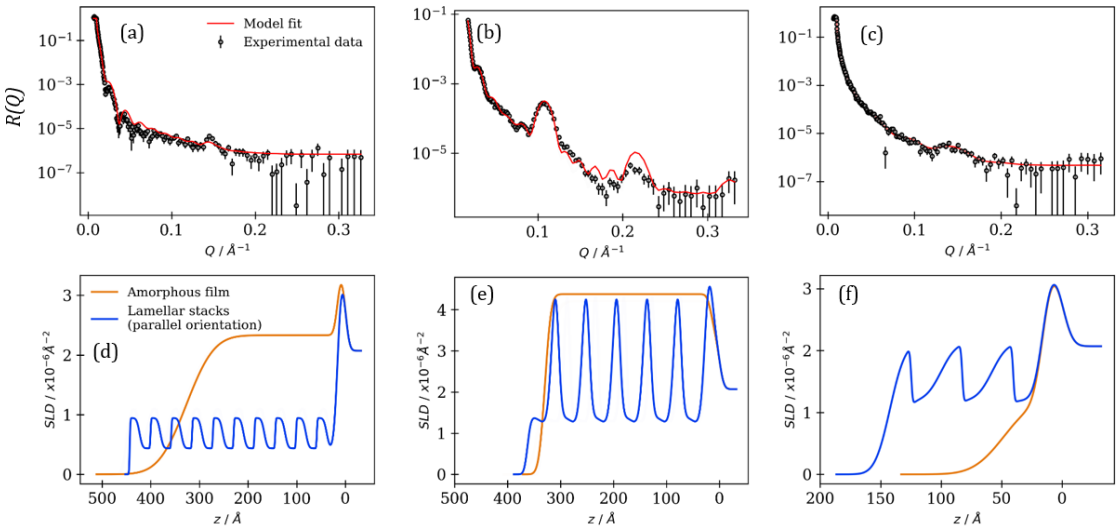

Figure 10-9. NR curves and model fits ((a) – (c)) and corresponding SLD profiles ((d) – (f)) for a film coated at 2000 rpm. These curves are stitched together measurements at low and high angles (0.5 and 2.3 º, respectively). (a) and (d): characterisation after ~ 700 min ozone exposure (4020 ppb). (b) and (e): characterisation after humidification to ~ 90 % RH. (c) and (f): characterisation after dehumidification to ~ 5 % RH.

Full high- and low-angle NR measurements demonstrate how the structure of the film changes with exposure to ozone and humidity. A Bragg peak is visible throughout the experiments (see peak at ~ 0.14 $Å^{-1}$ in NR curves in Fig. 10-9). There is a visible shift of the Bragg peak at high RH (90 %) to ~ 0.1 $Å^{-1}$ (Fig. 10-9(b)). The model fit returned a layer of D_2O 7.9 ± 0.2 Å thick between lamellar bilayers – indicating water uptake. Note also that the critical edge (maximum *R* region at low *Q*) is lower at high RH compared with the two dry measurements (compare Fig. 10-9(b) to Fig. 10-9(a) and (c)). This is due to increased off-specular scattering corresponding to some lateral coherence in the surface structure (see next section) (Dalgliesh, 2002; Hafner et al., 2021). At the end of the ageing experiment, the film is not as uniform and homogeneous

as before. There is a lack of clear fringes and the model fit returns a very rough film and a lamellar region with 3 stacks parallel to the surface.

10.3.7 **Off-specular scattering**

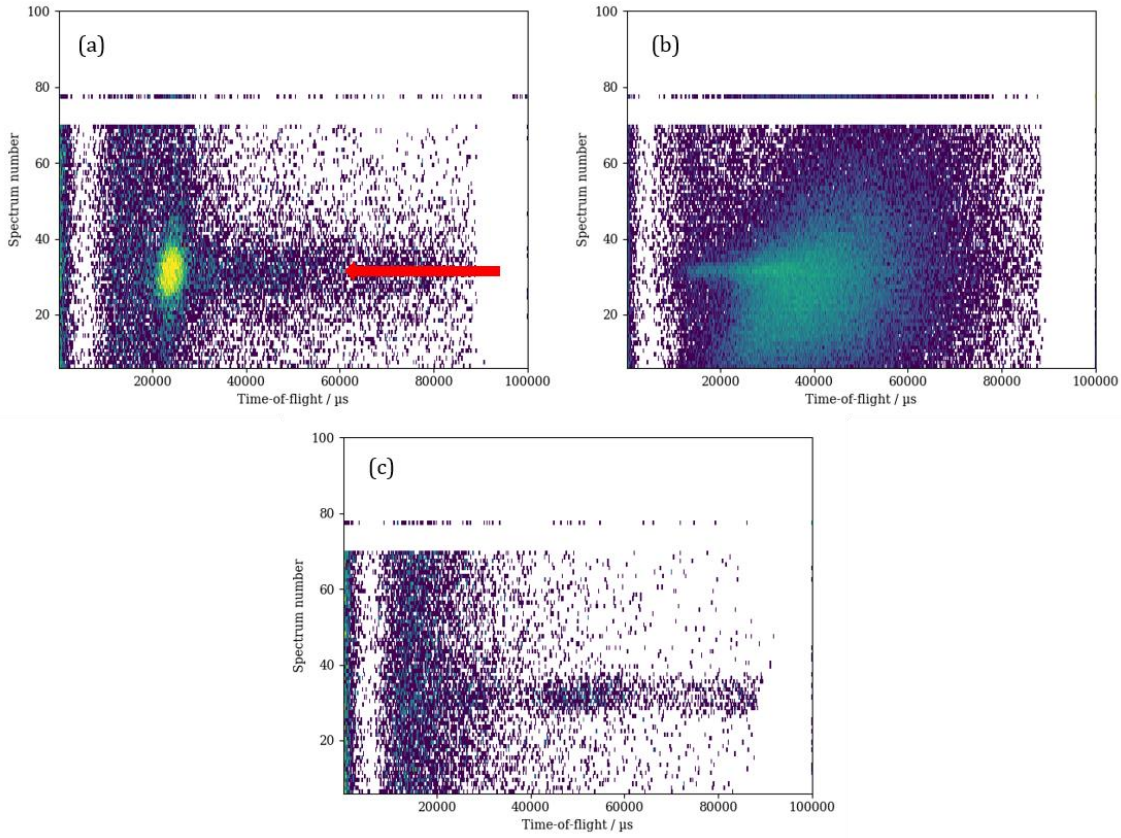

Figure 10-10. Off-specular scattering, plotted as spectrum number vs neutron time-of-flight. Higher time-of-flight corresponds to low-Q. A red arrow corresponding to the specular direction is drawn on panel (a) – any scattering signal above or below this line is off-specular. (a) and (b) are measurements on the same film at ~ 90 % RH (coated at 2000 rpm) at high- and low-angles (0.5 and 2.3 ^{o}, respectively). (c) is an off-specular measurement carried out at ~ 5 % RH (coated at 4000 rpm) after ~ 3 h ozone exposure (4020 ppb).

Off-specular neutron scattering measurements show that at high RH (~ 90 %), the specular Bragg peak is clearly visible Fig. 10-10(a), indicating parallel lamellar stack alignment. A low-angle measurement of the same sample at that humidity shows an appreciable amount of off-specular scattering at low-Q (higher time-of-flight), explaining the decrease in the maximum *R* observed in the specular NR curve (Fig. 10-10(b) and Fig. 10-10(b) – see previous discussion). An off-specular measurement of a separate film at low RH (~ 5 %) provides less evidence that the Bragg peak is predominantly specular and mostly randomly oriented (Fig. 10-10(c)) – see complementary GI-SAXS and model fitting in chapter 4.

10.4 **Supporting information for chapter 5**

10.4.1 **Kinetic data**

Observed pseudo-first order decay constants (k_{obs}) were measured in the same way as described in Milsom *et al*. – where the SAXS peak area was followed as a function of time (Milsom et al., 2021). Taking the natural log of each peak area normalised to the initial peak area, and plotting this against time, afforded a linear plot with the gradient being k_{obs} this is valid where the reaction is pseudo-first order.

The key points are: (i) k_{obs} was measured at the fastest point of the reaction – where the decay was pseudo-first order (see Fig. 6 in the main text); (ii) these k_{obs} values are a measure of the rate of decay of oleic acid *in that nanostructure* – it is clear from the Raman decay (Fig. 5-6(f) in section 5.4.3) that oleic acid remains in the film after the destruction of the initially observed ordered phases.

Nanostructure	***wt % fructose***	***k_{obs} / x 10^{-2} min^{-1}***	***k_{obs} (uncert.) / x 10^{-2} min^{-1}***	***Thickness / µm***
Liquid	0	23	3	50
Inv. Mic.	20	31	7	95
Inv. Mic.	50	45	10	95
Ord. Inv. Mic.	33	18	2	83
Lam.	0	7	5	0.59
Lam.	0	0.64	0.01	73
Solid	0	0.04	0.01	50

Table 10-3. Kinetic data with measured pseudo-first order decay constants (k_{obs}) and corresponding nanostructure, composition and film thickness data. The "liquid" and "solid" nanostructures correspond to oleic acid and sodium oleate on their own, respectively – these were measured using Raman spectroscopy as described in Milsom et al. (Milsom et al., 2021) *and chapter 2. All data with 0 wt % fructose are taken from Milsom et al.*(Milsom et al., 2021) *and chapter 2.*

10.4.2 The inverse micellar phase formed at high humidity without the addition of fructose

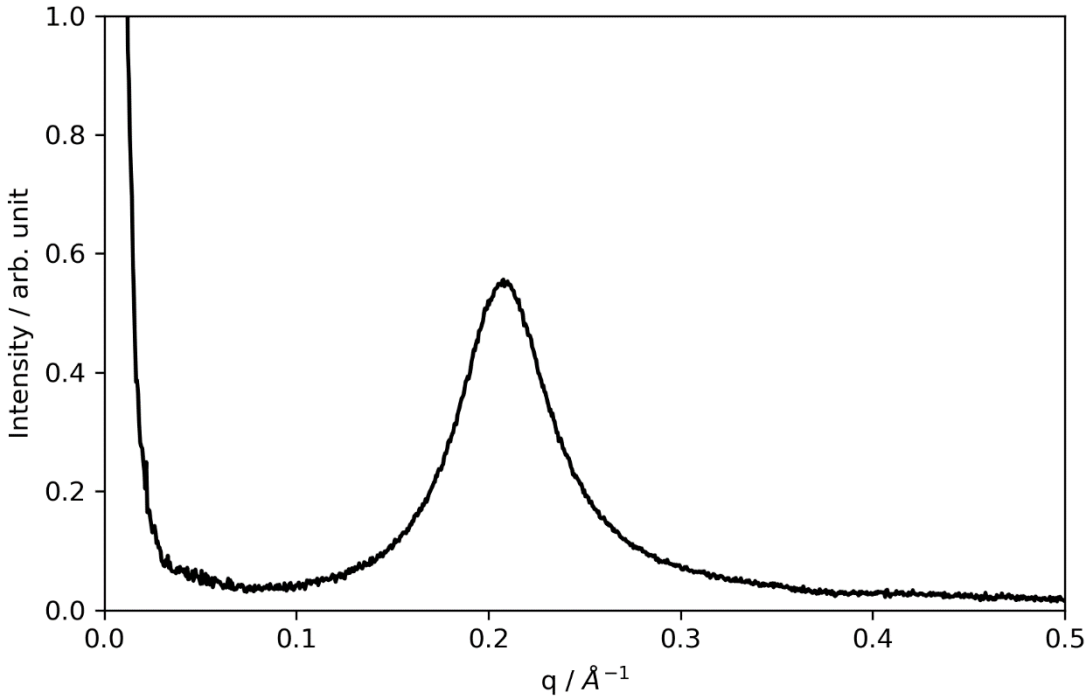

Figure 10-11. 1D SAXS pattern of a levitated particle of oleic acid:sodium oleate in a 1:1 wt held at 90 % RH for ~ 300 min. This peak corresponds to the inverse micellar phase with a d-spacing of 30.1 Å.

A sample of oleic acid-sodium oleate mixture (1:1 wt) was levitated and humidified to 90 % for ~ 300 min to afford the inverse micellar phase. The *d*-spacing observed for this system was 30.1 Å. There is a significant difference in *d*-spacing when compared with the *d*-spacings observed in our fructose-containing mixtures in the main text. The levitation-SAXS experiment is described in detail elsewhere (Pfrang et al., 2017; Seddon et al., 2016).

10.4.3 **Identifying the ordered inverse micellar phases observed**

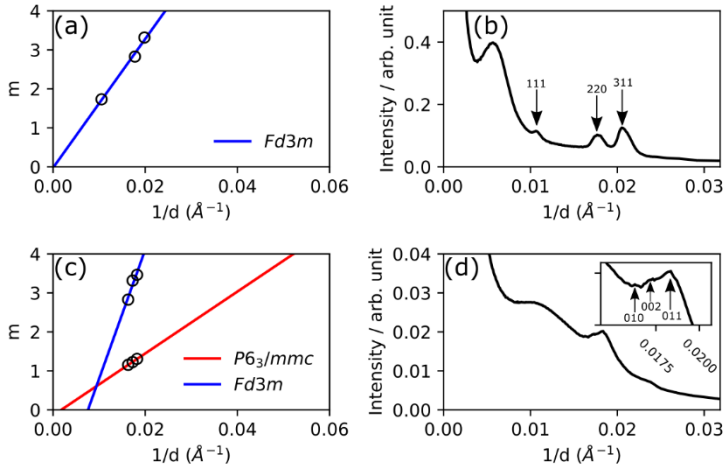

Figure 10-12. Indexing the inverse micellar cubic phases observed in this study. (a) - The m vs 1/d plot with linear fit for the Fd3m cubic phase symmetry observed at high RH and (b) - the corresponding SAXS pattern with the miller indices (hkl) of each scattered peak. (c) & (d) are the same plots for the P6₃/mmc symmetry observed during ozonolysis with an additional linear fit to the Fd3m symmetry, showing that the P6₃/mmc space group corresponds the best to the fitted peak positions.

In order to identify the cubic close-packed inverse micellar phases observed in this study, a relationship between the Miller indices (*hkl*) of each scattering plane and 1/*d* for each observed reflection is defined. We define a parameter (*m*) which is unique to each cubic symmetry group observed here:

$$m = \sqrt{(h^2 + k^2 + l^2)} \quad \text{(Fd3m symmetry)(Seddon et al., 1990)} \qquad (10\text{-}1)$$

$$m = \sqrt{\frac{4}{3}(h^2 + k^2 + hk) + \frac{l^2}{R^2}} \quad \text{(P6}_3\text{/mmc symmetry)(Clerc, 1996)} \qquad (10\text{-}2)$$

R is the ratio of the cubic unit cell dimensions (*c*/*a*) for the hexagonal close-packing of spheres for the $P6_3/mmc$ space group, with a theoretical value of 1.663 (Clerc, 1996). A linear relationship between *m* and experimentally observed peak positions 1/*d* with an intercept at 0 would mean that the phase assignment is correct. This is the case for the Fd3m phase observed at high RH and with an organic composition of 50 wt % fructose (Fig. 10-12(a)). The cubic phase observed during ozonolysis of a 33 wt % fructose film is assigned to the $P6_3/mmc$ arrangement, although the intercept was not quite 0. This may be due to the difficulty in fitting peaks which clearly have an overlapping scattering peak, affecting peak position determination (Fig. 10-12(c) & (d)). What is certain is that this set of peaks did not correspond to the Fd3m phase.

The slopes of these plots give the unit cell dimension (*a*) for each phase. These were 165 Å for the Fd3m phase and 79 Å for the $P6_3/mmc$ phase. This corresponds to a micellar diameter of 117 Å for the Fd3m phase (where $a = \sqrt{2}$ x diameter) and 79 Å for the $P6_3/mmc$ phase (where *a* = diameter). These values are higher than the 80 Å (Fd3m) and 76 Å ($P6_3/mmc$) indexed in a previous study on levitated particles of this system without fructose (Pfrang et al., 2017). This further corroborates what was discussed in the main text: the addition of fructose increases the size of inverse micelles formed.

10.4.4 Explanation of the calculation of the hygroscopicity parameter (κ)

Calculation of κ for the inverse micellar (close-packed and disordered) is based on using the *d*-spacing as the distance between the centres of two adjacent inverse micelles. The diameter of the core (d_{core}) is therefore determined by knowledge of the lipid monolayer thickness (l_m) and *d*-spacing (d):

$$d_{core} = d - 2l_m \tag{10-3}$$

The volume fraction of the core (ϕ_{core}), which under dry conditions is the volume fraction of fructose, is therefore easily calculated:

$$\emptyset_{core} = \left(\frac{V_{core}}{V_{total}}\right) = \left(\frac{d_{core}}{d}\right)^3 \tag{10-4}$$

Taking a 20 wt % fructose mixture with a dry *d*-spacing of 41 Å, the weight percentage of fructose in the mixture can be calculated – this should be close to 20 wt % if the assumption of l_m = 10 Å is valid. For 1 cm^3 of lipid:

$$m_{fruc} = \emptyset_{core} \times \rho_{fruc} \tag{10-5}$$

$$\frac{m_{fruc}}{m_{total}} = \frac{m_{fruc}}{\rho_{lip} + m_{fruc}} \tag{10-6}$$

Where ρ_{lip} and ρ_{fruc} are the densities of the lipid and fructose, respectively. m_{fruc} and m_{total} are the masses of fructose per cm^3 of lipid and total mass, respectively. With ρ_{lip} = 1 g cm^{-3}, the predicted weight percentage of fructose in the mixture is ~ 22 wt %, this is similar to the amount weighed into the mixture.

For a hydrated inverse micelle, the volume of core per volume of lipid ($\phi_{core,lip}$) can be measured under dry and wet conditions with knowledge of the volume of fructose per

volume of lipid ($\phi_{fruc,lip}$) calculated from the dry *d*-spacing. The volume of water (V_w) can then be calculated by subtraction of $\phi_{fruc,lip}$ from $\phi_{core,lip}$ assuming 1 cm^3 lipid:

$$\emptyset_{fruc,lip} = \frac{\emptyset_{core,dry}}{(1-\emptyset_{core,dry})} \quad (10\text{-}7)$$

$$\emptyset_{core,lip} = \frac{\emptyset_{core,wet}}{(1-\emptyset_{core,wet})} \quad (10\text{-}8)$$

$$V_w = \emptyset_{core,wet} - \emptyset_{core,dry} \quad (10\text{-}9)$$

Calculation of the dry volume (V_d) is then simply a case of adding the volume of lipid to $\phi_{fruc,lip}$. This, along with water activity (a_w) is then plugged into equation 5-2 in the main text to calculate κ. In this example case, a value of 0.034 is returned at 90 % RH and a wet *d*-spacing of 66 Å.

Calculations are similar for the lamellar phase, which consists of a bilayer. l_m is calculated as follows from the dry *d*-spacing and volume fraction of fructose (ϕ_{fruc}):

$$d_{fruc} = \emptyset_{fruc} \times d_{dry} \quad (10\text{-}10)$$

$$\emptyset_{lip,dry} = 1 - (\frac{d_{fruc}}{d_{dry}}) \quad (10\text{-}11)$$

$$\emptyset_{fruc,dry} = 1 - \emptyset_{lip,dry} \quad (10\text{-}12)$$

$$l_m = \frac{(\emptyset_{lip,dry} \times d_{dry})}{2} \quad (10\text{-}13)$$

From this V_w and V_d can be calculated at each humidity and κ calculated. Note that $\phi_{core,dry}$ for the inverse micellar phase is equivalent to $\phi_{fruc,dry}$ in these lamellar phase calculations – there is technically no "core" to the lamellar phase.

For the inverse hexagonal phase the area of a neutral surface (A_n), defined at a place along the length of the cylinder formed by the lipid molecule, can be derived (Asghar et al., 2015). This area is constant for any nanostructure formed by that lipid, hence "neutral". Knowing this and the molecular volume of the lipid (V_m), A_n can be derived from the dry lamellar phase formed by this system (Asghar et al., 2015):

$$A_n = \frac{2V_m}{d_{lam}\emptyset_{lip}} \quad (10\text{-}14)$$

The volume of the molecule based on the location of the neutral surface (V_n) for the inverse hexagonal phase is defined via the following relationship and plugging in V_m and A_n from the lamellar phase:

$$\emptyset_{lip} = \frac{8\pi}{\sqrt{3}} \frac{V_n V_m}{(A_n d)} \quad (10\text{-}15)$$

ϕ_{lip} can now be calculated from the *d*-spacings derived from the hexagonal phase SAXS data. Calculations then proceed by assuming 1 cm^3 of lipid and deriving the mass of fructose per mass of liquid from the mixture composition. From that, volume fractions can be calculated as per the inverse micellar calculations and V_w calculated. V_d = volume of lipid + volume of fructose.

10.5 Supporting information for chapter 6

10.5.1 Wide-angle X-ray scattering (WAXS) pattern of an oleic acid-stearic acid mixture

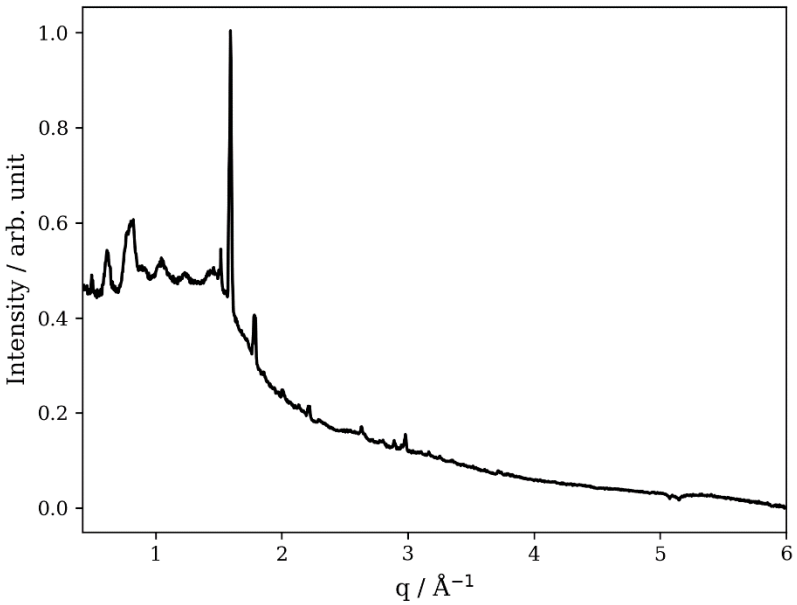

Figure 10-13. WAXS pattern of a 1:1 wt oleic acid-stearic acid mixture, background subtracted. The sharp peaks observed here correspond to the short-distance correlations between adjacent alkyl chains in the crystalline lamellar phase formed by this mixture.

10.5.2 **Phase-composition data**

Experiment series (figure in main text)	**wt % of organic mixture**			**aqueous phase wt %**		
Stearic acid + oleic acid (Fig. 6-2(a))	*OA*	*SO*	*StA*	*H_2O*	*Phase(s) observed*	*d-spacing(s)/ Å*
	20	0	80	0	Lam.	40.6
	50	0	50	0	Lam. | Lam.	40.9 | 39.9
	80	0	20	0	Lam. | Lam.	41.2 | 39.4
Sodium oleate in H_2O (Fig. 6-2(b))	*OA*	*SO*		*H_2O*	*Phase(s) observed*	*d-spacing(s)/ Å*
	80	20		50	Fd3m	135.3
	66	33		50	Fd3m | Hex.	147.3 | 48.4
	33	66		50	Hex.	54
	29	71		50	Lam.	91.8
	20	80		50	Lam. | Mic. (poor mixing)	44.7
Sodium oleate in 1% NaCl (Fig. 6-2(c))	*OA*	*SO*		*NaCl (1%)*	*Phase(s) observed*	*d-spacing(s)/ Å*
	66	33		50	Fd3m	126.9
	33	66		50	Hex. | n.d.	54.5
	20	80		50	Hex.	52.3
[NaCl] (Fig. 6-2(d))	*OA*	*SO*		*NaCl (% concentration)*	*Phase(s) observed*	*d-spacing(s)/ Å*
	50	50		0	Hex.	52.2
	50	50		5	Fd3m	110.3
	50	50		10	Fd3m	138.3
	50	50		20	Fd3m | Lam.	101.1 | 44.5
	50	50		60 (saturated)	Lam. | Mic. (poor mixing)	45.3 | 32.5
wt % H_2O (Fig. 6-2(e))	*OA*	*SO*		*H_2O*	*Phase(s) observed*	*d-spacing(s)/ Å*
	50	50		10	Fd3m | n.d.	114
	50	50		30	Hex.	41.1
	50	50		50	Hex.	54.1

	50	50		70	Hex.	54.8
	50	50		90	Fd3m | n.d.	160.2
wt % NaCl (1%) (Fig. 6-2(f))	*OA*	*SO*		*NaCl (1%)*	*Phase(s) observed*	*d-spacing(s)/ Å*
	50	50		10	Mic. | Lam.	29.2 | 41.1
	50	50		30	Hex.	40
	50	50		70	Hex.	53.7
	50	50		90	Hex.	42.7
wt % fructose (Fig. 6-3(a))	*OA*	*SO*	*Fructose*	*H_2O*	*Phase(s) observed*	*d-spacing(s)/ Å*
	50	50	20	50	Hex.	52
	50	50	33	50	Hex. | Fm3m	48.7 | 67.8
	50	50	50	50	Hex. | Fd3m	47.6 | 135
wt % glucose (Fig. 6-3(b))	*OA*	*SO*	*Glucose*	*H_2O*	*Phase(s) observed*	*d-spacing(s)/ Å*
	50	50	20	50	Hex.	52.8
	50	50	33	50	Fd3m	158.3
	50	50	50	50	Hex. | Fd3m	55.9 | 158.3
wt % sucrose (Fig. 6-3(c))	*OA*	*SO*	*Sucrose*	*H_2O*	*Phase(s) observed*	*d-spacing(s)/ Å*
	50	50	20	50	Hex. | Fd3m	44 | 140.3
	50	50	33	50	Hex. | n.d.	52
	50	50	50	50	Fd3m	135.1

Table 10-4. Composition-phase-d-spacing data supporting the figures presented in chapter 6. The observed phases are abbreviated as follows: Inverse micellar (Mic.); close-packed inverse micellar with Fd3m symmetry (Fd3m); close-packed inverse micellar with Fm3m symmetry (Fm3m); inverse hexagonal (Hex.); Lamellar bilayers (Lam.); not determined due to hidden/overlapping peaks in the SAXS pattern (n.d.).

10.5.3 Indexing the Fd3m phase formed by the 5- and 6- component mixtures

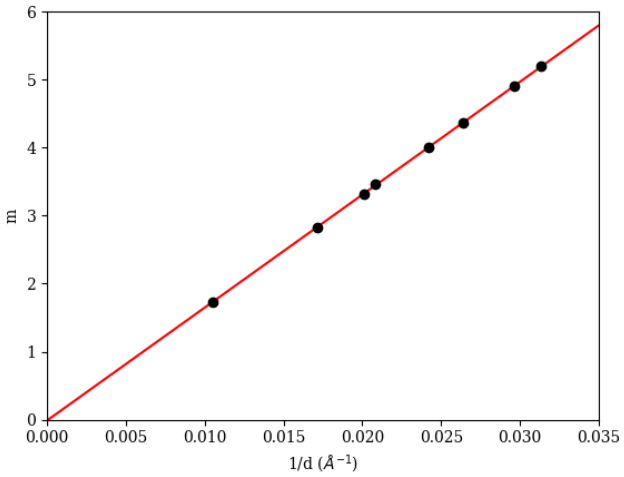

Figure 10-14. A plot of m vs 1/d for each observed reflection for the oleic acid-sodium oleate-glucose-fructose (1:1:1:1 wt) 50 wt % H_2O mixture, showing a linear plot with an origin at 0. The Fd3m symmetry.

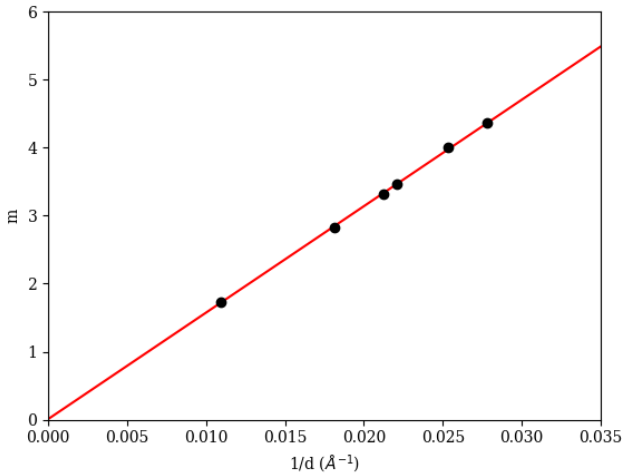

Figure 10-15. A plot of m vs 1/d for each observed reflection for the oleic acid-sodium oleate-glucose-fructose-sucrose (1:1:1:1:1 wt) 50 wt % H_2O mixture, showing a linear plot with an origin at 0. The Fd3m symmetry.

A relationship between the Miller indices (*hkl*) of each scattering plane and 1/*d* for each observed reflection is defined:

$$m = \sqrt{(h^2 + k^2 + l^2)} \quad (10\text{-}16)$$

The parameter, *m*, is unique to Fd3m symmetry group. A linear relationship between *m* and experimentally observed peak positions 1/*d* with an intercept at 0 would mean that the phase assignment is correct (Kulkarni et al., 2011).

Both the 5- and 6- component mixtures return linear plots with intercepts at 0, confirming the cubic close-packed inverse micellar phase for these mixtures. The lattice parameter for each is 166 and 157 Å for the 5- and 6-component mixtures, respectively.

10.6 **Supporting information for chapter 7**

This is the supporting information published as part of the preprint under review for *Atmospheric Chemistry and Physics*:

Milsom, A., Squires, A. M., Boswell, J. A., Terrill, N. J., Ward, A. D. and Pfrang, C.: An organic crystalline state in ageing atmospheric aerosol proxies: spatially resolved structural changes in levitated fatty acid particles, Atmos. Chem. Phys. Discuss. [preprint], doi: 10.5194/acp-2021-270, in review, 2021.

10.6.1 **Acid-soap characterisation**

	Lamellar *d*-spacing / nm (uncertainty)	
	This work [21 ^{o}C]	Literature [*T*]***
OA:SO (1:1) Acid–Soap	4.5773 (0.0001)*	4.61 (0.05) [5 ^{o}C](Tandon et al., 2001)
Sodium Oleate	4.35 (0.02)**	4.51 (0.05) [15 ^{o}C](Tandon et al., 2000b)
Oleic Acid	Liquid at this temperature	4.14 (0.05) [5 ^{o}C](Tandon et al., 2000a)

Table 10-5. Comparison of measured lamellar d-spacings for the oleic acid–sodium oleate acid–soap complex with pure sodium oleate and oleic acid (:levitated particle; **: capillary coating, ***: bulk sample; OA: oleic acid; SO: sodium oleate).*

	WAXS Spacings / nm (uncertainty)							
This work (21 °C)	0.467 (0.001)	0.455 (0.004)	0.444 (0.006)	0.407 (0.001)	0.399 (0.001)	0.378 (0.002)	0.369 (0.001)	0.363 (0.001)
Tandon et al. **(Tandon et al., 2001)** (5 °C)	0.470	0.462	0.452	0.404	0.396	0.376	0.368	0.362
Tandon et al. **(Tandon et al., 2001)** (30 °C)	0.471	0.451	0.412	0.408	0.400	0.379	0.371	0.365

Table 10-6. WAXS spacings measuring the repeat distance between scattering planes in the hydrophobic tail.

Table 10-6 compares our measured *d*-spacing with that obtained by Tandon *et al.* for the same system, but in a bulk sample and at a lower temperature. This table also includes the spacings of oleic acid and sodium oleate at low temperatures (Tandon et al., 2000a, 2000b). The value for the acid–soap complex is significantly different from the oleic

acid and sodium oleate *d*-spacings. It is however within the error of the 4.61 ± 0.05 nm quoted by Tandon *et al.*(Tandon et al., 2001) for a bulk sample. The substantial difference in uncertainty is due to the difference in techniques used: the present study utilised synchrotron radiation many times more intense than the X-rays from the laboratory-based powder diffraction instrument used in the literature. The number quoted in this study therefore has much better statistics associated with it.

The WAXS spacings measured in this study in general agree with the literature values (Table 10-6). Signals in the WAXS region suggest that a sample is crystalline, exhibiting shorter distance order in addition to the longer distance lamellar spacings. These characteristic spacings measure the sub-cell packing arrangements. Tandon *et al.* computed three sets of sub-cell parameters which accommodate the spectroscopically-deduced parallel fatty acid chain packing, all with $O_{\parallel}$ sub-cell symmetry (Tandon et al., 2001).

The melting temperature for this acid–soap complex has been reported as ~ 32 ^{o}C (Tandon et al., 2001). Exploiting the birefringent property of the acid–soap complex, a POM experiment was carried out on the acid–soap sample used in this study along with oleic acid–sodium oleate mixtures of varying ratios. The decomposition of the acid–soap structure occurred in agreement with the literature at ~ 32 ^{o}C. Further details are provided in the appendix section 10.6.3.

Oleic acid and sodium oleate have markedly different Raman spectra (Fig. 10-16). The packing of the alkyl chains in sodium oleate is more ordered than that of oleic acid. This is exhibited by the difference in peak profile in the C–H stretching region (~ 2840–3050 cm^{-1}) (Tandon et al., 2000a, 2000b, 2001). The acid–soap complex has features similar

to sodium oleate due to its crystallinity. However, the acid–soap complex spectrum is clearly distinct from those of its constituent species (see Fig. 10-16: panel (a) *vs.* (b)–(d)).

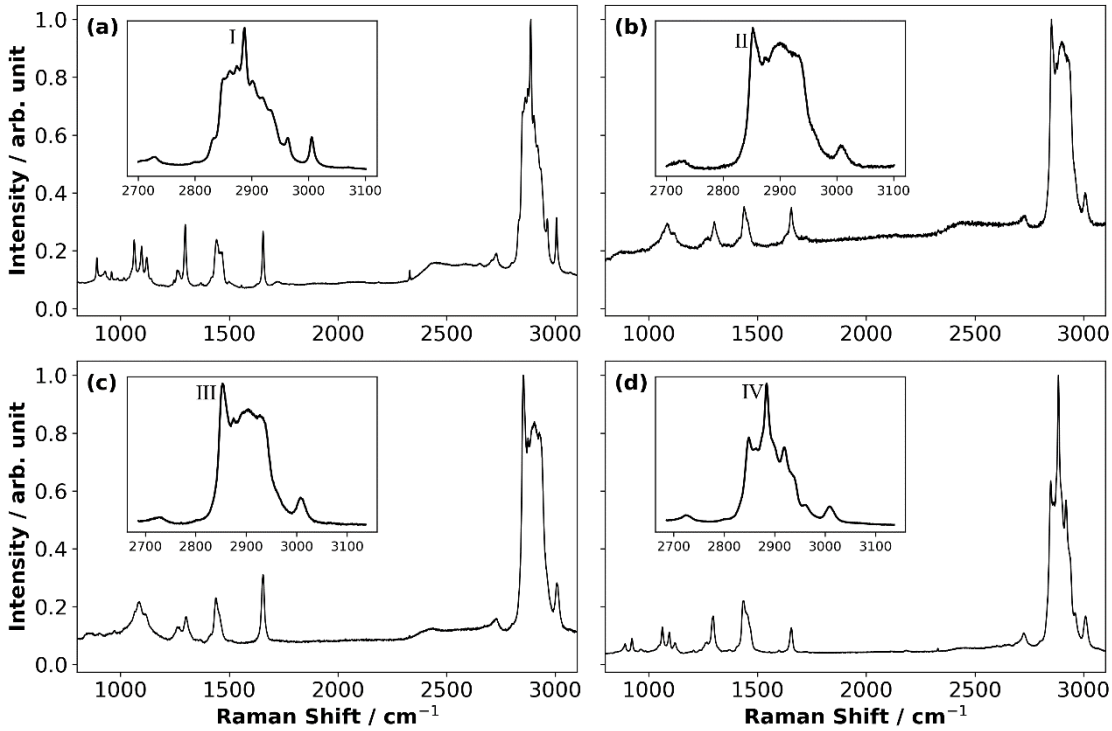

Figure 10-16. Raman spectra of (a) the acid–soap complex; (b) a bulk mixture of oleic acid:sodium oleate (1:1 wt) 30 wt % in water - the hexagonal LLC phase; (c) oleic acid and (d) sodium oleate. All samples deposited on microscope slides. C–H stretching region is enlarged and displayed as an inset. Key peaks associated with alkyl chain ordering are labelled: I = 2887 cm^{-1} , II & III = 2854 cm^{-1} and IV = 2884 cm^{-1}.

Figure 10-16 shows a comparison of the acid–soap complex (panel (a)) and its components (panels (c) and (d)). The Raman spectrum for a bulk LLC hexagonal phase (confirmed by SAXS) of oleic acid:sodium oleate (1:1 wt) 30 wt % in H_2O is also presented for comparison (panel (b)). The strong peak at 2887 cm^{-1} is characteristic of

the ordered packing of the acid–soap complex alkyl chains and is similar to the findings of Tandon *et al* (Tandon et al., 2001), distinguishing it from its components. The oleic acid and liquid crystal spectra exhibit a stronger peak at 2854 cm^{-1} with the peak originally at 2887 cm^{-1} significantly weaker, up-shifted and broadened, arising from the disordered state of the alkyl chains in both of these systems. Additionally, there are sharp C–C stretching peaks between ~ 1050–1150 cm^{-1} which suggest that there are multiple trans conformers in the hydrocarbon chain (Tandon et al., 2001). Raman spectra of levitated acid–soap complex particles exhibited peaks in similar positions, however these spectra were subject to very high background scattering (see the appendix section 10.6.4). Superimposed Raman spectra of the C–H stretching region of these components are presented in the appendix (Fig. 10-17).

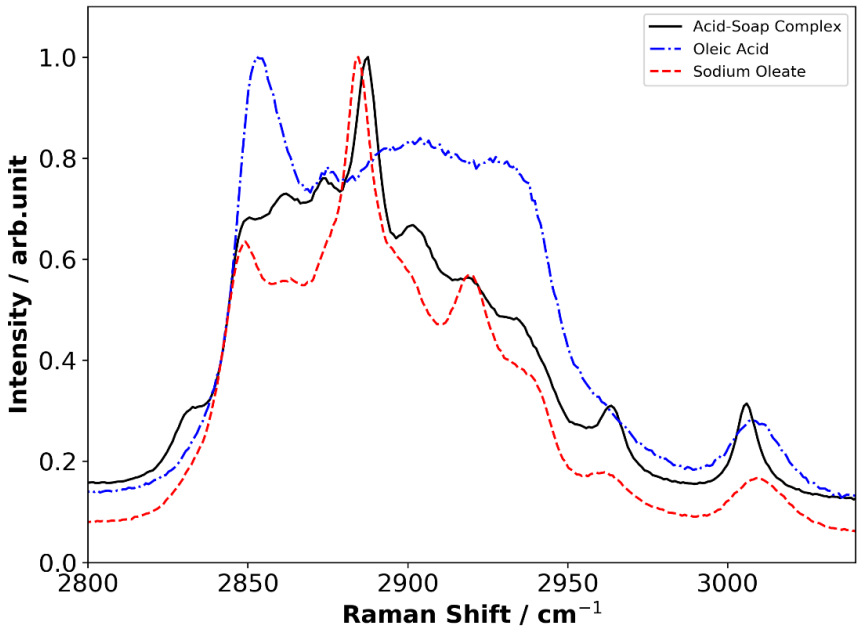

Figure 10-17. Superimposed Raman spectra of the 2800-3100 cm^{-1} region exhibiting differences in peak positions.

The carboxylate C=O bond peak is strong in IR spectroscopy. The position and intensity of this peak eludes to the environment the C=O bond is found in. This is structure-dependent: both oleic acid and sodium oleate have carboxyl peaks; oleic acid has its peak at 1707 cm^{-1}, while sodium oleate has its peak shifted by nearly 150 cm^{-1} to 1558 cm^{-1} (see Fig. 10-17).

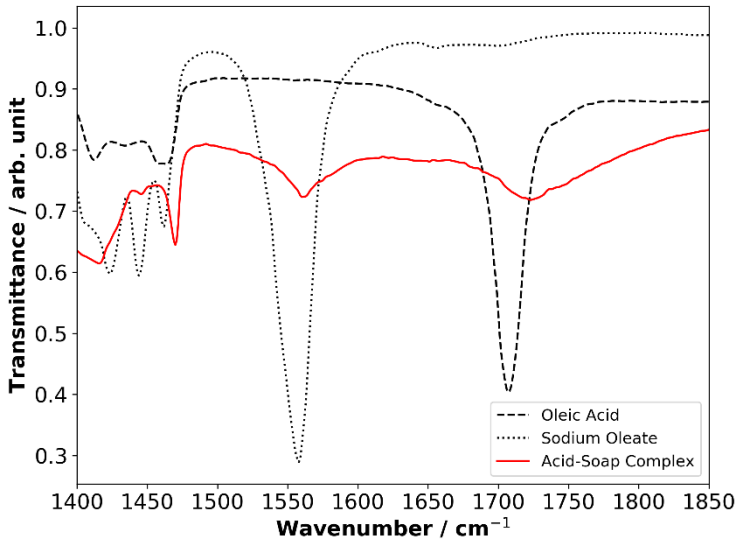

Figure 10-18. IR spectra of the acid–soap complex, oleic acid and sodium oleate. The CH_2 scissoring region is in the range of 1400-1500 cm^{-1}. The C=O bond peak region is in the range of 1500-1800 cm^{-1}.

The acid–soap complex exhibits a mixture of these two C=O/$(-CO_2)^-$-related peaks. The carboxyl signal has been shifted slightly higher to 1712 cm^{-1} and is broader, consistent with the findings of Tandon *et al*. (Tandon et al., 2001). The broadening and partial disappearance of the two signals associated with oleic acid and sodium oleate suggest that the carboxylate groups are involved in hydrogen bonding, reported previously for similar complexes: sodium palmitate–palmitic acid(1:2) (Lynch et al., 1996) and C_4 – C_{24} (1:1) acid–soap complexes (Mantsch et al., 1994).

The appearance of an un-split signal in the CH_2 scissoring region at 1469 cm^{-1} suggests the parallel chain arrangement as opposed to a perpendicular arrangement found in other acid–soaps (Lynch et al., 1996; Tandon et al., 2001). This region of the acid–soap IR spectrum is significantly different to its components.

10.6.2 SAXS/WAXS of the levitated particle centre during humidity changes

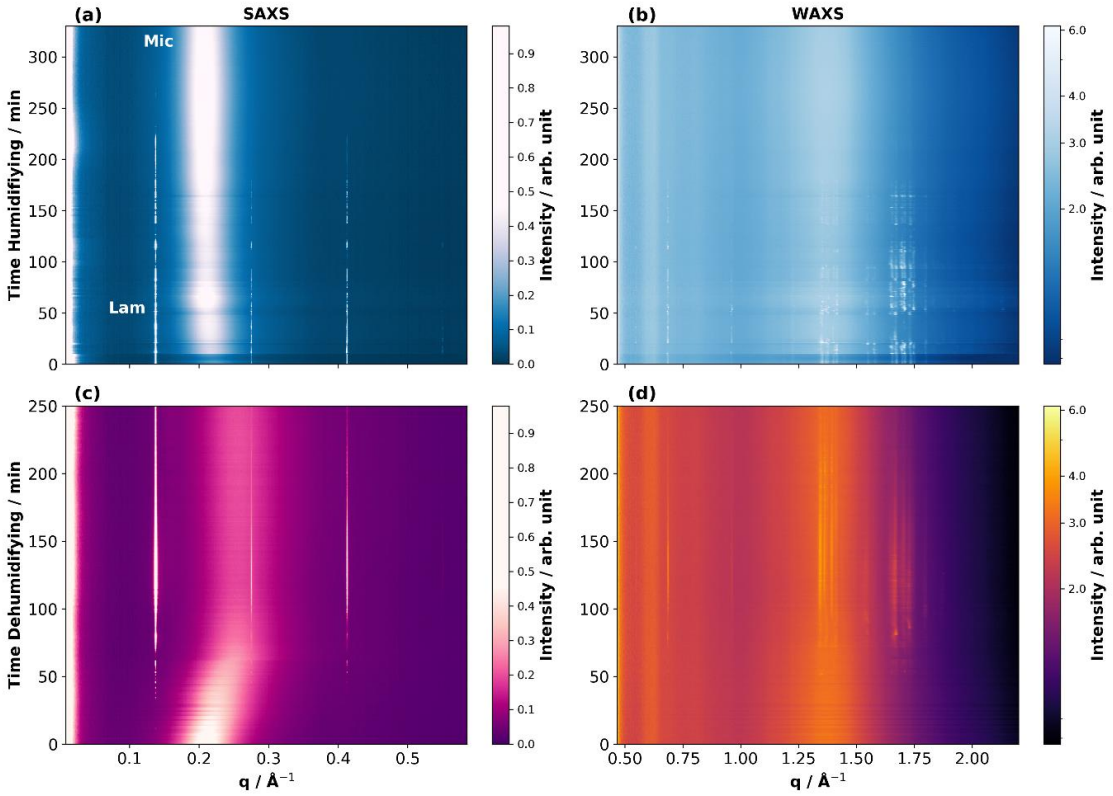

Figure 10-19. Evolution of the 1–D SAXS and WAXS patterns at the centre of a levitated acid–soap complex particle during humidification to 90 % RH (a) & (b) and dehumidification from 90 % RH to ~ 38 % RH (c) & (d). Peak positions for both SAXS and WAXS patterns are analogous to those in Fig. 7-1. The sharp first lamellar peak is labelled as 'Lam' and the broad inverse micellar peak is labelled as 'Mic' in panel (a) for clarity.

10.6.3 Polarising optical microscopy (POM) – thermal decomposition of the acid-soap complex

The oleic acid-sodium oleate acid–soap complex is reported to have a thermal decomposition temperature of ~ 32 ºC (Tandon et al., 2001). As this complex is birefringent, it is possible to view it using cross-polarised light. The crystals exhibit a bright pattern (Fig. 10-20). Using a heating stage, it was possible to heat the sample from room temperature to the decomposition temperature reported in the literature.

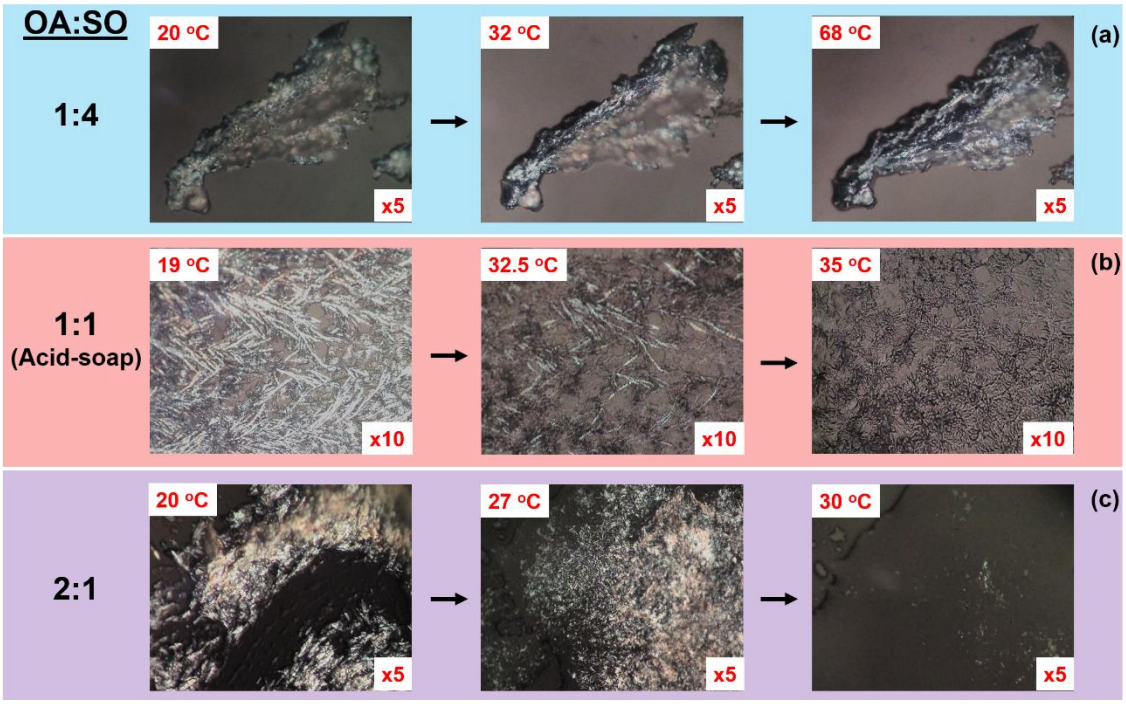

Figure 10-20. Polarising microscopy-temperature experiments of differing oleic acid:sodium oleate weight ratios deposited from ethanol onto microscope slides. OA = Oleic acid, SO = Sodium oleate. (a) 1: 4, (b) 1:1 (acid-soap complex) and (c) 2:1. RH ~ 50 %.

The acid–soap complex clearly starts to break down at ~ 32 ºC. The pattern started to disappear rapidly once the temperature approached this value. No more birefringence was observed and the sample became ‘dark’. This is a qualitative visual confirmation of the literature’s observations obtained by Raman microscopy and X-ray diffraction. On

inspection of the reported literature phase diagram, the acid-soap at this composition breaks down and forms an isotropic liquid (Tandon et al., 2001).

Two other oleic acid:sodium oleate ratios were made and tested in the same way, 2:1 and 1:4. Interestingly, the 2:1 ratio mixture became fluid at ~ 27 ^{o}C and lost its birefringence at ~ 30 ^{o}C. This is consistent with the phase diagram for the dry oleic acid/sodium oleate system. According to the reported phase diagram, this system becomes an isotropic liquid above the decomposition temperature and the decomposition temperature decreases as a function of the amount of oleic acid in the system (Tandon et al., 2001). The 1:4 system was heated to 68 ^{o}C. Some of the birefringence disappeared at ~ 32 ^{o}C. This is ascribed to the acid–soap complex in this system breaking down. The sample remained birefringent for the whole experiment, suggesting that only sodium oleate was left in the crystalline state as its melting point is > 200 ^{o}C.

10.6.4 **Raman spectra of the levitated acid-soap complex**

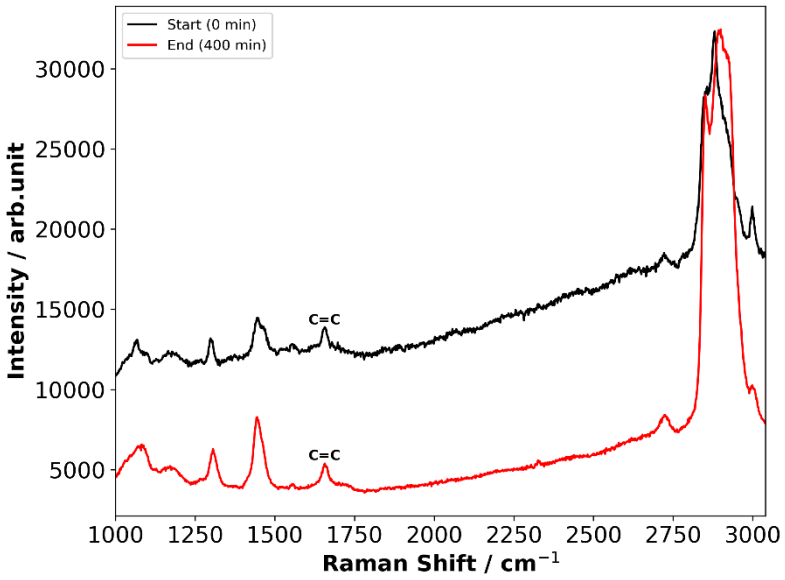

Figure 10-21. Raman spectra of the levitated acid-soap complex before and after ozonolysis for 400 min ([O_3] = 51.9 ± 0.5 ppm). The carbon-carbon double bond peak used to measure reaction kinetics is labelled.

Figure 10-21 presents the Raman spectrum before and after ozonolysis. Note that the plot is not adjusted in order to stack the spectra, meaning that there is a significantly high background signal at the beginning of the experiment compared with the end. This is thought to be due to the high background scattering encountered when measuring Raman spectra of solid crystalline material such as the acid-soap complex.

The C=C bond has decreased in intensity compared to the C-H peak observed at ~ 1442 cm^{-1} indicating that oleic acid has reacted. However, there is still a clear signal remaining at the end of the experiment corresponding to 34.0 ± 8.5 % of oleic acid remaining in the particle (7-2(i)). Note the change in profile of the region 2750-3050 cm^{-1}. This is evidence of the acid-soap complex breaking down and is presented and

discussed in the *Evolution of the SAXS pattern during Ozonolysis* section of the main text.

10.6.5 **Optical images of a levitated sodium oleate particle – humidification**

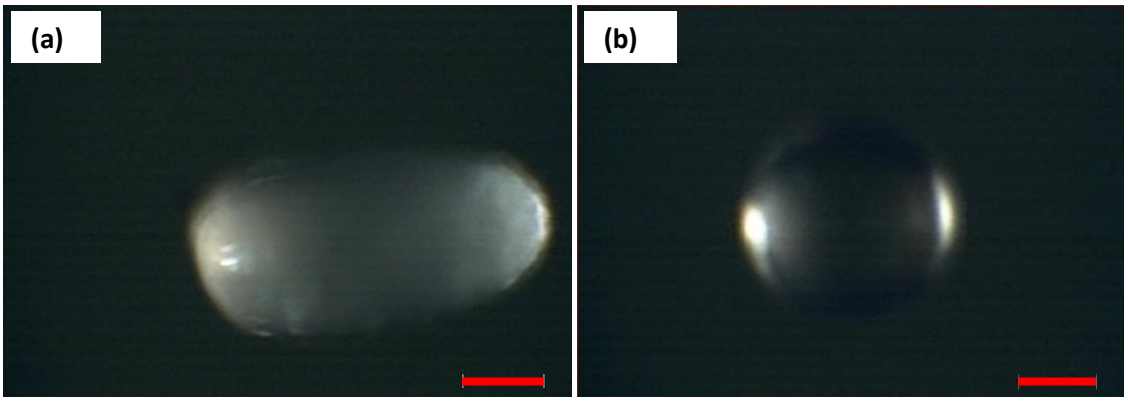

Figure 10-22. Two optical images of a levitated sodium oleate particle before humidification (a) and after humidification to > 90 % RH for ~ 3 h (b). Red scale bar represents 50 µm.

A particle of sodium oleate was levitated at ~ 50 % RH and exposed to > 90 % RH for a prolonged period (~ 3 h) in order to demonstrate the change in size and shape of a solid hygroscopic particle, such as sodium oleate, after water uptake. The deliquescence point of sodium oleate has been measured to be 88 ± 2 % (Nájera, 2007). There is a clear difference in size and shape between a dry and deliquesced particle.

10.6.6 Low-*q* SAXS evidence for high-molecular-weight product formation during ozonolysis

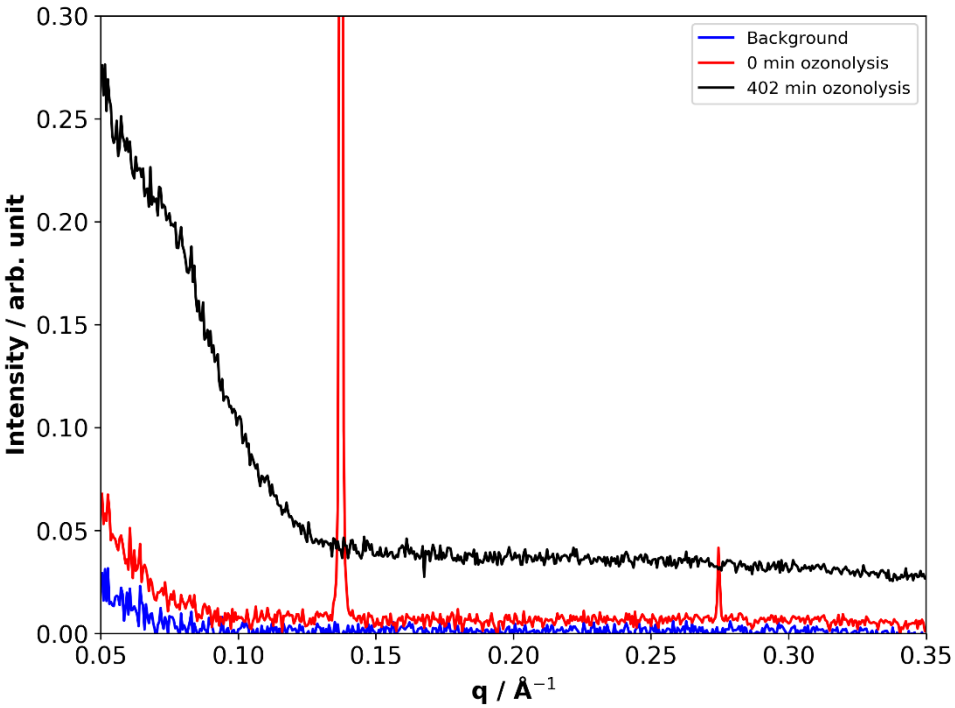

Figure 10-23. SAXS patterns of a levitated acid-soap complex before and after ozonolysis compared with an empty-levitator background. There is a clear increase in low-q scattering as a result of ozonolysis. [O_3] = 52 ± 0.5 ppm.

Figure 10-23 clearly shows an increase in low-q SAXS signal and the appearance of a shoulder at ~ 0.07 Å^{-1} as a result of ozonolysis. Low-q scattering signals are observed for species with large repeat distances between equivalent scattering centres. Structures formed by polymeric molecules exhibit patterns at low q due to the larger size of those molecules compared to our fatty acid precursors (Meznarich et al., 2011). As the particle is a complex mixture of products, it is not possible to discern much about the structure from this scattering curve because of the impure nature of the scattering phase. Better low-*q* resolution would be required to study structures with larger repeat distances than the self-assembled structures of smaller molecules (oleic acid-sodium

oleate) we focus on in this study. This can be achieved by increasing the sample-to-detector distance of the SAXS setup – not practicable during a time-critical synchrotron beamtime experiment. Nevertheless, the presence of a structure with low-q scattering peak even after ozonolysis suggests that products themselves exhibit some ordering.

10.6.7 **POM of the humidified and dehumidified acid-soap complex**

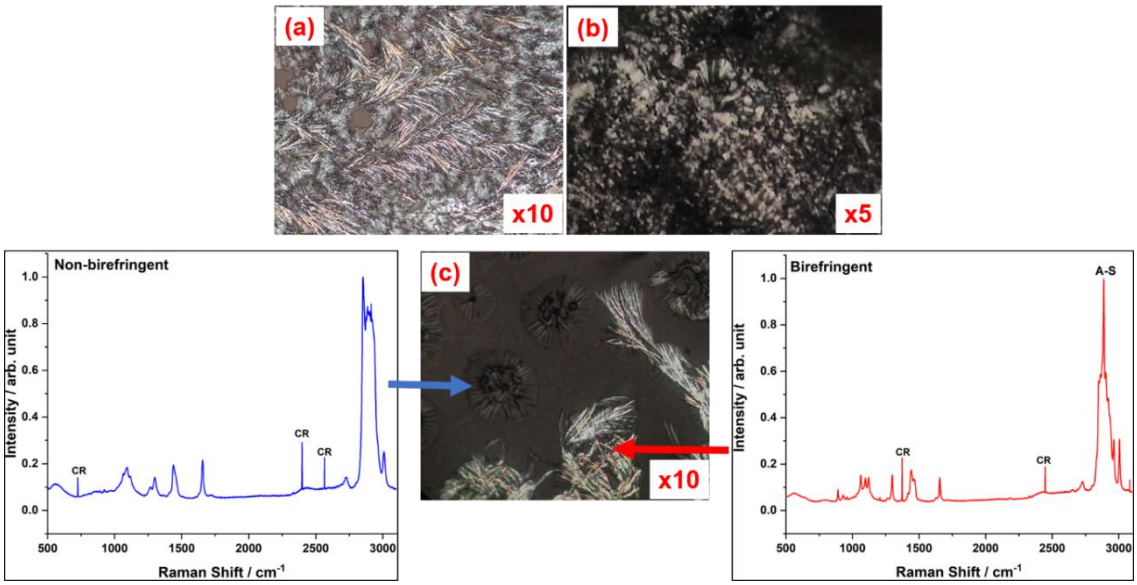

Figure 10-24. POM images of the oleic acid:sodium oleate (1:1 wt) acid–soap complex. (a) At ~ 50 % RH, showing a birefringent needle-like/streaky lamellar pattern. (b) Immediately after removal from the saturated humidity chamber. A "charcoal-like" pattern is observed, suggesting a hexagonal phase. (c) 5 h after removal from humidity chamber. Birefringent needles have returned along with a non-birefringent phase. Raman spectra of each portion presented both sides – A–S = Acid–Soap Complex Peak, CR = Cosmic Ray.

Visual and spectroscopic evidence for a phase separation was obtained using POM (see section 10.6.3) and Raman microscopy; a summary of which is in Fig. 10-24. A film of the acid–soap complex was deposited on a microscope slide and initially allowed to dry over 6 days. A POM picture was taken at room RH (~ 50 %, Fig 10-24(a)). The acid–

soap complex sample was birefringent with characteristic lamellar “streaks”. The sample was then exposed to a saturated humidity chamber which was created by half-filling a small container with ultrapure water and suspending the microscope slide within it. The sample was left in the chamber for 7 days.

A POM picture was taken immediately after removal from the humidity chamber and exhibited a “charcoal” texture under the polarising microscope known to be the hexagonal phase texture for this system (Mele et al., 2018) (Fig. 10-24(b)), which disappeared within ~ 5 min of being in room RH (~ 50 %). This is evidence for an inverse hexagonal lyotropic liquid crystal phase which has been shown to form in the *potassium* oleate variant of this acid–soap complex (Cistola et al., 1986) and also for the oleic acid/sodium oleate/water/NaCl solution system (Engblom et al., 1995; Mele et al., 2018; Pfrang et al., 2017; Seddon et al., 1990). The fast disappearance of this texture suggests that this phase exists at high water content. Indeed, the hexagonal phase has been observed in our offline SAXS experiments using bulk mixtures of this fatty acid composition in excess water (Fig. 10-27). The hexagonal phase was not observed in the SAXS patterns for levitated acid–soap complex particles. The POM samples were allowed to equilibrate for a week at > 90 % RH as opposed to 340 min for the levitated particles. Longer experiments are not practicable during a synchrotron beamtime. Therefore the inverse hexagonal phase may indeed form in a levitated acid-soap complex particle if left to equilibrate over a period of days.

5 h after removal from the humidification chamber into room RH (~ 50 %), a phase separation is observed. Polarising microscopy pictures, in combination with Raman spectra of the birefringent and non-birefringent regions, confirm that there are two physically-distinct phases present after a 5 h equilibration time. It is suggested that the

birefringent phase, now presented as needle-like structures, is the acid–soap complex. This is confirmed by the Raman spectrum taken of this region (Fig. 10-24(c)). The non-birefringent region is assumed to be the inverse micellar phase, possibly with an excess of oleic acid as there was an excess to begin with.

10.6.8 **Water content determination and water uptake/loss model**

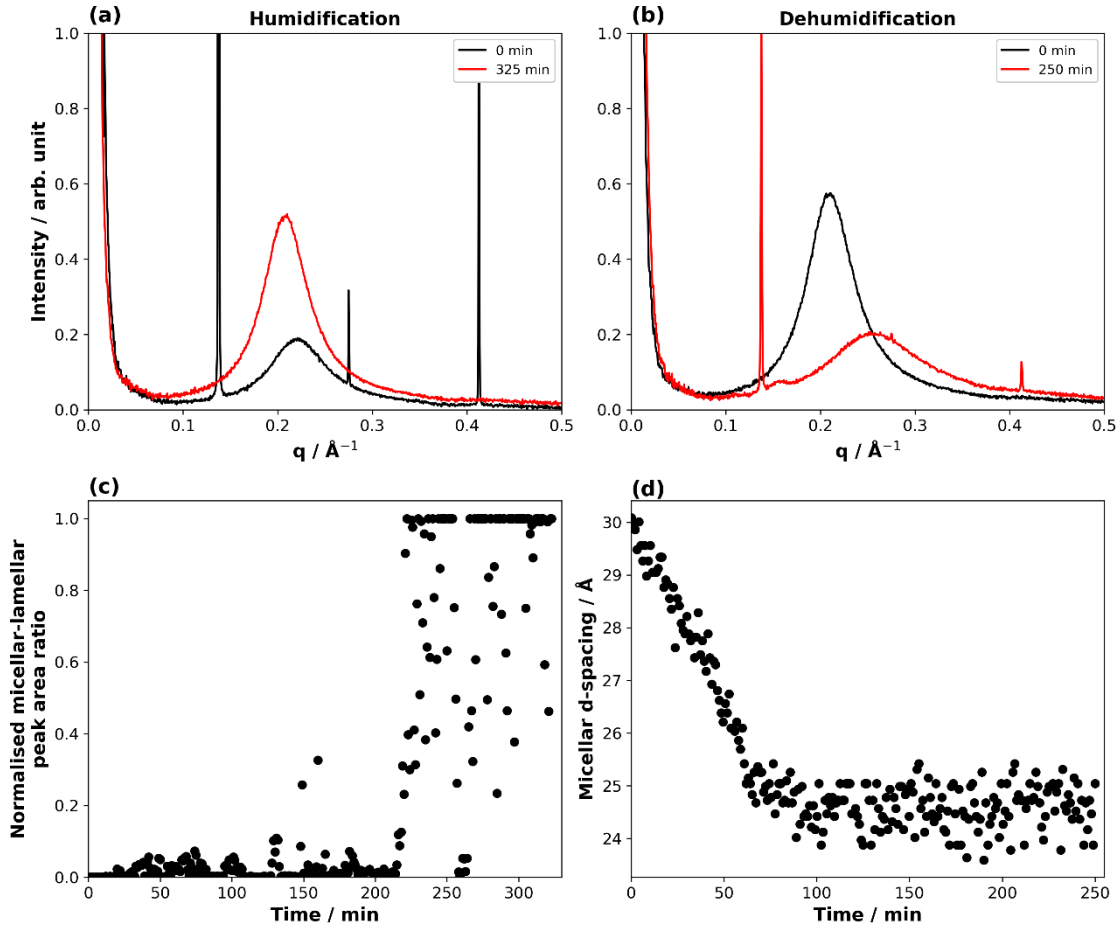

Figure 10-25. (a) & (b) SAXS patterns during humidification and dehumidification at the centre of the particle. Initial and final patterns presented to show the broad micellar peak centre (~ 0.20-0.26 Å^{-1}) change position and intensity relative to the lamellar peak. (c) normalised micellar-lamellar peak ratio vs time humidifying; (d) inverse micellar d-spacing vs time humidifying and dehumidifying.

As described in the *Water Diffusion Gradient during Humidity Change* section of the main text, the micellar-lamellar peak area ratio and micellar *d*-spacing were chosen as measures of water content for humidification and dehumidification, respectively. Micellar-lamellar peak area ratio data were noisy, especially once the particle had taken up a relatively large amount of water at ~ 230 min (Fig. 10-25(c)). Experimental micellar-lamellar peak area ratios which were greater than the median of ratios from 230 min onwards (*i.e.* the average maximum micellar-lamellar peak area ratio, accounting for the occasional large fluctuation) were set as that median value (2315) and this was assumed to be the value at maximum water content – all values are normalised to this number in Fig. 10-25(c). Very few datapoints were above this value and they occurred towards the end of the experiment, where the particle was completely inverse micellar (Fig. 7-1(i) in the main text – where there is no lamellar peak and integration of the lamellar peak position range returned the area of the noise around the background, resulting in some large apparent micellar-lamellar peak ratios).

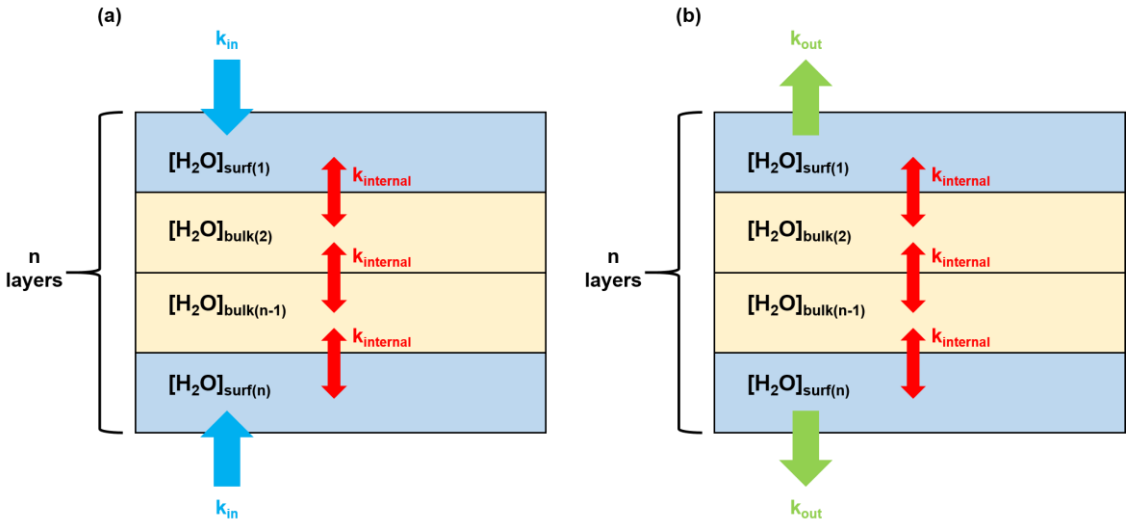

Figure 10-26. A schematic representation of the water uptake (a) and loss (b) model employed in this study.

Internal water diffusion was evolved in a Vignes-type fashion (*e.g.* Price *et al.*) (Price et al., 2015), relating water diffusion and layer composition (Eq. 10-17).

$$k_{internal,k} = (k_{micellar})^{\alpha[H_2O]_k}(k_{lamellar})^{1-\alpha[H_2O]_k} \quad (10\text{-}17)$$

$k_{\text{internal,k}}$ is the rate of internal diffusion in layer k; k_{micellar} and k_{lamellar} are the rates of water diffusion in the inverse micellar and crystalline lamellar phases, respectively; α is an activity coefficient which is assumed to be 1, analogous to the assumption of Davies and Wilson.(Davies and Wilson, 2016) $[H_2O]_k$ is the amount of water as a fraction of the maximum water content in layer k, which is assumed to be the equilibrium water content for the inverse micellar phase.

The water uptake model (Fig. 10-26(a)) is described by Eq. 10-18 and 10-19:

$$\frac{d[H_2O]_{surf}}{dt} = k_{in}([H_2O]_{max} - [H_2O]_{surf}) + k_{internal}([H_2O]_k - [H_2O]_{surf}) \quad (10\text{-}18)$$

$$\frac{d[H_2O]_k}{dt} = k_{internal,k}([H_2O]_{k+1} + [H_2O]_{k-1} - 2[H_2O]_k) \qquad 2 < k < n-1 \quad (10\text{-}19)$$

The water loss model (Fig. 10-26(b)) is described by Eq. 10-20 with internal diffusion described by Eq. 10-19:

$$\frac{d[H_2O]_{surf}}{dt} = -k_{out}([H_2O]_{surf} - [H_2O]_{min}) + k_{internal}([H_2O]_k - [H_2O]_{surf}) \quad (10\text{-}20)$$

The model splits the particle into a number of layers equivalent to the number of experimental positions (*n*) measured. The maximum ($[H_2O]_{max}$) and minimum ($[H_2O]_{min}$) amounts of water were set to 1 and 0, respectively in order to fit with the normalised experimental data. Each layer is given a number (*k*) with *k* = 1 & n being the top and bottom surface layers, with their respective amounts of water defined as $[H_2O]_{surf}$ in Eq. 10-18 & 10-20. The key parameters varied to fit the model with the data

were the rate of water uptake (k_{in} – water uptake), the rate of water loss (k_{out} – water loss), k_{micellar} and k_{lamellar}.

This model assumes: (i) constant rate of water uptake/loss into the particle – water uptake is expected to change with changing particle phase, however to avoid adding too many unknown parameters to the model we assume that it does not change; (ii) The particle is relatively flat and non-spherical – the particles levitated in this study are not spherical and spatially resolved data were of a vertical slice of the particle, the model reproduces this; (iii) there is a negligible rate of water loss during water uptake and *vice versa*; (iv) each model layer is well-mixed with no diffusion/water content gradient. Detailed modelling of differences in water uptake/loss rates into and from particles of different self-assembled phases is beyond the scope of this study and is the subject of ongoing work. The model presented here allows us to estimate the difference in water diffusivity between the inverse micellar and lamellar phases.

A Residual Sum of Squares (RSS) was calculated between the model and experiment and was used as a measure of goodness of fit, with lower values corresponding to better fits. Parameters were varied using a differential evolution algorithm whereby bounds are set for each parameter and parameter values are randomly selected from a population (Wormington et al., 1999). Each parameter is then "mutated" in an iterative process, each time the better-fitting parameter is kept. The algorithm eventually converges to an output which returns the minimum RSS value. The best fitting parameters are summarised in Table 10-7.

Model	k_{in} / x10^{-3}	k_{out} / x10^{-3}	$k_{micellar}$ / x 10^{-3}	$k_{lamellar}$ / x 10^{-3}	RSS_{fit}
Uptake	3.9	N/A	590	16	209
Loss	N/A	23	600	18	25

Table 10-7. Optimised water uptake and loss model parameters with the minimised RSS (RSS_{fit}) quoted for both models.

Although the parameters obtained from the model have no physically meaningful units, the ratio between $k_{micellar}$ and $k_{lamellar}$ is ~ 33, highlighting the large difference in water diffusivity between the inverse micellar and crystalline lamellar phase. We must stress that the model fails to capture the prompt deliquescence well during humidification.

10.6.9 **Hexagonal phase in an excess-water mixture of oleic acid-sodium oleate**

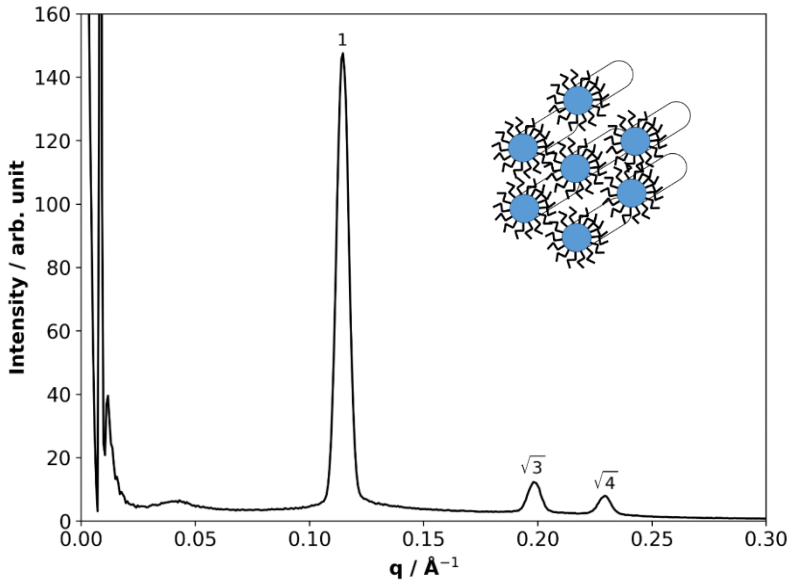

Figure 10-27. 1–D SAXS pattern of oleic acid-sodium oleate (1:1 wt) mixed with water as a 30 wt % organic mixture. Numbers above the peaks represent the characteristic peak position ratios expected for the inverse hexagonal phase. A cartoon representation of the inverse hexagonal phase is also presented.

10.6.10 **WAXS pattern of levitated oleic acid**

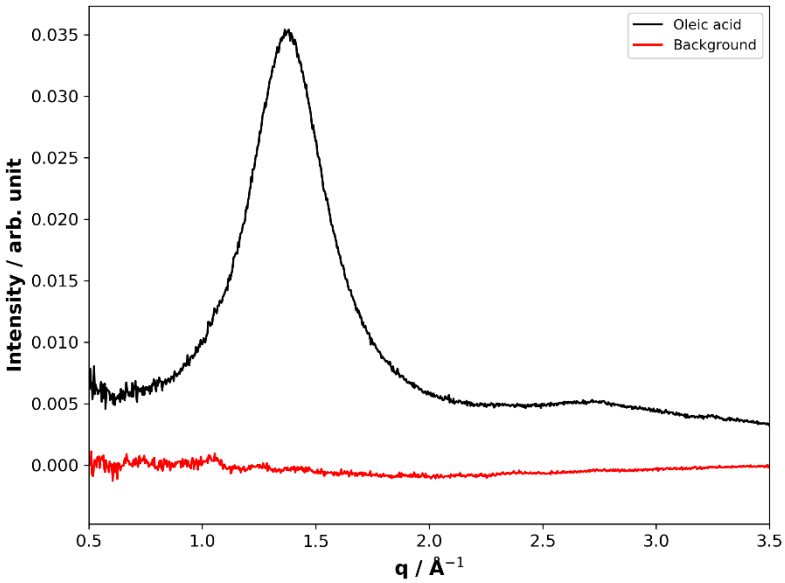

Figure 10-28. WAXS pattern of the centre of a levitated droplet of oleic acid compared with a background pattern of an empty levitator. This clearly demonstrates that oleic acid has a WAXS pattern. The alkyl chain spacing measured from this pattern is ~ 4.57 Å.

10.6.11 **SAXS pattern of a levitated particle of 2:1 wt (oleic acid : sodium oleate) composition**

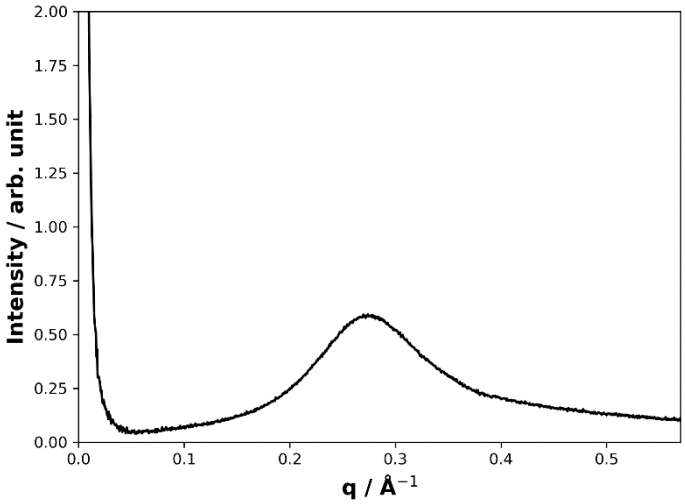

Figure 10-29. A levitated particle of 2:1 wt (oleic acid : sodium oleate) composition demonstrating a broad peak characteristic of the inverse micellar phase with a d-spacing of 36 Å. RH ~ 50 %.

10.7 Supporting information for chapter 8

10.7.1 Image analysis

Images taken by the macroscope were processed using a *Python* script. The image was read-in and the levitated particles were defined by setting a threshold light intensity. Particles were easily defined due to the very low background light afforded by the polarising filters (see Fig. 8-1). The sum of the intensity for each droplet was calculated for each image taken during humidification. This was then normalised to the initial intensity value to form the experimental data presented in this study.

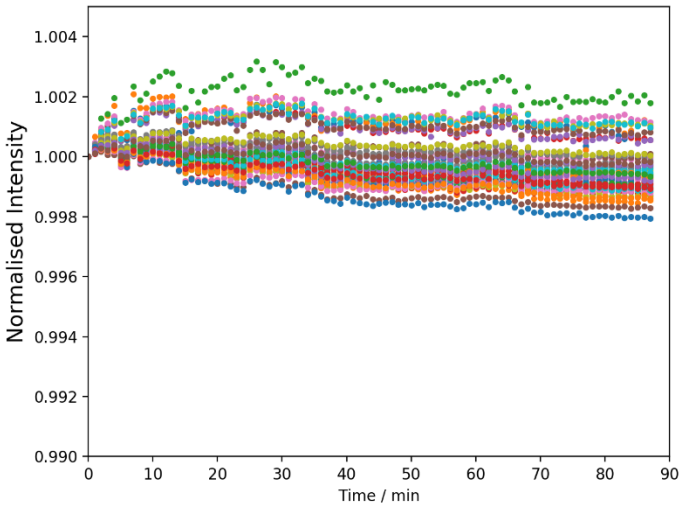

Figure 10-30. Normalised intensity vs time for 46 particles deposited simultaneously on a microscope slide. Data from each particle is represented by a different colour.

Uncertainty due to variations in the light source intensity was determined by nebulising the proxy sample and collecting 46 particles on a microscope slide. This microscope slide was placed inside the levitation-POM chamber and the intensity of each of these birefringent particles was measured for 89 min. We found that the light intensity for each particle varied on by *ca.* ± 0.15 % of the initial intensity. This was used as the absolute uncertainty associated with each experimental data point.

There seems to be a systematic increase or decrease in particle birefringence intensity depending on the particle measured. These variations are however very small and would have had little impact on the experimental data presented in chapter 8.

Particle size was determined by measuring the diameter of the particle in pixels, a graticule was used to calibrate the particle size in physical units (µm). Particles were 165 – 260 µm in diameter.

10.7.2 **Multi-layer water uptake model description**

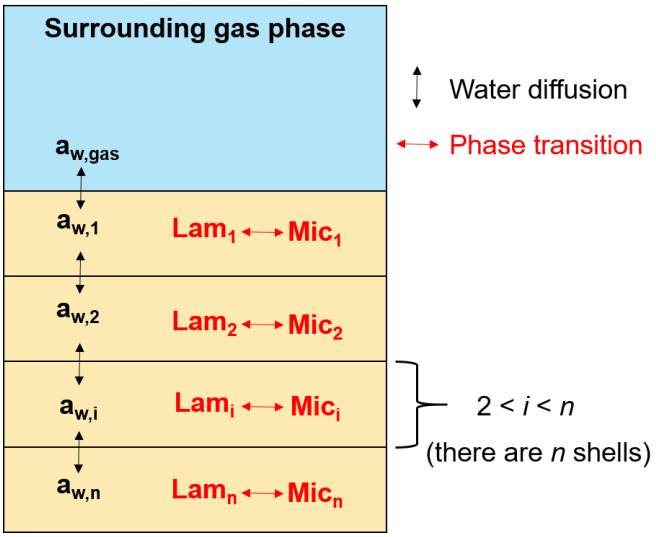

Figure 10-31. A schematic of the water uptake model created for this study. Water diffusion between the gas phase and particle layers is represented by the black arrows. Phase transition between the lamellar (Lam) and the close-packed inverse micellar (Mic) phase in each layer is represented by the red arrows. a_w is the water activity. There are n layers (shells) in the model.

Figure 10-31 describes the model, which accounts for: composition-dependent uptake and loss of water to and from the particle; composition-dependent diffusion of water between model layers and the surfactant phase transition from lamellar bilayer to close-packed inverse micelles.

The amount of water is represented as water activity (a_w) in the model. The use of a_w returned the best fits to the experimental data.

The spherical particle is split into a number (n) of layers. The amount of water in model layer i is described by eq. 10-21, where $1< i < n$-1:

$$\frac{d(a_w)_i}{dt} = k_{b,b,w,i}\left(a_{w,i-1} - a_{w,i}\right)\frac{A_i}{V_i} + k_{b,b,w,i+1}\left(a_{w,i+1} - a_{w,i}\right)\frac{A_{i+1}}{V_i} \qquad (10\text{-}21)$$

A_i is the surface area of layer i, V_i is the volume of shell i and $k_{b,b,w,i}$ is the rate of water transport within layer i. The core layer (n) only includes water transfer between this layer and layer n -1.

A relationship between $k_{b,b,w,I}$, water diffusivity (D_w) and layer thickness (δ) for each layer is given as per Shiraiwa et al.:

$$k_{b,b,w,i} = \frac{4D_{w,i}}{\pi\delta} \qquad (10\text{-}22)$$

Water uptake and loss to and from the particle is accounted for in the first model layer:

$$\frac{d(a_w)_1}{dt} = k_{b,w,1}\left(a_{w,2} - a_{w,1}\right)\frac{A_2}{V_1} + \left(J_{abs} - J_{des}\right)\frac{A_1}{V_1} \qquad (10\text{-}23)$$

This model accounts for differences in the rate of water uptake to the surface layer due to differences in water diffusivity that are expected between phases. Most notably, diffusion in the lamellar phase is highly anisotropic and depends on the orientation of the lamellar planes.(Lindblom and Orädd, 1994; Lindblom and Wennerström, 1977) We observed that the lamellae are highly oriented at the surface in this study. This difference is accounted for by introducing J_{abs} and J_{des}, which are the rate of water absorption and desorption, respectively:

$$J_{ads} = \{k_{a,lam}\, f_{lam,1} + k_{a,mic}\ (1 - f_{lam,1})\} \times (a_{w,gas} - a_{w,1}) \qquad (10\text{-}24)$$

$$J_{des} = -\{k_{d,lam} f_{lam,1} + k_{d,mic} (1 - f_{lam,1})\} \times (a_{w,1} - a_{w,gas}) \quad (10\text{-}25)$$

J_{ads} and J_{des} are incorporate the rate constant for water adsorption ($k_{a,lam}$ / $k_{a,mic}$) and loss ($k_{d,lam}$ / $k_{d,mic}$) for the lamellar and inverse micellar phases, respectively. The dependence on the amount of surface layer lamellar phase is accounted for by calculating the fraction of the lamellar phase in the first layer ($f_{lam,1}$). J_{ads} and J_{des} are also dependent on the a_w gradient between the first layer ($a_{w,1}$) and the gas phase ($a_{w,gas}$).

Phase change from the lamellar to the close-packed inverse micellar phase, observed for this system, is accounted for in the model. This was dependent on rate constants for micellar phase (k_{mic}) and lamellar phase (k_{lam}) formation and a_w in each layer:

$$\frac{d[Lam]_i}{dt} = k_{lam}[Mic]_i - k_{mic}[Lam]_i a_{w,i} \quad (10\text{-}26)$$

$$\frac{d[Mic]_i}{dt} = k_{mic}[Lam]_i a_{w,i} - k_{lam}[Mic]_i \quad (10\text{-}27)$$

The amount of lamellar ([*Lam*]) and (ordered) inverse micellar ([*Mic*]) phase in each layer is effectively their mass fraction. The model was initialised so that [*Lam*] = 100 and [*Mic*] = 0 in each layer. Written this way, the model maintains the total amount of self-assembled surfactant – *i.e.* [*Lam*] + [*Mic*] = 100. The assumption that no organic mass is lost is valid due to the low vapour pressure of oleic acid and sodium oleate.

k_{mic} was parameterised as a function of a_w in order to consider phase transition boundaries. We determined the lamellar-to-inverse micellar phase transition to start at ~ 55 % RH (see ESI). Below this value, the following parameterisation was used to describe the steep decrease in lamellar-to-inverse micellar transition likelihood once a_w drops below phase transition water activity ($a_{w,trans}$).

$$k_{mic}\,(a_w) = \; k_{mic}\,\frac{(a_w)^p}{(a_{w,trans})^p} \quad , \; where\; a_w < \; a_{w,trans} \qquad (10\text{-}28)$$

p is a fitting parameter used during the optimisation process. $a_{w,trans}$ makes it possible to include other phase transitions in the model if other phase transitions are observed for a system.

10.7.3 Scattering pattern from a randomly oriented lamellar phase

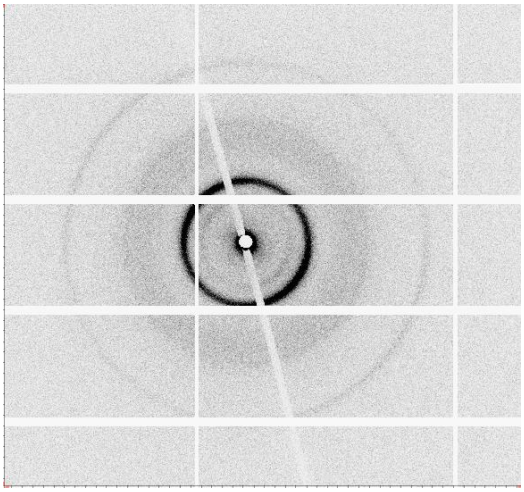

Figure 10-32. A 2-D SAXS pattern from the centre of a levitated oleic acid-sodium oleate particle at a 1:1 wt ratio. The intense inner scattering ring and outer two rings are consistent with the lamellar phase. There is no radial intensity variation for each ring, meaning this is an isotropic (randomly oriented) lamellar phase.

10.7.4 Optimised model parameters

Model parameter	*Description*	*Optimised value (220 & 260 µm diameter particles)*	*Optimised value (165 & 190 µm diameter particles)*
$k_{a,lam}$	Rate of water absorption into the surface lamellar phase (s^{-1})	7.59×10^{-2}	8.06×10^{-2}
$k_{a,mic}$	Rate of water absorption into the surface close-packed inverse micellar phase (s^{-1})	3.81×10^{-1}	7.69×10^{-1}
$k_{d,lam}$	Rate of water loss from the surface lamellar phase (s^{-1})	3.50×10^{-3}	6.94×10^{-4}
$k_{d,mic}$	Rate of water loss from the surface close-packed inverse micellar phase (s^{-1})	7.03×10^{-3}	7.84×10^{-3}
k_{mic}	Rate of close-packed inverse micellar phase formation (s^{-1})	4.09×10^{-3}	6.48×10^{-3}
k_{lam}	Rate of lamellar phase formation (s^{-1})	1.96×10^{-3}	1.51×10^{-3}
$D_{w,lam}$	Diffusion coefficient of water through the lamellar phase ($cm^2\ s^{-1}$)	[2.79×10^{-9}]*	[3.08×10^{-9}]*
$D_{w,mic}$	Diffusion coefficient of water through the close-packed inverse micellar phase ($cm^2\ s^{-1}$)	[9.51×10^{-4}]*	[9.00×10^{-4}]*
p	Fitting parameter to account for the lamellar-to-close-packed inverse micellar phase boundary	9.97	9.88

*Table 10-8. Model parameters varied during global optimisation. *Diffusion coefficients were converted from model values to physically meaningful values utilising Dw,mic reported by Hendrikx et al. (2.4 x 10^{-8} cm^2 s^{-1})*(Hendrikx et al., 1994).

10.7.5 **The levitation-polarising optical experiment with a webcam**

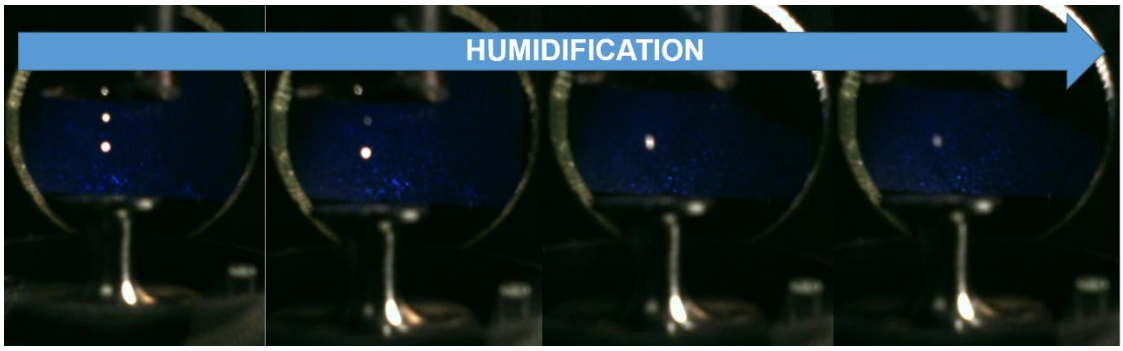

Figure 10-33. Images of an experiment carried out with the experimental setup described in this study, but with a webcam in place of the macroscope. 3 droplets are levitated and humidified. The birefringence of the particles decreased with continued exposure to 90 % RH. Focussing was not as optimal as was achieved with the macroscope.

10.8 **Ozoniser calibration**

The ozonisers were calibrated by UV-VIS spectroscopy by following the absorption band of ozone at 254 nm. Using the absorption cross-section (σ_{ext}) for ozone at this wavelength ((1.14 ± 0.07) x 10^{-17} cm^2) (Mauersberger et al., 1986), one can calculate the ozone concentration:

$$[O_3] = \frac{A_{254}}{(\sigma_{ext} \times l)} \qquad (10\text{-}29)$$

Where A_{254} is the mean absorbance of the gas cell (at least 3 measurements taken at a particular ozoniser/flow setting) and l is the path length of the gas cell.

The desired ozone-oxygen mixture was flowed through the gas cell in order to ensure the volume of the gas cell was replaced at least 3 times. The UV-VIS measurement was carried out immediately after.

For studies in chapter 2, 5 and 7, the ozone concentration was calibrated at the one oxygen flow/ozoniser setting used for these studies. The ozoniser setting refers to how much of the flowing gas is exposed to the UV lamp, controlled by a graduated metal sleeve.

An example calibration plot over a range of ozoniser settings is presented below.

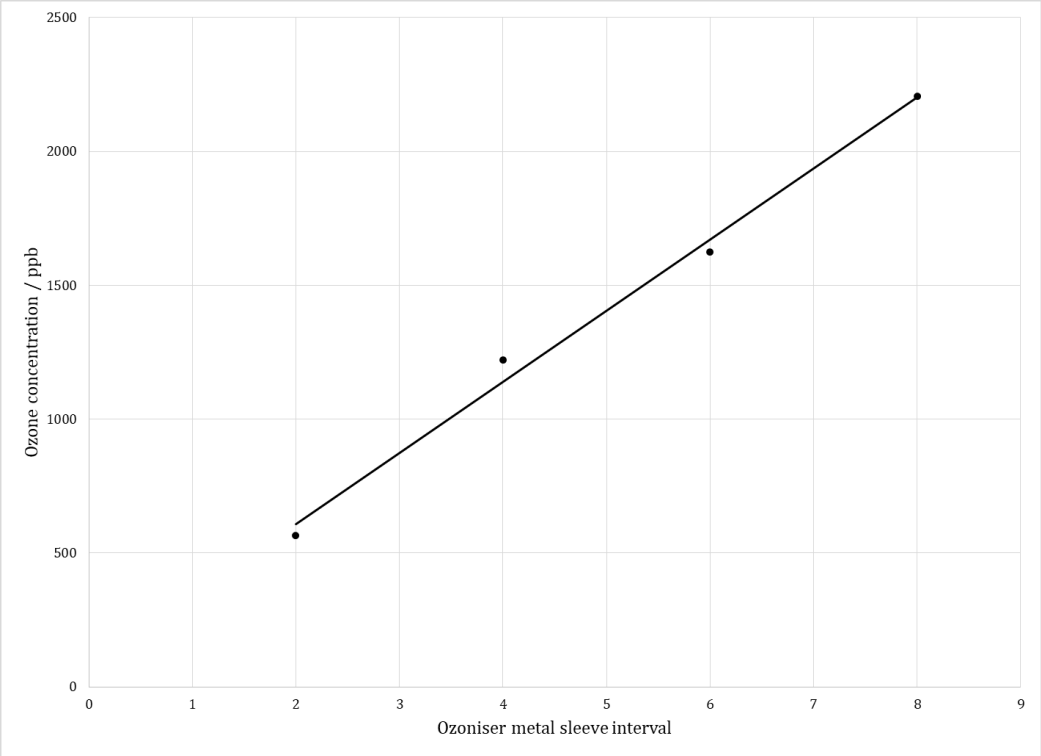

Figure 10-34. Ozoniser calibration plot. Ozone concentration (ppb) vs ozoniser metal sleeve interval. Higher intervals means more UV light exposure. Flow rate = 1.2 L min^{-1}.

10.9 **References**

Asghar, K. A., Rowlands, D. A., Elliott, J. M. and Squires, A. M.: Predicting Sizes of Hexagonal and Gyroid Metal Nanostructures from Liquid Crystal Templating, ACS Nano, 9(11), 10970–10978, doi:10.1021/acsnano.5b04176, 2015.

Cistola, D. P., Atkinson, D., Hamilton, J. A. and Small, D. M.: Phase Behavior and Bilayer Properties of Fatty Acids: Hydrated 1:1 Acid-Soaps, Biochemistry, 25(10), 2804–2812, doi:10.1021/bi00358a011, 1986.

Clerc, M.: A New Symmetry for the Packing of Amphiphilic Direct Micelles, J. Phys. II, 6(7), 961–968, doi:10.1051/jp2:1996110, 1996.

Dalgliesh, R.: Application of off-specular scattering of X-rays and neutrons to the study

of soft matter, Curr. Opin. Colloid Interface Sci., 7(3–4), 244–248, doi:10.1016/S1359-0294(02)00054-7, 2002.

Davies, J. F. and Wilson, K. R.: Raman Spectroscopy of Isotopic Water Diffusion in Ultraviscous, Glassy, and Gel States in Aerosol by Use of Optical Tweezers, Anal. Chem., 88(4), 2361–2366, doi:10.1021/acs.analchem.5b04315, 2016.

Engblom, J., Engström, S. and Fontell, K.: The effect of the skin penetration enhancer Azone® on fatty acid-sodium soap-water mixtures, J. Control. Release, 33(2), 299–305, doi:10.1016/0168-3659(94)00105-4, 1995.

Hafner, A., Gutfreund, P., Toperverg, B. P., Jones, A. O. F., de Silva, J. P., Wildes, A., Fischer, H. E., Geoghegan, M. and Sferrazza, M.: Combined specular and off-specular reflectometry: elucidating the complex structure of soft buried interfaces, J. Appl. Crystallogr., 54(3), 924–948, doi:10.1107/S1600576721003575, 2021.

Hendrikx, Y., Sotta, P., Seddon, J. M., Dutheillet, Y. and Bartle, E. A.: NMR self-diffusion measurements in inverse micellar cubic phases, Liq. Cryst., 16(5), 893–903, doi:10.1080/02678299408027860, 1994.

Hosny, N. A., Fitzgerald, C., Vyšniauskas, A., Athanasiadis, A., Berkemeier, T., Uygur, N., Pöschl, U., Shiraiwa, M., Kalberer, M., Pope, F. D. and Kuimova, M. K.: Direct imaging of changes in aerosol particle viscosity upon hydration and chemical aging, Chem. Sci., 7(2), 1357–1367, doi:10.1039/c5sc02959g, 2016.

Kulkarni, C. V., Wachter, W., Iglesias-Salto, G., Engelskirchen, S. and Ahualli, S.: Monoolein: a magic lipid?, Phys. Chem. Chem. Phys., 13(8), 3004–3021, doi:10.1039/C0CP01539C, 2011.

Lindblom, G. and Orädd, G.: NMR Studies of translational diffusion in lyotropic liquid crystals and lipid membranes, Prog. Nucl. Magn. Reson. Spectrosc., 26, 483–515, doi:10.1016/0079-6565(94)80014-6, 1994.

Lindblom, G. and Wennerström, H.: Amphiphile diffusion in model membrane systems studied by pulsed NMR, Biophys. Chem., 6(2), 167–171, doi:10.1016/0301-4622(77)87006-3, 1977.

Lynch, M. L., Pan, Y. and Laughlin, R. G.: Spectroscopic and thermal characterization of 1:2 sodium soap/fatty acid acid-soap crystals, J. Phys. Chem., 100(1), 357–361, doi:10.1021/jp952124h, 1996.

Mantsch, H. H., Weng, S. F., Yang, P. W. and Eysel, H. H.: Structure and thermotropic phase behavior of sodium and potassium carboxylate ionomers, J. Mol. Struct., 324(1–2), 133–141, doi:10.1016/0022-2860(93)08234-U, 1994.

Mauersberger, K., Barnes, J., Hanson, D. and Morton, J.: Measurement of the ozone absorption cross-section at the 253.7 nm mercury line, Geophys. Res. Lett., 13(7), 671–673, doi:10.1029/GL013i007p00671, 1986.

Mele, S., Söderman, O., Ljusberg-Wahrén, H., Thuresson, K., Monduzzi, M. and Nylander, T.: Phase behavior in the biologically important oleic acid/sodium oleate/water system, Chem. Phys. Lipids, 211, 30–36, doi:10.1016/j.chemphyslip.2017.11.017, 2018.

Meznarich, N. A. K., Juggernauth, K. A., Batzli, K. M. and Love, B. J.: Structural changes in PEO-PPO-PEO gels induced by methylparaben and dexamethasone observed using time-resolved SAXS, Macromolecules, 44(19), 7792–7798, doi:10.1021/ma2015358, 2011.

Milsom, A., Squires, A. M., Woden, B., Terrill, N. J., Ward, A. D. and Pfrang, C.: The persistence of a proxy for cooking emissions in megacities: a kinetic study of the ozonolysis of self-assembled films by simultaneous small and wide angle X-ray scattering (SAXS/WAXS) and Raman microscopy, Faraday Discuss., 226, 364–381, doi:10.1039/D0FD00088D, 2021.

Nájera, J. J.: Phase transition behaviour of sodium oleate aerosol particles, Atmos. Environ., 41(5), 1041–1052, doi:10.1016/j.atmosenv.2006.09.016, 2007.

Pfrang, C., Rastogi, K., Cabrera-Martinez, E. R., Seddon, A. M., Dicko, C., Labrador, A., Plivelic, T. S., Cowieson, N. and Squires, A. M.: Complex three-dimensional self-assembly in proxies for atmospheric aerosols, Nat. Commun., 8(1), 1724, doi:10.1038/s41467-017-01918-1, 2017.

Price, H. C., Mattsson, J., Zhang, Y., Bertram, A. K., Davies, J. F., Grayson, J. W., Martin, S. T., O'Sullivan, D., Reid, J. P., Rickards, A. M. J. and Murray, B. J.: Water diffusion in atmospherically relevant α-pinene secondary organic material, Chem. Sci., 6(8), 4876–4883, doi:10.1039/c5sc00685f, 2015.

Seddon, A. M., Richardson, S. J., Rastogi, K., Plivelic, T. S., Squires, A. M. and Pfrang, C.: Control of Nanomaterial Self-Assembly in Ultrasonically Levitated Droplets, J. Phys. Chem. Lett., 7(7), 1341–1345, doi:10.1021/acs.jpclett.6b00449, 2016.

Seddon, J. M., Bartle, E. A. and Mingins, J.: Inverse cubic liquid-crystalline phases of phospholipids and related lyotropic systems, J. Phys. Condens. Matter, 2, SA285–SA290, doi:10.1088/0953-8984/2/S/043, 1990.

Speagle, J. S.: DYNESTY: a dynamic nested sampling package for estimating Bayesian posteriors and evidences, Mon. Not. R. Astron. Soc., 493(3), 3132–3158,

doi:10.1093/MNRAS/STAA278, 2020.

Tandon, P., Förster, G., Neubert, R. and Wartewig, S.: Phase transitions in oleic acid as studied by X-ray diffraction and FT- Raman spectroscopy, J. Mol. Struct., 524(1–3), 201–215, doi:10.1016/S0022-2860(00)00378-1, 2000a.

Tandon, P., Neubert, R. and Wartewig, S.: Thermotropic phase behaviour of sodium oleate as studied by FT-Raman spectroscopy and X-ray diffraction, J. Mol. Struct., 526(1–3), 49–57, doi:10.1016/S0022-2860(00)00441-5, 2000b.

Tandon, P., Raudenkolb, S., Neubert, R. H. H., Rettig, W. and Wartewig, S.: X-ray diffraction and spectroscopic studies of oleic acid-sodium oleate, Chem. Phys. Lipids, 109(1), 37–45, doi:10.1016/S0009-3084(00)00207-3, 2001.

Wormington, M., Panaccione, C., Matney, K. M. and Bowen, D. K.: Characterization of structures from X-ray scattering data using genetic algorithms, Philos. Trans. R. Soc. London A A, 357, 2827–2848, 1999.